Creep behaviour of Laser Powder Bed Fused alloy 718

January 2022

Salomé Sanchez
Department of Mechanical, Materials and Manufacturing Engineering
University of Nottingham

Supervisors: C. J. Hyde, A. T. Clare, I. A. Ashcroft

Keywords: Laser Powder Bed Fusion; Alloy 718; Nickel-based superalloys; Creep; Fractography; Microstructural evolution

Abstract

Laser Powder Bed Fusion (LPBF) is characterised by high design flexibility and no tooling requirement. This makes LPBF attractive to many modern manufacturing sectors (e.g. aerospace, defence, energy and automotive). Nickel-based superalloys are crucial materials in modern engineering and underpin the performance of many advanced mechanical systems. Their physical properties (high mechanical integrity at high temperature) make them difficult to process via traditional techniques. Consequently, manufacture of nickel-based superalloys using LPBF has attracted significant attention.

However, components manufactured by LPBF are currently limited by their performance for use in critical applications. LPBF materials have microstructural defects, such as suboptimal grain size and morphology, and macroscale anomalies, such as lack of fusion. This results in LPBF materials performing below their wrought counterparts for various mechanical properties, such as creep, which has seldom been researched. Consequently, heat treatment of products post additive manufacture is now considered hugely important and the development of appropriate heat treatment is required to ensure material performance. Furthermore, the build time of LPBF can be slower than traditional manufacturing processes, especially for higher volumes of parts. Multi-laser machines, which have the potential to significantly reduce process time do exist, but there is currently little understanding of how interlaced scan strategies impact mechanical properties.

Therefore, to permit a wider application, a deeper understanding of the mechanical behaviour, particularly of creep properties, of LPBF nickel-based superalloys needs to be achieved. Hence, the aim of this work is to establish process-structure-property relationships for the creep properties of LPBF nickel-based superalloy, to benchmark it against wrought equivalents and to provide insights on how to improve the creep performance.

To do this, LPBF alloy 718 parts were fabricated using various scan strategies, build orientations and both single and multi-laser strategies, before being heat treated and creep tested. Results confirmed the necessity for heat treatment, which increased the creep life by a factor of 5. The build orientation, and its effect on the grain orientation as well as the stress state of the material were shown to be determining factors in the creep failure mechanisms. The meander scanning strategy resulted in a 58% increase in creep life compared to the stripe strategy, due to the detrimental effects of the numerous laser overlapping regions in the stripe strategy. There are numerous parameters, such as the fraction area of solidified layer, the fraction of powder underneath the layer and the interlayer rotation of the scan strategy that vary for each layer and means the layers themselves as well as the samples were heterogenous. Despite this, the creep life for any given sample was within 73h (i.e.17%) of its repeats, giving confidence in the results.

The results also showed that multi-laser scan strategies have no adverse effects on the creep properties of LPBF alloy 718 at different build orientations, demonstrating the potential of using multi-laser strategies for faster build rates without compromising the mechanical properties. Indeed, it is shown that for samples built vertically (i.e. where the build direction is parallel to the loading direction), multi-laser samples outperformed their single-laser counterparts and had a similar creep life and secondary creep rate to wrought alloy (1% difference). The presence of numerous large globular carbides in the wrought alloy 718 were also identified as the reason for the material's curtailed creep life, compared to its LPBF counterpart, despite having a similar creep rate. Finally, for a given strategy, a 24% increase in creep life compared to wrought alloy 718 was observed. This specimen was explored under thermomechanical and thermal exposure conditions for the purpose of illustrating textural and microstructural evolution and inform a potential heat treatment to improve creep performance.

The results showed the instability of the LPBF microstructure in terms of grain size, precipitate density and crystallographic orientation during creep and thermal exposure, proof of the need for an appropriate heat treatment. The texture increased throughout creep testing for the wrought and LPBF alloy 718, reaching a maximum at the time of fracture. This contrasted with the thermal exposure only, where the instability of the LPBF alloy 718 microstructure was evident as the texture increased with time before decreasing and almost disappearing at the time of fracture. This also highlighted the different roles of the build and loading directions on the texture creation and evolution during creep. Finally, an ideal microstructure for improved creep performance was identified and recommendations on how to heat treat LPBF alloy 718 to reach this microstructure were given.

Overall, this thesis shows that LPBF components can become more performant than wrought and conventional equivalents by developing an appropriate heat treatment and provides an insight into process-structure-property relationships for the creep properties of LPBF alloy 718. The results are promising, despite future work being required and this work demonstrates the applicability of using LPBF for critical high temperature applications.

Publications

Included in thesis:

- Salomé Sanchez, Peter Smith, Zhengkai Xu, Gabriele Gaspard, Christopher J. Hyde, Wessel W. Wits, Ian A. Ashcroft, Hao Chen, Adam T. Clare, **Powder Bed Fusion of nickel-based superalloys: A review**, *International Journal of Machine Tools and Manufacture*, Volume 165, 2021, 103729, ISSN 0890-6955, https://doi.org/10.1016/j.ijmachtools.2021.103729.

- S. Sanchez, G. Gaspard, C.J. Hyde, I.A. Ashcroft, Ravi G.A., A.T. Clare, **The creep behaviour of nickel alloy 718 manufactured by laser powder bed fusion**, *Materials & Design*, Volume 204, 2021, 109647, ISSN 0264-1275, https://doi.org/10.1016/j.matdes.2021.109647.

- Salomé Sanchez, C.J. Hyde, I.A. Ashcroft, Ravi G.A., A.T. Clare, **Multi-laser scan strategies for enhancing creep performance in LPBF**, *Additive Manufacturing*, Volume 41, 2021, 101948, ISSN 2214-8604, https://doi.org/10.1016/j.addma.2021.101948.

- Submitted - S. Sanchez, G. Gaspard, C.J. Hyde, I.A. Ashcroft, Ravi G.A., A.T. Clare, **On the thermomechanical aging of LPBF alloy 718**, *Materials Engineering and Science A.*

Not included in thesis:

- Sanchez, S., Rengasamy, D., Hyde, C.J., G.P. Figueredo, B. Rothwell, **Machine learning to determine the main factors affecting creep rates in laser powder bed fusion**. *Journal of Intelligent Manufacturing* (2021). https://doi-org.ezproxy.nottingham.ac.uk/10.1007/s10845-021-01785-0.

Table of contents

Abstract 3
Publications 5
Table of contents 6
List of figures 8
List of tables 25
Nomenclature 28
1 Introduction 29
2 Literature review 39
2.1 Powder bed fusion 39
2.1.1 Process 39
2.1.2 Microstructure 40
2.2 Alloy 718 46
2.2.1 Process parameters driven phenomena 48
2.2.2 Post-processing for component performance 53
2.3 Creep properties 67
2.3.1 Fundamentals of creep 67
2.3.2 Creep of PBF materials 71
2.3.3 Effect of laser powder bed fusion process parameters 75
2.3.4 Heat treatment for enhanced creep performance 76
2.4 Summary of findings 77
3 Experimental methods 79
3.1 Laser powder bed fusion 79
3.2 Post-processing 83
3.3 Creep testing 84
3.4 Analysis and data processing 85
4 Microstructure 91
4.1 Wrought alloy 718 91
4.2 Laser powder bed fused alloy 718 93
4.2.1 As-built and heat-treated 93
4.2.2 Meander and stripe scan strategies 98
4.2.3 Build orientations 101
4.2.4 Multi-laser scan strategies 103
4.3 Effect of heat treatment 108

4.4 Effect of laser powder bed fusion process parameters 109
4.4.1 Effect of scan strategies..............................109
4.4.2 Effect of build orientation..............................110
4.4.3 Effect of multi-laser scan strategies..............................112
4.5 Summary of findings..............................114
5 Creep behaviour..............................115
5.1 Wrought alloy 718 115
5.2 Laser powder bed fused alloy 718 117
5.2.1 As-built and heat treated..............................120
5.2.2 Meander and stripe scan strategies 123
5.2.3 Build orientations..............................126
5.2.4 Multi-laser scan strategies 130
5.3 Effect of laser powder bed fusion microstructure 135
5.3.1 Effect of porosity 135
5.3.2 Effect of precipitates 135
5.3.3 Effect of grain size and morphology..............................138
5.3.4 Effect of crystallographic orientation..............................140
5.4 Effect of heat treatment 141
5.5 Effect of laser powder bed fusion process parameters 142
5.5.1 Effect of scan strategies..............................142
5.5.2 Effect of build orientation..............................143
5.5.3 Effect of multi-laser scan strategies..............................145
5.6 Summary of findings..............................146
6 Microstructural evolution 147
6.1 Microstructure during creep 147
6.1.1 Wrought alloy 718..............................150
6.1.2 90° single-laser Meander HT specimen 151
6.1.3 90° single-laser Meander HT specimen during thermal exposure ... 154
6.2 Evolution of microstructural features 155
6.2.1 Evolution of porosity..............................155
6.2.2 Evolution of texture 156
6.2.3 Evolution of grain size and morphology 158
6.2.4 Evolution of precipitates..............................159
6.3 Strategies for improved creep performance..............................162
6.4 Summary of findings..............................166
Conclusion 167

Acknowledgments **169**
References **171**

List of figures

Figure 6.1: Layout of the build directions and principal planes commonly used when highlighting anisotropy in PBF specimens. Noting the orientation of this primitive is commonly considered to align with the machine coordinate system......................28

Figure 1.1: 'Weldability' diagram for a range of nickel-based superalloys as a function of their Ti and Al alloy element composition. Figure from Catchpole-Smith et al. [11]. Weldability is considered poor above the dashed line and deteriorates with increasing Ti and Al content. This work will inform future research on alloy compositions...31

Figure 1.2: Number of publications on AM of nickel-based superalloys (from Scopus database) with major milestones [12-18].This shows an increase in publications associated with nickel-based materials in AM. 32

Figure 1.3: Inconel 625 filter with placement specific pore orientation and cross-sectional area. These samples were manufacture by powder bed fusion, demonstrating the ability of powder bed fusion to manufacture highly optimised geometries with features < 1 mm. This is an exemplary use of LPBF technology [22]. 33

Figure 1.4: Example of novel cooling channels in a leading edge. a) the overview. b) Computer Aided Design model of the internal structure of the cooling channels [20]. The average measured cooling hole size (0.39 mm) was slightly smaller than the nominal size (0.5 mm), highlighting tolerancing challenges still to be conquered in LPBF. 33

Figure 1.5: Pie chart showing the nickel-based superalloys studied in powder bed fusion research to date, from 290 studies (IN = Inconel). Inconel 718 and Inconel 625 are the most studied alloys given their level of usage primarily in the aerospace markets where there are immediate opportunities for aerospace. 35

Figure 1.6: Pie chart summarising the mechanical properties investigated in PBF nickel-based superalloys research, across 290 papers. Almost half of the studies investigated tensile properties, while a third studied hardness properties. Other properties, especially shear and toughness, have been the subject of limited studies. 35

Figure 2.1: Diagram of the two main PBF processes. a) LPBF. b) EBM. The two main differences, power sources and power transmission systems, are visible. After [37]. 39

Figure 2.2: Summary of defects present in PBF processes. This can serve as reference for commonly used terminology by practitioners [41]. 40

Figure 2.3: Images of as-built LPBF Inconel 718 specimens. a) Side view. b) Top view. c) The melt pool boundaries between layers. d) The melt pool boundaries between adjacent tracks from the side. The arrow in a) indicates the build direction (BD) and the circle in b) indicates the plane is perpendicular to the build direction. Melt pools in a) and laser scan tracks in b) are clearly visible. The yellow arrows in c) and d) represent the dendrite growth direction. They follow the build direction in c) and have no preferred direction in d) [42]. These images illustrate the particular anisotropic microstructure resulting from the PBF processes................................. 41

Figure 2.4: EBSD maps of an as-built LPBF Inconel 718 specimen [43]. This shows the dominant direction of grain growth and strong <100> crystallographic texture in the build direction, which is characteristic of PBF processes. Individual laser scan tracks with small equiaxed grains track the overlapping regions can also be seen in the XY plane (perpendicular to the building direction). 41

Figure 2.5: Typical examples of SEM images of phenomena in AM nickel-based superalloys. a) An overview of the interface between adjacent layers. b) The interdendritic region. Mark 1 indicates the layer-layer melt pool boundary, 2 indicates the dendritic cell tips, 3 and 4 highlight some γ + Laves phase eutectic, 5 points a MC carbide [47]. These features are caused by the rapid heating and cooling during the LPBF process...42

Figure 2.6: As-built EBM Inconel 718 microstructure and EDS results (quantified in Table 2.2) [48]. This shows that Laves phases and MC carbides are present in the as-built state, as well as large disk-shaped γ'' particles...43

Figure 2.7: SEM micrographs of an as-built EBM Inconel 718 sample. a) The top of the sample (few thermal cycles). b) The bottom of the sample (many thermal cycles) [49]. This shows a variation in microstructure along the build direction, particularly regarding δ particles which are coarser at the top a)...44

Figure 2.8: EBSD data of grains surrounding a defect. a) The columnar grains surrounding the fusion defect. b) The equiaxed grains above the defect [51]. This shows that defects also affect the build process and resulting microstructural morphology in PBF processes. 44

Figure 2.9: Microstructural cubes of hot isostatically pressed Inconel 625. a) Processed by EBM. b) Processed by LPBF. Showing the differences in microstructure produced by the different processes [52], such as grain morphology and size.........46

Figure 2.10: Transformation-time-temperature diagram of alloy 718 [66]. Copyright American Welding Society, 1986. 47

Figure 2.11: Powders and corresponding laser powder bed fused specimens [87]. a) Gas atomized powder at 100 µm scale. b) Rotary atomized powder at 100 µm scale. c) Plasma rotated electrode processed powder at 100 µm scale. d) Gas atomized powder at 200 µm scale. e) Rotary atomized powder at 200 µm scale. f) Plasma rotated electrode processed powder at 200 µm scale. The plasma rotated electrode processed powder showed a smoother surface and almost no internal trapped gas, compared to the others, illustrating the importance and effect of powder types on the resulting microstructure of PBF materials. 49

Figure 2.12: Typical scan strategies as demonstrated in the Renishaw 'QuantAM' material editor. These result in markedly different microstructures and mechanical properties. 51

Figure 2.13: EBSD maps of EBM specimens manufactured with different parameters. a) Parameters: E_1= 1.8 Jmm^{-2}, v=2.2 ms^{-1}, h=150 µm. b) Parameters: E_2=1.9 Jmm^{-2}, v=8.8 ms^{-1}, h= 37.5 µm [103]. Varying process parameters result in different microstructures and textures. 52

Figure 2.14: Optical micrographs of etched LPBF Inconel 718 specimens manufactured with varying laser power [109]. a) Power = 250 W. b) Power = 950 W. The melt pools across layers can be clearly observed and show that a difference in laser power can significantly affect the melt pool shape. 52

Figure 2.15: Variation of required solution time for solution temperature for LPBF Inconel 718 [54]. This shows that there is a minimum solution time for a given solution temperature which results in similar microstructures and properties. 55

Figure 2.16: Microstructure of LPBF Inconel 718 specimens with varying thermal treatments[139]. a) Heat treated sample microstructure with EDS results of the section squared in a). b) HIP+ HT. This shows obvious evidence of the elimination of scan strategy effects through thermal treatments. 56

Figure 2.17: EBSD maps of LPBF Inconel 718 specimens showing grain morphology and misorientation angle distributions [142]. a) Heat-treated sample. b) HIP and heat treated sample. The broad distribution in the heat treated sample indicates no preferred growth direction as compared to the HIP and heat treated sample. 57

Figure 2.18: This figure demonstrates that grain boundaries with a high misorientation angle are prone to crack propagation in as-built and heat treated EBM samples [144]. a) An EBSD map showing the cracked grain boundary along the high angle grain boundary (misorientation > 15°). b) The distribution of grain boundary misorientation and cracked grain boundaries. 58

Figure 2.19: Illustration of the hot cracking mechanism in the LPBF process [145], demonstrating crack formation and growth within a single melt pool. This shows that the difference in interdendritic liquid pressure between the dendrite tip and the root causes an insufficient feeding of molten material at the dendrite root, promoting void generation and therefore highly affecting the hot cracking behaviour of the part. 58

Figure 2.20: Grain morphology of planes parallel (XZ) and perpendicular (XY) to the build direction with varying thermal treatments [146]. a) As-built specimen parallel to the build direction. b) As-built specimen perpendicular to the build direction. c) Heat treated specimen parallel to the build direction. d) Heat treated specimen perpendicular to the build direction. e) HIP specimen parallel to the build direction.

f) HIP specimen perpendicular to the build direction. g) HIP and heat treated specimen parallel to the build direction. h) HIP and heat treated specimen perpendicular to the build direction. Heat treatment and Hot isostatic pressing effectively reduced the strong texture in the build direction in as-built specimens. 59

Figure 2.21: TEM visualisation of γ'' precipitates in EBM Inconel 718 specimens [150]. a) As-built samples (low cooling rate). b) In-situ heat treated samples. This illustrates the effect of heat treatment on the size of strengthening precipitates, γ'' in this case. 60

Figure 2.22: Dislocations and γ' phases in LPBF CM247LC [151]. a)- c) As-built. d), e) Heat treated. Dislocations are entangled and tend to accumulate at the grain boundaries. Heat treatment decreases the dislocation network density, especially at the grain centre. 61

Figure 2.23: δ phases in the interdendritic region of LPBF Inconel 718 specimens [42]. a) As-Built. b) Solution + ageing treated. c) Direct aged. The solution treated and aged specimen contained much coarser δ phase than their non-solution-treated equivalents due to the dissolution of γ'' phase and the consequent formation of needle-shaped δ phase during this first thermal treatment. This shows that thermal treatments affect the presence, size and morphology of precipitates in PBF materials. 61

Figure 2.24: A time-temperature-transformation diagram for the formation of δ phase in LPBF and wrought Inconel 625 components. The red dot indicates the industry recommended stress-relief Heat Treatment conditions [154]. This shows that the formation of δ phase is much faster during LPBF than for the wrought process. The stress relief heat treatment (red dot) was shown to promote the formation of δ phase during LPBF but not for wrought equivalents. 62

Figure 2.25: TEM images showing the laves phase in the as-built LPBF Inconel 718 [157]. a) Bright field. b) Dark field. Only Laves phases are visible due to the fast heating and cooling cycles, which suppressed other secondary phase precipitation during LPBF. 63

Figure 2.26: TEM images and diffraction pattern of LPBF specimens [138]. a), b) Solution treated. c), d) HIP. e), f) Solution treated and aged. g)-i) HIP and aged. After solution treatment, diffraction shows the dissolution of Laves phases usually present in as-built condition. Following HIP, grains are recrystallised, and secondary phases dissolved. After solution and ageing treatment, the TEM images and diffraction patterns reveal the presence of secondary phases, such as γ''. This demonstrates that solution and ageing treatments are able to precipitate secondary phases. 64

Figure 2.27: Bright field TEM images showing dislocations in LPBF alloy 718 specimens [152]. a) As-built. b) Heat treated. This reveals the presence of Laves phase. 65

Figure 2.28: This shows the effect of the PBF build orientation on the subsequent machining. The greatest cutting force is generated when the feed direction is parallel to the build direction, which gives rise to anisotropy at machined faces. 66

Figure 2.29: Creep deformation mechanisms at different stresses and temperatures (τ is the equivalent shear stress and G is the shear modulus). From [58]. 67

Figure 2.30: Creep Mechanisms. a) Dislocation creep. b) Diffusion creep. From [58]. 68

Figure 2.31: Illustration of creep damage due to cavitation and the effects on the creep curve, mainly in the tertiary region. From [58]. 69

Figure 2.32: Pie chart of the materials and the PBF parameters investigated in the creep studies to date, from 21 papers. a) The materials studied. b) The parameters studied (the label “Basic” refers to studies which only tested the material in one condition, focusing on performance without looking into the effect of a certain parameter.) Inconel 718 is the main material investigated and the effect of thermal treatments and build direction have been studied the most. 71

Figure 2.33: Schematic showing tests on two non-standard specimens. a) Small Punch test. b) Two Bar Specimen test. This illustrates the potential of small and non-conventional specimen testing in PBF. 73

Figure 2.34: Creep deflection vs creep time results for specimens in different conditions (Forged-N: loading direction parallel to the forging direction; Forged-P: loading direction perpendicular to the forging direction) [199]. Indicating that the as-built LPBF specimens possessed similar creep lifetime to the forged ones, but far lower than the cast specimen. 74

Figure 2.35: Porosity distribution in the specimen at different stages of creep testing [190]. Showing the potential of using X-ray Computed Tomography (XCT) to determine where failure will occur in a specimen and for investigating evolution during tests..75

Figure 2.36: Creep fracture surfaces of LPBF Inconel 718 specimen built with varying laser power [196]. a),b) Laser power of 250 W (59.5 J/mm3). c),d) Laser power of 950 W (59.4 J/mm3). This highlights the catastrophic failure associated with lack of fusion. 76

Figure 2.37: TEM images showing the γ” phase after different thermal treatments [157]. a) Direct aged. b) Solution treated at 1000 ˚C then aged (SHT1000˚C). c) Solution treated at 930˚C then aged (SHT930˚C) conditions. Using a solution temperature of 1000˚C followed by a two-stage ageing treatment resulted in better creep resistance than specimens directly aged, but when the solution temperature was decreased below 1000˚C, direct aged specimens performed better. 77

Figure 3.1: Flowchart of the methodology followed in the project. 79

Figure 3.2: Schematic representation of the Stripe scanning strategy showing the different parameters used. With the build direction (BD) indicated...................... 80

Figure 3.3: Schematic representation of the different build orientations, scan strategies and number of lasers used for this research. The differences in surface area being melted are visible...82

Figure 3.4: ATSM E8/E8M [210] uniaxial specimen after turning and grinding. 84

Figure 3.5: Schematic representation of specimen sections used for microscopy analysis. a) Fracture surface and cross section analysis. b) General microstructure section analysis from cubes.. 86

Figure 3.6: Detection of porosity using MATLAB image processing. a) Original image with porosity as black voids. b) Black and white image with porosity labelled as white pixel. 87

Figure 3.7: Schematic of XCT scan images obtained. 88

Figure 3.8: Processing a SEM image of 90° single-laser Meander HT specimen with ImageJ, by modifying the contract/brightness threshold, to obtain precipitate density (δ, carbide and laves phase). a) original SEM image with precipitates in white. b) Processed ImageJ image with precipitates in black. 88

Figure 4.1: Microstructural observations for wrought alloy 718. a) Microstructure parallel to the loading direction. b) Microstructure perpendicular to the loading direction. c) Microstructure at higher magnification where precipitates are visible. d) EBSD map of wrought alloy 718. e) Inverse Pole Figure of the EBSD scan. The microstructure of wrought alloy 718 is composed of small equiaxed grains in perpendicular planes, showing the isotropic nature of the material. The precipitates on the grain boundaries are large and there is little texture in the material. 92

Figure 4.2: Annealing twins (in red) present in wrought alloy 718 before creep...... 93

Figure 4.3: SEM images of the microstructure of 90° single-laser Meander AB and HT specimens. a)-c) 90° single-laser Meander AB. d)-f) 90° single-laser Meander HT. Both specimens had elongated grains parallel to the build direction and more equiaxed grains perpendicular to the build direction where the laser overlapping paths can be seen. At higher magnification, the AB specimen had more ill-defined grain boundaries and less precipitates. 95

Figure 4.4: EBSD maps and Inverse Pole Figures of 90° single-laser Meander AB and HT specimens. a) 90° single-laser Meander AB. b) 90° single-laser Meander HT. The AB specimen has a much stronger texture in the Z direction, which corresponds to the build direction, compared to its heat treated counterpart. 97

Figure 4.5: Histogram of grain size distribution. a) Wrought alloy 718. b) 90° single-laser Meander AB. c) 90° single-laser Meander HT. This shows that the majority of the grains in all three specimens had an area between 0 and 50 μm^2. 98

Figure 4.6: SEM images of the microstructure of 90° single-laser HT specimens with different scan strategies. a)-c) Meander strategy. b)-d) Stripe Strategy. Both microstructures are similar and laser overlapping areas (labelled) can be observed in the plane normal to the build direction. 99

Figure 4.7: EBSD maps and Inverse Pole Figures of 90° single-laser HT specimens with different scan strategies. a) Meander strategy. b) Stripe strategy. This shows that the Stripe strategy results in weaker texture than the Meander strategy. 100

Figure 4.8: SEM images of the microstructure of single-laser Stripe specimens with different build orientations. a)-c) 90°. d)-f) 45°. g)-i) 0°. The images are oriented with respect to the loading direction. This shows elongated grains parallel to the build direction for all specimens with equiaxed perpendicular to the build direction. At higher magnification, δ phase precipitates can be observed on the grain boundaries with some pores. 101

Figure 4.9: EBSD maps and Inverse pole figures for LPBF alloy 718 single-laser Stripe specimens built with different build orientations. a) 90°. b) 45°. c) 0°. This shows a <001> texture parallel to the build orientation for each test case. 103

Figure 4.10: SEM images of the pre-creep microstructure of LPBF specimens with Stripe strategy, different build orientations and single or multi-lasers. a)-c) 90° single-laser. d)-f) 90° multi-laser. g)-i) 45° single-laser. j)-l) 45° multi-laser. m)-o) 0° single-laser. p)-r) 0° multi-laser. Showing elongated grains parallel to the build direction, equiaxed grains perpendicular to build direction and some δ and Laves precipitates. All specimens aligned with the loading direction. 104

Figure 4.11: EBSD maps and Inverse Pole Figures of LPBF Stripe specimen with different build orientations and single or multi-laser strategies. a) 90° single-laser. b) 90° multi-laser. c) 45° single-laser. d) 45° multi-laser. e) 0° single-laser. f) 0° multi-laser. Showing a <001> texture parallel to the build direction. The use of multi-laser affects the texture strength for the 90° and 0° specimens, while it has a negligeable effect on the 45° specimens. 108

Figure 4.12: Meltpool and grain formation schematic, showing the columnar and equiaxed grains. With the build direction and Hatch Distance (HD) indicated. 110

Figure 4.13: Schematic representation of the effect of build orientation on the microstructure of LPBF alloy 718. a) 90° specimens. b) 45° specimens. c) 0° specimens. The dominant grain growth direction is dependent on the direction of heat loss, which varies for the different build orientations. 111

Figure 5.1: Creep curves for all test cases, showing the higher elongation at fracture of wrought material, and some LPBF specimens having longer creep lives. 115

Figure 5.2: Fracture after creep of wrought alloy 718. a) The fracture cross-section showing the damage incurred during creep. b) Crack initiation at Carbides and Laves phase. c) Microvoid initiation on the grain boundaries in δ phase gaps. d) The fracture surface showing clear signs of necking and reduction in area. e), f) Clear indicators of ductile failure with dimples, fibrous appearance and shear lips. All indicators indicate a fully ductile fracture in the wrought specimen. 116

Figure 5.3: Creep curves for the LPBF specimens only, where the different shapes of the creep curves, most notably in terms of tertiary creep, are visible. 118

Figure 5.4: Minimum creep rate (black bars in top graph), creep life (black bars in bottom graph) and elongation at fracture (white square scatter points in bottom graph) for all the specimens. This shows that the 90° single and multi-laser specimens had similar minimum creep rates and lives as the wrought material. The 90° AB specimen performed the worst both in terms of creep rate and life. The elongation at fracture of the wrought material is the highest, followed by the 90° specimens. 119

Figure 5.5: Creep curves for 90° single-laser Meander AB and 90° single-laser Meander HT, clearly displaying the differences in minimum creep rate, creep life and elongation at fracture between as-built and heat treated specimens. 120

Figure 5.6: Fracture images of the AB and HT 90° single-laser Meander specimens. a), b) Fracture cross-section of the AB specimen, with very little creep damage, although microvoid coalescence is still occurring. c)-e) Fracture surface of the AB specimen with signs of quasi-cleavage failure. f), g) Fracture cross-section of the HT specimen, with creep damage and microvoid coalescence visible on the short side of the grains. h)-j) Fracture surface of the HT specimen with scan tracks visible on the fracture surface and indicators of quasi-cleavage failure. 123

Figure 5.7: Creep curves for 90° single-laser Meander HT and 90° single-laser Stripe HT. Both specimens had full creep curves and the Stripe specimen had a shorter creep life than its Meander counterpart. 123

Figure 5.8: SEM images of the Fracture cross-section for the 90° single-laser HT specimens with different scan strategies. a), b) Meander strategy. c), d) Stripe strategy. Both types of specimens showed signs of creep damage with microvoid coalescence on the short side of the grains. 124

Figure 5.9: Fracture surface for the 90° single-laser HT specimens built with different scan strategies. a)-c) Meander strategy. d)-f) Stripe strategy. Both specimens present scan lines on the fracture surface as well as dimples and cleavage steps, indicating a failure by quasi-cleavage. 125

Figure 5.10: Creep Curves for the different test cases, showing the clear differences in creep performance with regards to orientation, heat treatment and scan strategy. This also shows the differences in tertiary creep for the different specimens. 126

Figure 5.11: Fracture surface for the different build orientations. a)-c) 90° single-laser Stripe HT specimen. d)-f) 45° single-laser Stripe HT specimen. g)-i) 0° single-laser Stripe HT specimen. 90° and 0° spciemens failed by quasi-cleavage, as indicated by the mixture of dimples anc cleavage steps in their fracture surface. The 45° specimen failed by mixed mode failure. 127

Figure 5.12: Fracture cross-section for the different build orientations. a),b) 90° single-laser Stripe HT specimen. c),d) 45° single-laser Stripe HT specimen. e),f) 0° single-laser Stripe HT specimen. Cracks on the grain boundaries are clearly visible with material separation perpendicular to the loading direction........................... 128

Figure 5.13: Fracture indicators in 0° single-laser Stripe HT specimens. a) Transdendritic failure surface indicator. b) Transgranular crack. All images oriented with respect to the loading direction, with the build direction indicated...................... 129

Figure 5.14: Schematic of failure across layers for the different specimens, with respect to the loading direction and showing the build direction. a) 90° single-laser Stripe HT. b) 45° single-laser Stripe HT. c) 0° single-laser Stripe HT. This shows the number of layers failure occurred on. 129

Figure 5.15: Creep curves of the single and multi-laser LPBF specimens. This is showing similar performances for 0° and 45° single and multi-laser specimens and the longer creep life of the 90° multi-laser specimen, compared to its single laser counterpart.. 130

Figure 5.16: Cross sectional view of the fracture surface for the different single and multi-laser specimens in different build orientations. a),b) 90° single-laser. c),d) 90° multi-laser. e),f) 45° single-laser. g),h) 45° multi-laser. i),j) 0° single-laser. k),l) 0° multi-laser. Showing similar microstructures at failure for each build orientation, regardless of the number of lasers. 133

Figure 5.17: Fracture surfaces of the different single and multi-laser scan strategies for the various build orientations. a)-c) 90° single-laser. d)-f) 90° multi-laser. g)-i) 45° single-laser. j)-l) 45° multi-laser. m)-o) 0° single-laser. p)-r) 0° multi-laser. All specimens aligned with the loading direction, with the build direction clearly marked. This shows the similar fracture indicators in the single and multi-laser specimens for a given build orientation. 135

Figure 5.18: Effect of precipitate density on the minimum creep rate, creep life and elongation at fracture for all the specimens tested. a) Creep life VS precipitate density. b) Minimum creep rate VS precipitates density. c) Elongation at fracture VS precipitate density. 138

Figure 5.19: Effect of grain size on the minimum creep rate, creep life and elongation at fracture for all the specimens tested. a) Creep life VS grain size. b) Minimum creep rate VS grain size. c) Elongation at fracture VS grain size. The data points corresponding to the wrought material can be identified due to their small (almost absent) error bar. 139

Figure 5.20: Schematic representation of the failure planes of the different test cases, with respect to specimens' layers and build direction and with the loading direction shown. a) 90° specimens. b) 45° specimens. c) 0° specimens. This shows the effect of the stress state on the failure mode of the specimens. 144

Figure 5.21: Schematic representation of the crack paths for the different build orientations. a) 90° specimens, where intergranular cracking occurred with some cleavage steps. b) 45° single-laser Stripe HT specimens where the intergranular cracking caused grain boundaries decohesion and sliding. and c) 0° single-laser Stripe HT specimens where Quasi-Cleavage occurred. 145

Figure 6.1: EBSD maps and Inverse pole figures showing the evolution of texture with time for the different specimens. a)-d) Wrought alloy 718 during creep showing an increase in texture along the loading direction as creep progresses. e)-h) 90° single-laser Meander HT during creep where the texture increases in the loading direction (Z) as creep progresses before disappearing at fracture. i)-l) 90° single-laser Meander HT during thermal exposure showing an increase then decrease in texture, highlighting the instability of the microstructure. The Z direction corresponds to the loading direction for all specimens and to the build direction as well for the LPBF specimens. 149

Figure 6.2: SEM images of the microstructural evolution of wrought alloy 718 during creep. a),b) Pre-creep microstructure. c),d) Microstructure in the secondary region, after 123h of creep. e),f) Microstructure in the tertiary region, after 331h of creep test. g),h) Microstructure after fracture. This shows the increase in the number of carbides and carbide cracking. 151

Figure 6.3: SEM images of the microstructural evolution of 90° Meander HT specimen during creep. a),b) Pre-creep microstructure. c),d) Microstructure in the secondary region, after 121h of creep. e),f) Microstructure in the tertiary region, after 430h of creep test. g),h) Microstructure after fracture (505h). This shows microvoid initiation at δ-phase on the grain boundaries and their coalescence as creep progresses....153

Figure 6.4: SEM images of the microstructural evolution of 90° Meander HT specimen during creep. a)-c) Microstructure after 121h of thermal exposure. d)-f) Microstructure after 430h of thermal exposure. g)-i) Microstructure after 505h of thermal exposure. This shows the expansion of pores in the specimen and the increase in grain size. 155

Figure 6.5: Evolution of part density for the 90° Meander HT specimens during creep testing and thermal exposure. This figure was based on the data available in Table 6.2. This shows the increase in porosity in both specimens due to pore enlargement (thermal exposure) and creep damage (creep tested specimen)....156

Figure 6.6: Evolution of the grain size for the wrought alloy 718 during creep and the 90° Meander HT specimens during creep and thermal exposure. This figure was based off the data available in Table 6.2. This shows the dynamic recrystallisation of grains in the wrought alloy 718 during creep and the instability of the grains and their growth in both LPBF specimens. 158

Figure 6.7: Evolution of the average precipitate density in the wrought alloy 718 during creep and the 90° Meander HT specimens during creep and thermal exposure. This figure was based off the data obtained from SEM image analysis and is available in Table 6.2. This shows the increase in precipitate density in the wrought alloy, caused by an increasing number of carbides. It also shows the smaller increase in precipitate density between the creep tested and thermally exposed 90° Meander HT specimens.... 160

Figure 6.8: Schematic representation of the microstructural evolution of wrought and 90° Meander HT specimen during creep. The microstructures are drawn in relative scales, highlighting the bigger grain size of 90° Meander HT specimen, compared to its wrought equivalent. The colour in the figure symbolises the texture in the specimen, with warmer colours representing stronger textures. The time stamps given are approximately ± 50h. 163

List of tables

Table 1.1: Common applications of nickel-based superalloys [7]. This shows the numerous areas where additively manufactured nickel-based superalloys could be used. 29

Table 2.1: The major differences between LPBF and EBM. This provides an insight into process characteristics [36-38]. 40

Table 2.2: Chemical composition of phases marked in Figure 2.6 (wt %) [48]. This provides further proof of the present of Laves phase and MC carbides in the as-built state of EBM Inconel 718. 43

Table 2.3: Summary of common microstructural differences between LPBF and EBM material. The reader is advised to use this with caution as process technology evolves. This table is intended as a broad guide only and observations will vary between process configurations. 45

Table 2.4: Summary tables of LPBF alloy 718 creep studies. 72

Table 3.1: Renishaw© alloy 718 powder composition. 79

Table 3.2: List of process parameters employed for the build of all specimens. 80

Table 3.3: Summary of the different test cases investigated in this project. 83

Table 3.4: XCT Scan parameters used. 87

Table 4.1: Part density, precipitate (δ, Laves and carbides) density (± 0.15 %) and grain size comparison for the Wrought specimens (Loading Direction = LD). 92

Table 4.2: EDS analysis of the different phases present in LPBF material (Figure 4.3). (All values within ± 2 wt%) 94

Table 4.3: Part density, precipitate (δ, Laves and carbides) density (± 0.15 %) and grain size comparison for the 90° single-laser Meander AB and HT specimens (Loading Direction = LD). 96

Table 4.4: Part density, Precipitate (δ, Laves and carbides) density (± 0.15 %) and grain size comparison between 90° single-laser HT Meander and Stripe specimens (LD = Loading Direction). 100

Table 4.5: Part density, precipitate (δ, Laves and carbides) density (± 0.15 %) and grain size comparison for the single laser Stripe specimens with different build orientations (LD = Loading Direction). 101

Table 4.6: Part density, precipitate (δ, Laves and carbides) density (± 0.15 %) and grain size comparison between single and multi-laser Stripe specimens at different build orientations (LD = Loading Direction). 105

Table 5.1: Quantification of damage in wrought alloy 718. 117

Table 5.2: Quantification of the creep performance for all test cases. (Ordered from longest creep life to shortest). 118

Table 5.3: Quantification of the creep performance for the AB and HT 90° single-laser Meander specimens. 120

Table 5.4: Quantification of damage for LPBF 90° single-laser Meander AB and HT specimens. 121

Table 5.5: Quantification of the creep performance for the Stripe and Meander 90° single-laser HT specimens. 123

Table 5.6: Quantification of damage for the 90° single-laser Stripe and Meander HT specimens. 125

Table 5.7: Quantification of the creep performance for single-laser Stripe HT specimens built at 0°, 45° and 90°. 126

Table 5.8: Quantification of damage in the different build orientations. 128

Table 5.9: Quantification of the creep performance for Stripe HT single and multi-laser specimens at multiple build orientations. 130

Table 5.10: Quantification of damage in failed single and multi-laser specimens for different build orientations. 131

Table 6.1: Breakpoints for the Interrupted creep tests. 147

Table 6.2: Quantification of the evolution of damage during for wrought and 90° single-laser Meander HT specimen during creep and for the thermally exposed 90° single-laser Meander HT specimen. The average densities have an error of ±0.15 %Area. 149

Nomenclature

AB – As-Built
AM – Additive Manufacturing
BCT – Body Centred Tetragonal
BD – Build Direction (will be aligned with the Z-axis in figures, unless otherwise specified, see Figure 4.1)
CAD – Computer Aided Design
DA – Direct Ageing
EBM – Electron Beam Melting
EBSD – Electron Back Scatter Diffraction
EDM – Electrical Discharge Machining
EDS - Energy Dispersive X-Ray Spectroscopy
FCC – Face Centred Cubic
HCP – Hexagonally Closed Packed
HD – Hatch Distance
HIP – Hot Isostatic Pressing
HT – Heat Treatment
LCF – Low cycle Fatigue
LD – Loading Direction
LPBF – Laser Powder Bed Fusion
LVDT – Linear Variable Differential Transformer
OM – Optical Micrography
PBF – Powder Bed Fusion
PREP - Plasma Rotated Electrode Process
SEM – Scanning Electron Microscopy
ST – Solution treatment
STA – Solution treatment and Ageing
TCP - Topologically Close Packed
TEM – Transmission Electron Microscope
WEDM – Wire Electrical Discharge Machining
XCT – X-ray Computed Tomography

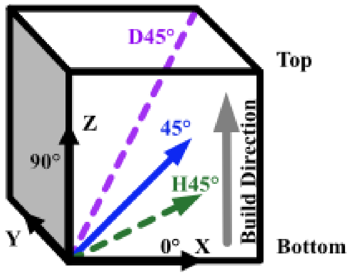

Figure 4.1: Layout of the build directions and principal planes commonly used when highlighting anisotropy in PBF specimens. Noting the orientation of this primitive is commonly considered to align with the machine coordinate system.

1 Introduction

Critical engineering applications, such as turbine blades and discs within aero-engines, require components to operate under extreme conditions [1]. Performance of these components is often limited by the mechanical properties of the material and by the geometric design of the part being constrained by conventional manufacturing methods. AM can be defined as "a process of joining materials to make objects from 3D model data, usually layer upon layer, as opposed to subtractive manufacturing methodologies" [2]. This technique has drawn significant attention due to its flexibility in design and fabrication as well as its potential to modify microstructures, and hence properties, through control of process and post-processing techniques, which may be different to wrought equivalents [1]. AM offers a potential solution to these limitations and to widening the design envelope into spaces previously unachievable, which can achieve greater part lightweighting and efficiency. Powder Bed Fusion (PBF) is a type of AM technology, typically used to process metals, which is composed of two sub-processes: LPBF and Electron Beam Melting (EBM). Commercially, AM has the potential to save both money and time by delivering enhanced functionality with respect to conventional subtractive manufacturing techniques [1]. This becomes apparent when highly customised parts with high value and low volume are required. Several researchers have previously reviewed the potential advantages of AM, as well as its positive impact on society [3]. These studies concluded that this process is driving a revolution to manufacturing technology.

Nickel-based superalloys are a family of modern aerospace engine materials [4, 5] which possess a combination of high-temperature strength, toughness, creep and oxidation/corrosion resistance. They have the highest temperature and strength combination of all cast and wrought superalloys, which makes them ideal for applications requiring creep resistance - which is resistance to deformation over time at elevated temperatures. For these reasons, this class of alloys has been widely used in components operating in critical environments [6]. These include land-based gas turbines, nuclear power plants and chemical containers. A summary of some common applications for nickel-based superalloys are reported in Table 1.1.

Table 1.1: Common applications of nickel-based superalloys [7]. This shows the numerous areas where additively manufactured nickel-based superalloys could be used.

Applications	**Examples**	**Typical alloys**
Aerospace Industry	Aircraft gas turbines: disks, combustion chambers, bolts, casings, shafts, exhaust systems, blades, vanes, burner cans, afterburners, thrust reversers, Space vehicles: aerodynamically heated skins, rocket engine parts	Inconel 600, Inconel 601, Inconel 617, Inconel 625, Inconel 706, Inconel 718, Inconel 738, Inconel 754, Inconel X-750, Nimonic 115, Nimonic 75, Nimonic 80, Nimonic 90, Rene 41, Waspaloy, Hastelloy X

Chemical and petrochemical industries	bolts, fans, valves, reaction vessels, tubing, transfer piping, pumps	Inconel 600, Inconel 625, alloy 690, alloy 718, Inconel 725, Inconel 925, Rene 41, Waspaloy
Pulp and paper mills	tubing, doctor blades, bleaching circuit equipment, scrubbers	Hastelloy G, Inconel 600, Inconel 671, Inconel 706, Inconel 718, Rene 41, Waspaloy
Nuclear power systems	control rod drive mechanisms, valve stems, springs, ducting	Hastelloy G, Inconel 600, Inconel 625, Inconel 706, Inconel 718, Rene 41, Waspaloy
Marine architecture	ships, submarines	Inconel 600, Inconel 625, Inconel 718, Rene 41, Waspaloy
Electronic Parts	resistors	Inconel 706, Inconel 718, Nichrome, Waspaloy
Steam turbine power plants	bolts, blades, stack gas reheaters	Inconel 706, Inconel X-750
Metals processing mills	ovens, furnace, afterburners, exhaust fans	Inconel 600, Inconel 625, Inconel 706, Inconel 718, N06008, Nichrome, Rene 41, Waspaloy
Heat-treating equipment and Metal processing	trays, fixtures, conveyor belts, baskets, fans, furnace mufflers, hot-work tools and dies	Inconel 600, Inconel 706, Nimonic 80, Rene 41, Waspaloy, Waspaloy
Automotive industry	spark plugs, glow plugs (in diesel engines), catalytic converters, combustion systems Reciprocating engines: turbochargers, exhaust valves, hot plugs, valve seat inserts	Inconel 625, Waspaloy
Medical applications	dentistry uses, prosthetic devices	Vitallium, Ni-Cr and Ni-Ti alloys
Pollution control equipment	scrubbers, flue gas desulfurization equipment (liners, fans, stack gas reheaters, ducting)	Inconel 718
Coal gasification and liquefaction systems	heat exchangers, repeaters, piping	Inconel 690

The first generation of nickel-based superalloys, designed for high-temperature applications in jet engines, included Nimonic 75, developed by Henry Wiggin Ltd, UK, in the 1940s [4]. Since then, nickel-based superalloys have been continuously produced, studied and used in building turbine blades, turbine discs, seals, rings, and other components in gas turbines. Nowadays, there are nearly 1.8 tonnes of nickel-based superalloys in a typical jet engine. These materials have greatly contributed to the increase of the continuous operating life of jet engines to above 20,000 h [8]. While coating technologies (e.g. Zirconia based thermal barrier coatings) have also served to enhance high temperature performance, the role of the substrate nickel-based superalloy cannot be overstated.

However, given the characteristic excellent mechanical properties of nickel-based superalloys, these parts are difficult to machine with conventional machining techniques [9]. As a result, particular attention must be paid to the selection of tooling, coolants, and processing parameters, leading to increasing production costs [10]. PBF's ability to manufacture complex geometries may allow the incorporation of new and additional functionalities to components, highlighting the potential of using AM for critical applications. Figure 1.1 shows the weldability and therefore the utility of nickel-based superalloys in fabrications. This is a useful indicator of how challenging high integrity AM will be for a given material. Effectively, the process window becomes greatly reduced above the broken red line and thus, Inconel 718, Inconel 625 and Hastelloy X are some of the more promising alloys for LPBF use.

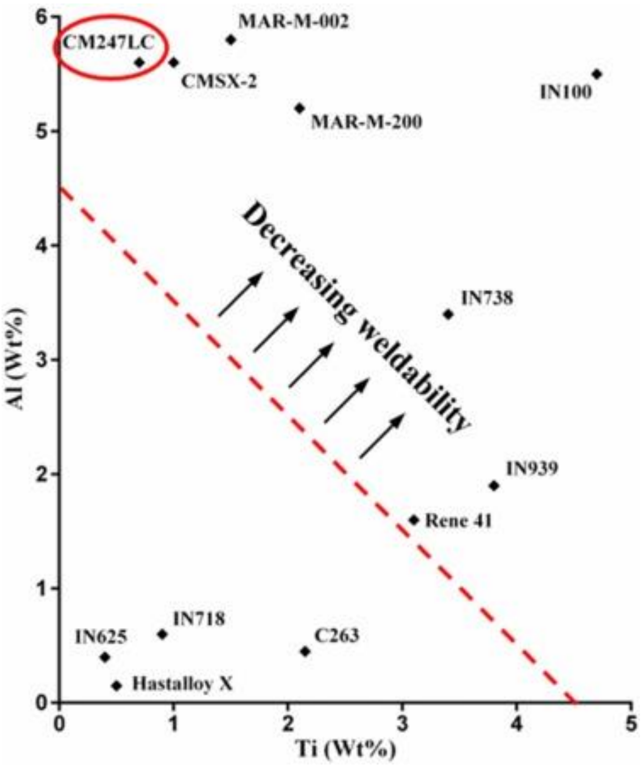

Figure 1.1: 'Weldability' diagram for a range of nickel-based superalloys as a function of their Ti and Al alloy element composition. Figure from Catchpole-Smith et al. [11]. Weldability is considered poor above the dashed line and deteriorates with increasing Ti and Al content. This work will inform future research on alloy compositions.

In the last two decades there has been a dramatic increase in the number of publications associated with nickel-based materials in AM, as shown in Figure 1.2. This increase in publications shows the interest of the research community for this topic.

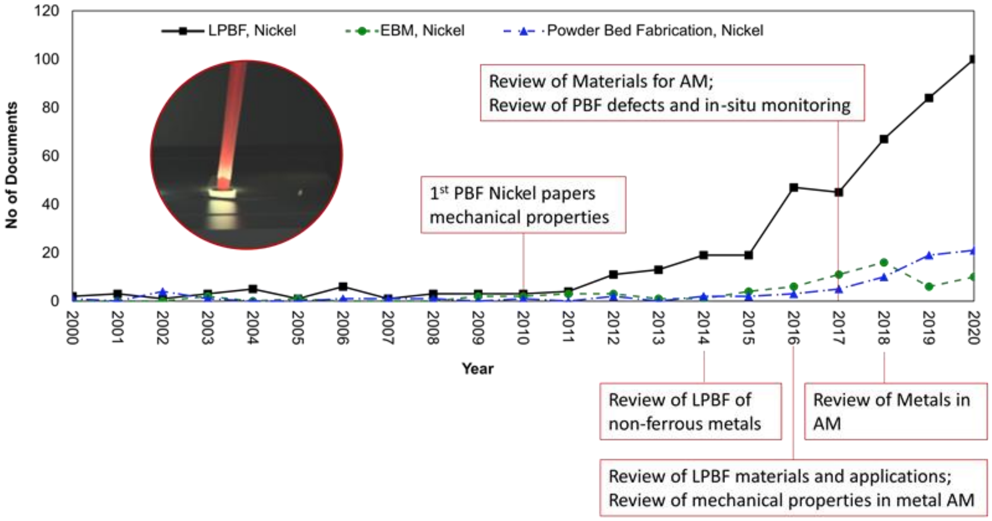

Figure 1.2: Number of publications on AM of nickel-based superalloys (from Scopus database) with major milestones [12-18].This shows an increase in publications associated with nickel-based materials in AM.

The aerospace industry represents a significant prize for AM machine producers, since a significant amount of components have a high part value and are produced using high value materials [10]. Indeed, nickel-based aerospace components are characterised by complex geometries and low production volumes. Furthermore, given the characteristic excellent mechanical properties of nickel-based superalloys, designed to work in safety critical applications, these parts are difficult and expensive to machine with conventional machining techniques [9, 19-21]. As a result, particular attention must be paid to the selection of tooling, coolants, and processing parameters, leading to increasing production costs [10]. On the contrary, PBF's ability to manufacture complex geometries allow the incorporation of new and additional functionalities to components. Hence, this area is an appropriate way to demonstrate the potential of using PBF in conjunction with nickel-based superalloys.

Work by Yadroitsev et al. [22] demonstrated the capability of LPBF in producing complex filters constituted of free-form structures from alloy 625. The parameters of the unit cell, or even of individual cells, can be easily modified at the modelling stage and optimised for specific applications with features below 1 mm (Figure 1.3). This demonstrates an immediate opportunity for AM technologies which cannot be achieved through conventional machining methods.

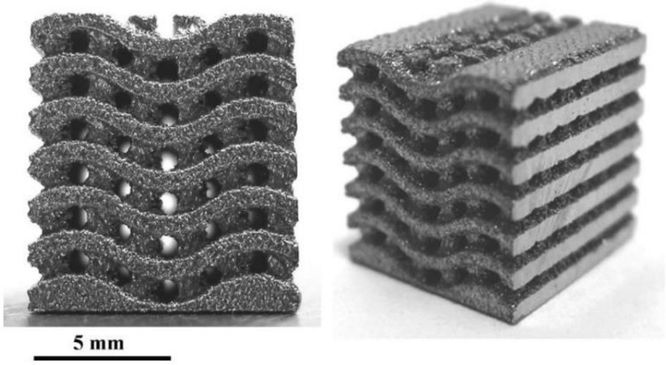

Figure 1.3: Inconel 625 filter with placement specific pore orientation and cross-sectional area. These samples were manufacture by powder bed fusion, demonstrating the ability of powder bed fusion to manufacture highly optimised geometries with features < 1 mm. This is an exemplary use of LPBF technology [22].

A further advance was demonstrated by Bernstein et al. [20], who developed and built a prototype turbine blade characterised by a leading edge with inbuilt cooling channels obtained via LPBF (Figure 1.4). The measured average cooling hole size (0.3945 mm) was slightly smaller than the nominal size (0.5 mm), highlighting tolerancing challenges remaining to be conquered in LPBF. The standard deviation for these hole diameters was small (0.0206 mm), indicating LPBF has potential as an accurate and effective technique to produce these features. Despite some promising results, this process cannot yet compete with the feature resolution obtained by laser processes or electrical discharge machining (EDM), which are common methods for cooling hole introduction. Indeed, Li et al. [23], amongst others, have demonstrated that by using a laser or EDM drilling process it is possible to obtain holes with a diameter <150 μm. However, common industrial processes for civil aircraft require cooling hole diameters in the range 300-500 μm. This is a fundamental technology limitation which governs turbine blade and nozzle guide vain thermodynamic performance. However, focus on AM research for aerospace applications has so far been focused on static components. The reasons behind this becomes evident with exploration of the mechanical properties exhibited by AM materials, a topic explored in more detail later in this review.

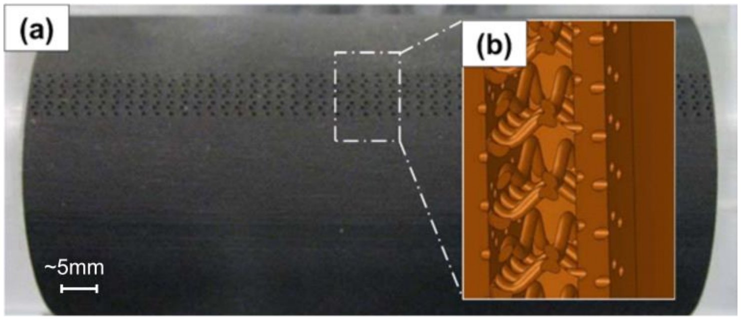

Figure 1.4: Example of novel cooling channels in a leading edge. a) the overview. b) Computer Aided Design model of the internal structure of the cooling channels [20]. The average measured cooling hole size (0.39 mm) was slightly smaller than the nominal size (0.5 mm), highlighting tolerancing challenges still to be conquered in LPBF.

Since LPBF has shown promising initial results in realising complex structures in aero-engine components, more and more companies are expressing intentions to invest in this technology. A review of metal AM use in the commercial aviation industry was written by Gisario et al. [24] and a review of the material characteristics of AM alloy 718 for high temperature applications was written by Yong et al. [25]. As an example, NASA has tested some LPBF built rocket injectors, demonstrating that these parts can withstand heat and pressures generated during space rocket launches [26]. MTU Aero Engines also announced that the borescope bosses for their PurePower PW1100G-JM engines will now be produced using LPBF [27]. Further, the Netherlands Aerospace Centre together with the University of Twente developed a novel micro-pump assembly for space application, composed of no moving parts, such as hydraulic valves [28]. The manufacture of this micropump was only possible using LPBF, due to the complex internal features which could not be obtained by other means. GE Aviation played a fundamental role in the introduction of AM to the aerospace industry, through the acquisition of both SLM Solutions and Arcam, two major AM companies specialising in LPBF and EBM, respectively. As a proof of principle, GE Aviation built a working miniature version of a jet engine using entirely LPBF [29]. Even though the scale was far smaller than commercial engines, this prototype was able to reach 33,000 RPM in functional testing and marks a significant step towards a more widespread use of LPBF in aero-engine manufacturing. They also created a sensor housing using only LPBF, which made it the first 3D printed part to be approved for use by the FAA [30]. Other demonstrators, such as turbine blades, were printed using EBM Inconel 738LC and were assembled onto a disk for spin pit testing to validate the mechanical integrity and design of the blades [31].

In summary, AM is a promising technique for the manufacture of nickel-based components. However, the knowledge gaps, which currently restrain LPBF from wider scale exploitation, remain significant. Failure to fully understand the microstructural and functional response of AM nickel-based superalloys will severely limit the applications for this technology/material combination. As such, we must obtain a fundamental understanding of the origin of defects in both material and process.

Indeed, components manufactured by LPBF are currently limited by their performance for use in critical applications. LPBF materials have microstructural defects, such as suboptimal grain size and morphology, and macroscale anomalies, such as lack of fusion. This results in LPBF materials performing below their wrought counterparts for various mechanical properties, such as creep. Creep is one of the leading causes of failure in high temperature, high stress components such as turbine blades. Creep resistance is therefore essential for such critical engineering components but the lack of understanding of the creep behaviour of LPBF nickel-based superalloys means there is a need and scope for further analyses and improvements. From the various nickel-based superalloys, alloy 718 has excellent creep resistance and one of the best LPBF manufacturability. This material is thus an excellent candidate to investigate the creep behaviour of LPBF nickel-based superalloys.

Figure 1.5. This is due to alloy 718's LPBF manufacturability (Figure 1.1) as well as its excellent mechanical integrity at high temperatures. Therefore, this work will focus on alloy 718.

Figure 1.5: Pie chart showing the nickel-based superalloys studied in powder bed fusion research to date, from 290 studies (IN = Inconel). Inconel 718 and Inconel 625 are the most studied alloys given their level of usage primarily in the aerospace markets where there are immediate opportunities for aerospace.

Figure 1.6 shows the mechanical properties of PBF nickel-based superalloys studied to date. At the current stage, studies have mainly focused on tensile and hardness performance and less on shear, toughness, fatigue and creep properties.

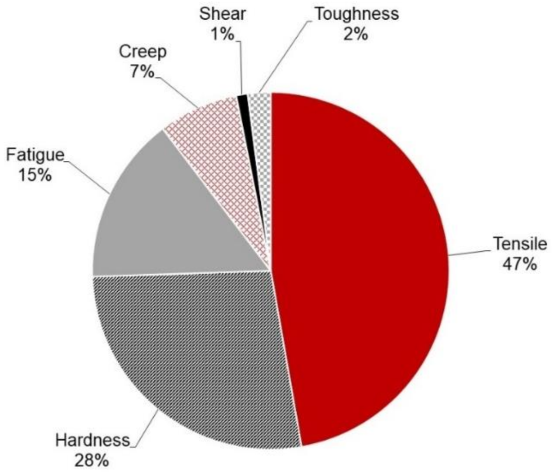

Figure 1.6: Pie chart summarising the mechanical properties investigated in PBF nickel-based superalloys research, across 290 papers. Almost half of the studies investigated tensile properties, while a third studied hardness properties. Other properties, especially shear and toughness, have been the subject of limited studies.

It is clear that there has been a limited number of studies on the creep behaviour of LPBF alloy 718, compared to other mechanical properties like tensile and hardness [32]. These studies have investigated the effects of some LPBF process parameters (build orientation [33] and scan strategy [34]) and some post-processing techniques (thermal treatment and machining [35]) on creep properties. There is a need for a deeper understanding to be reached, to establish process-structure-property relationships. Furthermore, the build time of LPBF can be slower than traditional manufacturing processes, especially for higher volumes of parts. Multi-laser machines have the potential to significantly reduce process time, but the process is currently poorly understood, particularly the impact of the interlaced scan strategies upon mechanical properties. Being able to reduce build time would make LPBF even more appealing to industry. Thus, the effect of multi-laser strategies should also be investigated. Additionally, research on developing appropriate heat treatments for LPBF materials is currently being undertaken as the standard heat treatments, designed for wrought and cast superalloys, lead to suboptimal microstructures.

However, to develop a LPBF specific heat treatment, an understanding of the microstructure and how it evolves during mechanical performance is required.

Overall, using LPBF to manufacture performant nickel-based superalloy components for critical engineering applications could result in significant increases in system efficiency and reduce material waste. However, the current lack of understanding of process-microstructure relationships and the resulting mechanical properties makes LPBF currently unsuitable for such applications. Furthermore, at the time of writing, there are no LPBF specific heat treatment standards, which leads to suboptimal LPBF microstructures and hence, mechanical properties. The aerospace industry represents a significant prize for LPBF as the parts in aero engines, such as turbine blades, which operate under high temperature and high stress conditions, have complex designs, low production volumes and utilise nickel-based superalloys. Creep is one of the main causes of failure of turbine blades and is also one of the properties least investigated by the AM research community. Thus, there are opportunities to establish process-structure-property relationships and appropriate post-processing techniques, such as heat treatments, to understand and improve creep properties. There are challenges in terms of isolating and understanding the individual effects of the various LPBF process parameters and to understand the behaviour of LPBF nickel-based superalloy under creep.

Therefore, the overall aim of this work is to establish process-structure-property relationships for the creep properties of LPBF alloy 718, to benchmark it against wrought alloy 718 and to provide insights to improve creep performance in LPBF materials. To accomplish this aim, the research will focus on the following objectives:

1. Understanding the effects of LPBF process parameters – build orientation, scan strategies, the use of multi-lasers – on the resulting microstructure of alloy 718.
2. Performing creep tests using appropriate loading conditions and benchmarking the performance of LPBF alloy 718 to its wrought counterpart.
3. Analysing the effects of LPBF process parameters on the creep behaviour of LPBF alloy 718.
4. Analysing the effects of heat treatment on the microstructure and creep behaviour of LPBF alloy 718.
5. Recommending a desired microstructure and heat treatment to improve creep performance by investigating the microstructure evolution during creep of LPBF alloy 718.

Fulfilling these objectives will result in an enhanced understanding of process-structure-property relationships, which will aid the development of future process parameters and thermal treatments to improve creep performance of LPBF alloy 718. This will increase the appeal of using AM for critical engineering applications.

To achieve these aims and objectives, LPBF alloy specimens will be built using different build orientations and scan strategies. Some specimens will be heat treated, while others will remain as built, and all specimens will be creep tested before being analysed using electron microscopy and fractography. Interrupted creep tests will also be conducted to observe the evolution of LPBF specimens during creep before an appropriate heat treatment is suggested. Overall, this work will lead to a significant advance in knowledge regarding the creep behaviour of LPBF alloy 718 and how it can be improved through process parameters and heat treatments.

The following sections will provide a review of the literature which will highlight the current knowledge on the topic, then present the experimental methods used to carry out the work (Chapter 3) before going to the results and discussion. Chapter 0 will present the microstructure of the LPBF alloy 718 specimens and the effects of the heat treatment and process parameters will be discussed. Chapter 5 will focus on the creep performance of the materials and how process parameters and heat treatment affect creep properties. Chapter 6 will then investigate the microstructural evolution of the best performing creep specimen to deepen the understanding of the effect of LPBF microstructure on the creep properties and inform a beneficial heat treatment. Lastly, conclusions and recommended future work will be presented in the final chapter.

2 Literature review

The following sections of this literature review will provide a review of PBF processes, nickel-based superalloys (specifically alloy 718) and mechanical properties of LPBF alloy 718, with a focus on creep. The findings will then be summarised and used to justify the aims and objectives of this project.

2.1 Powder bed fusion

PBF is one of the most common AM techniques for metal part fabrication. LPBF and EBM processes and microstructures will now be explored.

2.1.1 Process

The PBF process consists of two stages: firstly, the powder is spread uniformly on the working area, then an energy source (a laser beam for LPBF and an electron beam for EBM) selectively melts the powder bed according to a 3D model and hence build the final component [36]. The two main differences between these fabrication methods are their power sources and power transmission systems. Two diagrams representing typical LPBF and EBM systems are presented in Figure 2.1 [37]. Both methods have been reviewed previously and Table 2.1 summarises the relevant differences between the two systems [36-38]. PBF can be used to process a variety of materials, ranging from metals to ceramics, for many applications, such as aerospace, biomedical and automotive.

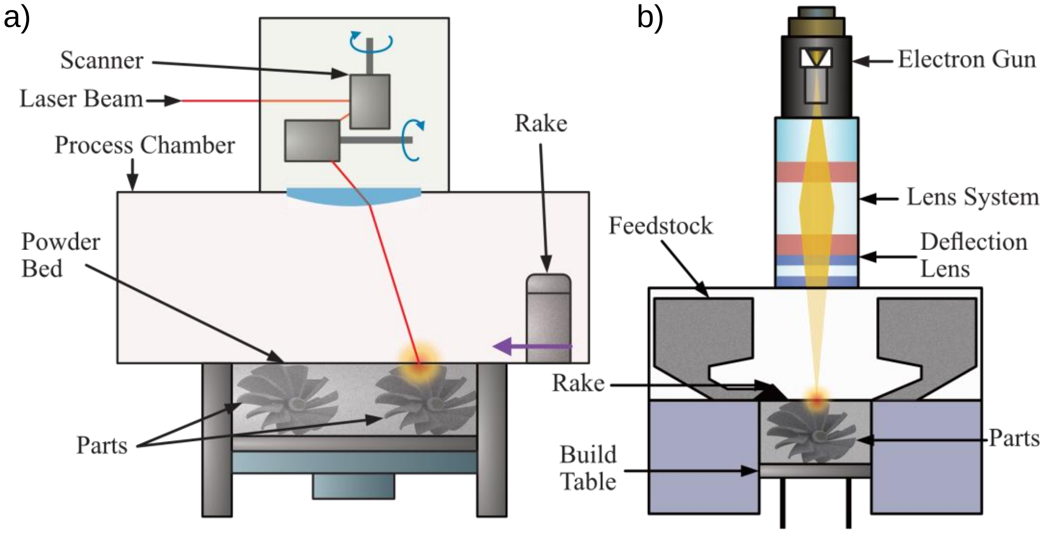

Figure 2.1: Diagram of the two main PBF processes. a) LPBF. b) EBM. The two main differences, power sources and power transmission systems, are visible. After [37].

Table 2.1: The major differences between LPBF and EBM. This provides an insight into process characteristics [36-38].

Aspects	**LPBF**	**EBM**
Power source	Laser	Electron beam
Power range	20 W ~ 1 kW	Several kW, much higher than the laser power
Energy beam spot size	50 μm ~ 180 μm	50 μm ~ 200 μm
Power transmission system	High-frequency scanning mirrors	Electromagnetic lenses and magnetic scan coil
Scan speed range	Up to 15 m/s	Up to 10 m/s
Powder bed thickness range	20 μm ~ 100 μm	50 μm ~ 200 μm
Powder bed temperature range	Significant substrate heating is not usual but can range from 20°C [39] to 975°C [40]	Can be very high, slightly below the materials' melting temperature
Build chamber condition	Normally filled with protective gases, with an oxygen content less than 0.1%	Vacuum, $<10^2$ Pa

2.1.2 Microstructure

Typical PBF microstructures have specific process defects. Reviews on these defects and how process parameters affect them have been presented by Malekipour et al. [41] and Grasso et al. [17]. Figure 2.2 shows some of the typical defects in PBF processes. For more details, the reader is referred to the papers aforementioned.

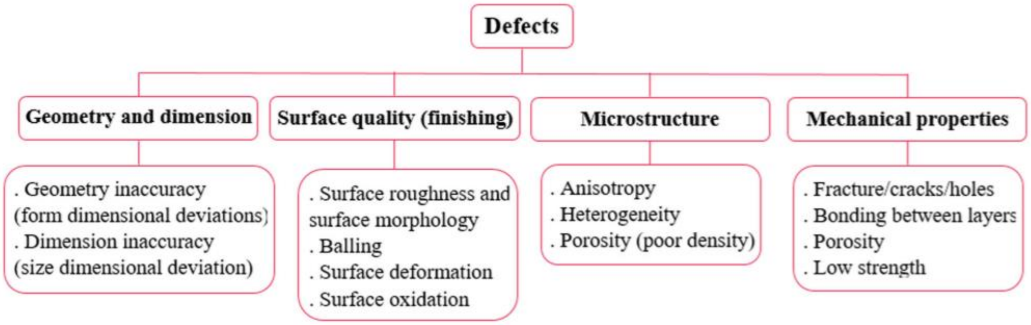
Defects
Geometry and dimension
Surface quality (finishing)
Microstructure
Mechanical properties
. Geometry inaccuracy
(form dimensional deviations)
. Dimension inaccuracy
(size dimensional deviation)
. Surface roughness and
surface morphology
. Balling
. Surface deformation
. Surface oxidation
. Anisotropy
. Heterogeneity
. Porosity (poor density)
. Fracture/cracks/holes
. Bonding between layers
. Porosity
. Low strength

Figure 2.2: Summary of defects present in PBF processes. This can serve as reference for commonly used terminology by practitioners [41].

Figure 2.3 presents an overview of the microstructures observed in as-built (AB) LPBF alloy 718 specimens [42]. The morphology of melt pools can be clearly observed in the plane parallel to the build direction (Figure 2.3a), while the laser scan tracks are recognisable in the plane perpendicular to the build direction (Figure 2.3b) [42]. Figure 2.4 shows an Electron BackScatter Diffraction (EBSD) image with individual laser scan tracks with a width of ~75 μm on the plane perpendicular to the build direction [43]. AB samples have a strong <100> crystallographic texture in the build direction [44]. Small equiaxed grains with an average size of 10 μm can be recognized at the track the overlapping regions between the tracks [43]. These microstructural differences in the two directions are responsible for the mechanical anisotropy of PBF nickel-based superalloys components, which represents a tremendous challenge to researchers.

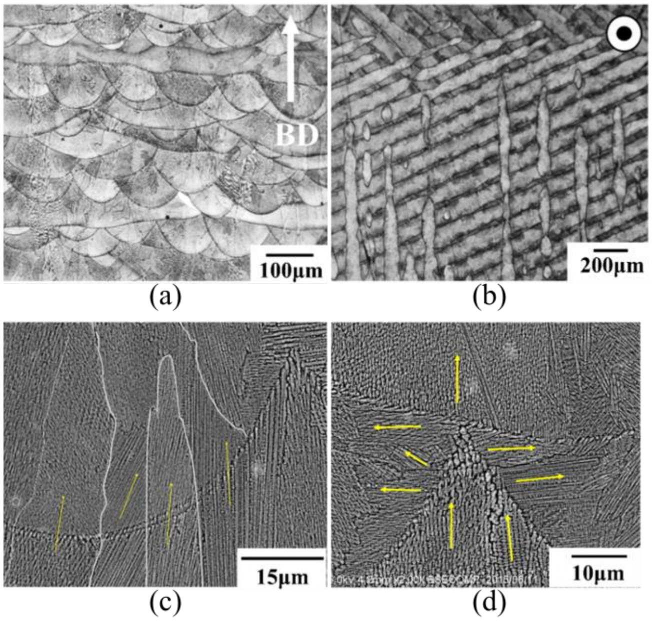

Figure 2.3: Images of as-built LPBF Inconel 718 specimens. a) Side view. b) Top view. c) The melt pool boundaries between layers. d) The melt pool boundaries between adjacent tracks from the side. The arrow in a) indicates the build direction (BD) and the circle in b) indicates the plane is perpendicular to the build direction. Melt pools in a) and laser scan tracks in b) are clearly visible. The yellow arrows in c) and d) represent the dendrite growth direction. They follow the build direction in c) and have no preferred direction in d) [42]. These images illustrate the particular anisotropic microstructure resulting from the PBF processes.

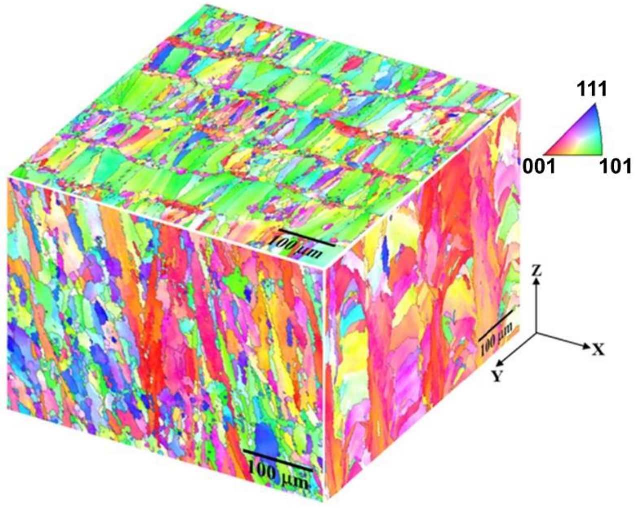

Figure 2.4: EBSD maps of an as-built LPBF Inconel 718 specimen [43]. This shows the dominant direction of grain growth and strong <100> crystallographic texture in the build direction, which is characteristic of PBF processes. Individual laser scan tracks with small equiaxed grains track the overlapping regions can also be seen in the XY plane (perpendicular to the building direction).

The dendritic growth directions (yellow arrows in Figure 2.3c) follow the build direction (z). However, the growth of dendrites on both sides of the track interfaces does not show any preferential direction (Figure 2.3d) [42]. In contrast, another study found that the newly-formed crystals grow into cellular dendrites in a direction which is either parallel to the original direction or rotated by 90° [45]. This allows the grains to interpenetrate from one layer to another. Chlebus et al. [46] investigated the features in the dendritic (Figure 2.5a) and interdendritic (Figure 2.5b) regions of AB LPBF alloy 718 specimens. The fast heating and cooling cycles produced during PBF, results in small interdendritic regions (in the range of nm). Microsegregation of some alloying elements, such as Nb, Mo and C, are also produced during the dendrite formation, because of the rapid cooling rate. Some chemical composition inhomogeneities can be observed in Figure 2.5a, indicated by arrow 2 [46]. This segregation promotes the formation of NbC carbides and Laves phase in the interdendritic region, as shown in Figure 2.5b [46].

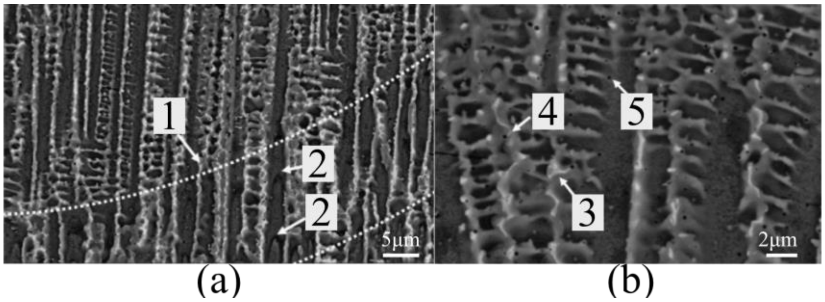

Figure 2.5: Typical examples of SEM images of phenomena in AM nickel-based superalloys. a) An overview of the interface between adjacent layers. b) The interdendritic region. Mark 1 indicates the layer-layer melt pool boundary, 2 indicates the dendritic cell tips, 3 and 4 highlight some γ + Laves phase eutectic, 5 points a MC carbide [47]. These features are caused by the rapid heating and cooling during the LPBF process.

EBM specimens show slightly different microstructures compared to the LPBF equivalents. Kirka et al. [48] analysed the microstructure and chemical compositions of EBM alloy 718 specimens. Different phases were identified using Energy Dispersive X-Ray Spectroscopy (EDS), their chemical compositions are reported in Table 2.2. The micrographs of AB EBM specimens Figure 2.6 show that EBM specimens have a lower dislocation density than LPBF materials, Laves phase and MC carbides in AB state, and large disk-shaped γ” particles (average size of 80 nm).

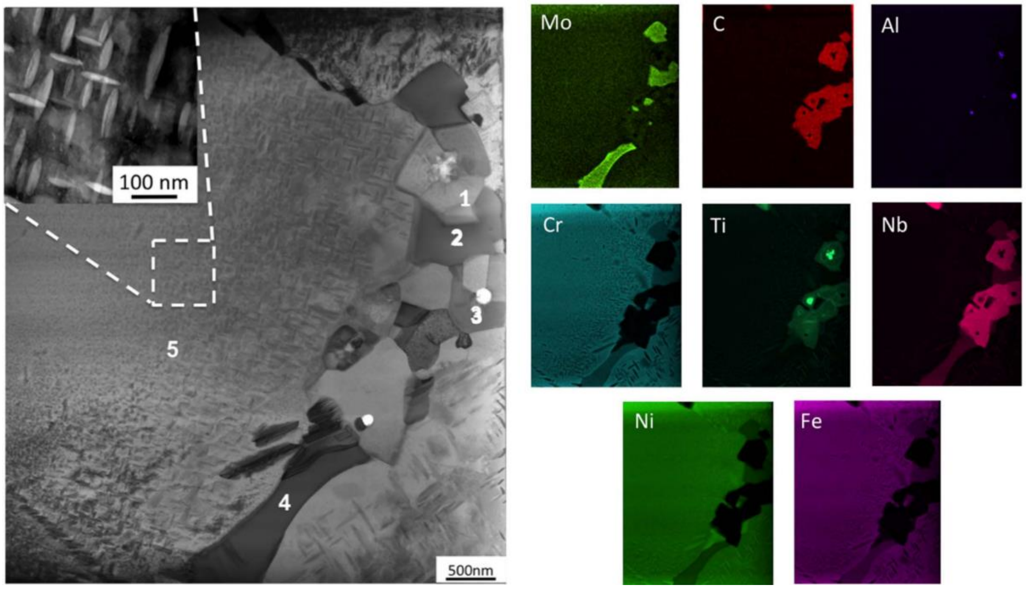

Figure 2.6: As-built EBM Inconel 718 microstructure and EDS results (quantified in Table 2.2) [48]. This shows that Laves phases and MC carbides are present in the as-built state, as well as large disk-shaped γ'' particles.

Table 2.2: Chemical composition of phases marked in Figure 2.6 (wt %) [48]. This provides further proof of the present of Laves phase and MC carbides in the as-built state of EBM Inconel 718.

Items	**Phase**	**Ni**	**Nb**	**Ti**	**Fe**	**Cr**	**Mo**	**Si**	**C**
1	MC Carbide	0.43	89.91	6.01	0.15	0.62	-	-	2.73
2	Laves phase	42.20	22.87	0.11	13.54	11.24	9.53	0.5	-
3	MC Carbide	0.4	90.38	6.31	0.17	0.7	0.71	-	0.99
4	Laves phase	38.8	28.55	0.23	11.70	9.40	11.19	0.77	-
5	γ matrix	56.19	4.14	0.68	18.99	15.91	3.80	0.04	-

Sames et al. [49] observed a variation in microstructure along the build direction of the AB EBM alloy 718 specimens (Figure 2.7). The needle-shaped δ particles at the top were much coarser than those at the bottom. Additionally, the material in this area showed a greater contrast upon etching, indicating a more severe secondary element segregation. Deng et al. [50] provided more detailed information about the precipitate morphologies as well as the microstructural variations occurring during EBM of alloy 718. All these results indicated that thermal cycling varied during the build, influenced by the number of layers already deposited. Hence localised heat treatments (HT) are a common phenomenon in PBF and should be considered in-process optimisation.

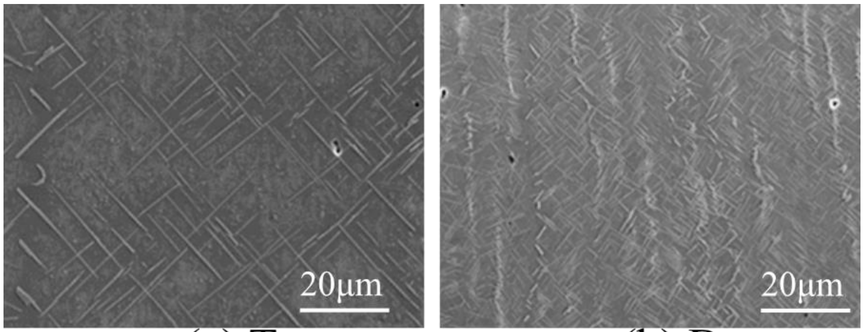

(a) Top (b) Bottom

Figure 2.7: SEM micrographs of an as-built EBM Inconel 718 sample. a) The top of the sample (few thermal cycles). b) The bottom of the sample (many thermal cycles) [49]. This shows a variation in microstructure along the build direction, particularly regarding δ particles which are coarser at the top a).

Polonsky et al. [51] studied the presence and morphology of fusion defects in EBM alloy 718 specimens. Columnar grains, with a primary aspect ratio smaller than 0.2 and oriented in the build direction, were found to surround the defects on the XY plane (Figure 2.8a). Instead, the regions above the defects had small equiaxed grains with almost no discernible texture. This shows that defects drive the recrystallisation phenomena and influence the resulting microstructure.

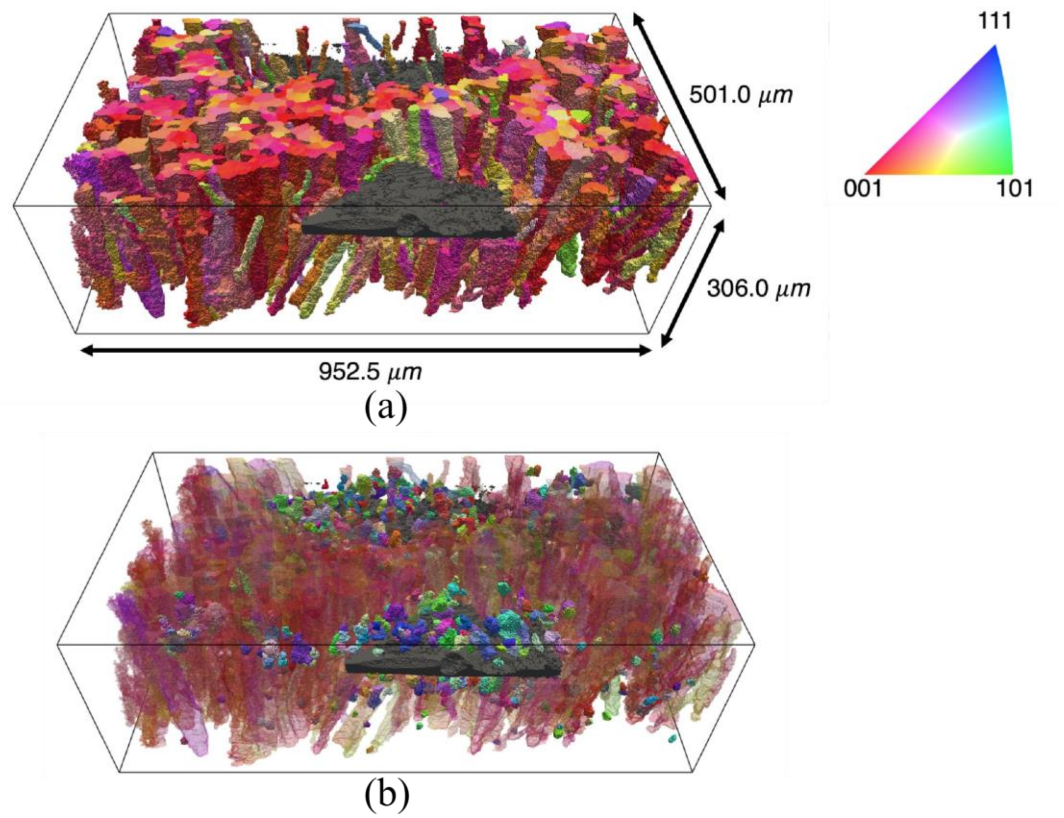

Figure 2.8: EBSD data of grains surrounding a defect. a) The columnar grains surrounding the fusion defect. b) The equiaxed grains above the defect [51]. This shows that defects also affect the build process and resulting microstructural morphology in PBF processes.

Table 2.3 summarises the commonly observed differences in microstructure between LPBF and EBM and Figure 2.9 illustrates some of these differences.

Table 2.3: Summary of common microstructural differences between LPBF and EBM material. The reader is advised to use this with caution as process technology evolves. This table is intended as a broad guide only and observations will vary between process configurations.

Characteristics	LPBF	EBM
Porosity	Both have similar densities in AB or post-processed conditions (~99.9 % with appropriate processing parameters)	
Grain morphology	Elongated grain parallel to the build direction with ill-defined grain boundaries and very fine columnar cellular structures at higher magnifications. Some equiaxed grain formation perpendicular to the build direction which can be recognized at overlapping regions between tracks.	More columnar grain formation than LPBF parallel to the build direction. Perpendicular to the build direction, grains have a more uniform and equiaxed pattern.
Precipitates	Microsegregation of some alloying elements (e.g. Nb, Mo and C) promotes the formation of NbC carbides and Laves phase in the interdendritic region and precipitates on the grain boundaries.	Laves and MC carbides present in AB condition. Disk-shaped γ'' particles, much larger than those found in LPBF, exhibit a directional growth parallel to the build direction. Microstructural variation along the build direction is also present (with δ precipitates much coarser at the top than near the substrate).
Texture	AB samples have a strong <100> crystallographic texture in the build direction.	Texture in the <100> planes along the build direction.

The majority of PBF research has focused on LPBF. EBM microstructures are slightly more anisotropic than LPBF counterparts – more columnar grains and variations in microstructure with the build height – and therefore, LPBF was selected for this project. The fact that this method has also been more researched will allow more comparisons to literature, resulting in a better understanding of mechanical behaviour of nickel-based superalloys.

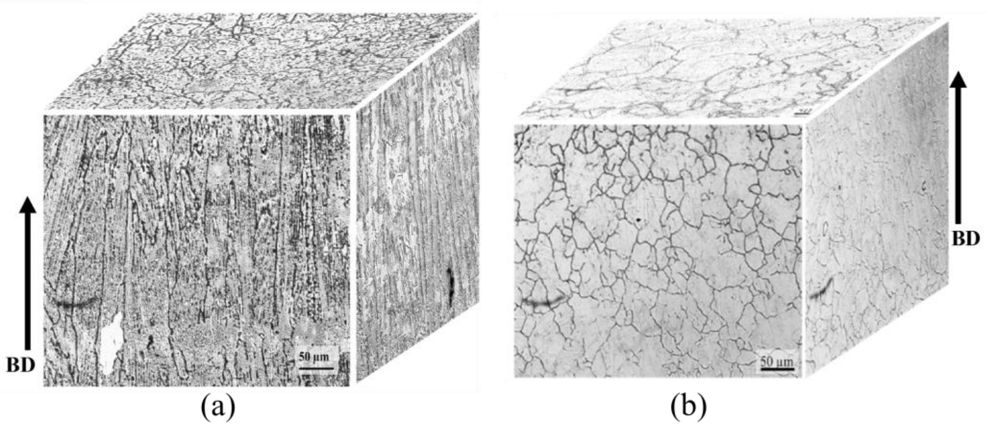

Figure 2.9: Microstructural cubes of hot isostatically pressed Inconel 625. a) Processed by EBM. b) Processed by LPBF. Showing the differences in microstructure produced by the different processes [52], such as grain morphology and size.

Compared to conventional manufacturing, the AM layer-by-layer approach can lead to residual stresses that are both directionally and spatially heterogeneous [53]. Indeed, residual stresses are usually accumulated in PBF parts because of the rapid heating and cooling which results in high dislocation density and acts as strain hardening [54-56]. Usually the first portion of the part to cool is left with compressive residual stress whereas the last portion to cool is left with a tensile residual stress [57]. So PBF materials are usually leftover with a tensile residual stress on the top surface of the build. Unfortunately, tensile residual stresses are detrimental to creep and fatigue performance. The most common way to counteract PBF induced residual stresses is through post-processing [55]. Thermal treatments can reduce or eliminate residual stresses while other treatments, such as shot peening, induce a compressive residual stress on the surface of the material, which is beneficial for mechanical properties, such as fatigue [57]. However, residual stresses can also be reduced through the use of appropriate process parameters. Indeed, studies have found that base plate heating, beam/laser power and scan speed are some of the key parameters affecting residual stresses [55].

Since powder fusion and recrystallisation of the melt pool are the central phenomenon in PBF, different building parameters and post-processing techniques will lead to different characteristics, which can be quantified using the different methods. Exploration of these in more detail is a key concern.

2.2 Alloy 718

This section will highlight the characteristics of nickel-based superalloys, specifically of alloy 718, why they are appropriate for PBF use and examples of their applications, particularly in the aerospace sector. For further information on materials science and nickel-based superalloys, the reader is referred to these textbooks: [58-61].

Alloy 718, like other alloys has multiple phases which are responsible for the material's different properties. The microstructure of superalloys is very complex. It contains a large number of dispersed intermetallics and other phases that modify the alloy's behaviour by their composition, morphology and location [62]. Alloy 718's main phase is the γ-phase – NiCr Face Centred Cubic (FCC) solid solution – which contains multiple secondary phases. These include:

- γ' → $Ni_3(Al, Ti)$ FCC strengthening phase [62];
- γ'' → Ni_3Nb Body Centred Tetragonal (BCT) strengthening phase [62];
- δ phase → Ni_3Nb orthorhombic needle-shaped precipitate [62];
- Laves phase → $(Ni, Fe, Cr)_2$ (Nb, Mo, Ti) Hexagonally Closed Packed (HCP) brittle intermetallic phase [63];
- Carbides → square or spherical particles rich in Ti and Nb [64, 65];
- Topologically Close Packed (TCP) phase → undesirable σ phase which has a hexagonal symmetry
- Other phases → borides, nitrides, sulfocarbides

The size, morphology and type of these phases evolve with time and temperature. Figure 2.10 shows the transformation of the different phases of alloy 718 with time and temperature.

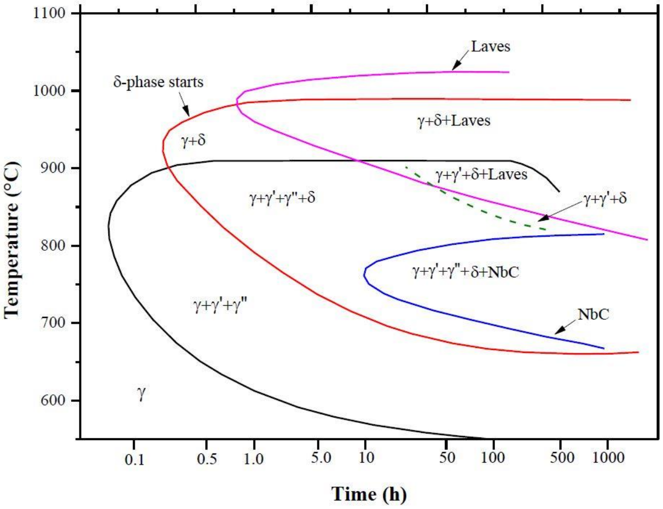

Figure 2.10: Transformation-time-temperature diagram of alloy 718 [66]. Copyright American Welding Society, 1986.

From the phases aforementioned, γ'' is the main strengthening phase of alloy 718. This phase mainly controls the tensile, fatigue [67] and creep properties of the alloy. Indeed, Chaturvedi et al. [68] have observed that the steady state creep rate decreased with an increase in γ'' precipitates, up until an optimum precipitate size. This study also observed an increase in room temperature tensile strength with the increase of γ'' precipitate size [68]. It is therefore clear that γ'' is a key strengthening phase in alloy 718 and responsible for its excellent mechanical properties. However, above 650℃, γ'' transforms into δ phase, which has the same elemental composition. This transformation has a significant impact on the mechanical properties of the alloy 718 as studies have observed a rapid decrease in strength [62], an increase in creep damage [69] and a reduction in elongation at fracture [70]. Thus, in theory, the fewer the number of δ-precipitates, the higher the number of γ'' precipitates which results in better mechanical performance. Therefore, the dynamics between γ'' and δ phase are key to alloy 718 properties, especially for creep.

Material microstructure, and hence, mechanical properties, in superalloys are highly dependent on the manufacturing method [62]. For example, wrought nickel superalloys are used when high toughness is needed, while cast nickel superalloys - which have a relatively large grain size (ASTM 0 or greater) - are used for high strength and creep resistance in high temperature applications [62]. Despite this, the industry standard is wrought alloy and so wrought alloy 718 will be used to benchmark the performance of the LPBF alloy 718 in this project.

2.2.1 Process parameters driven phenomena

LPBF process parameters naturally affect the print quality and the resulting microstructure. The use of optimised process parameters can suppress the formation of voids and build defects, such as micro-cracks [71-73]. Review papers on the process-microstructure relationship for LPBF of metallic materials have been presented previously [74-76] and Kumara et al. [77] also investigated phase transformations of PBF alloy 718. An overview of the different effects of build parameters on PBF of nickel-based superalloys microstructure is given below.

Powder characteristics driving build quality

Powder quality plays a key role in determining LPBF components' final quality. Powders can be rotary, gas or water atomised and exhibit different morphologies, particle size distributions, flowability, surface roughness and chemical composition. These can vary from supplier to supplier [78]. Sutton et al. [79] reviewed the most commonly used powder characterisation techniques, paying attention to the impact of powder quality on final material properties. A similar review by Tan et al. [80] also focused on powder characterisation techniques, with a particular emphasis on powder granulometry. This was identified as a key method to ensure a high performance of the feedstock, leading to high quality and, importantly, dense parts. Studies have found that chemical composition had the strongest impact on the microstructure, as higher content of certain elements resulted in the precipitation of detrimental elements and prevented recrystallisation during heat treatment, which decreased mechanical performance, particularly fatigue [78]. Another work found that the segregation of alloying elements in LPBF Hastelloy X during solidification resulted in variations in composition which caused cracking in the build direction [81]. By investigating four powders with different contents of various alloying elements, Mancisidor et al. [81] achieved a defect free material.

The recyclability of nickel-based powders has been studied by several researchers [82-85]. These generally observed that, as long as the recycled powder is well sieved and stored, little or no difference in properties was found between the specimens manufactured using recycled and fresh powder over ~10 build cycles. However, it was found that the presence of minor alloying elements in the metal powder, can influence the crack formation mechanism in PBF specimens [86].

Sames et al. [87] evaluated the properties of components manufactured using powders obtained from various production methods, namely gas atomiser, rotary atomiser, and plasma rotated electrode process (PREP). From the SEM observations, PREP powder showed a smoother surface and almost no internal trapped gas, compared to the others (Figure 2.11a-c). These voids in the starting powder particles may lead to increased porosity in the final PBF part, which is the case for the powders obtained with the first two methods (Figure 2.11d,e).

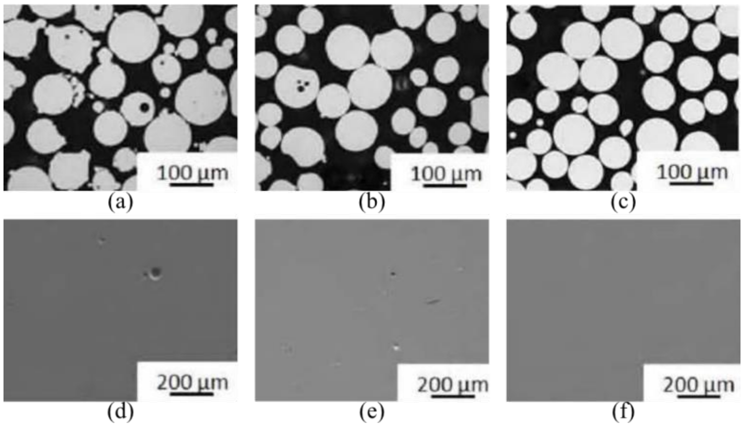

Figure 2.11: Powders and corresponding laser powder bed fused specimens [87]. a) Gas atomized powder at 100 µm scale. b) Rotary atomized powder at 100 µm scale. c) Plasma rotated electrode processed powder at 100 µm scale. d) Gas atomized powder at 200 µm scale. e) Rotary atomized powder at 200 µm scale. f) Plasma rotated electrode processed powder at 200 µm scale. The plasma rotated electrode processed powder showed a smoother surface and almost no internal trapped gas, compared to the others, illustrating the importance and effect of powder types on the resulting microstructure of PBF materials.

Another study compared powder atomisation methods and found that LPBF parts made using water atomised powder resulted in higher sample porosity than gas atomised powder. This was thought to be caused by the more irregular morphology of water atomised powder and hence better packing density but this observation is far from conclusive [88]. However, there are still limitations to gas atomised powder, such as hollow and/or satellite balls [89]. It was also found that the laser absorption rate can be increased by increasing the surface roughness of powder particles [89].

In terms of particle size, work has found that the presence of powder particles smaller than 10 µm resulted in severe agglomeration and impeded LPBF process through spreading problems [90]. Additionally, a method of rapidly characterising powders (morphology, flowability and size distribution) was developed in order to evaluate the influence of different alloy compositions on LPBF processability [91].

It is evident that many parameters combine to define powder quality, which in turn affects the LPBF process and the resulting mechanical properties. Hence, it is essential to understand and control powder quality to produce adequate parts. Therefore, the role of the powder is critical in determining both the interaction with the incident energy beam but also in assuring spread-ability upon the powder bed. Furthermore, the recyclability of powder and its effects on mechanical properties and in-situ alloying [92, 93] are emerging topics and should be investigated. There is significant opportunity to explore this space further as in many cases the economic viability of PBF processes is driven by new powder cost but also how easily it may be recycled.

Controlling the build environment

A review of the build environment in PBF was written by Poorganji et al. [94]. PBF build chambers usually operate under vacuum or an inert gas (e.g. Argon or Nitrogen) in order to avoid oxidation of the part and powder. Traore et al. [95] researched the influence of gas atmosphere on nickel-based superalloys. However, despite processing in an Argon atmosphere with <0.2%, oxidation may still occur, resulting in oxide inclusions in built parts and oxide spatter particles, which were in the size range to be recycled [96]. Zhao et al. [97] investigated the role of the build environment on melt pool dynamics in EBM and LPBF. The LPBF build environment, which has high atmospheric pressure and multiple laser reflections, is the source of more build quality issues, such as vapor recoil pressure on the melt surface, than the EBM build environment. Furthermore, an investigation was conducted on the differences in surface morphology and composition during multicycle EBM with alloy 718 powder reuse and there was a significant change after exposing the powder to the build chamber environment [98]. A study confirmed Al_2O_3 particles were formed in alloy 718 alloys during PBF, which act as nucleation sites for the precipitation of Nb/Ti carbides, leading to the formation of unique core-shell composites with Al_2O_3 in the centre and Ti/Nb at the periphery [99].

Energy beam driven phenomenon

Laser parameters, such as the laser power, scan speed, hatch distance and scan strategy, are some of the main factors influencing PBF microstructures. ‘Stripe’, ‘Meander’, ‘Total fill’ and ‘Chessboard’ (also known as ‘Island’) strategies are some of the main scan strategies used in LPBF currently (Figure 2.12). Different and customised strategies, including multi-laser [100], residual heat factor [101] and ‘unit-cell’ strategies [102], are also being developed in order to obtain and control microstructural characteristics, such as grain morphology, density, defects, cracking, and surface quality.

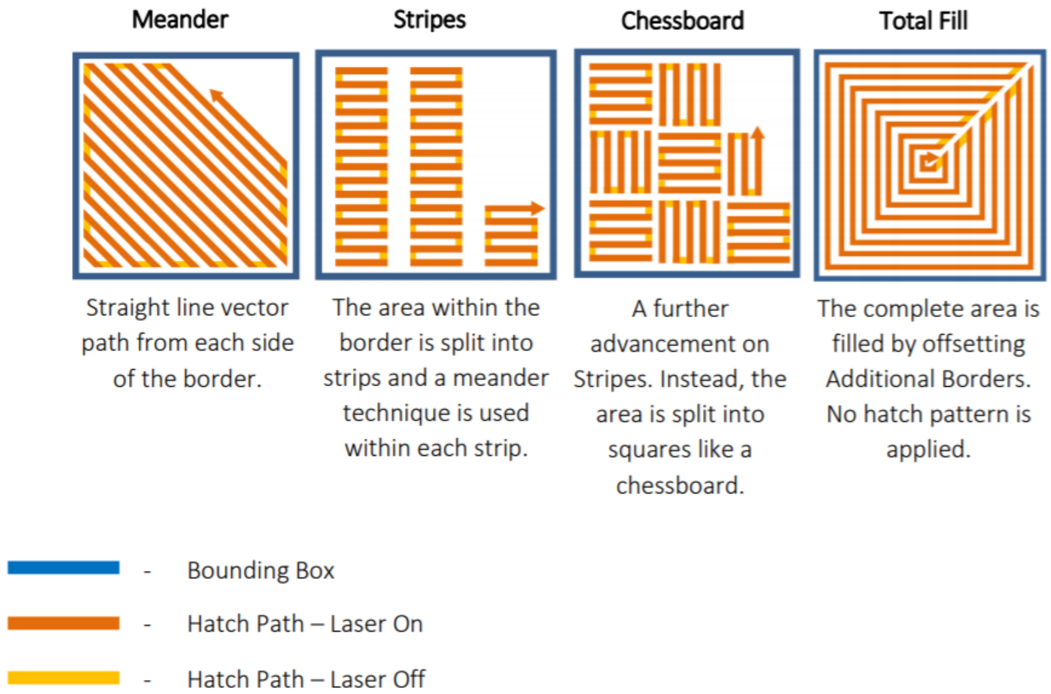

Meander: Straight line vector path from each side of the border.

Stripes: The area within the border is split into strips and a meander technique is used within each strip.

Chessboard: A further advancement on Stripes. Instead, the area is split into squares like a chessboard.

Total Fill: The complete area is filled by offsetting Additional Borders. No hatch pattern is applied.

🟦 - Bounding Box
🟧 - Hatch Path – Laser On
🟨 - Hatch Path – Laser Off

Figure 2.12: Typical scan strategies as demonstrated in the Renishaw ‘QuantAM’ material editor. These result in markedly different microstructures and mechanical properties.

In a study on EBM by Helmer et al. [103], the area energy density E [J mm^{-2}] was used as a comparison parameter to evaluate the overall effects of laser power P [W], scan speed v [m s^{-1}] and hatch distance h [µm] on grain morphology. To allow a comparison, the energy density applied to two specimens was similar, respectively 1.8 J mm^{-2} for the first and 1.9 J mm^{-2} for the second specimen [94]. As expected, different values of scan speed and hatch distance produced two clearly distinct grain morphologies, as shown in Figure 2.13. Additionally, in another study by Karimi et al. [104], it was found that the electron beam focus offset also directly affected the grain morphology. Fernandez-Zelaia et al. [105] also showed that the morphology and texture of the mesoscale can be controlled by the melting sequence. Similar results were found for LPBF processes [106]. Indeed, in a LPBF study, using a flat top laser beam changed grain morphology to a wide and planar geometry with a 150% increase in grain size, compared to 200 W Gaussian beam [107]. Sow et al. [108] also compared a 80 µm diameter Gaussian laser spot and a 500 µm diameter top-hat laser beam and found that the 500 µm diameter top-hat laser beam increased productivity, suppressed spatter and produced fully dense alloy 625 parts.

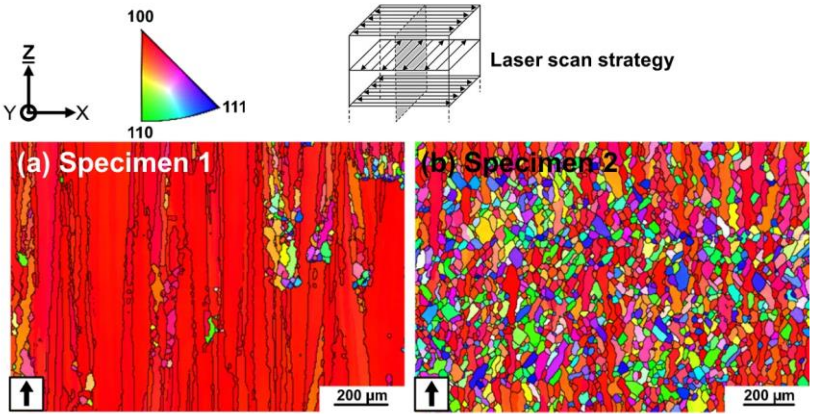

Figure 2.13: EBSD maps of EBM specimens manufactured with different parameters. a) Parameters: E_1= 1.8 Jmm^{-2}, v=2.2 ms^{-1}, h=150 µm. b) Parameters: E_2=1.9 Jmm^{-2}, v=8.8 ms^{-1}, h= 37.5 µm [103]. Varying process parameters result in different microstructures and textures.

Figure 2.14 compared the features of two LPBF alloy 718 specimens, produced with different laser power (250 W and 950 W) [109]. The shape and size of melt pools can be easily recognised in the OM, highlighting a clear influence of the laser power. Indeed, lower power generates smaller melt pools and results in a reduced heat treatment of underlying layers. This, combined with a consequent faster solidification, leads to smaller grains. For LPBF alloy 738LC, using higher laser power increased the depth of keyholes, causing instability and increasing pore formation due to the periodic collapse of the keyholes [110]. Furthermore, laser volume energy density was found to be the main parameter affecting cracking and porosity. For example, increasing the laser volume energy density resulted in an increase in number and size of cracks in the SRR99 nickel-based superalloy [111] and minimal solidification cracking was observed in alloy 738LC with narrow melt pools with a strong melt pool overlap [111]. In LPBF René 104 superalloy was built with 3 different strategies (meander, stripe, chessboard) and these were found to have a significant effect on cracking and relative density [110]. The scan strategies with more partitions were shown to increase the emergence of cracks while the overlapping zone increased the size, number and frequency of cracks [110]. Likewise, residual stresses were shown to be caused by scan-strategy induced microstructure [112] and it was found that a more uniform scan strategy resulted in lower residual stresses [113]. Marchese et al. [114] also confirmed that high thermal residual stresses resulted in hot cracks during LPBF of Hastelloy X.

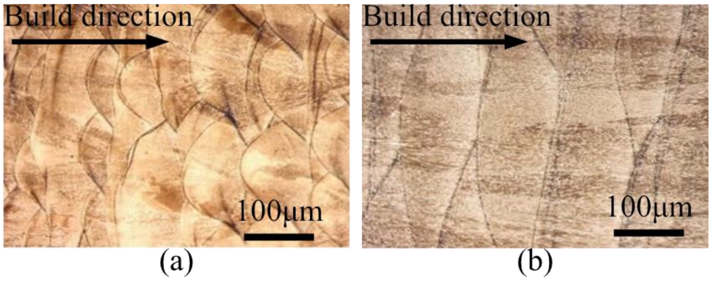

Figure 2.14: Optical micrographs of etched LPBF Inconel 718 specimens manufactured with varying laser power [109]. a) Power = 250 W. b) Power = 950 W. The melt pools across layers can be clearly observed and show that a difference in laser power can significantly affect the melt pool shape.

Part density is also influenced by the laser parameters. Indeed, a study found that the relationship between density and laser input energy during LPBF of GH3536 was found to comply with a quadratic function and presented an inverted U-shaped distribution [113]. Furthermore, results showed that in a given scanning strategy, the density decreased as the scanning speed increased for a fixed energy density [115].

Insufficient laser overlap (large hatch spacing) can deteriorate the surface of materials [116]. Indeed, the laser energy input improved density and surface quality of Ni-Cr-B-Si, with a fine grain microstructure and strengthening precipitates [117]. Attard et al. [118] investigated these effects and produced a controlled functionally graded microstructure by varying the process parameters.

It is apparent that the combination of scan strategies, laser power and other process parameters affect the microstructure and final mechanical properties of PBF components. In order to optimise PBF process parameters, some researchers are using the Taguchi regression method [119, 120] and Artificial Neural Networks [121]. Even with optimised process parameters, it is still necessary to post-process LPBF parts.

2.2.2 Post-processing for component performance

Given the microstructural anisotropy and the defects generated during manufacturing, post-processing is necessary to improve the properties of most AB LPBF components. Post-processing, which includes thermal treatments, surface treatments and machining processes, is a prime method to create more favourable microstructures. The purpose of post-processing is to enhance both the form and integrity of the bulk and surface of a component to elevate performance characteristics. While the intent in all AM processes is to create a component within a single step, it is inevitable that, where shortfalls are apparent, additional measures must be taken. This is not entirely inconsistent with established manufacturing routes. For example, it is a common activity in modern manufacturing to machine a casting. However, in the case of AM where subsequent processing is required the business and design case for this technology will be undermined. Hence, while often currently essential, the research community must endeavour to achieve close geometrical tolerance and material condition in-process as possible. However, Lim et al. [122] wrote a review on reducing residual stress in metal PBF parts which informs us that while stresses may be substantially reduced by process optimisation they cannot be removed entirely within the PBF process itself.

2.2.2.1 Heat treatments for enhancing mechanical properties

In industry, almost all functional AM parts in mission critical applications are post-processed using heat treatment. Heat treatment allows the modification of the microstructure through controlled heating and cooling of materials. By modifying the microstructure, materials can obtain enhanced mechanical properties. Indeed, performance of AB material is poor because of surface integrity defects and unfavourable microstructural formation [64] with secondary phases such as Laves phases that embrittle grain boundaries and are detrimental for mechanical properties [47]. Hence, HTs are used to increase grain size [123], obtain a more equiaxed microstructure, dissolve detrimental phases, such as Laves [124],to form strengthening precipitates such as δ phase, γ' and γ'' [64, 125], and to remove defects [126] to improve mechanical properties. Although sometimes the AB microstructure is more beneficial for certain properties, as in the case of Parizia et al. [127] who found that AB alloy 625 presented better oxidation resistance than its heat treated counterpart. There are different types of heat treatment, each giving different microstructures. Usually, samples are first stress relieved, which reduces texture and residual stress in samples [128]. Then, solution treatment (ST) is used to enhance the mechanical properties [54] by dissolving detrimental phases [129, 130]. Subsequently, samples are sometimes aged (single or double ageing) to favour the precipitation of strengthening phases [124]. Samples can be Solution treated then Aged (STA) or Directly Aged (DA). Thermal techniques, such as homogenisation and HIP treatments are also used. Homogenisation is usually used prior to HIP and is similar to stress relief as it reorients columnar grains [123]. Zhao et al. [131] observed that during homogenisation of LPBF alloy 718, the grains would continue recrystallisation whereas the suction-cast alloy showed abnormal grain growth, which showed the potential of engineering the microstructure of AM materials through heat treatments to obtain superior mechanical properties than in conventionally manufactured alloys. HIP results in recrystallisation, grain coarsening and change from highly textured columnar grains to randomly oriented equiaxed grains which are larger than after homogenisation [123, 132-134]. Moreover, a slightly weaker texture is obtained, compared to STA [133], although it is still strong [132]. HIP was also found to be effective at closing defects, resulting in a higher density [135].

Heat treatment standards exist for conventionally manufactured material, however, as no PBF-specific heat treatment standards have been defined at this time, significant research has gone into exploring the effects of wrought heat treatments and modified heat treatments on PBF microstructure

The Standard Specification for Additive Manufacturing Nickel Alloy (UNS N07718) with Powder Bed Fusion [136] gives guidelines for thermal processing of PBF nickel-based superalloys. For HIPing, components should be processed in an inert atmosphere at no less than 100 MPa, within the range of 1120°C and 1185°C within ± 15°C, and held for 240 min ± 60 min followed by cooling under and inert atmosphere below 425°C [136]. For heat treatment, it states that components should be solution treated and aged following the AMS2774 standard for Heat Treatment of wrought nickel alloy and cobalt alloy parts [137]. This standard gives the range of possible heat treatments to use for different geometries of nickel-based superalloys. It should be noted that none of these heat treatments are specific for AM, but rather are for conventional manufacturing processes. This highlights the need for the development of PBF specific microstructures. Some practitioners, such as Huang et al. [54] and Aydinöz et al. [138], have started to research this area. For example, Huang et al. [54] investigated the effect of solution time, solution temperature, cooling method and ageing process on the mechanical properties of LPBF alloy 718 and identified that there was a minimum solution time for a given temperature to obtain similar microstructures and mechanical properties than materials with a longer solution time (Figure 2.15).

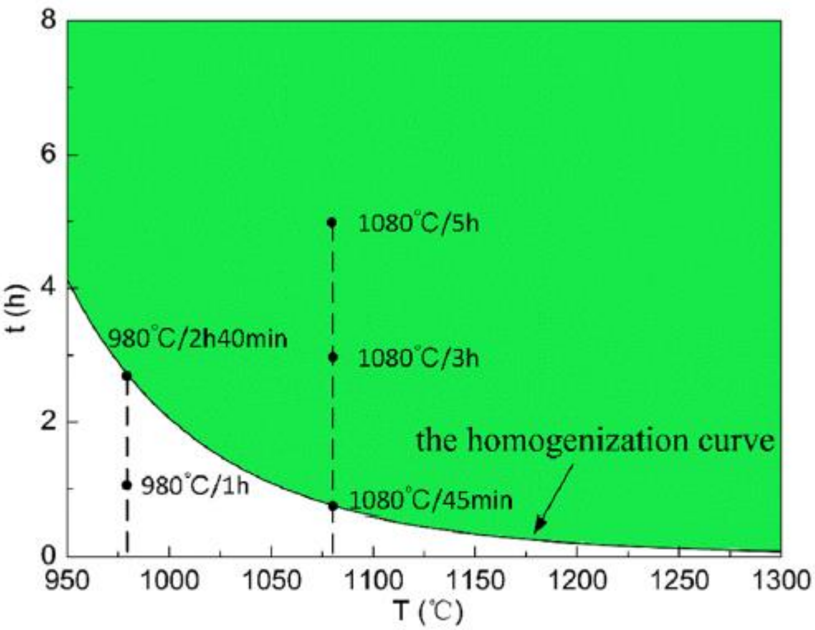

Figure 2.15: Variation of required solution time for solution temperature for LPBF Inconel 718 [54]. This shows that there is a minimum solution time for a given solution temperature which results in similar microstructures and properties.

Grain structure

Although grain boundaries normally occupy a small fraction of material volume, they play a crucial role in controlling material properties. The sensitivity associated with this behaviour drives significant efforts in optimising processes. Figure 2.16a,b compared the microstructures of a heat treated and HIP+HT LPBF alloy 718 specimens [139]. Obvious evidence of the scan strategy used is eliminated in both cases [139]. From the measurements, it was found that the average grain size for heat treated specimens was 15.5 ± 2.0 µm, which was 30% smaller than HIP+HT equivalents.

Holland et al. [140] investigated the evolution of the grain boundary network in AB and heat treated LPBF alloy 718 specimens. It was observed that non-specific grain boundaries dominated in the AB specimens, whereas after heat treatment, the number of specific grain boundaries increased significantly from 9% to around 60%. This second class of grain boundaries includes twin boundaries and twin-related grain boundaries, able to improve material strength and resistance to intergranular degradation. Another study on LPBF alloy 625 provided similar results [141]. It was also found that above a certain annealing temperature (1150°C), these grain boundaries developed in prevalence significantly.

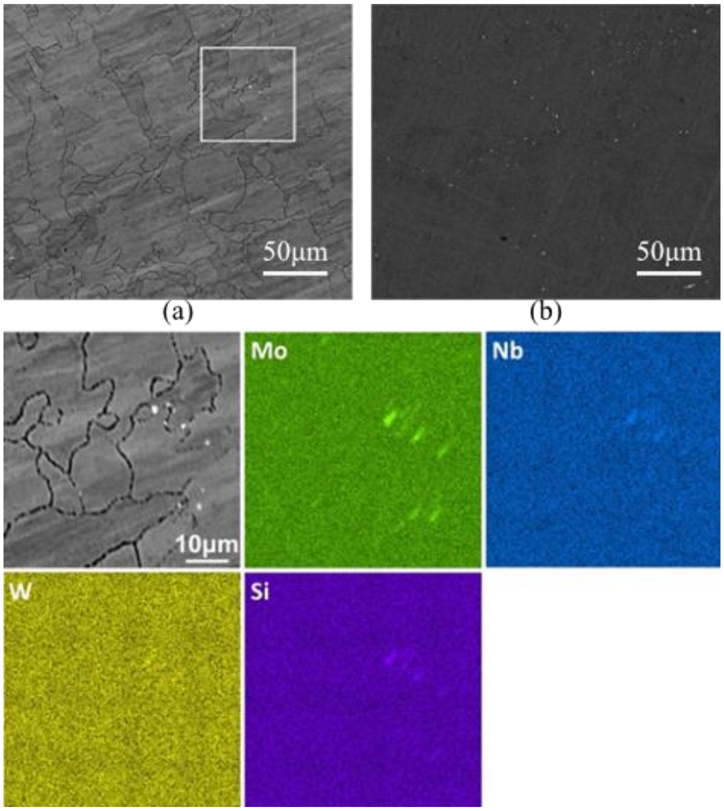

Figure 2.16: Microstructure of LPBF Inconel 718 specimens with varying thermal treatments[139]. a) Heat treated sample microstructure with EDS results of the section squared in a). b) HIP+ HT. This shows obvious evidence of the elimination of scan strategy effects through thermal treatments.

“Grain boundary misorientation” is defined as the difference in crystallographic orientations between adjacent grains of the same phase. This microstructural feature can be characterised through EBSD. Gribbin et al. [142] evaluated the misorientation angle (Figure 2.17) in some heat treated and HIP+HT LPBF alloy 718 specimens. The distribution of the misorientation angles for heat treated specimens was broad, indicating no preferential growth direction. On the other hand, for HIP+HT specimens, the distribution showed a prominent peak at 60°, indicating an equiaxed grain structure with a high twin content caused by annealing. The detrimental effect on fatigue performance previously observed by Zhang et al. [143] correlates well with the misorientation effect.

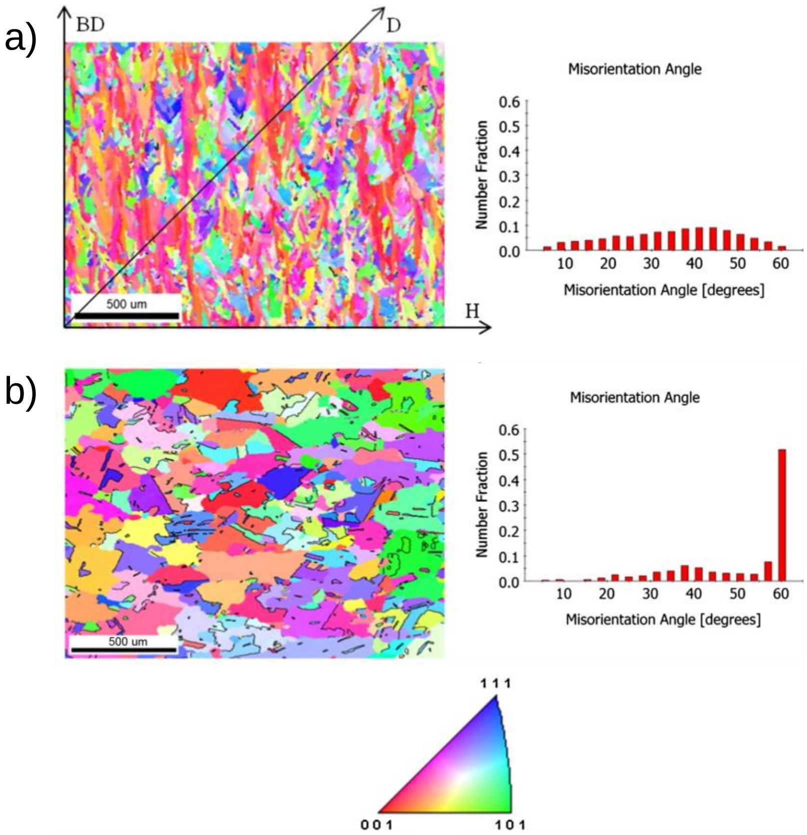

Figure 2.17: EBSD maps of LPBF Inconel 718 specimens showing grain morphology and misorientation angle distributions [142]. a) Heat-treated sample. b) HIP and heat treated sample. The broad distribution in the heat treated sample indicates no preferred growth direction as compared to the HIP and heat treated sample.

In a further study by Chauvet et al. [144], it was found that grain boundaries with a high misorientation angle were prone to crack propagation in AB and heat treated EBM samples (Figure 2.18). Han et al. [145] obtained similar results in this regard. Research also concluded that the difference in interdendritic liquid pressure between the dendrite tip and root, as illustrated in Figure 2.19, would cause an insufficient feeding of molten material at the dendrite root, promoting void generation and therefore highly affecting the part hot cracking behaviour.

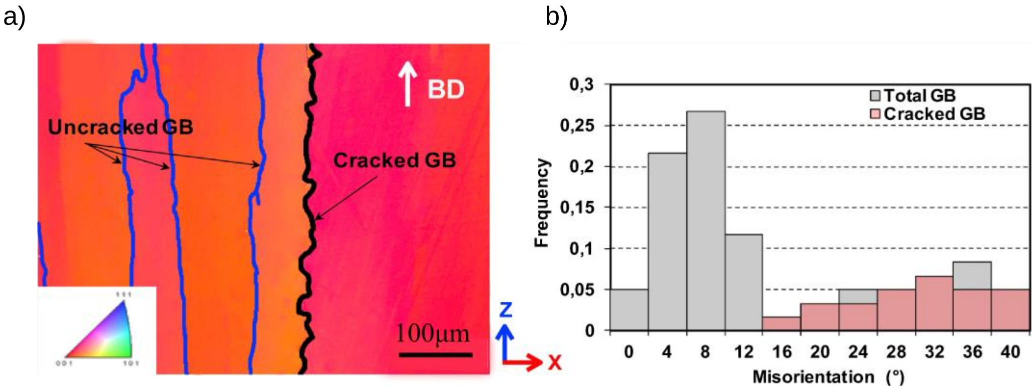

Figure 2.18: This figure demonstrates that grain boundaries with a high misorientation angle are prone to crack propagation in as-built and heat treated EBM samples [144]. a) An EBSD map showing the cracked grain boundary along the high angle grain boundary (misorientation > 15˚). b) The distribution of grain boundary misorientation and cracked grain boundaries.

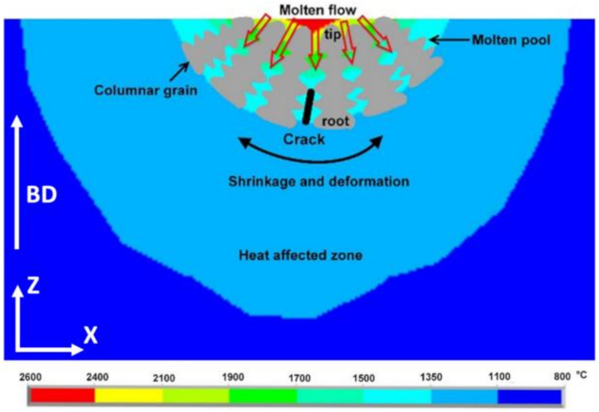

Figure 2.19: Illustration of the hot cracking mechanism in the LPBF process [145], demonstrating crack formation and growth within a single melt pool. This shows that the difference in interdendritic liquid pressure between the dendrite tip and the root causes an insufficient feeding of molten material at the dendrite root, promoting void generation and therefore highly affecting the hot cracking behaviour of the part.

Tomus et al. [146] compared the grain morphology of LPBF Hastelloy X specimens processed with various post-processing techniques. The heat treatment consisted in a single solution step (1175˚C / 2h), while HIP was performed using the same time and temperature, with an applied stress of 150 MPa. Figure 2.20a,c,e,g display a series of EBSD images illustrating the grain morphology in the XZ plane for AB, heat treated, HIP and HIP+HT specimens, respectively. Heat treated and HIP effectively reduced the strong texture in the build direction in the AB specimen [147]. Another study found that HIP of LPBF Hastelloy X 'closed' internal cracks, reduced porosity and generated equiaxed grains [148]. This was also observed in CMSX-4 [77]. Figure 2.20b,d,f,h illustrates the grain morphology perpendicular to the build direction (XY plane). HIP specimens showed a smaller gran size, because of recrystallisation. Similarly to previous results, individual laser scan tracks and small equiaxed grains were also observed in the XY planes [43]. Further studies on post-processing techniques indicated that HIP cannot be considered as an efficient tool to heal EBM induced cracks [149].

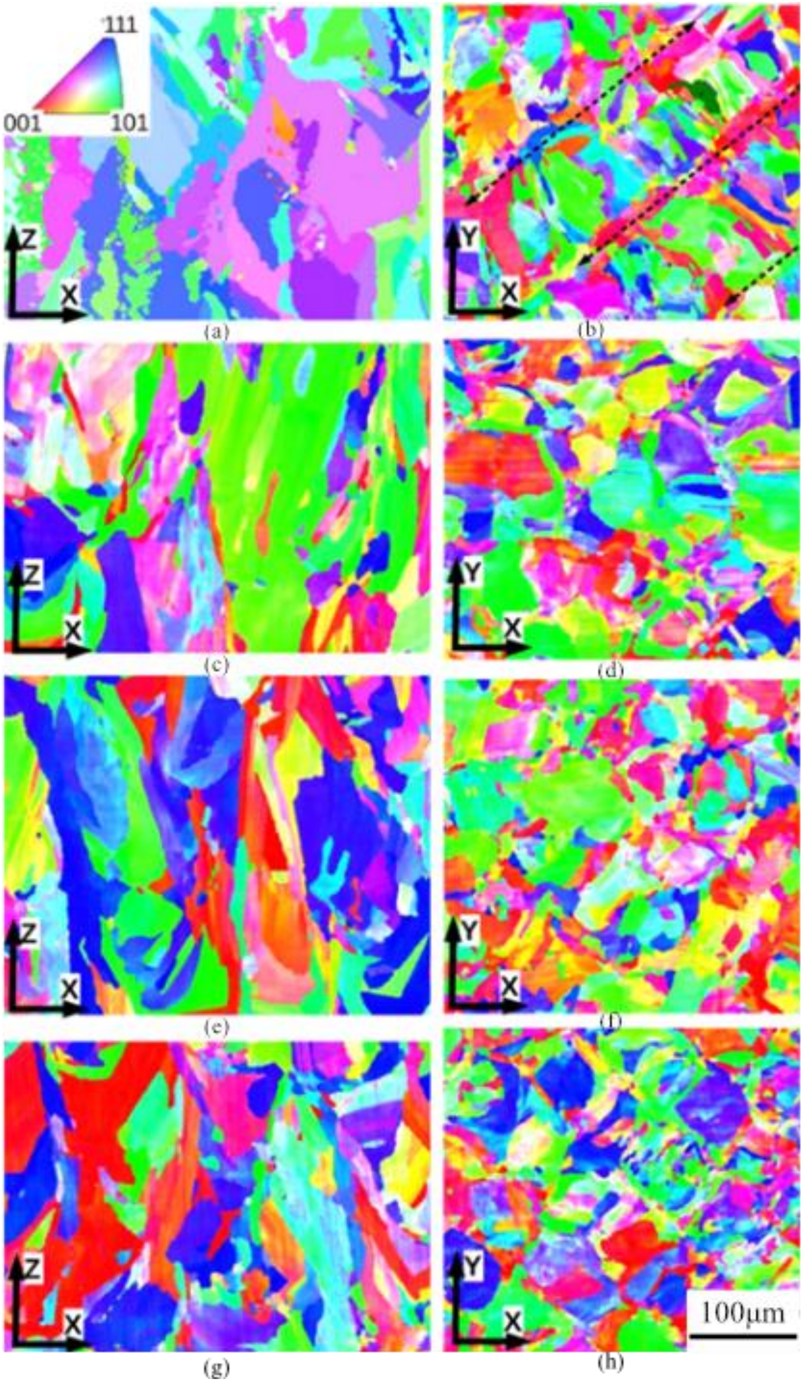

Figure 2.20: Grain morphology of planes parallel (XZ) and perpendicular (XY) to the build direction with varying thermal treatments [146]. a) As-built specimen parallel to the build direction. b) As-built specimen perpendicular to the build direction. c) Heat treated specimen parallel to the build direction. d) Heat treated specimen perpendicular to the build direction. e) HIP specimen parallel to the build direction. f) HIP specimen perpendicular to the build direction. g) HIP and heat treated specimen parallel to the build direction. h) HIP and heat treated specimen perpendicular to the build direction. Heat treatment and Hot isostatic pressing effectively reduced the strong texture in the build direction in as-built specimens.

Precipitate formation

Figure 2.21a,b compare the microstructures of a heat treated and HIP+HT LPBF alloy 718 specimens and shows that 'white' precipitates are clearly visible at grain boundaries [139]. EDS observations indicated that these are rich in Mo, Nb, W and Si, with stoichiometric ratios of $(MoNbW)_5Si_3$ [139]. However, the precipitates in both specimens were similar in size (~2.5 µm) [139]. Similarly, Sames et al. [150] investigated the effects of in-situ heat treatment on γ'/ γ'' phases in EBM alloy 718 specimens. The γ'/ γ'' phases in the AB specimen showed an elongated disk shape, with a diameter of ~20 nm and a thickness of ~10 nm (Figure 2.21a). From the micrographs comparison in Figure 2.21, both the diameter and thickness of these strengthening particles increased during the in-situ heat treatment. Since strengthening phases have an optimal size range and corresponding mechanical properties, this process was found to be effective in improving material strength [150] by impeding the dislocation movement at the grain boundaries [139].

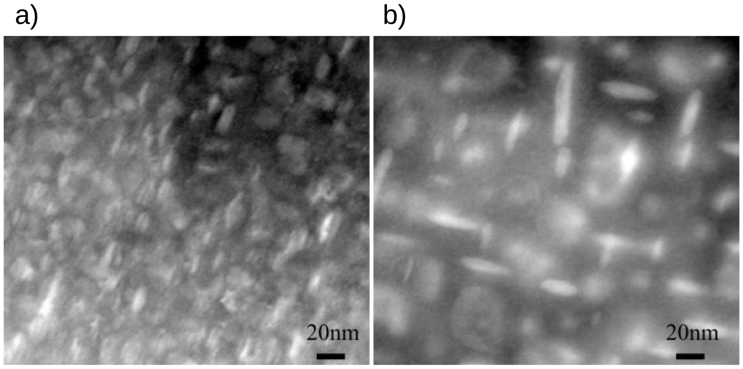

Figure 2.21: TEM visualisation of γ'' precipitates in EBM Inconel 718 specimens [150]. a) As-built samples (low cooling rate). b) In-situ heat treated samples. This illustrates the effect of heat treatment on the size of strengthening precipitates, γ'' in this case.

Furthermore, Divya et al. [151] investigated the heat treatment effects on dislocations and strengthening particles in LPBF CM237LC specimens. In the AB specimens (Figure 2.22a), dislocations entangled and tended to accumulate at the grain boundaries. As shown in Figure 2.22d, the heat treatment decreased the dislocation network density, especially at the grain centre. These observations are in accordance with results by Tucho et al. [152]. At the same time, the heat treatment significantly increased the size of the γ' phase. In fact, before heat treatment, two distinct types of γ' phase could be observed: one with a size of ~5 nm (Figure 2.22b) and another, much larger, with a size ~50 nm (Figure 2.22c). After the heat treatment (Figure 2.22d,e), the primary γ' particles reached a size of over 500 nm, while the secondary γ' particles, characterised by a cuboidal morphology, had a size of ~200-400 nm. Fine tertiary γ' particles were spread in the region between the secondary γ' particles. The influence on γ' particles size may the basis of the strengthening mechanisms caused by heat treatment. During a 3-step heat treatment on LPBF Haynes 282, γ' precipitation was found at 950˚C during TEM in-situ heat treatment [153]. After heat treatment, the morphology and size of γ' precipitates were comparable to powder metallurgy samples and annealing twins were present [78]. Heat treatment was also optimised for LPBF CMSX-4 to obtain segregation of γ/γ' microstructure [52].

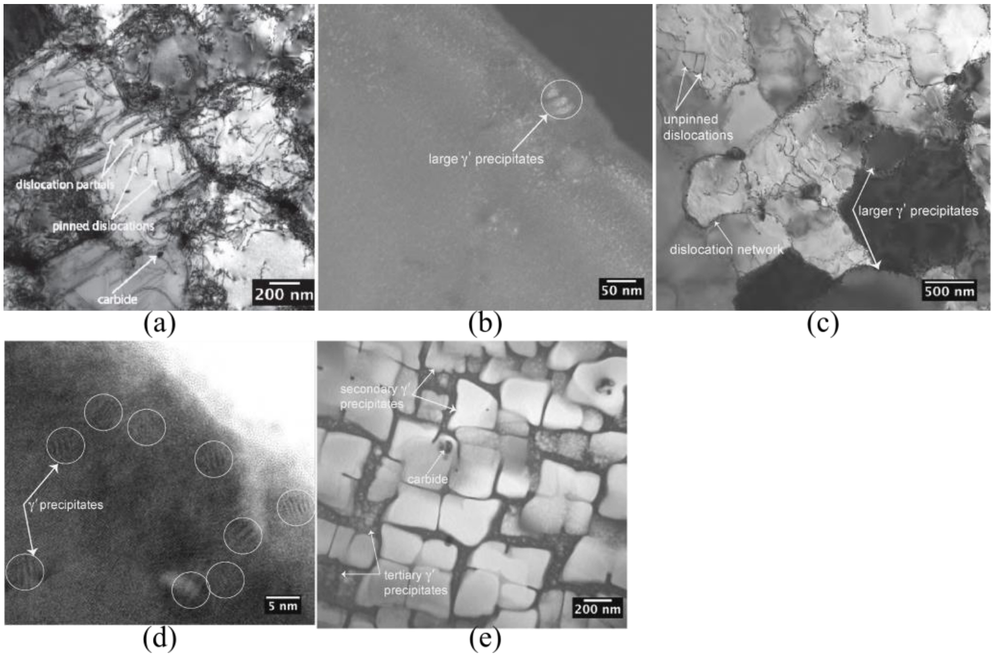
dislocation partials
pinned dislocations
carbide
200 nm
(a)
large γ' precipitates
50 nm
(b)
unpinned dislocations
larger γ' precipitates
dislocation network
500 nm
(c)
γ' precipitates
5 nm
(d)
secondary γ' precipitates
carbide
tertiary γ' precipitates
200 nm
(e)

Figure 2.22: Dislocations and γ' phases in LPBF CM247LC [151]. a)- c) As-built. d), e) Heat treated. Dislocations are entangled and tend to accumulate at the grain boundaries. Heat treatment decreases the dislocation network density, especially at the grain centre.

Kuo et al. [42] evaluated the effects of different heat treatment strategies on the δ phase in LPBF alloy 718 specimens. In the AB specimen, δ phase was found distributed parallel to the build direction, segregated in the interdendritic region due to the Nb segregation during the build process (Figure 2.23a). This was hypothesized to be a consequence of Nb segregation which occurred during the LPBF process. Specimens which underwent a solution treatment and aging (980°C / 1h then 718°C / 8h + 621°C / 10h) possessed a much coarser δ phase than their non-solution-treated equivalents (Figure 2.23b,c, respectively). This difference can be related to the dissolution of γ'' phase and the consequent formation of needle-shaped δ phase during this first thermal treatment. However, these elongated particles are undesirable since they degrade material mechanical properties, causing "δ phase embrittlement".

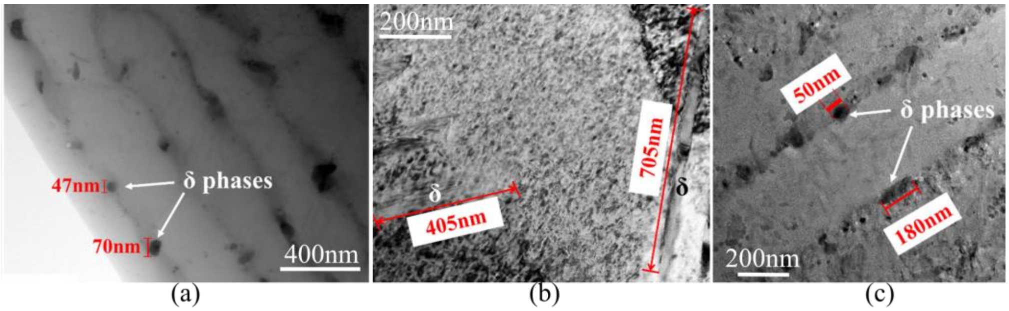
47nm
70nm
δ phases
400nm
(a)
200nm
δ
405nm
705nm
δ
(b)
50nm
δ phases
180nm
200nm
(c)

Figure 2.23: δ phases in the interdendritic region of LPBF Inconel 718 specimens [42]. a) As-Built. b) Solution + ageing treated. c) Direct aged. The solution treated and aged specimen contained much coarser δ phase than their non-solution-treated equivalents due to the dissolution of γ'' phase and the consequent formation of needle-shaped δ phase during this

first thermal treatment. This shows that thermal treatments affect the presence, size and morphology of precipitates in PBF materials.

Stoudt et al. [154] presented a time-temperature-transformation diagram for the δ phase in LPBF and wrought alloy 625 specimens. The formation of δ phase during a LPBF process was found to be much faster than in the conventional wrought process. Moreover, it was observed that the stress-relief heat treatment, normally used in industry for alloy 625 (870°C / 1h, red dot in Figure 2.24), would promote the formation of δ phase during LPBF and not for wrought equivalents. Zhang et al. [155] also proved that conducting this same heat treatment at 800°C can lead to the nucleation and growth of δ phase. The calculated activation energy for the growth of the δ phase was found to be (131 ± 0.69) kJ mol^{-1}. Another study also designed a two-step ST with a two-step aging treatment which facilitated the precipitation of δ phase at the grain boundaries [156]. These results highlight the fact that heat treatment conditions for LPBF processes need to be re-evaluated and distinguished from those used for conventional manufacturing methods.

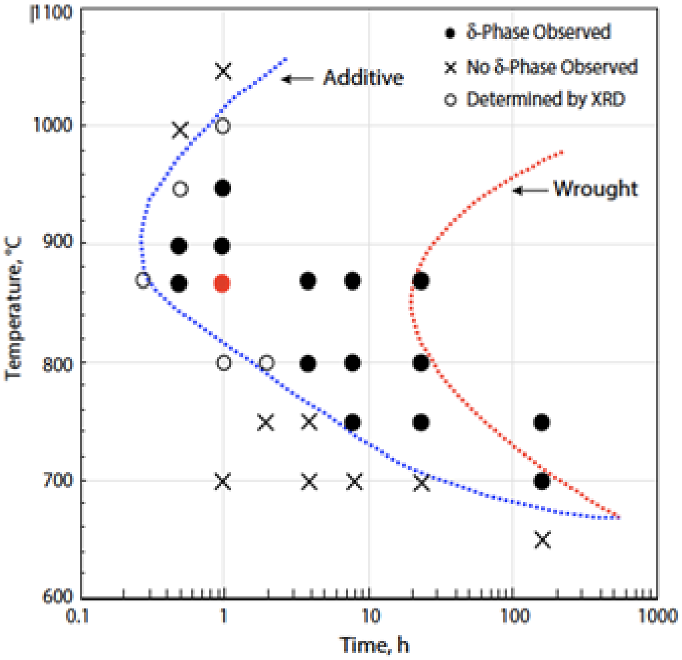

Figure 2.24: A time-temperature-transformation diagram for the formation of δ phase in LPBF and wrought Inconel 625 components. The red dot indicates the industry recommended stress-relief Heat Treatment conditions [154]. This shows that the formation of δ phase is much faster during LPBF than for the wrought process. The stress relief heat treatment (red dot) was shown to promote the formation of δ phase during LPBF but not for wrought equivalents.

Laves phases are another common precipitate which are known to be detrimental to the mechanical properties of nickel-based superalloys. Laves phases subtract Nb from the two main strengthening phases, namely γ'' and δ phase. Pröbstle et al. [157] explained that, in agreement with other studies, only the Laves phases were visible on TEM of AB LPBF alloy 718 (Figure 2.25) because of the rapid heating and cooling cycles, which suppressed other secondary phase precipitation. Hence, heat treatment is necessary to dissolve these and create more wrought-like microstructures.

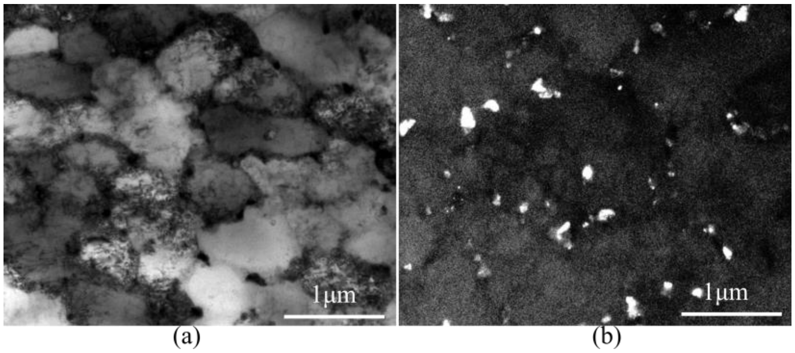

Figure 2.25: TEM images showing the laves phase in the as-built LPBF Inconel 718 [157]. a) Bright field. b) Dark field. Only Laves phases are visible due to the fast heating and cooling cycles, which suppressed other secondary phase precipitation during LPBF.

TEM micrographs and diffraction patterns of LPBF specimens post-processed with different techniques are shown in Figure 2.26. In the solution treated specimen (Figure 2.26a), the associated diffraction pattern (Figure 2.26b) indicated that there were no secondary phases. This means that the Laves phases, which are commonly observed in AB specimens (Figure 2.26), were fully dissolved during the solution treatment. In the HIP specimen, intense recrystallisation occurred (Figure 2.26c,d) due to the high temperature and deformation induced, dissolving all substructures present after build. As for the previous case, no secondary phases were revealed from the diffraction patterns, suggesting a complete dissolution during HIP. As stated, a combination of solution treatment and ageing represents one of the most used heat treatment strategies for alloy 718. Both TEM micrographs and diffraction patterns for this strategy (Figure 2.26e,f) revealed the presence of γ'' particles with a size ~30 nm. Similarly, for HIP + ageing treated specimens, reflections of γ'' phases were observed in the diffraction pattern (Figure 2.26i). From the TEM micrographs (Figure 2.26g,h), needle-shaped δ particles were individuated at the grain boundaries. These observations were similar to those made by Kuo et al. [42]. However, in this case, the needle-shaped δ precipitates were also found to lower the specimen strength. These results confirmed that the precipitation of δ particles reduced the amount of γ'' present in the surrounding area (Figure 2.26h).

Despite the general consensus that Laves phases are detrimental to mechanical properties and need to be dissolved, recent studies have found that certain combinations of size, morphology and distribution of Laves phases can prove beneficial to the mechanical properties of PBF nickel-based superalloys [158-160]. For example, Sui et al. [158] managed to dissolve the sharp corners and grooves of the Laves phase through heat treatment, causing it to change from a long-striped to a granular shape. They then found in another study that granular Laves phases were more beneficial to the plastic deformation of PBF alloy 718 than long-striped Laves phases and that a certain amount of Laves phase was the best match between strength and ductility of the sample [159]. Similarly, Xiao et al. [160] found that fine discrete Laves phase improved the tensile properties of LPBF alloy 718, even outperforming wrought alloy 718, and had good elongation, whereas, the presence of long-chain-like Laves phase resulted in a more brittle nature and suboptimal properties.

Overall, an optimised heat treatment can control the size, shape and distribution of precipitates to engineer the mechanical properties desired. More work should be undertaken to explore this aspect of the PBF processing of nickel superalloys.

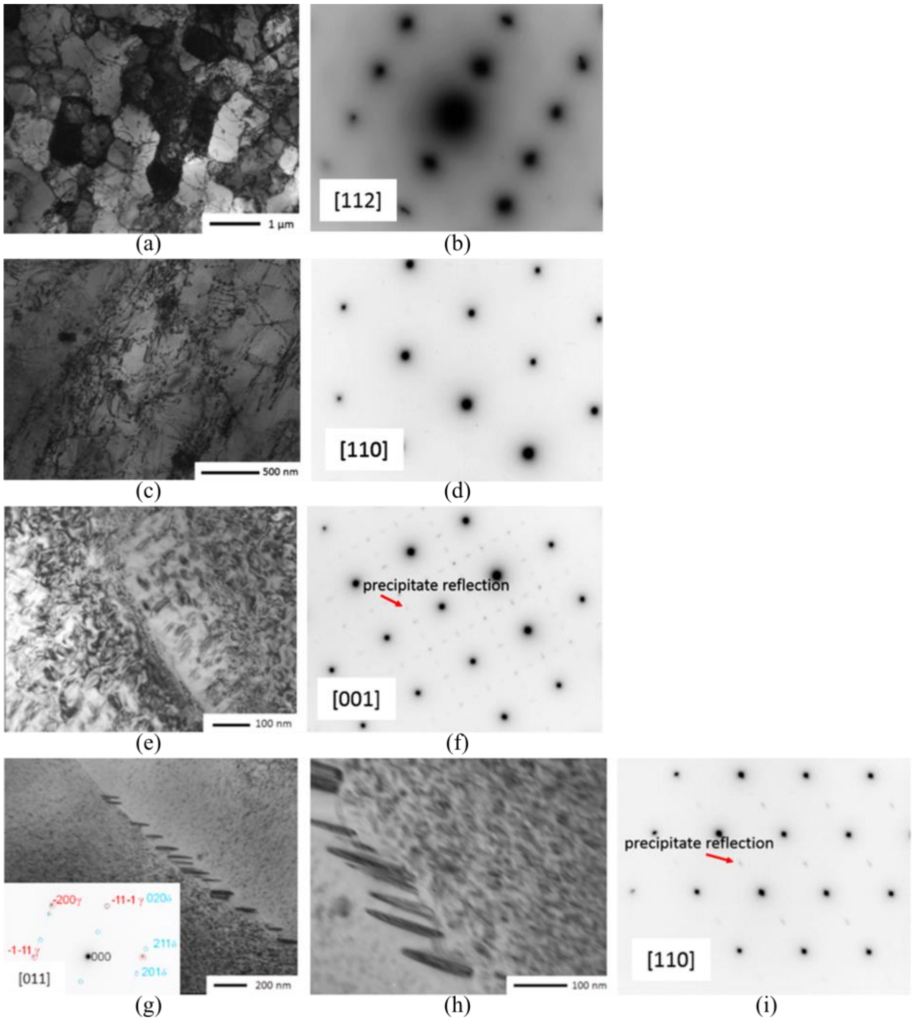

Figure 2.26: TEM images and diffraction pattern of LPBF specimens [138]. a), b) Solution treated. c), d) HIP. e), f) Solution treated and aged. g)-i) HIP and aged. After solution treatment, diffraction shows the dissolution of Laves phases usually present in as-built condition. Following HIP, grains are recrystallised, and secondary phases dissolved. After solution and ageing treatment, the TEM images and diffraction patterns reveal the presence of secondary phases, such as γ''. This demonstrates that solution and ageing treatments are able to precipitate secondary phases.

Residual stress

Tucho et al. [152] demonstrated that thermal cycling during the building process induced residual stresses in the material (a common observation in energy beam processes), producing plastic deformation and dislocation networks (Figure 2.27a).

However, since these are caused by internal stresses, the dislocation networks can be removed using an appropriate heat treatment, as shown in Figure 2.27b.

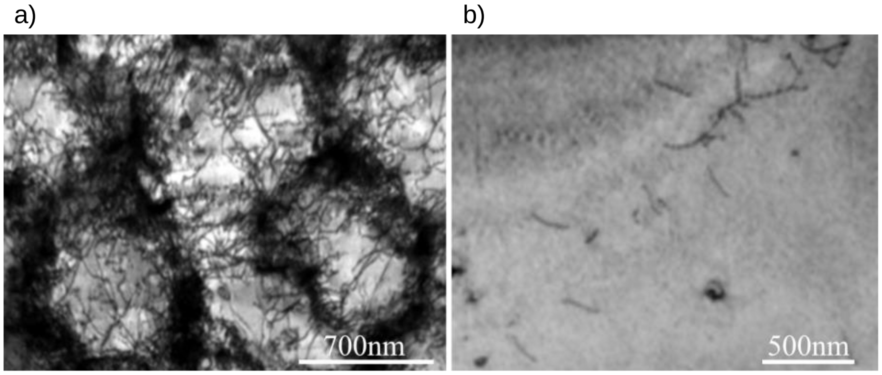

Figure 2.27: Bright field TEM images showing dislocations in LPBF alloy 718 specimens [152]. a) As-built. b) Heat treated. This reveals the presence of Laves phase.

Overall, with the appropriate heat treatment, it is possible to obtain a microstructure which resembles that of a cast nickel-based superalloy, as was the case for LPBF high-strength alloy VZhL21 after progressive stages of post-treatment [161] and Hastelloy X after solution annealing [148]. However, a combination of ductility dip cracking and strain age cracking mechanisms were identified as the primary causes of cracking in LPBF CM247LC following post-build thermal treatments [162]. This shows that heat treatment still requires optimisation to obtain a defect free LPBF material.

Surface integrity following machining

Machining is often required to obtain the desired geometry following LPBF. AM components present new machining challenges given material inhomogeneity and intricate geometries. Given the implicit part-to-part variation traditional datum acquisition challenges associated with casting are apparent. However, given the limitations of current class LPBF systems it is likely that additional value add to AM components will be derived by machining processes.

Machining processes affect materials' microstructure, surface quality and induce residual stress. As stated previously, PBF materials have different microstructures, surface roughness and residual stresses than conventionally cast or wrought nickel-based superalloys. A review on the machinability of conventionally manufactured nickel-based superalloys was conducted by Ezugwu et al. [163] and discusses the issues with the machining of nickel-based alloys and the cause of tool wear and failure. Hence, the effects of machining will be different and it is important to understand their impact in order to control part quality. A study compared the effect of different post-processing techniques - namely barrel finishing, ultrasonic shot peening, ultrasonic impact treatment and shot peening – and their effects on surface roughness, hardness and residual porosity [164]. Ultrasonic impact treatment had the best reduction in surface roughness (by 57.4%) and in residual porosity (by 84%), while shot peening improved hardness the most (by 66.5%) [164]. A different study also showed that shot peening and ultrasonic impact treatment improved the surface texture parameters and residual stresses of HIP LPBF alloy 718 [165].

Furthermore, the use of electropolishing surface treatment with anhydrous electrolyte solution was studied to improve the surface quality of LPBF alloy 718 [166]. The results clearly indicated the potential benefit of introducing highly regulated electrolyte flow in the polishing of AM metal parts [166].

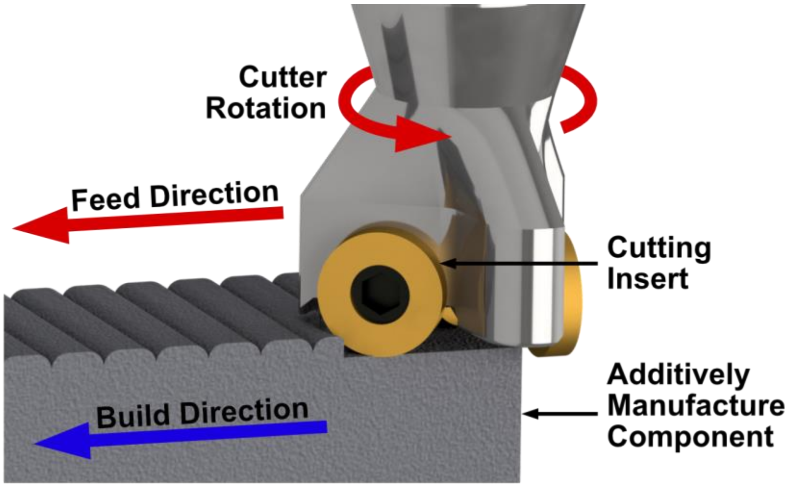

Figure 2.28: This shows the effect of the PBF build orientation on the subsequent machining. The greatest cutting force is generated when the feed direction is parallel to the build direction, which gives rise to anisotropy at machined faces.

Studies have shown that the PBF microstructure of nickel-based superalloys has implications for the machining process as well. For example, there are peculiar interactions between build orientation and machining strategy [167]. It has been shown that the surface topography and integrity of LPBF alloy 625 was affected by the relative orientation of cutting direction to the build direction and scan strategy orientation [168]. Indeed, Patel et al. [168] showed that machining with the feed in the build direction generated the greatest cutting force (as shown in Figure 2.28) of the orientations tested. Similarly, another study found that feeding the cutter against the build direction resulted in lower peak forces with larger deviations while feeding along the build direction resulted in higher peak forces with lower deviations [169]. Further, LPBF alloy 718 with HIP and heat treatment were found to have better minimum specific cutting energy, minimum tool wear and minimum surface roughness during milling than wrought alloy 718 [170]. The peak milling cutting force was found to be dependent upon the feed direction as well as the layer-wise scan rotation employed in fabricating LPBF alloy 625 [169]. Hence, these studies reveal that, in a similar theme as “Design for Manufacture”, the need to select PBF build parameters for post-processing needs to be considered [167].

A development area is the use of hybrid machines which build and machine the part during the same process [171, 172]. For example, using a new hybrid method which combines LPBF and Laser Shock Peening, a 95% decrease in CM247LC cracks was obtained [72]. Hence, more research should be conducted on hybrid machines as they have the potential to further control the microstructure and mechanical properties of PBF materials.

2.3 Creep properties

The characterisation of mechanical properties is essential before AM components can safely be used in beyond static applications. A review of the mechanical properties of metal AM parts was written by Lewandowski et al. [14] should the reader require broader context.

2.3.1 Fundamentals of creep

Creep is a time-dependent continuous deformation which occurs at high temperatures (above 0.3-0.4 T_m (in Kelvin)) and stresses [57, 58, 173]. Therefore, the creep strain (ϵ) depends on stress (σ), time (t) and temperature (T), resulting in the following relationship: $\epsilon = f(\sigma, t, T)$ [58]. A brief overview of the different creep mechanisms and micro-mechanisms is discussed below.

There are two main creep mechanisms: diffusional creep and dislocation creep. The creep rate of both mechanisms is limited by diffusion [57, 58]. These mechanisms occur at different temperature and stress ranges and in the intermediate temperature regime, creep deformation can be a mix of the both mechanisms [57]. The deformation mechanism diagram (Figure 2.29) summarises the competition between the two mechanisms [58].

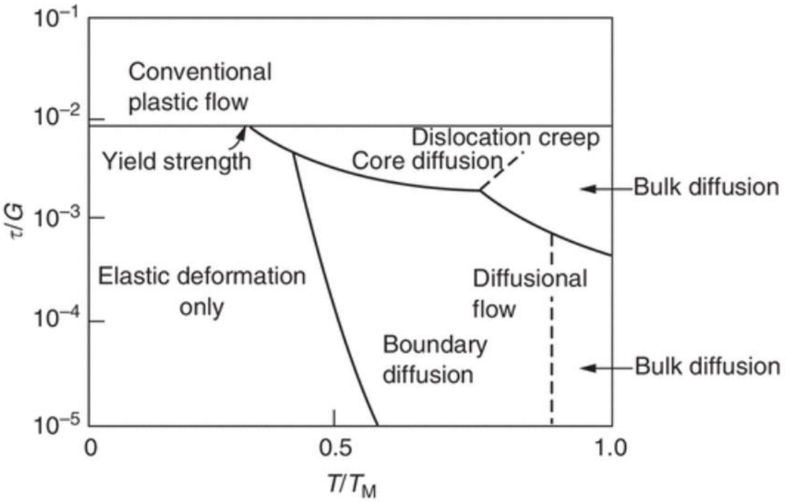

Figure 2.29: Creep deformation mechanisms at different stresses and temperatures (τ is the equivalent shear stress and G is the shear modulus). From [58].

Diffusion creep mostly occurs at high temperatures (above $0.6T_m$) and low stresses and causes creep fracture [57, 173]. Under stress, crystals extend and grains elongate [58]. Hence, voids appear on the grain boundaries that lie normal to the tensile stress. Then, atoms at these boundaries diffuse, coming from the boundaries parallel to the stress (Figure 2.30b) [58]. What's more, boundaries with voids also act as sources of atoms. The voids cannot support the load and so the stress increases on the boundaries. Grain boundary sliding happens and voids grow more and more quickly and finally link and cause fracture [58]. The diffusional flow is more important when grains are small, thus single crystals are the best to avoid diffusional creep [58], which is why turbine blades are directionally solidified as a single crystal. Furthermore, at the end of the creep regime (0.5-0.99 T_m), bulk diffusion inside the crystal is dominant [58] and the creep rate is controlled by lattice diffusion [57]. There are different types of diffusional creep mechanisms, such as the Nabarro-Herring and Cobble creep mechanisms.

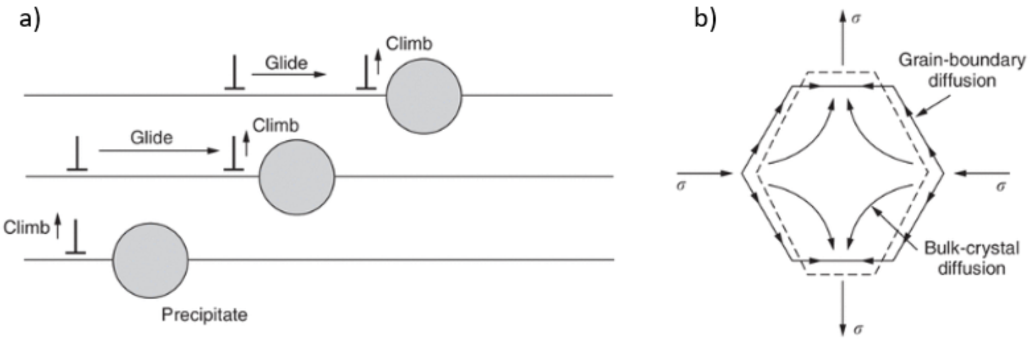

Figure 2.30: Creep Mechanisms. a) Dislocation creep. b) Diffusion creep. From [58].

Dislocation creep mostly occurs at low temperatures (inferior to 0.4T_m) and high stresses [57, 173]. The deformation is controlled by dislocation glide, as diffusion is negligible [57, 173]. The stress required to make crystalline materials deform plastically is the one needed to make the dislocations move [58]. Their movements are restricted by the intrinsic lattice resistance and the obstacles present in the lattice. The low temperature also impedes dislocation motion as they need diffusion (which can only happen above 0.3$T_{m,}$) to be able to “climb” over atoms [58]. Climbing unlocks dislocations from the precipitates and hence further dislocations are started (Figure 2.30a) [58]. Furthermore, in dislocation creep, the diffusion of atoms can “unlock” dislocations from obstacles, and hence, the movement of dislocations under the applied stress leads to dislocation creep [58]. Indeed, at the lower temperatures, core diffusion seems to be the dominant mechanism [58]. Creep rates in dislocation creep are much higher than in diffusional creep [173]. There are also different types of dislocation creep, such as solute drag creep and Harper-Dorn creep.

Regardless of the mechanism, creep damage, which is material degradation that gives rise to tertiary creep, occurs in specimens [174]. There are four different types of damage: damage by loss of external section, by loss of internal section, damage by degradation of microstructure and damage by environmental attack [174]. One of the most common type of damage is by loss of internal section with cavitation perpendicular to tensile stress or the growth of a dominant crack, which reduces the section and accelerates the creep rate [174]. Figure 2.31 illustrates this type of cavitation damage and how it corresponds to the creep curve, particularly to the tertiary region.

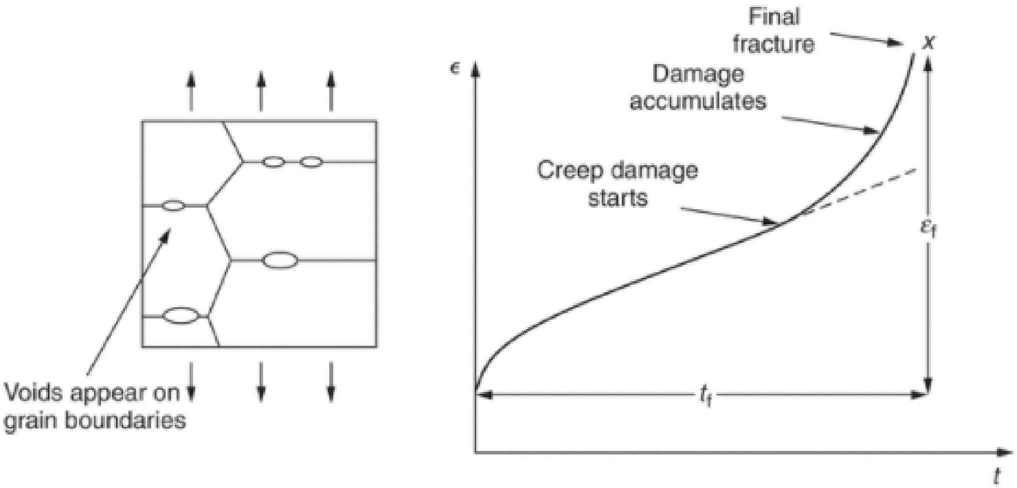

Figure 2.31: Illustration of creep damage due to cavitation and the effects on the creep curve, mainly in the tertiary region. From [58].

It is possible to model creep using various models. Commonly used models include the Norton Power Law, the damage models and microstructure models.

One of the simplest models is the Norton Power Law model which can model the steady state creep rate of materials. This model is dependent mainly on stress and shows close correlation between experiments in prediction for secondary creep rates. However, this model greatly deviates from experiment results for tertiary creep rates. So other models may be better fit, as was the case for Hayhurst et al. [175] who found that a sinh function of stress, rather than the power law was best to describe the strain rate and rupture behaviour of an aluminium alloy.

Damage models take into account damage sustained by the material prior and during creep. The Liu-Murakami model works on the assumption that creep strain rate depends not only on the applied stress, but also takes into account the amount of damage sustained. This model shows a very high correlation in the primary and secondary creep between the experiments and predictions, and a slight deviation is noticed when the material gets into the tertiary creep stage. Therefore, the Liu-Murakami model can be satisfactorily applied across the whole range of creep damage of materials.

Continuum damage models are used to describe damage in materials, such as microvoids or microcracks initiation and propagation until failure. The Kachanov model takes into account the continuous degradation of a material during creep by using a ratio of intact area over original area, to predict creep failure times. This type of model can be very useful in modelling creep where microvoid initiation and coalescence occurs. This can also be even more applicable to PBF materials which have higher porosities than their conventionally manufactured equivalents.

Damage models can have a number of variables, which can result in better predictions. For example, Hayhurst found that a 2-state variable theory was able to describe the shape of the tertiary curve [175] and was used to describe softening mechanisms, damage initiation and growth for a low alloy ferritic steel within continuum damage mechanics framework [176]. Similarly, Hyde et al. [177] found that single-state variable and three-state variable creep damage constitutive models were appropriate to model uniaxial and notched bar creep tests of P91 steels, using Finite Element Analysis.

Other models have used the physical properties and microstructure of materials to model creep. Spigarelli developed a microstructure-based model - which took the presence and evolution of different types of precipitates, subgrain recovery process and strengthening mechanisms into account - to assess the long-term creep strength in 9Cr steels [178]. Other studies have also combined microstructure-based modelling with damage models, such as Murchú et al. [179] who developed a physically-based creep model which used precipitate coarsening continuum damage mechanics. These types of models could become very useful for modelling LPBF as their starting microstructure is different from that of conventionally manufactured materials.

Although modelling will not be in the scope of this thesis, this is still a very important element that needs to be researched if PBF nickel-based superalloys are to be used in real-life applications.

It is very important to be able to extrapolate creep data as it is usually not possible to undertake creep tests which will last as long as real service conditions. Therefore, some models are needed. One of the most common models are the Larson-Miller [180] and Monkman Grant models [181].

The Larson-Miller relation, is a parametric relation that takes both time and temperature into account used to extrapolate experimental creep data. Modified versions of the Larson-Miller parameter exist and take into account various types of materials.

The Monkman-Grant relationship can characterise the interrelationships between steady state creep rate ($\dot{\epsilon}^c$), time to fracture (t_f) and elongation at fracture (ϵ_f) as:

$$\frac{\dot{\epsilon}^c t_f}{\epsilon_f} = constant \text{ [181]}$$

The Monkman-Grant relationship also has numerous variations and modifications to better suit different materials and conditions.

For more information about the fundamentals of creep, the reader is directed to the following textbooks: [58, 60, 173, 182].

Alloy 718 has long been used for creep performance and hence, its creep behaviour is well documented. Studies have investigated the creep deformation of conventionally manufactured alloy 718 at different temperatures, loads, after different heat treatments etc [183]. During these studies, γ” has been shown to control the steady creep rate and cavities formed on grain boundaries during tertiary creep, which is a typical creep mechanism [183].

Due to the specific PBF process which melts metal to build parts layer-upon-layer, PBF metals have long since been compared to welds. PBF and welded metals also have higher number of cavities than base metal counterparts [184]. The creep of welds has previously been studied by numerous authors. For example, the creep strength of P91 welds was found to be slightly below lower bound values for P91 [185] .Other studies also found significant differences in creep performance between base metal, weld metal and heat affected zone material [186]. The microstructural changes in welded joints were also studied and found that carbides coarsened faster in the heat affected zone compared to the base metal [184]. Therefore, it is clear that welded joints and PBF metals have similar aspects, however, the PBF process parameters are capable of changing and controlling the metal microstructure of parts and hence, there are many aspects of creep performance that are PBF specific.

2.3.2 Creep of PBF materials

Creep is one of the main causes of failure in aero-engine turbine blades and hence, it is important to study this mechanical property if nickel-based AM components are to be used in critical engineering applications. However, the creep performance of LPBF nickel-based superalloys has not yet been fully researched yet. Studies have focused mainly on alloy 718 (Figure 2.32a) and on the effect of thermal treatments and build orientation (Figure 2.32b) on the creep properties. Figure 2.32 also highlights the areas which require more research, such as the effect of surface condition and complex geometries on the creep properties of PBF nickel-based superalloys. Investigations to date also report significant shortfalls with respect to counterparts machined from wrought material. Table 2.4 summaries the creep studies to date for LPBF alloy 718 which is of interest in this work.

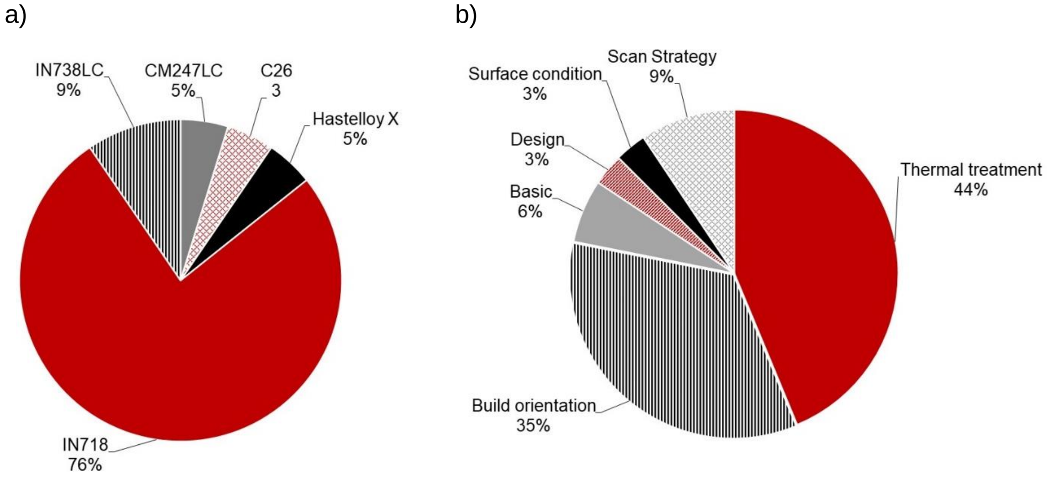

Figure 2.32: Pie chart of the materials and the PBF parameters investigated in the creep studies to date, from 21 papers. a) The materials studied. b) The parameters studied (the label “Basic” refers to studies which only tested the material in one condition, focusing on performance without looking into the effect of a certain parameter.) Inconel 718 is the main material investigated and the effect of thermal treatments and build direction have been studied the most.

Table 2.4: Summary tables of LPBF alloy 718 creep studies.

Parameters tested	Creep conditions	Observations	Ref
Build orientation	650°C, 550 MPa	90° samples performed better than 0° ones in terms of creep life and elongation at fracture by a factor of 8. Creep rupture lives and elongation at fracture were lower than wrought alloy 718 for both LPBF specimens by a factor of 2 and 5, repsectively.	[33]
Build orientation; **Heat treatment**	700°C 250-375 MPa	90° samples heat treated following AMS5664 had creep properties, equivalent to a cast alloy 718 master curve, with a creep life of up to 2500h when creep tested at 250 MPa.	[187]
Heat treatment	Compressive creep 630°C, 725 MPa	With solution treatment + ageing, the creep rate obtained (~10^{-8} s^{-1}), was thought to be equivalent to wrought alloy 718.	[188]
Heat treatment	Compressive creep 630°C 900-1100 MPa	Irrespective of heat treatment, LPBF had superior creep strength than cast and wrought alloy 718 by one order of magnitude.	[157]
Post-processing	650°C, 550 MPa	HIP + direct ageing was found to be the best post-process for creep rupture life, which approached 800h.	[35]
Post-processing	650°C, 747.5 MPa	WEDM heat treated material, with a creep life of 48.27h, performed 4 times better that As-built creep samples, but both had a 33% lower creep life than wrought material (~150h of creep life).	[64]
Scan strategies	650°C, 690 MPa	Meander scan strategy resulted in enhanced creep performance (24% increase in ductility and 22% increase in time to fracture) compared to the Island strategy.	[34]
N/A	650°C, 550 MPa	300h creep life for LPBF alloy 718, inferior to wrought material which had a life of ~1200h.	[189]
N/A	700°C, 560 MPa	24.4h creep life for LPBF alloy 718, inferior to forged material, which had a life of 63.9h.	[69]

This table shows that the build orientation, scan strategy, heat treatment and post-processing are the main parameters which have been studied to this date for creep of LPBF alloy 718. Few creep studies have been conducted to date for LPBF processed metals, and some of the tests reported were too short in duration for true creep mechanisms to occur [190]. Other parameters, such as laser power, scanning speed, additional build orientations, hatch spacing, scan strategy, etc., and the effect that these have on the creep behaviour of the material, have not so far been investigated. One of the most recent build parameter options to be added to modern LPBF machines is the use of multiple lasers, which can significantly decrease build time, and hence cost. Wong et al. [100]evaluated the effects of using a single-laser per part with the machine's 4 lasers operating at the same time, for various parts. It was observed that the build time was reduced by 63% and that the mechanical properties under consideration (tensile strength and hardness) were not compromised in comparison to those measured from samples built on single-laser machines. They state that future work should consider the effect of using multiple lasers for a single part, which will be undertaken here.

The two most common types of creep tests are tensile loading tests [190-197] and compressive loading tests [157, 188, 198]. The former can provide information on creep fracture. For example, Brodin et al. [191] observed the creep fracture surface of LPBF Hastelloy X tested at 815˚C with a tensile load. Unlike tensile tests, compression creep tests are usually interrupted when a predetermined plastic deformation is achieved. Some non-standard creep specimens, such as two bar specimens have also been used [190]. Small punch creep specimens are another commonly used specimen geometry, these tests are shown schematically in Figure 2.33.

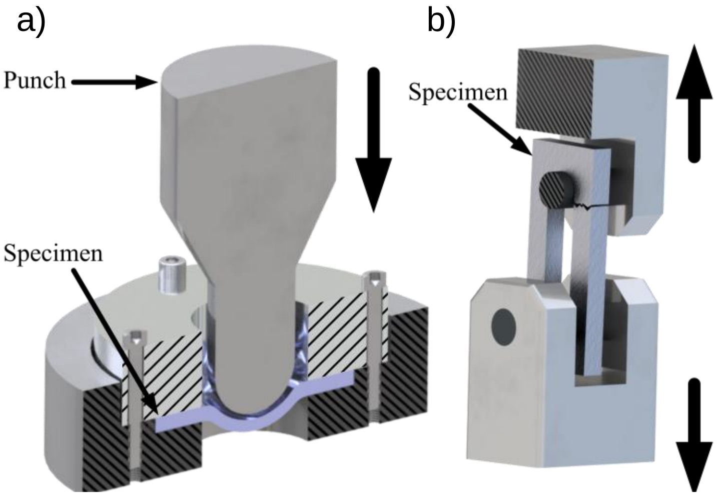

Figure 2.33: Schematic showing tests on two non-standard specimens. a) Small Punch test. b) Two Bar Specimen test. This illustrates the potential of small and non-conventional specimen testing in PBF.

Wang et al. [199] used a small punch creep test to compare the creep performance of forged, cast and LPBF material. The results (Figure 2.34) indicated that the AB LPBF specimens possessed similar creep lifetime to the forged ones, but far lower than the cast specimen. Laves phase at the grain boundaries may have led to poor creep performance in the LPBF specimens. Moreover, the local tensile stress induced by the experimental loading in the fracture region also the reduced time to rupture. Another study also found that LPBF alloy 718 had a lower creep ductility than its wrought equivalent due to oxide contamination from the powder surface [200].

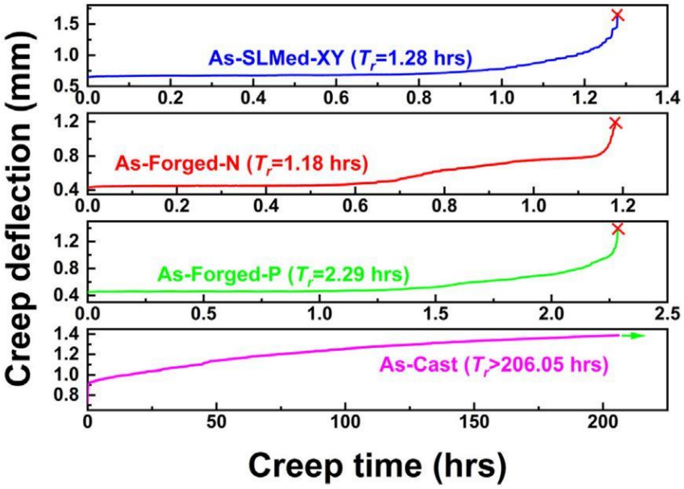

Figure 2.34: Creep deflection vs creep time results for specimens in different conditions (Forged-N: loading direction parallel to the forging direction; Forged-P: loading direction perpendicular to the forging direction) [199]. Indicating that the as-built LPBF specimens possessed similar creep lifetime to the forged ones, but far lower than the cast specimen.

New AM 'specific' approaches for creep testing inspection have been investigated. Xu et al. [190] conducted a new staged thermal-mechanical testing method which looked at the defect evolution in the LPBF alloy 718 specimens during creep. The idea was to interrupt the testing and characterise the defects using X-ray computed tomography. For example, Figure 2.35 shows the porosity distribution along the specimen length at different stages: before testing, at 7.3% strain, at 11.5% strain and after failure, showing the increase in porosity during creep. This also allowed the characterisation of the porosity accumulation during creep and the localisation of the position of the weakest point (Peak 1').

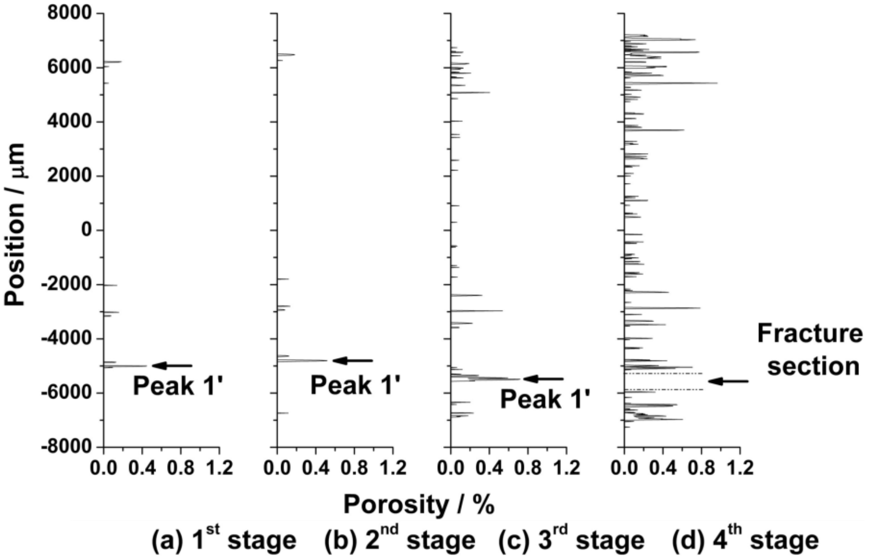

Figure 2.35: Porosity distribution in the specimen at different stages of creep testing [190]. Showing the potential of using X-ray Computed Tomography (XCT) to determine where failure will occur in a specimen and for investigating evolution during tests.

2.3.3 Effect of laser powder bed fusion process parameters

The effect of LPBF build orientation on creep performance has been widely studied [191-195]. Rickenbacher et al. [192] considered the creep performance of horizontally and vertically built LPBF alloy 738LC specimens. The results indicated that the vertically built specimens had better creep resistance than cast equivalents. Hautfenne et al. [187], Kuo et al. [195] and Kunze et al. [193] obtained similar results, explaining that vertical samples had the stress applied parallel to the columnar elongated grains, behaving similarly to the creep resistance strengthening mechanisms in directionally solidified and single crystal superalloys [201]. Small Punch Creep testing of LPBF CM247LC with different process parameter (beam power, layer thickness and energy density) and build orientations (30° and 90°) found that 90° samples performed better for creep deformation [202]. Shassere et al. [203] also studied the influence of microstructure on creep performance of EBM alloy 718 specimens. The results indicated that specimens with columnar grains possessed better minimum creep rate and longer creep rupture lives than the ones with equiaxed grains, especially when the loading direction was parallel to the columnar grain growth direction. In fact, having the grain boundaries transverse to the loading direction was found to be particularly detrimental to creep resistance.

Laser power is also an important factor which can affect creep performance. Popovich et al. [196] investigated the creep performance of LPBF alloy 718 specimens manufactured with two different laser powers, namely 250 W (59.5 J/mm3) and 950 W (59.4 J/mm3). In general, ductile fracture (Figure 2.36a) dominated in specimens produced with lower power, except in some regions rich in brittle precipitates (Figure 2.36b) [196]. On the other hand, specimens manufactured using higher power failed before reaching the required testing conditions. This was mainly due to the presence of a large number of built-in defects (Figure 2.36c,d) caused by the excessive power.

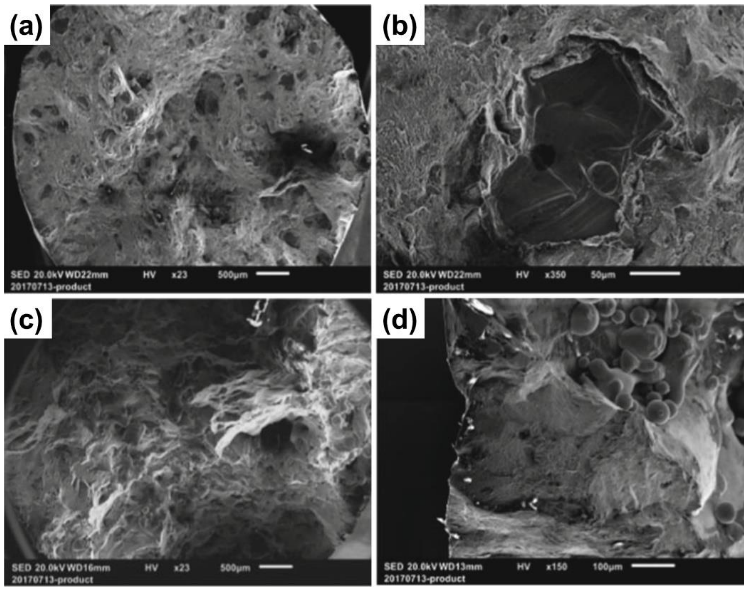
(a)
(b)
(c)
(d)
SED 20.0kV WD22mm HV x23 500µm
20170713-product
SED 20.0kV WD22mm HV x350 50µm
20170713-product
SED 20.0kV WD16mm HV x23 500µm
20170713-product
SED 20.0kV WD13mm HV x150 100µm
20170713-product

Figure 2.36: Creep fracture surfaces of LPBF Inconel 718 specimen built with varying laser power [196]. a),b) Laser power of 250 W (59.5 J/mm3). c),d) Laser power of 950 W (59.4 J/mm3). This highlights the catastrophic failure associated with lack of fusion.

Assessing functional performance of functionally graded materials produced by AM is an interesting emergent research area. Popovich et al. [196] analysed and compared the performance of post-treated LPBF alloy 718 specimens and functionally graded specimens [196].

2.3.4 Heat treatment for enhanced creep performance

To improve LPBF specimens creep performance, post-processing is still necessary at the present. Multiple studies compared the effects of heat treatment on LPBF alloy 718 specimens [157, 188, 195, 204, 205]. Pröbstle et al. [157] characterised the creep performance of cylindrical specimens subjected to different HTs, including direct ageing and STA. The post-treated specimens showed an improved creep strength. As a confirmation, Hautfenne et al. [194] proved that the use of a solution temperature higher than 1000°C could contribute to better creep performance. Using a solution temperature of 1000°C followed by a two-stage ageing treatment resulted in better creep resistance than specimens directly aged [157, 188]. However, when the solution temperature was decreased below 1000°C, direct aged specimens performed better [157, 195]. Two possible reasons were identified to explain these results [157]. The first might be related to the strengthening phases composition. In nickel-based superalloys, Nb content is critical since it forms the main strengthening precipitates. When solution treated at 1000°C, δ phase dissolves, releasing Nb in the surrounding matrix and hence allowing more γ” precipitation. On the contrary, when treated at 930°C, more δ phase is formed at the expense of γ” phase. But since these precipitates contribute more to creep resistance than the δ particles, specimens treated at 1000°C perform better. The second possible reason might have been the size of γ” (Figure 2.37), with the largest average size of these precipitates was found in specimens treated at 1000°C (13.4 ± 5.8 nm), followed by direct aged ones (9.4 ± 3.2 nm) and lastly the 930°C treated ones (9.1 ± 5.8 nm) [157]. Wang et al. [206] however, noted that using STA resulted in a shorter creep life than using homogenisation ad ageing treatments. Another study found that creep life and ductility was improved after heat treatment by adding Y (yttrium) as Y-oxide (yttria) precipitated around the δ phase instead of Al-oxides, which impeded δ phase precipitate growth and improved creep properties [205].

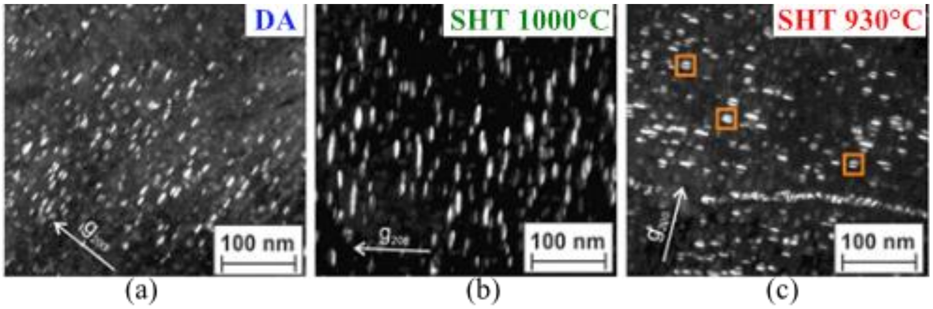

Figure 2.37: TEM images showing the γ'' phase after different thermal treatments [157]. a) Direct aged. b) Solution treated at 1000 ˚C then aged (SHT1000˚C). c) Solution treated at 930˚C then aged (SHT930˚C) conditions. Using a solution temperature of 1000˚C followed by a two-stage ageing treatment resulted in better creep resistance than specimens directly aged, but when the solution temperature was decreased below 1000˚C, direct aged specimens performed better.

Similarly, Davies et al. [207] tried two heat treatment strategies with different solution temperatures (1150˚C and 1275˚C) to improve the creep performance of LPBF C263 and found that the higher solution temperature increased creep resistance. This was because a higher solution temperature generated a more equiaxed microstructure, smaller average local misorientation, shorter random grain boundary network segment length and carbides (MC and M_6C) precipitation at grain boundaries. It was concluded that shorter random grain boundary network segment length, meant shorter potential intergranular crack paths. In turn carbides could hinder grain boundaries deformation, further improving creep resistance.

There is only limited understanding of the creep performance of LPBF materials due to the low number of papers published and the difficulty to creep test LPBF materials, which resulted in premature failure in some studies. The effect of build parameters and heat treatment on creep performance of LPBF nickel alloys is also poorly understood. It is therefore necessary to evaluate the sensitivity to build orientation effects, which gives rise to anisotropic behaviour, scanning strategies, multi-laser strategies and the role of post-build heat treatment.

2.4 Summary of findings

Overall, this literature review highlighted the potential of using LPBF to manufacture nickel-based superalloy components for critical engineering applications. This area of research is rapidly expanding and is the subject of numerous studies. However, the lack of understanding and the sometimes poor performance of LPBF materials (e.g. ductility, fatigue, creep) means that components are not yet suitable for "real-life" applications. Alloy 718 is the main material used in nickel-based superalloys research as it has excellent LPBF processability and mechanical integrity at high temperatures. The mechanical properties of this alloy have been researched, however, most of the studies focused on tensile and hardness properties, leaving a knowledge gap in terms of other properties such as fatigue and creep. Understanding creep properties is vital if LPBF alloy 718 is to be used in critical engineering applications, such as turbine blades, where creep is one of the main causes of failure. The limited amount of creep studies to date have investigated some LPBF process parameters, such as build orientation, as well as the effect of thermal treatments. However, these investigations were limited and, in most cases, LPBF alloy 718 components performed well below their conventionally manufactured counterparts. It is hence necessary to provide a deeper understanding of the effect of process parameters, such as build orientation and scan strategy, and heat treatment on the creep behaviour of LPBF alloy 718 and comparing it against wrought alloy 718. Further, the use of multi-laser scan strategies, which can increase process speed, would make the use of LPBF more appealing to more industries and applications. Hence, it would be beneficial for this aspect to be researched. Finally, to allow a deeper understanding of creep properties, the evolution of microstructure during creep can also be investigated, especially since this has not been done for LPBF alloy 718. This in turn will give a clearer idea of what microstructural features are desired for creep performance and a heat treatment to obtain such features will be proposed. By investigating the formerly mentioned aspects, a deeper understanding of the creep behaviour of LPBF alloy 718 can be achieved which will serve as a steppingstone for future research on microstructural engineering, heat treatment and other high temperature properties. This will allow LPBF to become more attractive and one step closer to real life applications.

3 Experimental methods

To investigate the creep behaviour of LPBF alloy 718, the effect of heat treatment and process parameters on the creep performance were investigated. Specimens were LPBF with varying build orientation, scan strategies and number of lasers per part before being, post-processed, creep tested and analysed (Figure 3.1). From these results the best performing specimen in terms of creep life and minimum creep rate was chosen to undertake interrupted creep testing to investigate the textural and microstructural evolution of LPBF alloy 718 during thermomechanical testing.

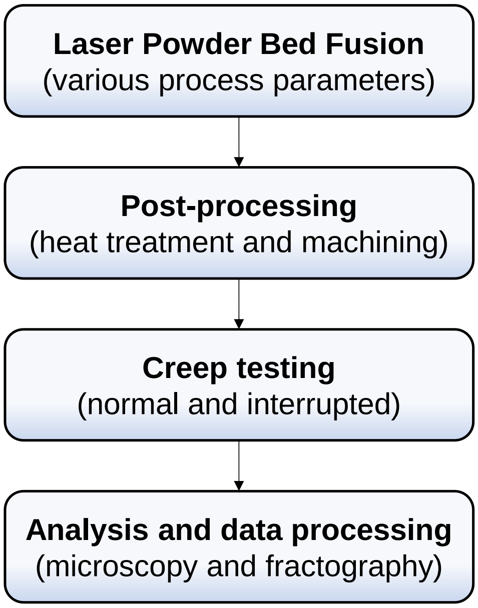
Laser Powder Bed Fusion
(various process parameters)
Post-processing
(heat treatment and machining)
Creep testing
(normal and interrupted)
Analysis and data processing
(microscopy and fractography)

Figure 3.1: Flowchart of the methodology followed in the project.

3.1 Laser powder bed fusion

All specimens were built using a Renishaw© and commercially available alloy 718 powder, whose composition is shown in Table 3.1.

Table 3.1: Renishaw© alloy 718 powder composition.

Element	Weight %	Element	Weight %
Ni	52.5	**Co**	0.04
Cr	19.1	**C**	0.03
Fe	Bal.	**Mn**	0.02
Nb + Ta	4.89	**N**	0.01
Mo	3.2	**Cu**	0.01
Ti	0.86	**P**	< 0.01
Al	0.42	**S**	0.001
Si	0.04	**B**	< 0.001

Single and multi-laser built parts were manufactured in 3 build orientations (0°, 45° and 90°), using 2 different scan strategies (Stripe and Meander), as shown in Figure 3.3. Optimised process parameters (schematically shown in Figure 3.2), developed to reduce build uncertainty and defects caused by phenomena such as powder spattering [208], were employed for the creep specimens and are shown in Table 3.2.

Table 3.2: List of process parameters employed for the build of all specimens.

Parameter	Value
Layer thickness	60 µm
Laser power	212.5 W
Exposure time	20 µs
Hatch point distance	17 µm
Scan speed	0.85 m/s
Hatch distance	90 µm
Stripe size	10 mm
Stripe offset	-0.2 mm (-0.4 mm for 0° creep specimens **only**)

It should be noted that the 0° Creep specimen has a different Stripe offset than its 90° and 45° equivalents as the parameters were not optimised at that time. The results and discussion will be presented with this in mind.

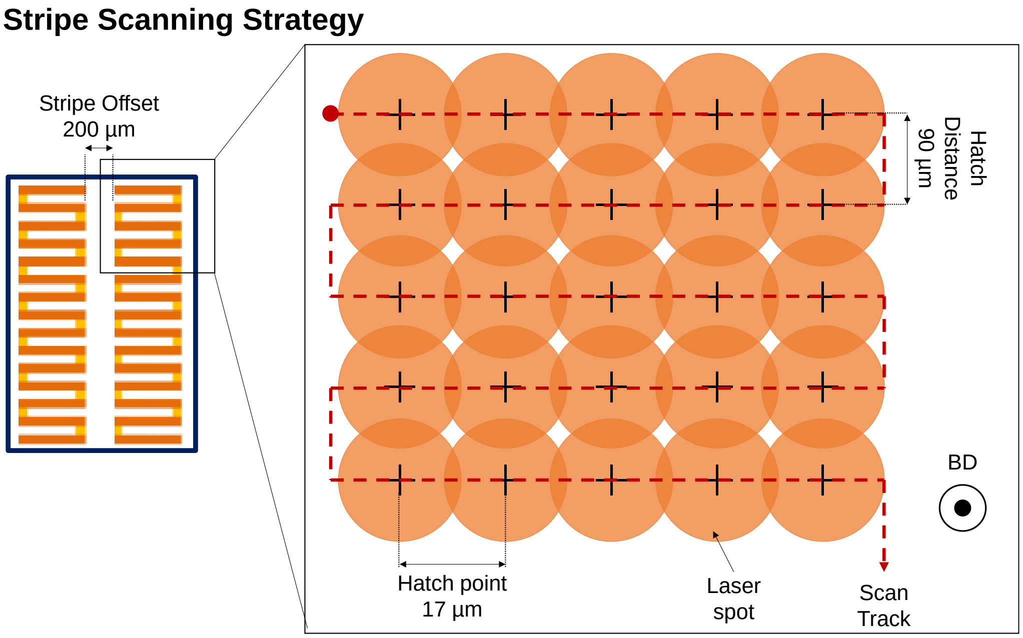

Figure 3.2: Schematic representation of the Stripe scanning strategy showing the different parameters used. With the build direction (BD) indicated.

The uniaxial creep specimen blanks - 14 mm diameter 100 mm long cylinder - were built on a Renishaw© RenAM 500Q quad-laser machine. The machine is equipped with four 500 W lasers (which can be used in continuous or modulated modes), that can be fired simultaneously. All four lasers have the same power so when two lasers are firing at the same cross-section at once, the power input on the build plate is doubled at that time. The overlap between two different laser is the same as the overlap selected for the scan strategy. This gives the freedom to either assign one laser per part or assign multiple lasers to melt a single specimen cross section. The slicing software, QuantAM, was used to assign build parameters, scan strategies and the number of lasers per part. To have multiple lasers build a single part, each laser needs to be assigned a segment of the cross section. Here, the Stripe strategy (shown in Figure 3.2) was used for multi-laser parts as it is one of the most common strategies currently employed and multi-lasers cannot be employed to melt the same layer for the Meander strategy (as there is only one segment). Hence, the number of lasers melting each cross section was dependent on the number of standard 10 mm stripe segments that could be fitted onto the dimensions of the layers.

Figure 3.3 shows a schematic of how the different creep specimens were built. 90° specimens were built by melting 14 mm diameter circles; hence it was possible to fit 2 stripe segments, as shown in Figure 3.3. This means that during the 90° build, two lasers worked simultaneously on the same layer. For most layers, one stripe segment occupied a much smaller fraction area of the cross section than the other. The 45° specimen cross section was an ellipse of about 20 mm major diameter and 14 mm minor diameter, as well as support structures. There were 2 stripe segments within the ellipse, but multiple segments in the support structures, as shown in Figure 3.3. This means that 2 lasers melted the ellipse and the main cross section although all four lasers were employed in melting the full layer, including the supports. 90° and 45° specimens may have had their contour melted by a third laser, depending on laser availability. 0° creep specimens had a 100 mm long rectangular cross section and hence all four lasers participated in the cross section melting, as over 4 Stripe segments could be accommodated. Hence, it is important to understand that each layer of each specimen, even for the same build angle, is different and therefore each specimen is unique. This was taken into account when analysing the results.

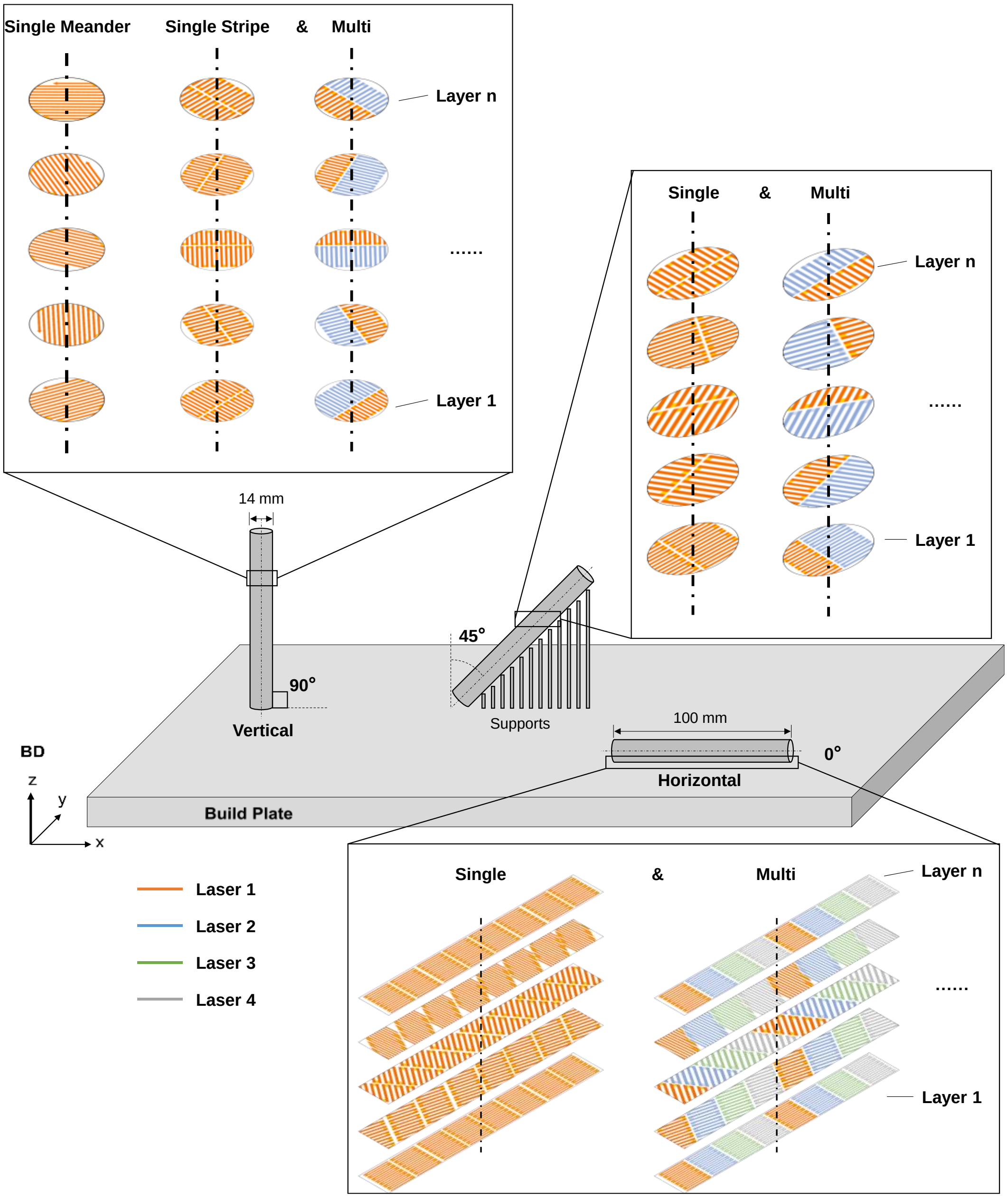
Single Meander
Single Stripe
&
Multi
Layer n
......
Layer 1
Single
&
Multi
Layer n
......
Layer 1
14 mm
45°
90°
Vertical
Supports
100 mm
0°
Horizontal
BD
z
y
x
Build Plate
Laser 1
Laser 2
Laser 3
Laser 4
Single
&
Multi
Layer n
......
Layer 1

Figure 3.3: Schematic representation of the different build orientations, scan strategies and number of lasers used for this research. The differences in surface area being melted are visible.

A summary of all the test cases investigated for creep experiments can be found in Table 3.3.

Table 3.3: Summary of the different test cases investigated in this project.

Specimen	Build orientation	Scan Strategy	Number of lasers	Heat treatment
90° single-laser Meander AB	90°	Meander	1	AB
90° single-laser Meander HT	90°	Meander	1	HT
90° single-laser Stripe HT	90°	Stripe	1	HT
90° multi-laser Stripe HT	90°	Stripe	4	HT
45° single-laser Stripe HT	45°	Stripe	1	HT
45° multi-laser Stripe HT	45°	Stripe	4	HT
0° single-laser Stripe HT	0°	Stripe	1	HT
0° multi-laser Stripe HT	0°	Stripe	4	HT
Wrought	N/A	N/A	N/A	HT

3.2 Post-processing

Once the specimens were built, they were heat treated on the build plate. As the wrought alloy 718 obtained from Carpenter Technology Corporation (Reading, UK) was heat treated following the AMS 5662 [209] standard, the LPBF specimens were also solution treated and aged according to the same standard (980°C/1h/Gas quench, 720°C/8h/Furnace cooling to 620°C/8h/Gas quench), with the exception of AB specimens. Although this heat treatment was not developed specifically for LPBF material, and hence is not optimised for its microstructure, it was used to allow comparison between the LPBF and wrought specimens.

Post heat treatment, Wire Electrical Discharge Machining (WEDM) was used to remove specimens from the build plate and supports from the 45° specimens were removed manually. The creep specimens were then turned using a slant lathe to ASTM E8/E8M standard [210] dimensions shown in Figure 3.4, which are recommended for creep testing. Knife edges were included in the specimen geometry to facilitate the use of LVDTs (linear variable differential transformers) for the measurement of specimen elongation. The creep specimen gauge length of 22 mm was then ground using a P46 grit aluminium oxide grinding wheel mounted on a Jones & Shipman Hardinge Ltd (Rugby, UK) 1302 cylindrical grinder to obtain a surface finish value of Ra=0.3 µm, which plays a major role in creep life.

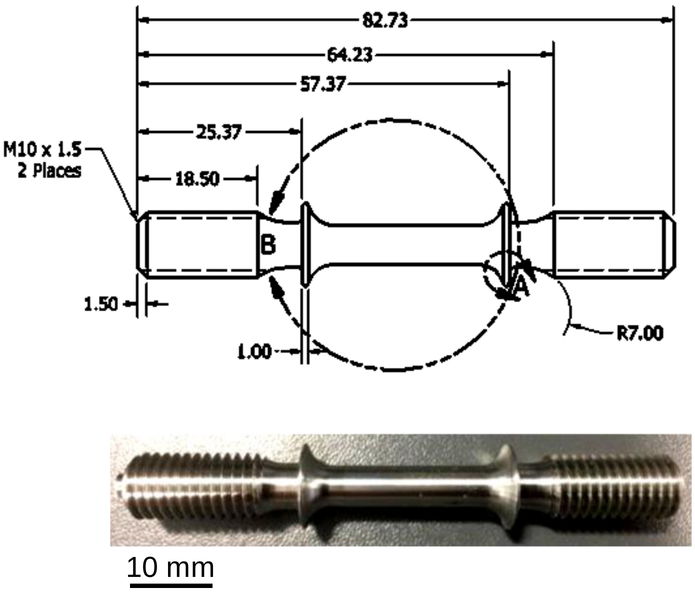

Figure 3.4: ATSM E8/E8M [210] uniaxial specimen after turning and grinding.

3.3 Creep testing

Uniaxial creep testing and interrupted creep tests were undertaken on the specimens at 600 MPa and 650°C on a Denison Mayes Group Ltd (Leeds, UK) constant load creep machine (T45A3), which outputs time and extensometer voltage (1 V = 1 mm), according to the ASTM E139 standard [211]. Contact thermocouples, attached at the top, centre and bottom of the specimen gauge length, were used to monitor the temperature of the furnace and ensure a uniform specimen heating throughout the test. Each type of specimen was tested 3 times.

The creep test temperature of 650°C was chosen as it is the highest temperature that alloy 718 can withstand before its mechanical properties deteriorate. Following this, initial tests were performed with a load of 747.5 MPa, which had previously been used by a similar study on the creep of alloy 718 [64]. The load was progressively lowered until a minimum creep life of 100h was obtained, this was the case for a load of 600 MPa.

To investigate the defect and microstructure evolution during creep interrupted creep tests were conducted. For this experiment, the LPBF specimen with the best minimum creep rate and creep life will be selected, alongside wrought alloy 718. The creep testing conditions will be the same as for the previous creep tests: 600 MPa and 650°C.

To observe specimen microstructural evolution, interrupted creep tests were conducted for both the LPBF and wrought alloy 718 specimens at mid-secondary and mid-tertiary breakpoints. At each breakpoint, the specimens were taken out of the creep test furnace and prepared for microstructural analysis. The specimens were not put back in the creep testing machine after analysis as they were cut in the process of sample preparation for SEM and EBSD analysis. Hence different specimens were used and stopped at the mid-secondary and mid-tertiary breakpoints. To minimise variability, specimens from the same build were used. These interrupted creep tests allowed the observation of the microstructural evolution undergone by specimens during creep.

To identify the separate effects of load and temperature during creep, more LPBF specimens were thermally exposed at 650°C in the creep furnace with no load and interrupted at the breakpoints mentioned previously before being analysed with SEM and EBSD. For this experiment, the specimens were mounted as usual in the creep testing machine to keep the heating and cooling down procedures as similar as possible to uniaxial creep testing.

3.4 Analysis and data processing

Microscopy and fractography were undertaken to understand the mechanisms leading to the failure of the material and how the different process parameters affected the microstructure and creep behaviour.

3.4.1.1 Sample preparation

Specimens were first cut in the required planes with a silicon carbide disk and mounted in conductive resin from Metprep Ltd (Coventry, UK) called Conducto-Mount. Then, the specimens followed the recommended Buehler polishing procedure for nickel-based superalloys [212].

3.4.1.2 Microscopy

Thereafter, reference cubes (from the same build as the creep specimens), fracture surfaces and sections just below the fracture surfaces (Figure 3.5) were analysed with a Philips XL30 SEM. These images were used to analyse the microstructure of the specimens (e.g. Figure 4.3). An Energy Dispersive X-Ray Spectroscopy (EDS) microanalysis system by Oxford Instruments (Abingdon, UK) was used in conjunction with the SEM system to perform chemical characterisation of the material and its different phases by using Point & ID in the INCA software by ETAS (Stuttgart, Germany). An example of this is shown in Table 4.2. Pre-creep microstructure (reference cubes) were also analysed with a Nikon Eclipse LV100ND Optical microscope and a Jeol JSM-7100F EBSD to investigate porosity and the effect of processing parameters on the crystallography, respectively. EBSD maps and Inverse pole figures were obtained from the EBSD data (e.g. Figure 4.4). A G5 Infinite Focus, focus variation microscope from Alicona Imaging GmbH (Raaba, Austria) was used to image 3D maps of the tested specimens' fracture surfaces. The microscopy images presented in this paper are all oriented parallel with respect to the creep test loading direction (LD) for easy comparison (i.e., the vertical axis of the 2D images corresponds to the loading axis). The build direction (BD) of the specimens is also indicated where relevant.

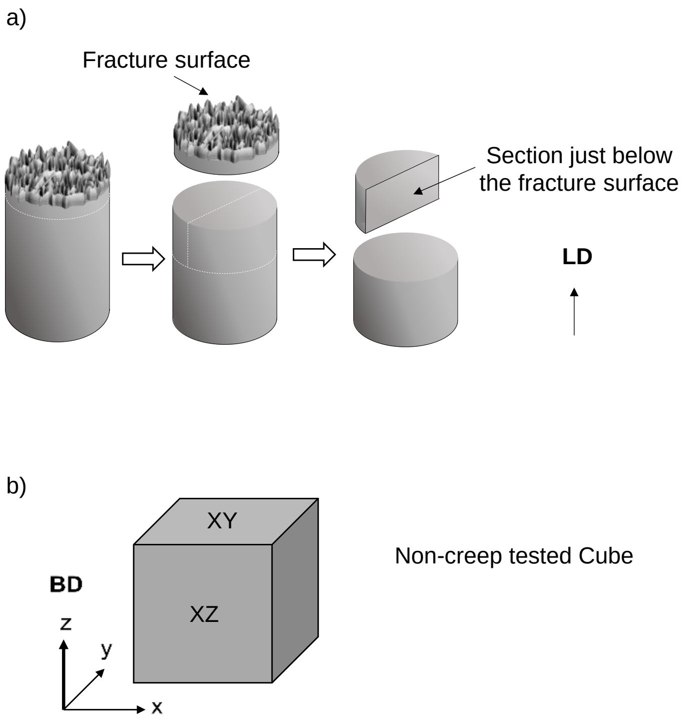

Figure 3.5: Schematic representation of specimen sections used for microscopy analysis. a) Fracture surface and cross section analysis. b) General microstructure section analysis from cubes.

3.4.1.3 Noise reduction and obtaining minimum creep rates

A Mathworks (Natick, Massachusetts, USA) commercial software, MATLAB, and its curve fitting toolbox, which uses regression, interpolation and smoothing to fit curves to data, was used to reduce the noise in the output creep curves data. For the noise reduction, the curves were fitted to follow the following curve equation:

$$y = A * (1 - \exp(Bx)) + Cx + D$$

Where A, B, C and D are curve coefficients which were obtained from the curve fitting tool in MATLAB. This allowed a noise-free curve to be plotted (e.g. Figure 5.1) and used to determine the minimum creep rate.

The secondary creep region was identified by finding the parts of the creep curve data where the gradient was constant, i.e. where the double derivative of the curve was 0 (in this case, the value 9.6×10^{-6} was used instead of 0). Then, the straight line was plotted, and the gradient of that straight line was reported as the minimum creep rate.

3.4.1.4 Processing Alicona images

MountainsMaps, a commercial software by Digital Surf (Besançon, France) was used to post-process the Alicona images, of which an example is visible in Figure 5.6.

3.4.1.5 Measuring porosity

An image processing programme was used to determine the porosity data on the commercial software, MATLAB from Mathworks (Natick, Massachusetts, USA) from the optical microscope images. An illustration of how this was performed is given in Figure 3.6. Although techniques such as the Archimedes method provide more precise porosity data, an image processing programme was used as the intent was not to communicate absolute values but rather to provide comparison between specimens. The minimum detectable void size was 5 µm.

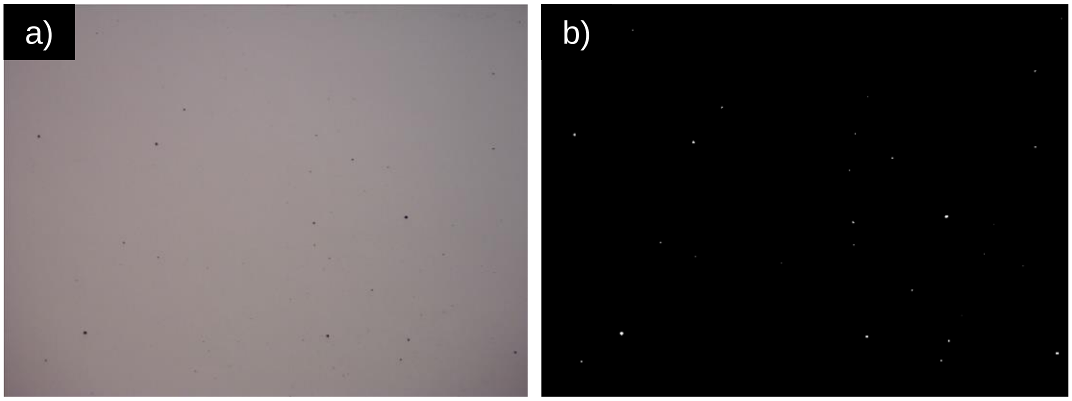

Figure 3.6: Detection of porosity using MATLAB image processing. a) Original image with porosity as black voids. b) Black and white image with porosity labelled as white pixel.

X-ray Computed Tomography (XCT) was also employed in order to determine the porosity size, distribution and morphology in the gauge length of the specimen. A ZEISS Xradia Versa XRM-500 XCT was used with the highest resolution possible and the scan parameters are given in Table 3.4. These values were considered adequate to detect all critical defects, and were also based on the similar study by Xu et al. [54].

Table 3.4: XCT Scan parameters used.

Parameter	**0, II and III**
Voxel resolution (µm)	15
Source Voltage (kV)	160
Source Current (µA)	63
Exposure time (ms)	$1.2{\cdot}10^4$ ms

All measurements were performed along the sample gauge length. Analysis of XCT data was performed on TIFF images outputted in the arrangement, shown in Figure 3.7.

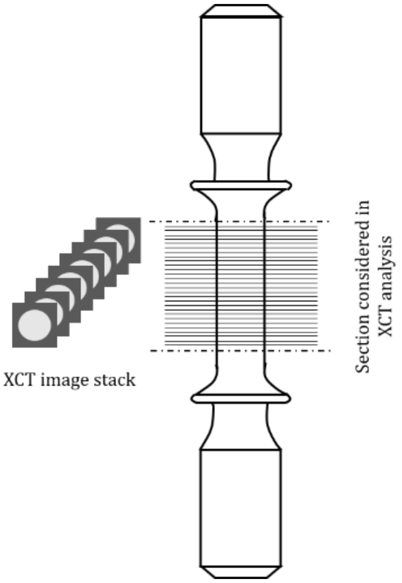

Figure 3.7: Schematic of XCT scan images obtained.

3.4.1.6 ImageJ use

ImageJ, an open-source image processing programme developed by the National Institutes of Health and the Laboratory for Optical and Computational Instrumentation (University of Wisconsin, Wisconsin, USA), was used to obtain crack length, crack density and precipitate density. The densities were found by varying the Contrast/Brightness threshold and using the maximum entropy (MaxEntropy) function with some minor manual adjustments if/when defects had been erroneously considered. The image was then turned into a binary image (Figure 3.8) and the "Measure" command outputted the percentage area (%Area) occupied by the cracks or precipitates. The precipitate density and part density were acquired in the planes perpendicular and parallel to the loading direction and averaged for each test case.

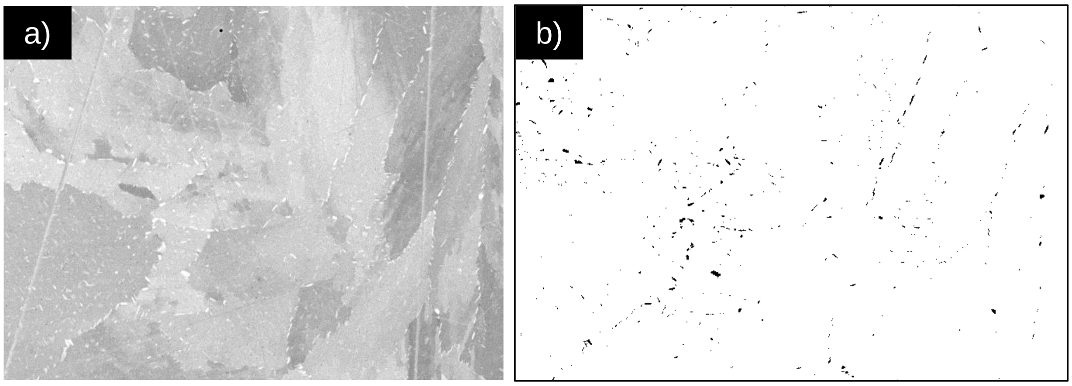

Figure 3.8: Processing a SEM image of 90° single-laser Meander HT specimen with ImageJ, by modifying the contract/brightness threshold, to obtain precipitate density (δ, carbide and laves phase). a) original SEM image with precipitates in white. b) Processed ImageJ image with precipitates in black.

3.4.1.7 Obtaining grain size

Grain size in the loading direction plane was obtained through the HKL Channel 5 software by Oxford Instruments (Abingdon, UK) which was also used to remove noise in the EBSD scans and plot Inverse Pole Figures. The grain size was measured as an area rather than a diameter to allow for comparisons to be made, due to the elongated aspect of LPBF grains (but an equivalent diameter is still given in the results, e.g. Table 4.1). The average grain size was taken for complete grains (not touching the border and/or corner of the image) and the standard error was calculated from the standard deviation and is indicated for all measurements in the results.

3.4.1.8 Analysis of interrupted creep tests

The specimens in the interrupted creep tests were analysed in a similar manner to the pre-creep microstructures. The samples were cut, ground and polished then analysed using SEM, EDS, EBSD as well as MATLAB, ImageJ, INCA and Channel5 software.

The following chapter will first look at the microstructure of the different specimens before creep.

4 Microstructure

In this chapter, the microstructure of wrought and LPBF alloy 718 specimens will be observed and analysed. This chapter will permit the understanding of the effect of LPBF alloy 718 microstructure on subsequent creep properties. First, the microstructure of wrought alloy 718 will be presented, followed by the microstructure of LPBF alloy 718. The latter will present the microstructure of as-built and heat treated specimens, followed by a comparison between specimens built with Meander or Stripe strategies. Then, the microstructure for the different build orientations will be shown, followed by the differences in microstructure between multi-laser and single-laser specimens. After this, a discussion of the effects of heat treatment and process parameters on the microstructure will be presented.

In this section, different microstructural parameters, such as grain size and precipitates will be observed and analysed. For the analysis of precipitates, it should be noted that this work will focus on δ-precipitates, Laves and carbides. γ'' precipitates are not part of this study but their effects have been 2.3.1in the literature review (Section 2.3.1) and will be mentioned in future discussions as well.

4.1 Wrought alloy 718

The microstructure of wrought alloy 718, which is the industry standard, is investigated to allow comparison with the LPBF equivalent and understand how the microstructures result in different creep performances. The LPBF alloy 718 microstructure will then be presented, highlighting the differences between the microstructures of the different parameters investigated.

Figure 4.1 shows the microstructure and crystallographic texture of wrought alloy 718. From this figure, it can be observed that the wrought material is composed of small equiaxed grains, which were measured to be 82 ± 2.45 μm^2 in area on average, in planes parallel and perpendicular to the loading direction (Figure 4.1a,b). This illustrates the isotropic nature of the material. Figure 4.1c reveals the precipitation of δ phase on the grain boundaries of the material. These precipitates are present in great quantity, with a density of 2.97 ± 0.15 %Area. The δ-precipitates in the wrought specimens also had a significant size range (particles size ranged from 1 μm to 12 μm in length and had an average radius of 0.64 ± 0.17 μm). Laves phases and carbides were also present as large globular precipitates (with an average diameter of 4.28 ± 1.93 μm) in the material, but in small numbers. The wrought specimens were fully dense, as observed from Optical and SEM images and in other studies [213]. Table 4.1 recaps the microstructural features of the wrought alloy 718.

Table 4.1: Part density, precipitate (δ, Laves and carbides) density (± 0.15 %) and grain size comparison for the Wrought specimens (Loading Direction = LD).

Specimen	**Part Density** *(%)*	**Average Precipitate Density** *(%Area)*	**Grain Size** *(μm^2)*	**Equivalent grain diameter** *(µm)*
Wrought	100.00	2.97	82 ± 2.45	10

Figure 4.1d,e, further reveals that there is no strong texture in the material and exposes the presence of annealing twins. The overall weak texture and isotropy in the wrought material could be a consequence of forging in hot conditions [213] and the texture in the <111> plane in the Y direction probably corresponds to the extruding direction of the material. The presence of annealing twins, which are highlighted in Figure 4.2, may also explain the presence of slight texture in the <111> direction observed in Figure 4.1e, as annealing twins tend to align parallel to the <111> plane.

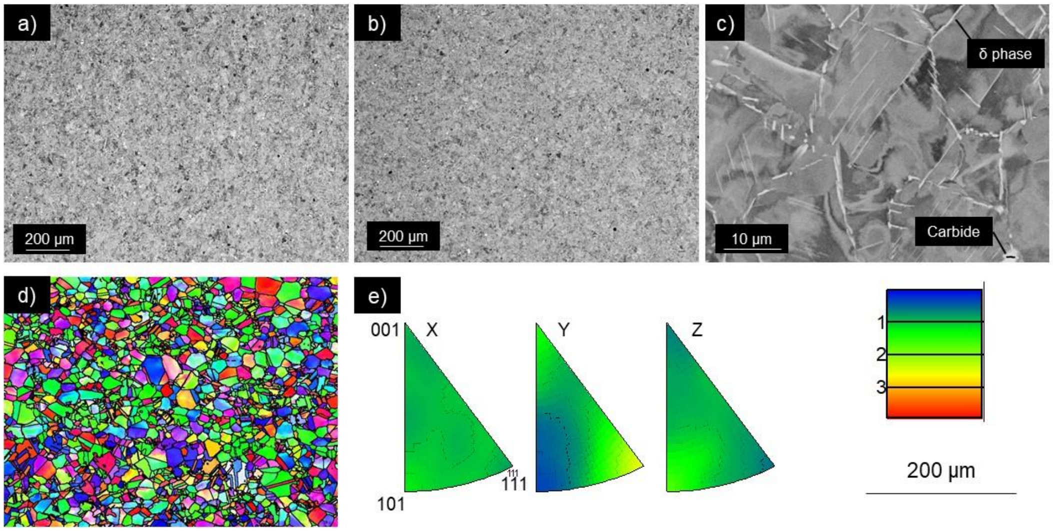

Figure 4.1: Microstructural observations for wrought alloy 718. a) Microstructure parallel to the loading direction. b) Microstructure perpendicular to the loading direction. c) Microstructure at higher magnification where precipitates are visible. d) EBSD map of wrought alloy 718. e) Inverse Pole Figure of the EBSD scan. The microstructure of wrought alloy 718 is composed of small equiaxed grains in perpendicular planes, showing the isotropic nature of the material. The precipitates on the grain boundaries are large and there is little texture in the material.

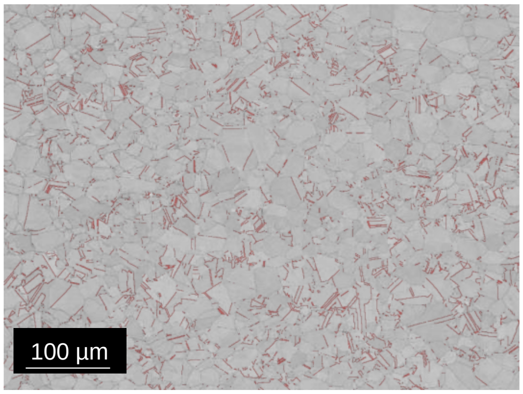

Figure 4.2: Annealing twins (in red) present in wrought alloy 718 before creep.

Overall, the microstructure of wrought alloy 718 is isotropic with small equiaxed grains and very little texture. A large number of δ-precipitates are present on the grain boundaries with some carbides and Laves phases throughout the specimen as well. This microstructure will be used as a point of reference to allow comparison with LPBF microstructures which will now be presented.

4.2 Laser powder bed fused alloy 718

This section will introduce the microstructure of LPBF alloy 718. As-built and heat treated microstructures will initially be compared, followed by a comparison of microstructures resulting from Stripe or Meander strategies. Thereafter, microstructures manufactured with the different build orientations will be presented and finally, multi-laser and single-laser microstructures will be evaluated.

4.2.1 As-built and heat-treated

Figure 4.3 compares the microstructure of the 90° single-laser Meander AB and 90° single-laser Meander HT specimens. Both have elongated grains parallel to the build direction (Figure 4.3a,d) and smaller equiaxed grains perpendicular to the build direction (Figure 4.3b,e). This is caused by epitaxial growth triggered by the direction of heat flux and is similar to microstructures observed in other studies on LPBF alloy 718 [42]. Some lines of small equiaxed grains perpendicular to the build direction correspond to laser overlapping areas (Figure 4.3b,e). The HT specimen has partially recrystallized grains while the AB specimen has ill-defined grain boundaries and sub-micron sized cell structures (Figure 4.3c,f) similar to results seen in other studies [214]. The heat treated specimen also has precipitates at the grain boundaries (Figure 4.3f), which were identified as carbides, laves and δ-precipitates from their globular and needle morphologies, and from EDS analysis (Table 4.2), with compositions closely resembling those found by Xu et al. [64]. EDS analysis of Laves phase, as noted in Table 4.2, showed a high weight% of Nb and Ti which, combined with the globular morphology, are all signs pointing to the presence of Laves. But due to the small size of these particles and the presence of carbides (which have similar indicators to Laves phase when viewed in SEM and EDS), the identification of Laves phase was inconclusive without recurring to TEM However, according to Chlebus et al. [47], Laves phases are formed on grain boundaries and layer interfaces by the microsegregation of Nb and Mo at high cooling rates, which is the case during LPBF. Tucho et al. [152] also identified Laves phase in LPBF alloy 718 in both as-built and heat treated specimens. Hence, it can be surmised that Laves phase are present in the specimens. For clarity, the globular precipitates in LPBF alloy 718 SEM images will be labelled as Laves/carbides and their effects on creep addressed separately. Similarly, γ'' precipitates, although not visible using SEM, are likely precipitated in the grain, as observed in other studies [134].

Table 4.2: EDS analysis of the different phases present in LPBF material (Figure 4.3). (All values within ± 2 wt%)

	Element composition (weight%)			
Elements	**γ matrix**	**δ phase**	**Carbide**	**Laves phase**
Al	0.53	0.36	-	0.31
Ti	1.03	1.72	5.49	1.75
Cr	19.13	11.82	5.77	12.07
Fe	18.54	11.33	5.37	11.06
Ni	52.04	56.43	13.29	56.70
Nb	5.63	16.12	67.37	15.92
Mo	3.10	2.22	-	2.04
Os	-	-	2.71	-

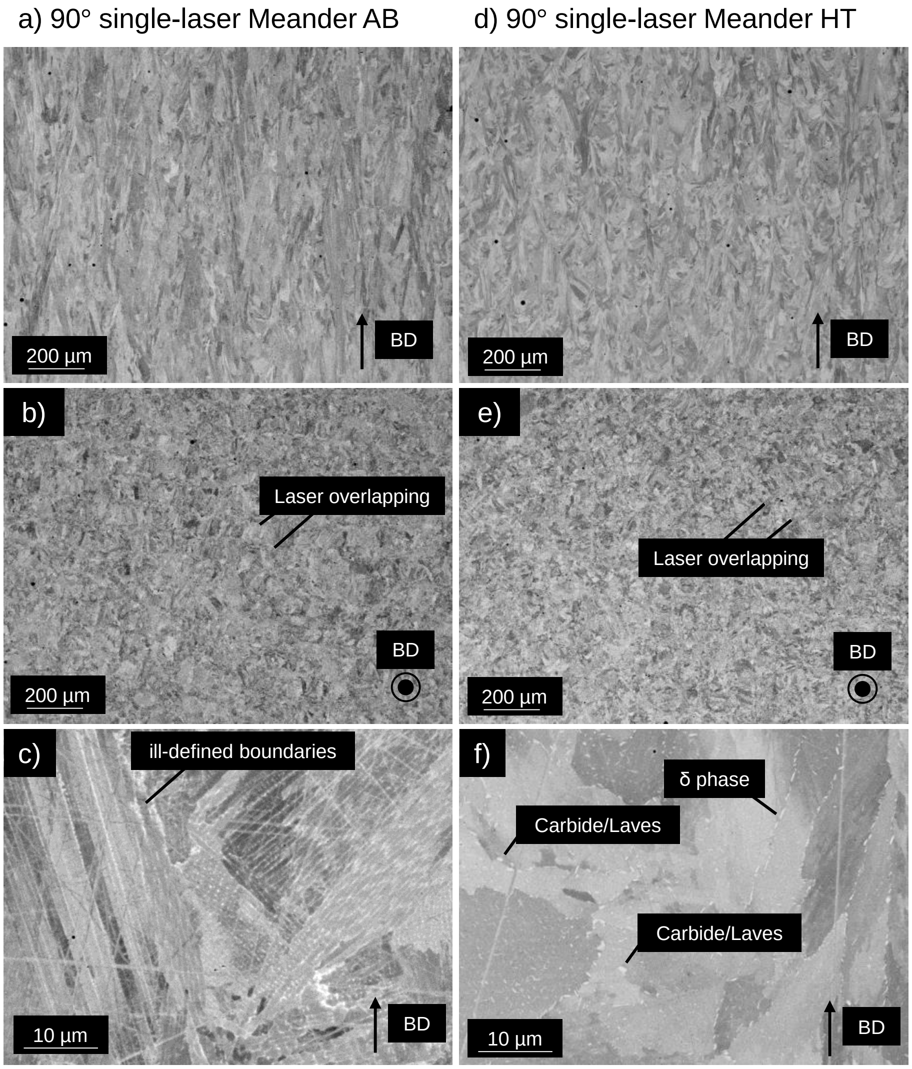
a) 90° single-laser Meander AB
d) 90° single-laser Meander HT
200 µm
BD
200 µm
BD
b)
Laser overlapping
BD
200 µm
e)
Laser overlapping
BD
200 µm
c)
ill-defined boundaries
10 µm
BD
f)
δ phase
Carbide/Laves
Carbide/Laves
10 µm
BD

Figure 4.3: SEM images of the microstructure of 90° single-laser Meander AB and HT specimens. a)-c) 90° single-laser Meander AB. d)-f) 90° single-laser Meander HT. Both specimens had elongated grains parallel to the build direction and more equiaxed grains perpendicular to the build direction where the laser overlapping paths can be seen. At higher magnification, the AB specimen had more ill-defined grain boundaries and less precipitates.

Table 4.3 shows the porosity data, the number of precipitates and the grain size for the AB and HT specimens.

From Table 4.3, it can be observed that the difference in porosity for the AB and HT specimens was 0.02%. This is negligible and shows that the heat treatment did not affect the porosity of the LPBF specimens. This agrees with other studies where, unlike HIP, heat treatment was not shown to close porosities and defects [215].

Furthermore, the XCT data obtained showed no signs of defects or pores which means that most porosities and defects present in the specimen were below the minimum detectable feature in XCT, which was 15 µm.

Table 4.3: Part density, precipitate (δ, Laves and carbides) density (± 0.15 %) and grain size comparison for the 90° single-laser Meander AB and HT specimens (Loading Direction = LD).

Specimen	**Part Density** *(%)*	**Precipitate Density** *Parallel to LD (%Area)*	**Precipitate Density** *Normal to LD (%Area)*	**Average Precipitate Density** *(%Area)*	**Grain Size** *(μm²)*	**Equivalent grain diameter** *(μm)*
90° single-laser Meander **AB**	99.962	0	0	0	193 ± 20	16
90° single-laser Meander **HT**	99.943	0.29	0.15	0.22	129 ± 13	13

In the HT specimen, δ-precipitates were present at the grain boundaries (Figure 4.3f). The wrought specimens had the highest density of δ-precipitates in this study, 12 times more than the 90° single-laser Meander HT specimen (Table 4.3). This is in contrast to Gribbin et al. [213] who found that LPBF alloy 718 had more δ-precipitates than wrought alloy 718, by a factor of two. This may be due to the different heat treatment and process parameters used. The 90° single-laser Meander HT specimens had the lowest density of δ-precipitates of all the LPBF specimens. However, all LPBF specimens had similar lengths and diameters of δ-precipitates, ranging about 0.5 μm to 1 μm in length, with an average diameter of 0.29 ± 0.12 μm. The smaller size of δ-precipitates in LPBF compared to wrought was also observed in another study by Gribbin et al. [213]. All LPBF specimens also had similar diameters for the globular carbide/Laves precipitates, which was on average 0.45 ± 0.19 μm.

Figure 4.4 shows the crystallographic orientations for both AB and HT specimens. Both specimens have a predominantly <001> texture in the Z direction, which corresponds to their build direction. The 90° single-laser Meander AB specimens had a stronger <001> crystallographic orientation parallel to the build direction, which was observed in other studies [216], and a slight texture perpendicular to the build direction (Figure 4.4a). The EBSD map clearly shows elongated and ill-defined grains in the build direction as well (Figure 4.4a). In comparison, the 90° single-laser Meander HT specimen had a weaker <001> texture in the build direction and more defined and recrystallised grains, although melt pools were still apparent (Figure 4.4b), which shows that there is a reduction in texture after heat treatment, which is in agreement with other studies [217].

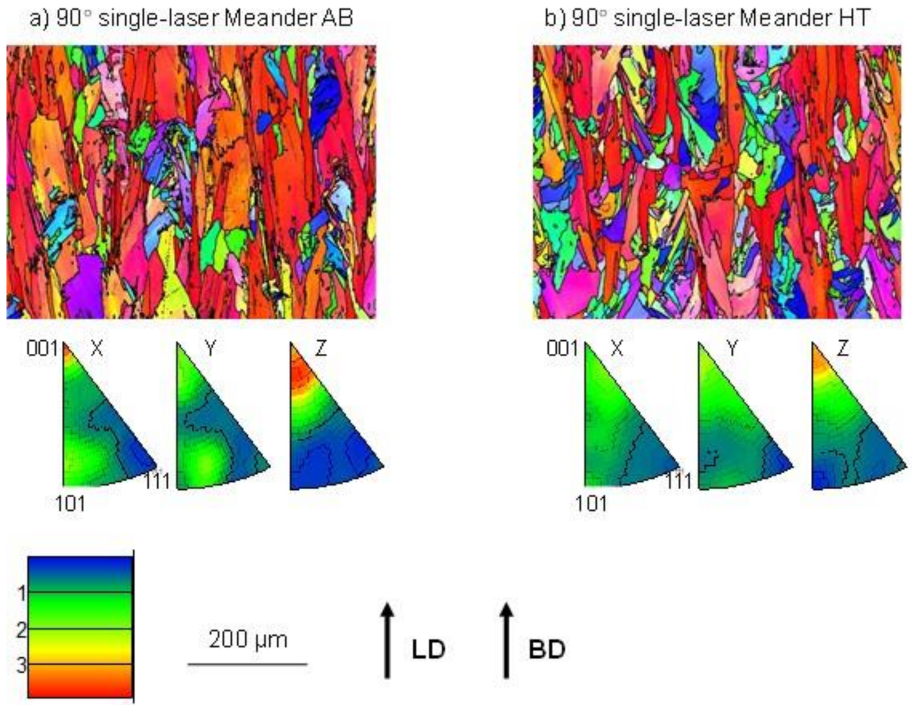

a) 90° single-laser Meander AB

b) 90° single-laser Meander HT

Figure 4.4: EBSD maps and Inverse Pole Figures of 90° single-laser Meander AB and HT specimens. a) 90° single-laser Meander AB. b) 90° single-laser Meander HT. The AB specimen has a much stronger texture in the Z direction, which corresponds to the build direction, compared to its heat treated counterpart.

Despite having similar processing parameters, the AB and HT specimens had a difference in grain size, shown in Table 4.3, due to their difference in thermal treatment. Although grain size usually increases after heat treatment [128] or HIPing [218], the 90° single-laser Meander AB specimens were found to have larger grains, by a factor of 1.5, than their heat treated counterparts. This observation is explained by the very long and elongated columnar grains in the AB specimen, which although have smaller diameters, represent a larger grain area than the slightly bigger diameter grains in the HT specimen.

Figure 4.5 further illustrates the grain size distribution for the AB and HT 90° Meander specimens and for wrought alloy 718. This shows that the majority of the grains were between 0 µm^2 and 50 µm^2 for all 3 specimens. However, both LPBF specimens also had a significant number of grains larger than 500 µm^2, with the largest ones reaching over 6000 µm^2. Also, it is logical that for a set area there would be a lesser number of larger grains than smaller ones, as you need many small grains to fill an area, compared to only a few larger grains. This explains the larger average observed in Table 4.3 for both specimens. These large grains probably correspond to the columnar grains present in the LPBF specimens, while the smaller ones may be caused by the laser overlapping areas. This distribution was also observed for the remaining LPBF specimens and hence will not be presented again.

a) Wrought

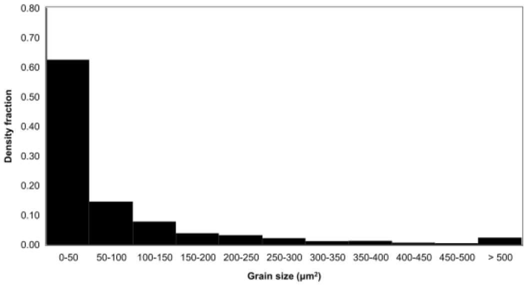

b) 90° single-laser Meander AB

c) 90° single-laser Meander HT

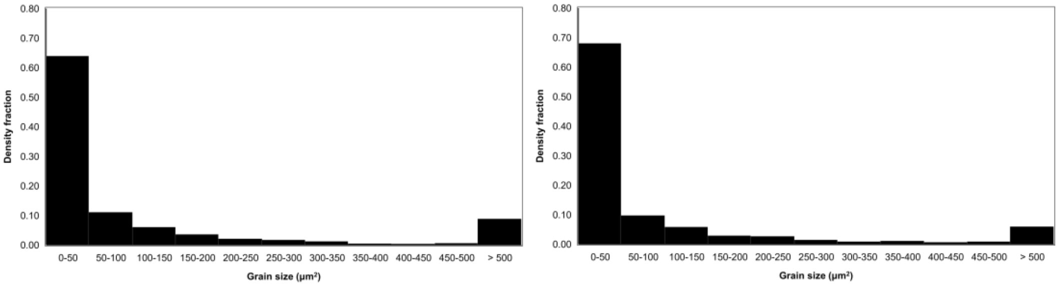

Figure 4.5: Histogram of grain size distribution. a) Wrought alloy 718. b) 90° single-laser Meander AB. c) 90° single-laser Meander HT. This shows that the majority of the grains in all three specimens had an area between 0 and 50 μm^2.

From the observations made in this section, it is fair to conclude that the LPBF alloy 718 specimens used in this study are representative of the larger LPBF alloy 718 population.

Overall, heat treating LPBF specimens resulted in more defined and partially-recrystallised grains, the partial dissolution of Laves phase and the precipitation of strengthening phases like δ-precipitates and γ'' phase. The texture was also reduced, and the porosity did not change with heat treatment. These numerous benefits justify why the remaining specimens were heat treated.

4.2.2 Meander and stripe scan strategies

Figure 4.6 compares the microstructure of 90° single-laser Meander HT and 90° single-laser Stripe HT specimens. The 90° single-laser Stripe HT specimen had a similar microstructure to its Meander counterpart, with elongated grains in the build direction. On the plane normal to the build direction, some lines of small equiaxed grains (≤ 150 μm^2) can also be observed, which correspond to laser overlap regions since they are on average 18 μm in width, which corresponds to the 20 μm Stripe offset, and about 77 ± 10 μm apart, which is close to the 90 μm hatch spacing.

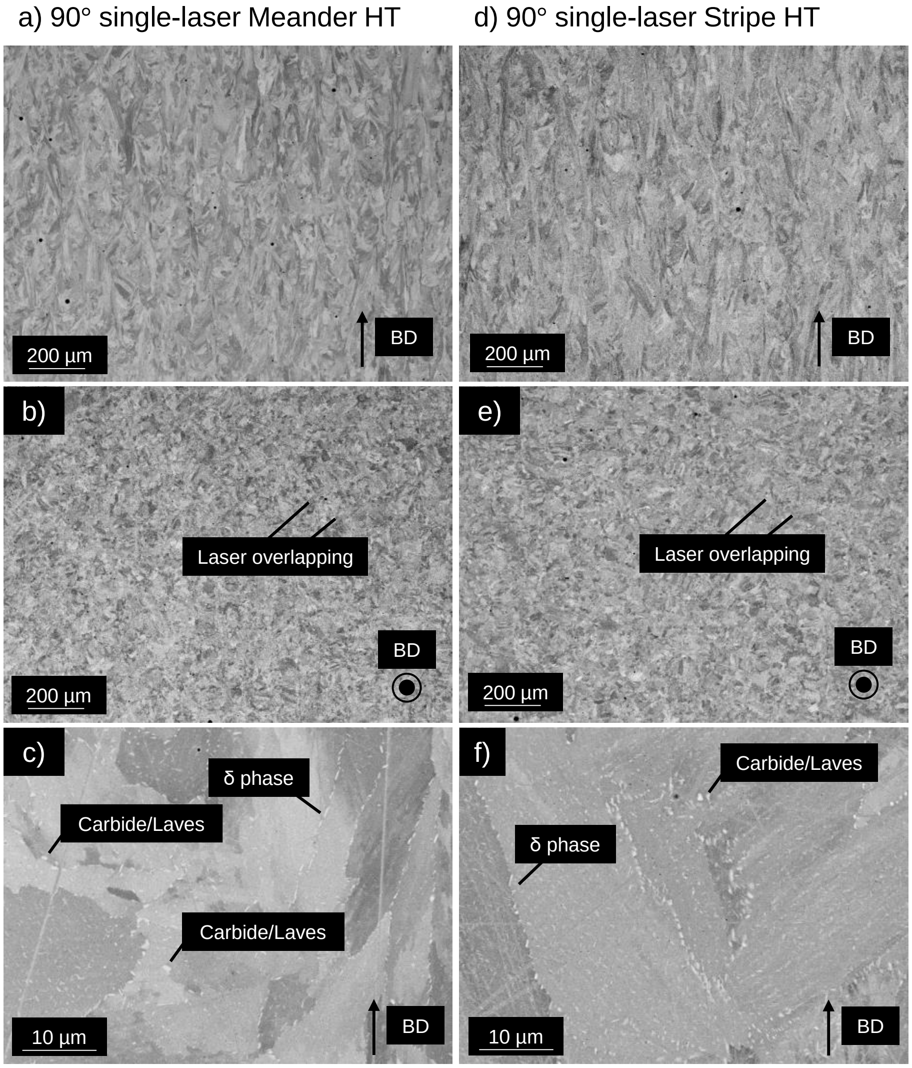
a) 90° single-laser Meander HT
d) 90° single-laser Stripe HT
200 µm
BD
200 µm
BD
b)
Laser overlapping
BD
200 µm
e)
Laser overlapping
BD
200 µm
c)
δ phase
Carbide/Laves
Carbide/Laves
10 µm
BD
f)
Carbide/Laves
δ phase
10 µm
BD

Figure 4.6: SEM images of the microstructure of 90° single-laser HT specimens with different scan strategies. a)-c) Meander strategy. b)-d) Stripe Strategy. Both microstructures are similar and laser overlapping areas (labelled) can be observed in the plane normal to the build direction.

Table 4.4 quantifies the differences in grain size, porosity and precipitate density. The 90° single-laser Meander HT specimen had the lowest concentration of δ-precipitates, 43% less than 90° single-laser Stripe HT. The porosity difference between the Stripe and Meander specimens is negligible while Stripe specimens had grains 20% larger than the Meander specimens. Grain size plays a critical role in creep performance so this observation can have key implications for the subsequent mechanical properties.

Figure 4.7 shows the EBSD mapping and the inverse pole figures of the two different strategies. Both the Stripe and Meander strategies resulted in a <001> texture parallel to build direction, but the Meander strategy had a stronger texture. Geiger et al. showed that different scan strategies resulted in different texture strength for LPBF alloy 738LC [219] and Newell et al. [217] also found that Stripe specimens retained less texture than Meander equivalents, which was also observed here.

Table 4.4: Part density, Precipitate (δ, Laves and carbides) density (± 0.15 %) and grain size comparison between 90° single-laser HT Meander and Stripe specimens (LD = Loading Direction).

Specimen	**Part Density** *(%)*	**Precipitate Density** *Parallel to LD (%Area)*	**Precipitate Density** *Normal to LD (%Area)*	**Average Precipitate Density** *(%Area)*	**Grain Size** *(μm²)*	**Equivalent grain diameter** *(μm)*
90° single-laser **Meander** HT	99.943	0.29	0.15	0.22	129 ± 13	13
90° single-laser **Stripe** HT	99.947	0.90	0.95	0.93	156 ± 9	14

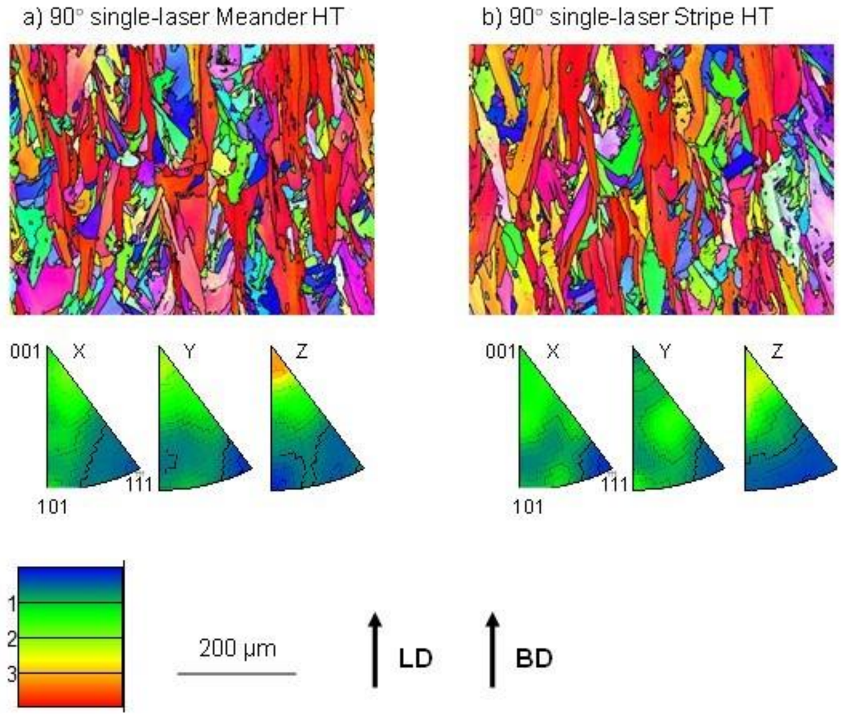

Figure 4.7: EBSD maps and Inverse Pole Figures of 90° single-laser HT specimens with different scan strategies. a) Meander strategy. b) Stripe strategy. This shows that the Stripe strategy results in weaker texture than the Meander strategy.

Overall, the Stripe and Meander scan strategies resulted in similar microstructures. There was no difference in porosity and a stronger texture was observed in the Meander strategy. The Stripe strategy was used for the remaining of the specimens as it allows the comparison with specimens built with multiple lasers. The Stripe strategy is also one of the most common strategies used in practice and allows comparison with other studies.

4.2.3 Build orientations

Figure 4.8 shows that all specimens had elongated grains in the build direction and a more equiaxed microstructure perpendicular to the build direction with some traces of laser overlapping areas, distinguishable as lines of small equiaxed grains. This anisotropic microstructure has been observed in many studies, e.g. [220]. The grain size for the different build orientations can be found in Table 4.5. The 45° specimen had the largest grains, by a factor of 1.8, compared to the 90° specimen which had the smallest.

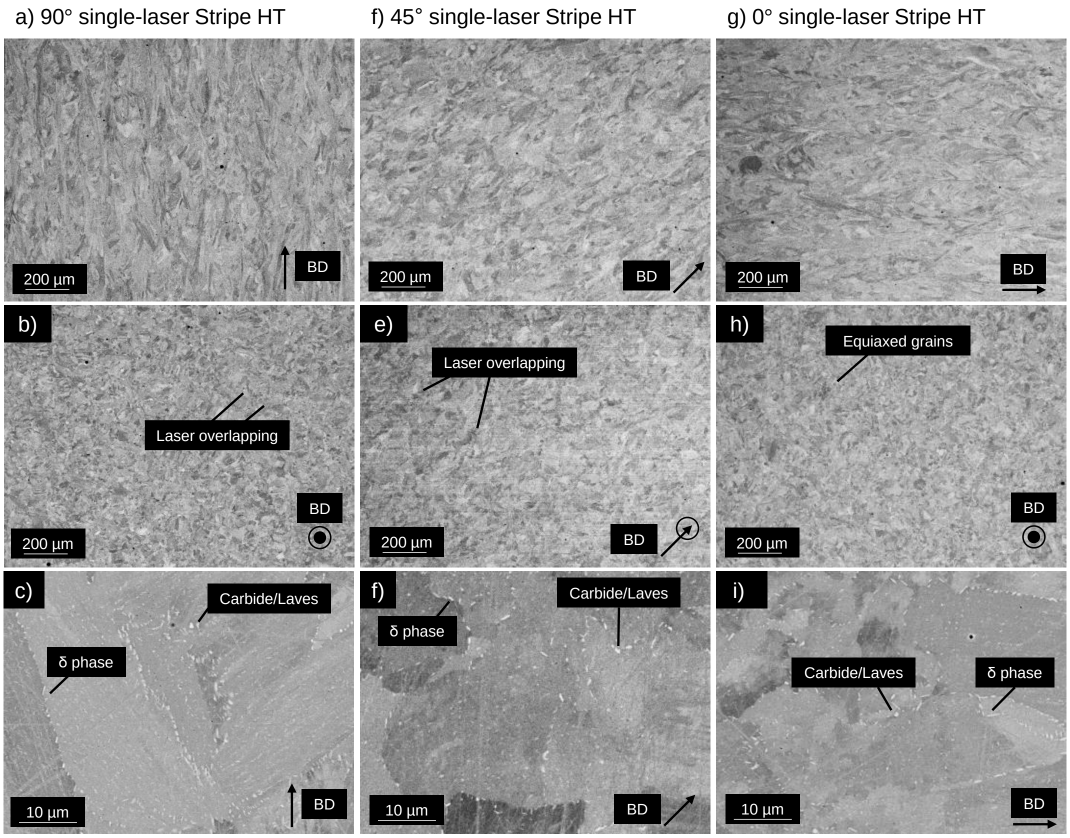
a) 90° single-laser Stripe HT
f) 45° single-laser Stripe HT
g) 0° single-laser Stripe HT
200 µm
BD
200 µm
BD
200 µm
BD
b)
Laser overlapping
BD
200 µm
e)
Laser overlapping
200 µm
BD
h)
Equiaxed grains
200 µm
BD
c)
Carbide/Laves
δ phase
10 µm
BD
f)
Carbide/Laves
δ phase
10 µm
BD
i)
Carbide/Laves
δ phase
10 µm
BD

Figure 4.8: SEM images of the microstructure of single-laser Stripe specimens with different build orientations. a)-c) 90°. d)-f) 45°. g)-i) 0°. The images are oriented with respect to the loading direction. This shows elongated grains parallel to the build direction for all specimens with equiaxed perpendicular to the build direction. At higher magnification, δ phase precipitates can be observed on the grain boundaries with some pores.

Table 4.5 shows that the difference in porosity between the different build orientations is 0.03%, which is negligible. Therefore, it is acceptable to conclude that the build orientation does not significantly affect the porosity in the LPBF specimens.

Table 4.5: Part density, precipitate (δ, Laves and carbides) density (± 0.15 %) and grain size comparison for the single laser Stripe specimens with different build orientations (LD = Loading Direction).

Specimen	**Part Density** *(%)*	**Precipitate Density** *Parallel to LD (%Area)*	**Precipitate Density** *Normal to LD (%Area)*	**Average Precipitate Density** *(%Area)*	**Grain Size** *(μm²)*	**Equivalent grain diameter** *(μm)*
90° single-laser Stripe HT	99.947	0.90	0.95	0.93	156 ± 9	14
45° single-laser Stripe HT	99.977	0.58	0.67	0.63	287 ± 35	19
0° single-laser Stripe HT	99.973	0.43	0.45	0.44	196 ± 19	16

At higher magnification, δ phase precipitates, carbides, Laves phase and pores can be observed (Figure 4.8c,f,i). The δ phase precipitates were oriented in line with the build direction due to the elongated grains in that direction. Furthermore, the size, quantity and orientation of the δ-precipitates varied for each test case and can be observed in Table 4.5. The 90° specimens had the highest δ-precipitate density for the different build orientations, however, this amount was 3 times smaller than wrought alloy 718 (Table 4.3).

Figure 4.9 shows the EBSD maps oriented according to the loading direction (with individual build directions specified for the different cases). The inverse pole figures were processed so that the Z direction corresponds to the build direction of the different specimens, except for the 45° single-laser Stripe HT specimen which is oriented so that Z is the loading direction. The 90° specimen had very little texture but still a local maximum in the <001> direction parallel to the build direction (Figure 4.9a). The 45° single-laser Stripe HT also presented a very small <111> texture slightly perpendicular to the loading direction, which likely corresponds to its build direction (Figure 4.9b). The 0° specimen had a <001> texture in line with its build direction (Figure 4.9c) which was the strongest out of the other Stripe HT orientations (but still less than the 90° Meander strategy). Watring et al. [221] and Bean et al. [222] also observed a predominant <001> texture in the build direction in specimens with different build orientations. Compared to the wrought specimen, which clearly presented small equiaxed grains and very little texture (Figure 4.1d,e), the anisotropy of the LPBF specimens with elongated grains and strong texture parallel to the build direction is evident.

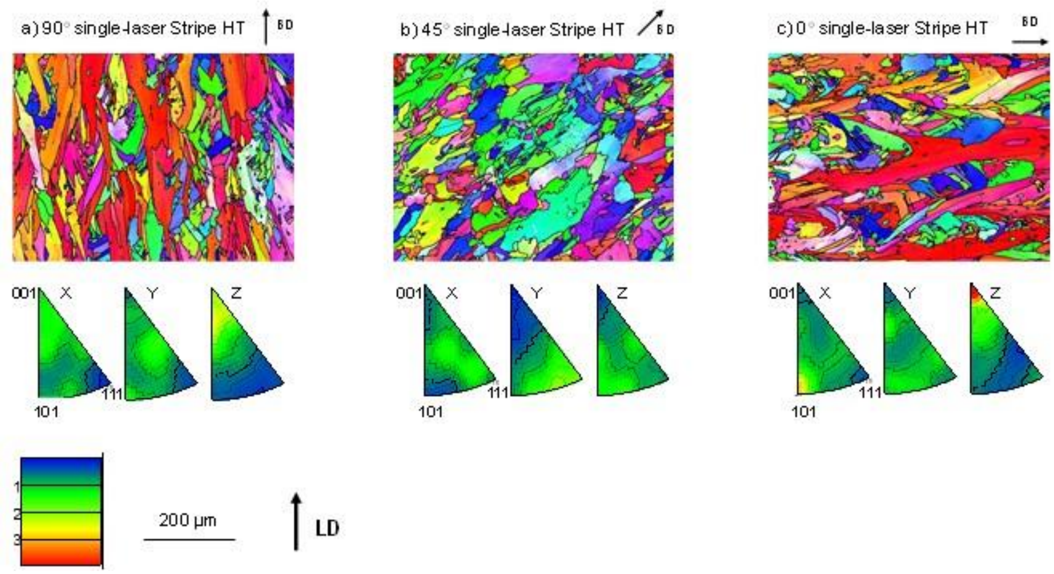
a) 90° single-laser Stripe HT
BD
b) 45° single-laser Stripe HT
BD
c) 0° single-laser Stripe HT
BD
001
X
Y
Z
111
101
1
2
3
200 µm
LD

Figure 4.9: EBSD maps and Inverse pole figures for LPBF alloy 718 single-laser Stripe specimens built with different build orientations. a) 90°. b) 45°. c) 0°. This shows a <001> texture parallel to the build orientation for each test case.

Overall, the build orientation affects the orientation of the grains as well as their size. However, the build orientation does not seem to affect the porosity or precipitation of strengthening phases in the specimen. A <001> texture was present parallel to the build direction for each specimen, which likely causes anisotropy in mechanical properties.

4.2.4 Multi-laser scan strategies

Figure 4.10 shows the microstructure of the 90°, 45° and 0° heat treated specimens for single and multi-laser scan strategies, in line with the loading direction. The microstructure of the different build orientations clearly shows elongated grains in the build direction, regardless of the number of lasers. Pores were also visible in all specimens, as well as precipitates such as Laves phase, carbides and δ-particles, indicated in Figure 4.10.

Despite having a similar microstructure morphology, multi-laser built specimens had different grain sizes and precipitate densities when compared to same orientation single-laser built counterparts, as shown in Table 4.6.

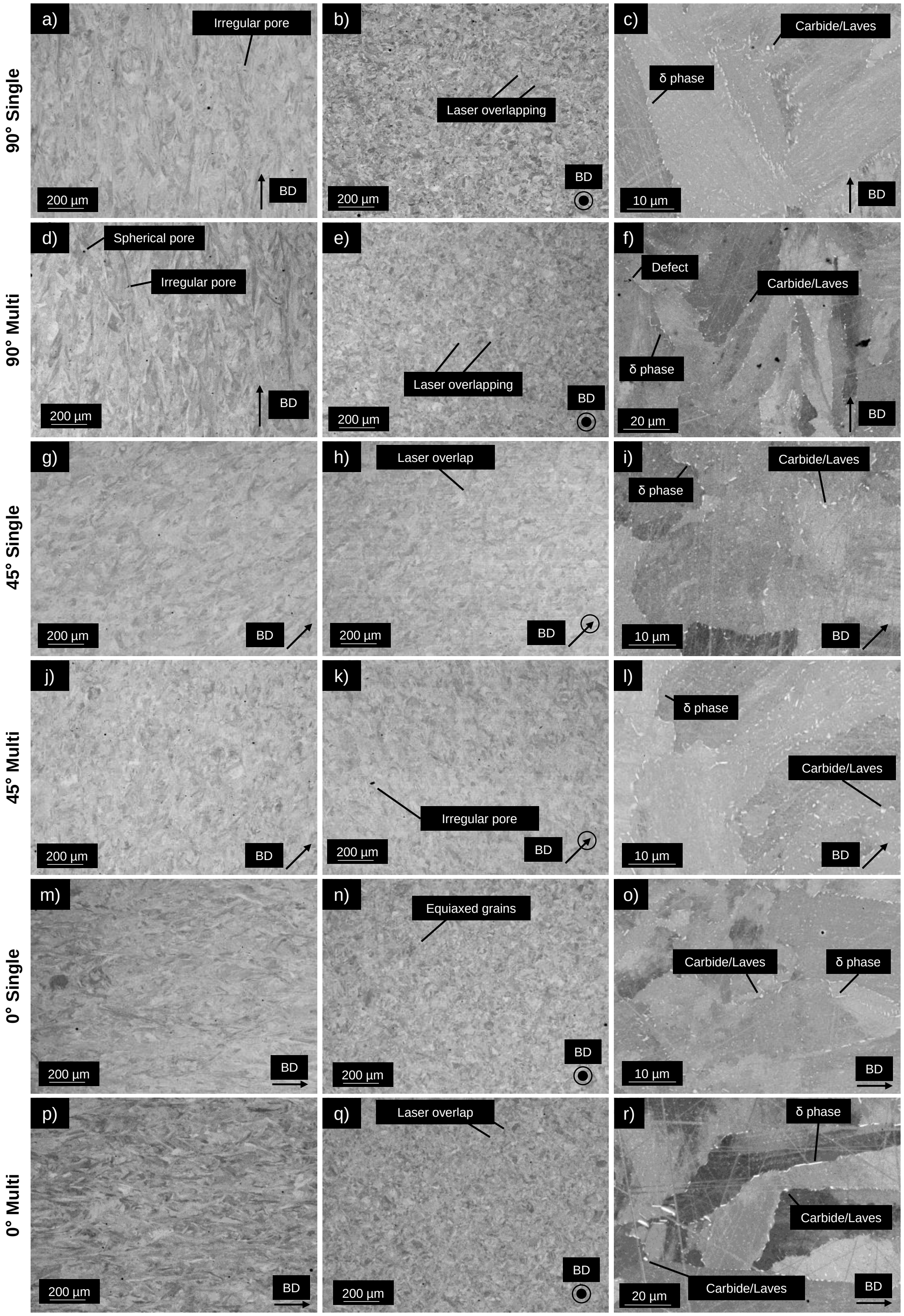
90° Single
a)
Irregular pore
200 µm
BD
b)
Laser overlapping
200 µm
BD
c)
Carbide/Laves
δ phase
10 µm
BD
90° Multi
d)
Spherical pore
Irregular pore
200 µm
BD
e)
Laser overlapping
200 µm
BD
f)
Defect
Carbide/Laves
δ phase
20 µm
BD
45° Single
g)
200 µm
BD
h)
Laser overlap
200 µm
BD
i)
δ phase
Carbide/Laves
10 µm
BD
45° Multi
j)
200 µm
BD
k)
Irregular pore
200 µm
BD
l)
δ phase
Carbide/Laves
10 µm
BD
0° Single
m)
200 µm
BD
n)
Equiaxed grains
200 µm
BD
o)
Carbide/Laves
δ phase
10 µm
BD
0° Multi
p)
200 µm
BD
q)
Laser overlap
200 µm
BD
r)
δ phase
Carbide/Laves
Carbide/Laves
20 µm
BD

Figure 4.10: SEM images of the pre-creep microstructure of LPBF specimens with Stripe strategy, different build orientations and single or multi-lasers. a)-c) 90° single-laser. d)-f) 90° multi-laser. g)-i) 45° single-laser. j)-l) 45° multi-laser. m)-o) 0° single-laser. p)-r) 0° multi-laser. Showing elongated grains parallel to the build direction, equiaxed grains perpendicular to build direction and some δ and Laves precipitates. All specimens aligned with the loading direction.

Table 4.6: Part density, precipitate (δ, Laves and carbides) density (± 0.15 %) and grain size comparison between single and multi-laser Stripe specimens at different build orientations (LD = Loading Direction).

Specimen	**Part Density** *(%)*	**Precipitate Density** *Parallel to LD (%Area)*	**Precipitate Density** *Normal to LD (%Area)*	**Average Precipitate Density** *(%Area)*	**Grain Size** *(μm^2)*	**Equivalent grain diameter** *(μm)*
90° single-laser Stripe HT	99.947	0.90	0.95	0.93	156 ± 9	14
90° multi-laser Stripe HT	99.984	0.21	0.58	0.40	177 ± 21	15
45° single-laser Stripe HT	99.977	0.58	0.67	0.63	287 ± 35	19
45° multi-laser Stripe HT	99.980	0.42	0.66	0.54	200 ± 14	16
0° single-laser Stripe HT	99.973	0.43	0.45	0.44	196 ± 19	16
0° multi-laser Stripe HT	99.960	0.68	0.41	0.55	252 ± 25	18

The grain size for the various specimens, shown in Table 4.6, reveals that 45° single-laser Stripe HT specimens had the biggest grains, at 287 μm^2 with a 35 μm^2 standard error, followed by 0° multi-laser, with grains 14% smaller. The 45° single-laser Stripe HT specimens' grains were also 71% larger than those of the wrought specimen. The 90° and 0° multi-laser specimens had larger grains than their single-laser counterpart by 12% and 29%, respectively.

Table 4.6 also presents the porosity data obtained which was similar to other single-laser studies [223, 224]. The 90° multi-laser Stripe HT Specimens had the highest density, however this was only 0.04% different from 90° single-laser Stripe HT specimens which had the lowest density. The density for the 90° and 45° multi-laser Stripe specimens was slightly higher than their single-laser counterparts, and slightly lower for the 0° specimens, but the differences were insignificant. Hence, it can safely be assumed that multi-laser scan strategies play a negligible role in porosity formation.

The precipitate density, both parallel and perpendicular to the loading direction, is shown in Table 4.6. From observations, these precipitates should mostly be δ particles, although they could also be Laves or carbides. Parallel to the build direction, 90° single-laser Stripe HT specimens had the highest precipitate density, 24% more than the 0° multi-laser specimens, which had the second highest amount and 76% more than the 90° multi-laser specimens, which had the lowest amount. Perpendicular to the build direction, 90° single-laser Stripe HT specimens still had the highest density of precipitates, but 0° multi-laser specimens had the lowest amount. The 0° and 90° components show significant difference in precipitates between single and multi-laser strategies, however, the 45° specimens had a similar density regardless of the number of lasers. This shows a difference in precipitate density between the single and multi-laser scan strategies for a given orientation.

Figure 4.11 shows the EBSD maps and inverse pole figures of the single and multi-laser specimens. As previously observed in former sections, all the specimens had a <001> texture in line with their build direction. From Figure 4.11a,b it seems that for the 90° orientation, the multi-laser specimen had more texture than their single-laser counterpart. For the 45° build orientation, the texture does not seem to vary significantly between the single and multi-laser components, where both have very little texture (Figure 4.11c,d). Whereas there seems to be a decrease in texture in the 0° multi-laser specimen Figure 4.11e,f). From these results it can be surmised that multi-laser scan strategies also affect the crystallographic orientation of specimens for a given orientation.

Overall, using a multi-laser scan strategy resulted in a similar microstructural morphology to that seen in the single-laser specimens and similar porosity. However, the grain size, precipitate density and texture strength varied between multi and single-laser scan strategy specimens.

The wrought and LPBF microstructures of alloy 718 have been found to be different in almost every way. Where wrought alloy 718 had an isotropic microstructure with small equiaxed grains and very little to no texture, LPBF alloy 718 had an anisotropic microstructure with long elongated columnar grains and texture parallel to the build direction. Grain size, precipitate density and porosity were also varied with the different process parameters. The reason for these differences will be explained in the following discussion sections.

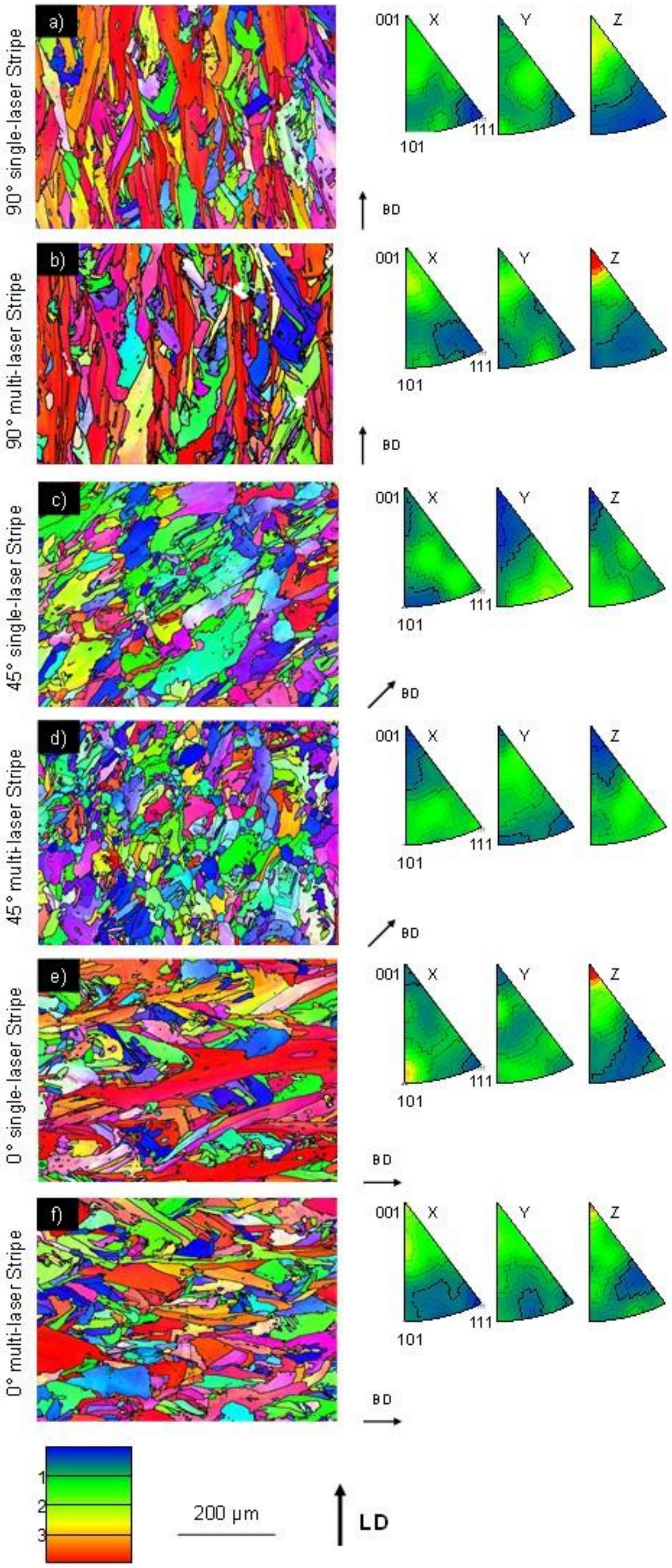
a)
90° single-laser Stripe
b)
90° multi-laser Stripe
c)
45° single-laser Stripe
d)
45° multi-laser Stripe
e)
0° single-laser Stripe
f)
0° multi-laser Stripe
001
X
Y
Z
111
101
BD
1
2
3
200 µm
LD

Figure 4.11: EBSD maps and Inverse Pole Figures of LPBF Stripe specimen with different build orientations and single or multi-laser strategies. a) 90° single-laser. b) 90° multi-laser. c) 45° single-laser. d) 45° multi-laser. e) 0° single-laser. f) 0° multi-laser. Showing a <001> texture parallel to the build direction. The use of multi-laser affects the texture strength for the 90° and 0° specimens, while it has a negligeable effect on the 45° specimens.

4.3 Effect of heat treatment

Appropriate heat treatments result in the precipitation of strengthening precipitates such as γ'' and δ phases [225], as well as the dissolution of detrimental phases such as the Laves phase. Since AB specimens were not heat treated, inter-dendritic Laves phases were present. Gribbin et al. [213] observed that carbides were absent in AB specimens, but present after HIP. They were also observed in other studies with different powder compositions [124] and build orientations [214]. Laves have been shown to result in a lack of ductility, as shown by Schirra et al. [226], which may impact creep performance. Huang et al. [54] states that when the solution temperature is below 1130°C (which was the case for the present study), the original dendritic microstructure is replaced by partially recrystallised grains that retain their orientation and that Laves phases are not fully dissolved. Another possible reason why the wrought specimens had a higher percentage of precipitates is that the heat treatment standard used was developed with a wrought microstructure in mind as a starting point. The fact that LPBF materials have an anisotropic microstructure of elongated columnar grains and equiaxed grains in different directions, dissimilar to wrought or cast materials which have an almost isotropic microstructure, means that the heat treatment is not optimal as it was not designed specifically for this starting microstructure. Huang et al. [54] researched new heat treatments for LPBF alloy 718 and found that reducing the cooling rate contributed to the precipitation of strengthening precipitates and that a lower solution time is required, compared to alloy 718 ingots. Furthermore, they found that LPBF materials have a faster ageing response compared to wrought material which led to the dissolution of Laves phases and allowed a higher precipitation of strengthening phases, resulting in higher tensile strength and ductility [54].

Heat treatment also affected the grain size of specimens. 90° single-laser Meander HT specimens were found to have smaller grains than their AB counterpart. A reason for this is that while the heat treatment partially-recrystallised the grains and resulted in more defined grain boundaries in the HT specimen, it did not necessarily result in grain growth. Zhao et al. [227] also showed that grain size did not vary significantly after a solution treatment at 1080℃ and hence, due to the different starting microstructures between LPBF and conventional nickel-based superalloys, the heat treatment does not yet result in larger and fully recrystallised grains in LPBF specimens. This shows that further work on heat treatment optimisation for LPBF alloy 718 could result in better control of the mechanical properties of the material.

4.4 Effect of laser powder bed fusion process parameters

The literature review highlighted that the process parameters affect the resulting LPBF microstructure. This discussion section will investigate the effects of the scan strategies, the build orientation and the use of multi-lasers on the microstructure. It should be noted that the number of lasers, the surface area being melted, the layout of the stripe segments, the 67° interlayer rotation and the fraction area of loose powder or solidified material underneath each layer being melted, changes from layer to layer, meaning that heat dissipation varies significantly within the layer and the specimen. Indeed, heat flux has been shown to greatly influence the LPBF microstructure on a layer-level [228]. This results in heterogeneity within the layer itself and within the specimen. Hence, the grain size, precipitate density and even porosity obtained, may not be representative of the whole specimen, as only the middle of the specimen was analysed, not the entire structure. The discussion will be presented with this in mind.

4.4.1 Effect of scan strategies

The difference between the Stripe and Meander strategies may be explained by the lesser quantity of laser overlapping zones in the latter. The laser overlapping areas undergo some re-melting that results in larger grains parallel to the build direction, due to the slower cooling rate caused by the 2nd heat input. This 2nd heat input causes the columnar grains to rotate [229], resulting in equiaxed grains normal to the build direction. This equiaxed overlapping laser region was observed here (Figure 4.6b') and by Ahmad et al. [123]. Choi et al. [43] also states that the laser overlapping area is subject to complex heat flows which changes the orientation of the grains and results in equiaxed microstructure at the melt-pool boundaries. The columnar grains were stated to grow from the boundary towards the centre of the melt-pool while equiaxed grains were formed by supercooling at the boundaries [140]. Parimi et al. [65] also observed inter-layer equiaxed grain structure. These equiaxed areas can be observed in the planes normal to the build direction (Figure 4.6a',b') and a schematic representation is shown in Figure 4.12. The higher quantity of equiaxed grains in the Stripe specimens could also be responsible for the higher density of δ-particles (Table 4.4). Indeed, smaller grains mean that there is a higher density of grain boundaries and hence, a higher density of δ-precipitates in Stripe specimens.

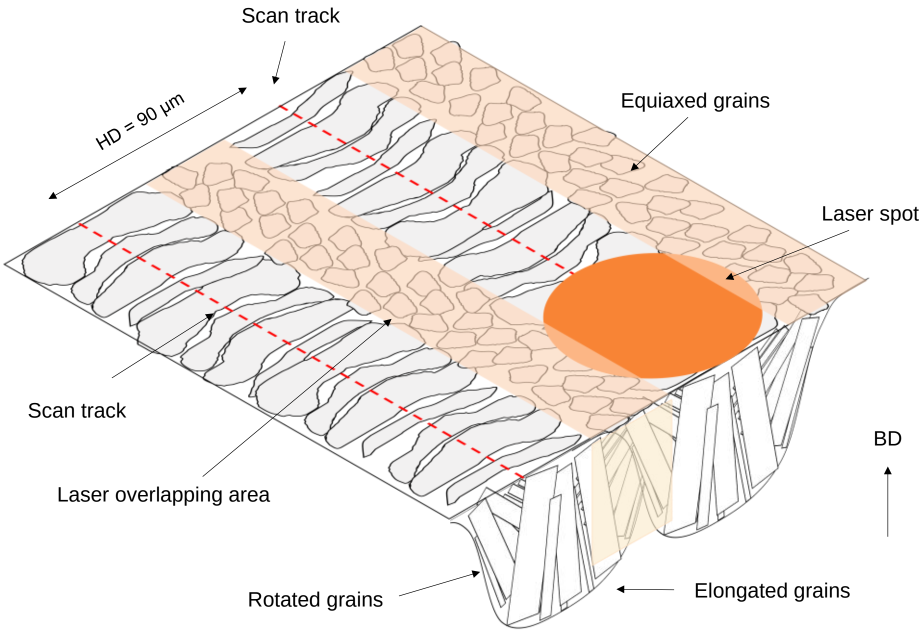

Figure 4.12: Meltpool and grain formation schematic, showing the columnar and equiaxed grains. With the build direction and Hatch Distance (HD) indicated.

The Stripe and Meander specimens also had a 20% difference in grain size. The difference in grain size between the strategies is caused by the different thermal gradients and cooling rates present in the specimen, where the higher energy density in the Stripe specimen produced larger grains. Indeed, Arisoy et al. [230] found that increasing the energy density resulted in larger grains and Wan et al. [231] stated that this was due to the different maximum temperature gradients and cooling rates. Therefore, as the Stripe strategy receives more heat input in the overlapping laser areas, this could have resulted in the larger grains observed parallel to the build direction. The higher texture in the Meander specimen is also probably due to the presumably faster cooling rates present during the process.

Scan strategies are important factors which contribute to porosity content within AM [232]. But the difference in porosity in this work was negligible between the Meander and Stripe strategies and hence, it seems that the scan strategy does not affect the porosity. However, other studies have shown that a higher heat input results in more porosity and defects [233]. The laser overlapping area (Figure 4.12) is prone to getting higher heat input and hence, more defects may be present in the 0° specimen which had a larger Stripe offset.

4.4.2 Effect of build orientation

One of the main microstructural differences observed in the different build orientations was the orientation and size of the grains. Figure 4.13 schematically shows the grain growth mechanisms in the different build orientations. For 90° and 0° specimens, primary heat loss occurs through the build towards the build plate, as well as a secondary heat loss through the powder on either side of the layers (Figure

4.13a,c). In the 45° specimens, there is heat loss both in the build and powders as well as in the support structures, resulting in different thermodynamic effects which favoured grain growth (Figure 4.13b). Du et al. [234] also suggested that the rate of thermal energy input increases and the heat dissipation decreases in the 45° specimen, compared to the 90° one. Hence, this input in thermal energy may also be contributing to the larger grains observed in the 45° specimens. Furthermore, the specimens were heat treated while still being attached to the build plate, which may have acted as a heat source during the cooling down. Indeed, the 45° specimens were built with numerous supports along its length whilst the 90° specimens had the least contact with the build plate and no supports. Having a large contact with this heat source may have slowed the cooling rate and allowed more time for grain growth in the 45° single-laser Stripe HT specimens.

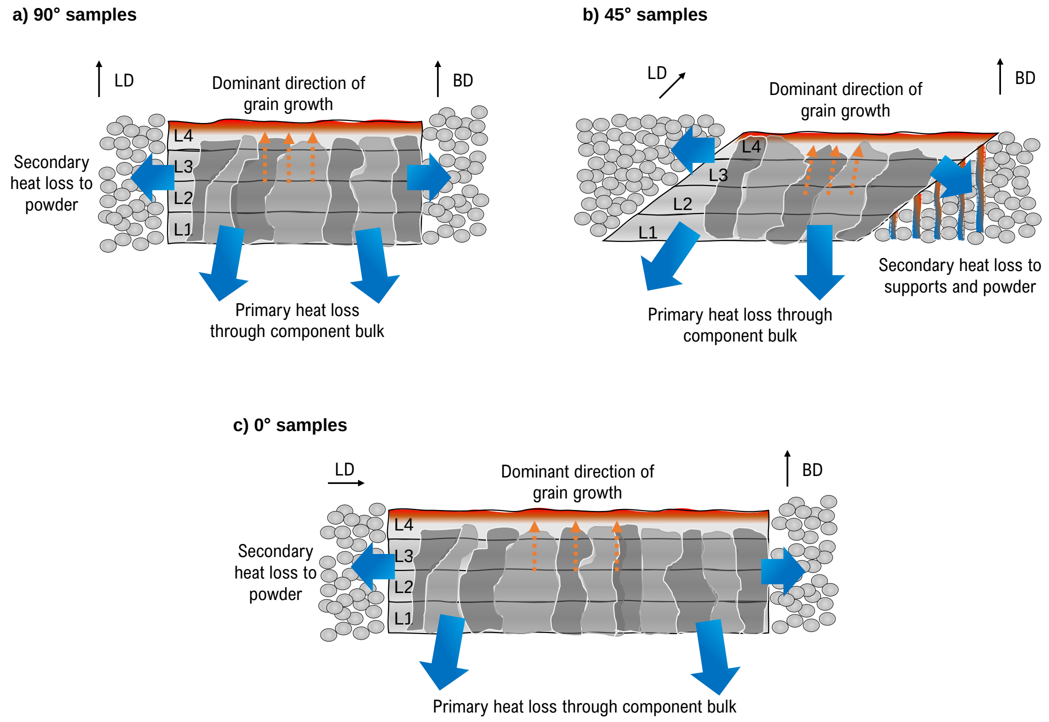
a) 90° samples
LD
Dominant direction of grain growth
BD
Secondary heat loss to powder
L4
L3
L2
L1
Primary heat loss through component bulk
b) 45° samples
LD
Dominant direction of grain growth
BD
L4
L3
L2
L1
Secondary heat loss to supports and powder
Primary heat loss through component bulk
c) 0° samples
LD
Dominant direction of grain growth
BD
Secondary heat loss to powder
L4
L3
L2
L1
Primary heat loss through component bulk

Figure 4.13: Schematic representation of the effect of build orientation on the microstructure of LPBF alloy 718. a) 90° specimens. b) 45° specimens. c) 0° specimens. The dominant grain growth direction is dependent on the direction of heat loss, which varies for the different build orientations.

Another difference between specimens built with different orientations was the amount and orientation of precipitates. Du et al. [234] found that specimens built at 90° orientation had less Laves phase than ones built at 45° and that the Laves phase morphology changed from discrete islands to continuous networks for 90° and 45°, respectively. This phenomenon is explained by the decrease in thermal gradient during solidification of the alloy in the melt pool which increases the concentration of Laves phase for the 45° specimen [234]. Furthermore, Section 4.2.2 showed that the 90° Stripe and Meander HT specimens had a 43% difference in precipitate density, whilst the 45° single-laser Stripe HT and 0° single-laser Stripe HT specimens had a similar amount. Hence, it is possible that the scan strategy is largely responsible for the difference in precipitate density.

Overall, the various thermal effects associated with each build orientation, with the differences in heat inputs and heat losses, impact grain and precipitate size and orientation.

4.4.3 Effect of multi-laser scan strategies

Multi-laser scan strategies affect the grain size in the specimens (Table 4.6). This is likely due to a difference in thermodynamic effects caused by the higher heat input from the use of multiple lasers. However, the mechanisms by which grains grow do not change compared to single-laser LPBF (Figure 4.13).Table 4.6 shows that multi-laser scan strategies resulted in bigger grains for 90° specimens and smaller grains for 45° specimens, compared to their single-laser counterparts. Similarly, Shi et al. [235] found that laser shaping strategies affected the subsequent grain morphology and size. The 90° and 0° multi-laser specimens had larger grains than their single-laser counterparts as the cross section being melted on each layer was identical and had a 100% fraction area of solidified layer underneath, making the conditions relatively constant. By comparison, when multiple lasers melted the surface, there was a higher heat input which may have promoted grain growth. Arisoy et al. [230] also found that increasing the energy density resulted in larger grains sizes in Inconel 625. The 21 μm^2 disparity in grain size for the 90° multi-laser Stripe HT specimen could be due to the interlayer rotation, which means that the smaller stripe segment had a solidification rate dependent on its placement relative to the layer underneath. For the 45° specimens, the conditions were not consistent layer-to-layer. Indeed, the ellipse shape needed to move across the bed to form a cylindrical specimen at a 45° angle. That meant that the amount of powder on the layer underneath and the amount of solidified material varied each time. Furthermore, the grain data was obtained from one surface of that specimen and so may not be representative of the whole specimen. This may explain the high deviation in the 45° specimens' grain size of 35 μm^2, which means that there was a wide disparity in grain size within the specimen. However, the smaller grains in the 45° multi-laser specimen could be due to thermodynamic effects caused by the higher heat input on the surface which may have caused a faster cooling rate to occur and hence, resulted in smaller grains than its single-laser equivalent. Furthermore, the lasers sometimes fired the supports first and then the core. This means that the supports were melted first and became a heat sink for the core. Indeed, support structures have been shown to remove heat away from the process zone and affect part quality [236]. However, Song et al. [237], who investigated the effect of different types of support structures on single-laser scan strategies, stated that the effect of supports on the local microstructure and hardness was marginal. Since this study did not investigate the effects of support structures on different scan strategies, the above hypothesis still stands. Hence, it can be deduced that the higher heat input produced by multi-laser scan strategies has the potential to control grain size, with suitable control. Indeed, a US Patent has been filed which claimed that using multiple laser beams from selected fibres of a diode laser could control the melt-pool cooling rate to form a single crystal microstructure [238].

Additionally, down streaming, which causes spatter, sometimes happened during the builds. This may have affected the porosity and, more importantly, the number of irregular pores in the specimens. Increasing the energy input, up to a certain threshold, has been shown to reduce the amount of pores, while an excessive heat input has also been shown to induce porosity [239]. The lower porosity in the 90° and 45° multi-laser specimens could be caused by the higher heat input, and hence better melting of the layer. While the reason the 0° multi-laser specimens seemed to have more porosity than their single-laser counterparts, may be explained by the larger stripe offset, compared to 90° and 45° specimens, and the fact that all 4 lasers were operating on the same layer at one time, resulting in excessive heat input. Hence, the bigger overlap region, already receiving more heat input than the 90° and 45° single-laser parts, would have received further energy input when multiple lasers were melting the surface, resulting in the increased number of pores. But despite the different stripe offset in the 0° specimens, the porosity was not significantly influenced. However, different scan strategies have been shown to result in different levels of porosity due to excessive heat inputs in the laser overlap region [233]. Hence, although no difference in porosity was observed in this case, the laser overlap region in 0° specimens could affect the mechanical performance and other microstructural aspects.

As shown in Table 4.6, multi-laser scan strategies affect the number of precipitates present in specimens. A possible explanation for this was given in a paper by Xiao et al. [240] who found that by using a quasi-continuous wave (QWC) laser at different frequencies, they could control the morphology, distribution and amount of Nb-rich precipitates, namely δ and γ'', in alloy 718. They explained that by controlling the cooling rate of the melt-pool, elemental diffusion could be controlled. They observed that a faster cooling rate gave insufficient time for element diffusion, resulting in Nb trapped in the γ matrix, whereas a slower cooling rate resulted in more Nb segregation. After a solution and ageing treatment, δ phases precipitated in the inter-dendritic zones and around the partly-dissolved Laves particles. Hence, the 50 Hz QWC laser, which resulted in a slower cooling rate, showed more δ precipitation than the 10 Hz QWC laser, which had a faster cooling rate. However, the 10 Hz QWC showed a higher presence of γ'' precipitates which are the main strengthening precipitates for alloy 718 and have been shown to be beneficial to creep performance [241]. It was stated previously that multi-laser scan strategies result in a different thermodynamic effect than their single-laser counterpart, depending on the build orientation. Hence, by controlling the build process, optimising the number of lasers, the surface area and the scan strategy, the cooling rate could be controlled which would result in the desired precipitate precipitation after heat treatment.

Geiger et al. [219] found that the texture in LPBF alloy 738LC was controlled by the thermal gradient during the build. Therefore, the differences in texture strength between the single and multi-laser 90° and 0° specimens can be explained by the higher heat input and thermal gradients present in the layer during melting. The reason why the 45° single and multi-laser specimens were similar may be due to the varying layer cross-section and supports which may have acted as heat sinks.

Overall, multi-laser strategies affect the thermodynamic effects during the build which result in differences in grain size, texture and precipitate density.

4.5 Summary of findings

This section showed that there were clear microstructural differences between wrought and LPBF alloy 718. Some of the key findings include:

- Wrought material had an equiaxed isotropic microstructure with large precipitates, while LPBF was characterised by its anisotropy and sub-optimal precipitates. All LPBF specimens displayed elongated columnar grains parallel to the build direction and more equiaxed grains normal to the build direction.
- Heat treatment of LPBF specimens reduced anisotropy and resulted in more defined grain boundaries, precipitation of strengthening phases and reduced crystallographic texture. However, the heat treatment employed was designed for wrought alloys and hence, resulted in sub-optimal results in terms of recrystallisation, dissolution of detrimental phases and precipitation of strengthening phases.
- The LPBF process parameters also affected the specimens' microstructures. The scan strategy influenced the amount of small equiaxed grains perpendicular to the build direction as well as the number of δ-precipitates.
- The build orientation mainly influenced the grain size and orientation of the different specimens.
- The use of multiple lasers affected the grain size and precipitate density.

In general, LPBF has a complex process-microstructure relationships which still need to be better understood. The findings from this section will enable a better understanding of why and how wrought and LPBF alloy 718 fail from creep. In the following section, the different creep behaviours of these materials are described and discussed.

5 Creep behaviour

Presented here are the creep curves for various LPBF specimens, from varying build conditions (as-built/heat treated, stripe/meander scan strategies and single/multi-laser scan strategies) as well as subsequent fractography in order to understand corresponding failure mechanisms. Comparison is also made to the equivalent performance of wrought alloy 718. Thereafter, discussion on the effects of the LPBF microstructure, heat treatment and the various LPBF process parameters on creep behaviour will be presented.

5.1 Wrought alloy 718

Figure 5.1 shows the creep curves obtained for all LPBF test cases and wrought material. The wrought alloy 718 specimens had an average creep life of 409h. From Figure 5.1, it is clear that the wrought material has a much higher elongation at fracture than the LPBF specimens. The wrought specimens' elongation at fracture of 29.3% is in line with literature [183] and about 4 times higher than the most ductile LPBF specimens (90° single-laser Meander HT). The minimum creep rate for the wrought specimen was 2.47 x 10^{-1} h^{-1} and was lower than most LPBF minimum creep rates, except for 90° single-laser Meander HT and 90° multi-laser Stripe HT, which had similar minimum creep rates and longer creep lives than the wrought specimens.

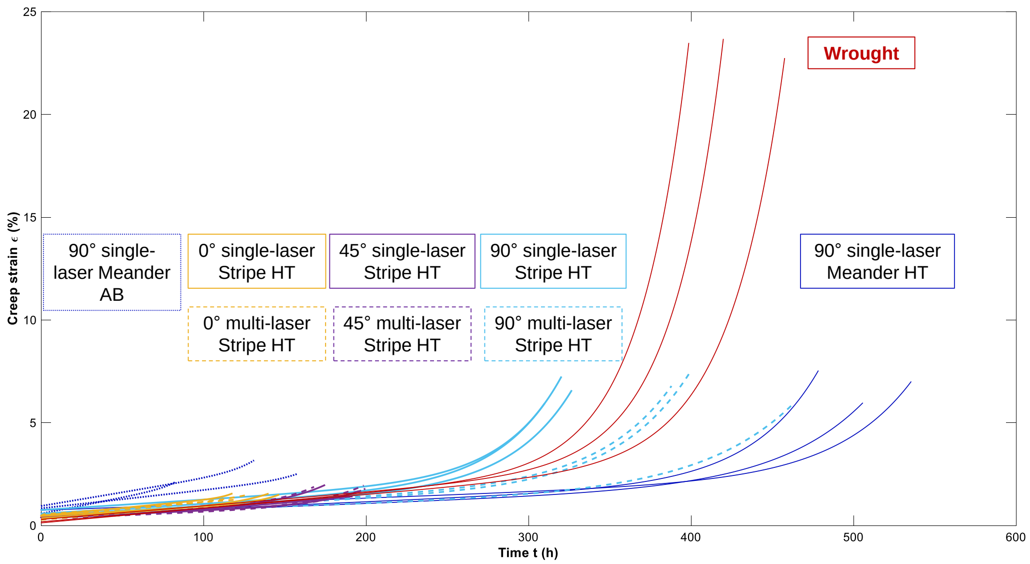

Figure 5.1: Creep curves for all test cases, showing the higher elongation at fracture of wrought material, and some LPBF specimens having longer creep lives.

Figure 5.2 shows the fracture surface and fracture cross section of the wrought specimen. The fracture surface had a fibrous appearance (Figure 5.2f) with numerous dimples and a shear lip (Figure 5.2e) at the specimen edge as well as a reduction in area (Figure 5.2d), which are all signs of totally ductile failure, typical for creep failure of nickel-based superalloys [242, 243].

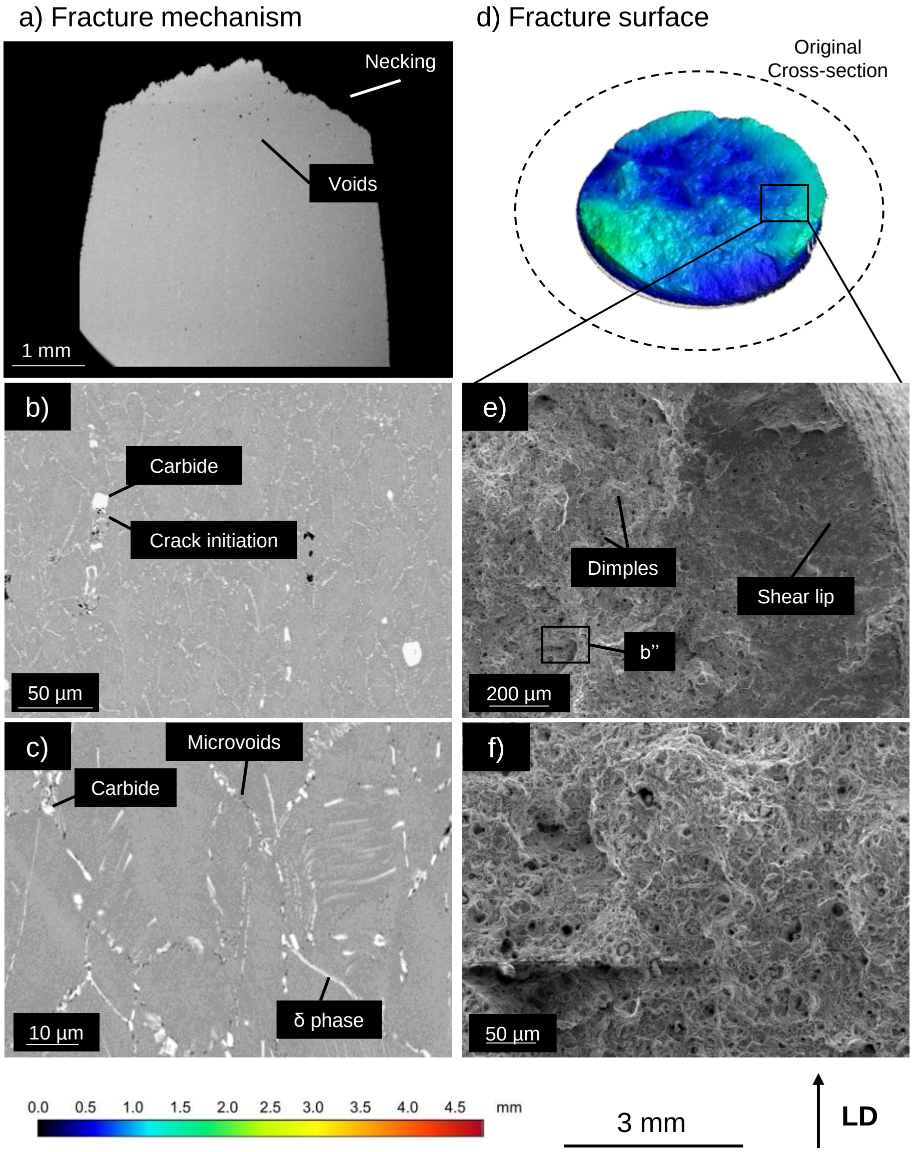
a) Fracture mechanism
Necking
Voids
1 mm
d) Fracture surface
Original
Cross-section
b)
Carbide
Crack initiation
50 µm
e)
Dimples
Shear lip
b''
200 µm
c)
Microvoids
Carbide
δ phase
10 µm
f)
50 µm
0.0
0.5
1.0
1.5
2.0
2.5
3.0
3.5
4.0
4.5
mm
3 mm
LD

Figure 5.2: Fracture after creep of wrought alloy 718. a) The fracture cross-section showing the damage incurred during creep. b) Crack initiation at Carbides and Laves phase. c) Microvoid initiation on the grain boundaries in δ phase gaps. d) The fracture surface showing clear signs of necking and reduction in area. e), f) Clear indicators of ductile failure with dimples, fibrous appearance and shear lips. All indicators indicate a fully ductile fracture in the wrought specimen.

There are clear signs of necking and reduction in area with a cone and cup shape at the top of the fracture surface (Figure 5.2a), which is typical for creep failure of this material [183]. The biggest defects seemed to be formed around carbides (Figure 5.2b) whereas at higher magnifications, some small microvoids can be observed adjacent to δ-precipitates (Figure 5.2c), which is a typical dislocation creep mechanism [58] and was observed in earlier studies [244].

Table 5.1 quantifies the damage seen in the wrought material. Several metrics are used to compare the damage sustained during the creep tests. The crack density represents the total area of cracks, as a percentage of the total area of the specimen. This is a representation of the total amount of damage incurred in a specimen. The maximum crack length metric indicates the degree of microvoids coalescence. This could be an indicator of a localised weakness in the material. Lastly, the height of the fracture surface represents the height difference between the highest and the lowest point on the fracture surface and can be used to understand how many layers the LPBF specimens failed over. The data shown for the wrought material will be used for comparison to the LPBF specimens at a later stage.

Table 5.1: Quantification of damage in wrought alloy 718.

Specimen	**Crack density** *(± 0.15 %Area)*	**Maximum crack length** *(± 0.5 μm)*	**Height difference in fracture surface** *(mm with ISO 4287 [245] error)*
Wrought	0.138	59	1.93

Overall, the wrought alloy 718 outperformed most LPBF specimens in terms of both minimum creep rate and creep life. The elongation at fracture of wrought alloy 718 was considerably higher than the LPBF specimens and the fracture surface showed clear signs of a fully ductile fracture. The creep behaviour of the wrought alloy 718 will serve as a benchmark against the creep properties and behaviour of the LPBF specimens, presented next.

5.2 Laser powder bed fused alloy 718

Figure 5.3 presents the creep curves without the wrought material, which enables a better visualisation of the difference in creep curves for the LPBF specimens. The 90° HT specimens had full creep curves whereas the remaining of the specimens failed at the onset of tertiary creep.

Figure 5.4 shows the differences in minimum creep rate, creep life and elongation at fracture for all the test cases. Table 5.2 presents the values corresponding to this plot and will be used to assess the creep performance. The 90° single-laser Meander HT specimens had the longest creep life, 24% longer than wrought alloy 718, and a similar minimum creep rate to the 90° multi-laser Stripe HT (8% difference) and wrought specimens (0.4% difference). This is in a contrast to a previous study which found that wrought specimens outperformed LPBF specimens by 33% [64]. However, in compression creep testing, Pröbstle et al. [157] showed that the minimum creep rate for heat treated LPBF specimens was lower than the wrought material. The repeats of the specimens had similar creep curves and creep lives. The individual 90° multi-laser Stripe HT specimens had the largest disparity, with 73h difference (17%) in creep life between specimens, while the remaining specimens had even less disparities. Hence, despite the uniqueness of each layer and of each specimen, similar characteristics were obtained during mechanical testing. This brings confidence to the results and allows some generalisation of properties and microstructures for the different specimens.

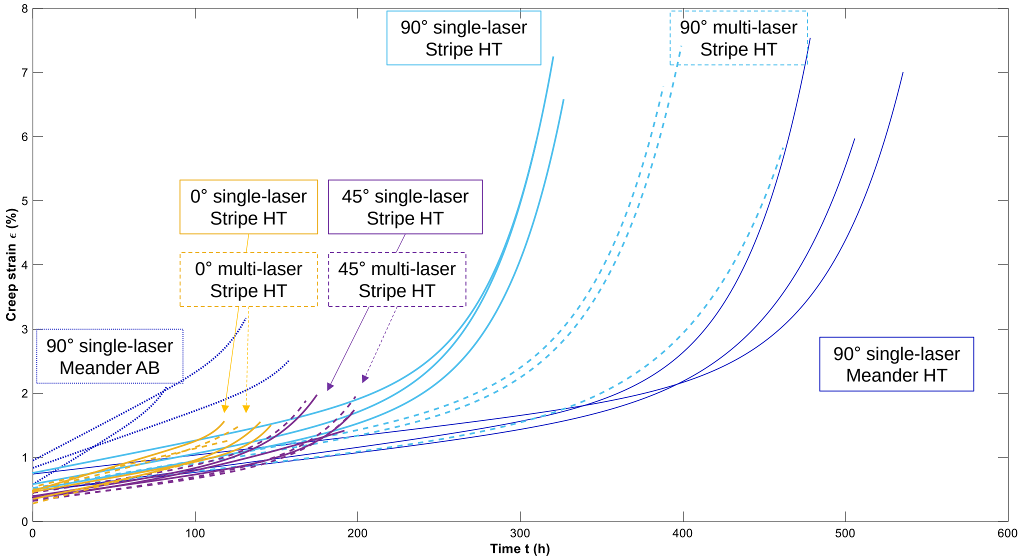

Figure 5.3: Creep curves for the LPBF specimens only, where the different shapes of the creep curves, most notably in terms of tertiary creep, are visible.

Table 5.2: Quantification of the creep performance for all test cases. (Ordered from longest creep life to shortest).

Specimen	**Creep Life** *(h)*	**Minimum creep rate** $(10^{-1}\ h^{-1})$	**Elongation at fracture** *(%)*
90° single-laser Meander HT	507 ± 13	2.46 ± 0.1	7.5 ± 0.5
90° multi-laser Stripe HT	416 ± 19	2.68 ± 0.2	7.0 ± 0.4
Wrought	409 ± 8	2.47 ± 0.2	29.3 ± 0.1
90° single-laser Stripe HT	320 ± 4	3.95 ± 0.1	6.9 ± 0.3
45° multi-laser Stripe HT	189 ± 8	3.05 ± 0.04	1.9 ± 0.03
45° single-laser Stripe HT	188 ± 5	3.36 ± 0.2	1.8 ± 0.1
0° single-laser Stripe HT	131 ± 16	4.86 ± 0.8	1.4 ± 0.1
0° multi-laser Stripe HT	122 ± 6	5.45 ± 0.2	1.8 ± 0.6
90° single-laser Meander AB	107 ± 17	12.4 ± 1.1	2.6 ± 0.3

The differences in creep behaviour for the various types of specimens are compared below, starting by differences between the as-built/heat treated, the meander/stripe scan strategies, the different build orientations and the single/multi-laser scan strategies.

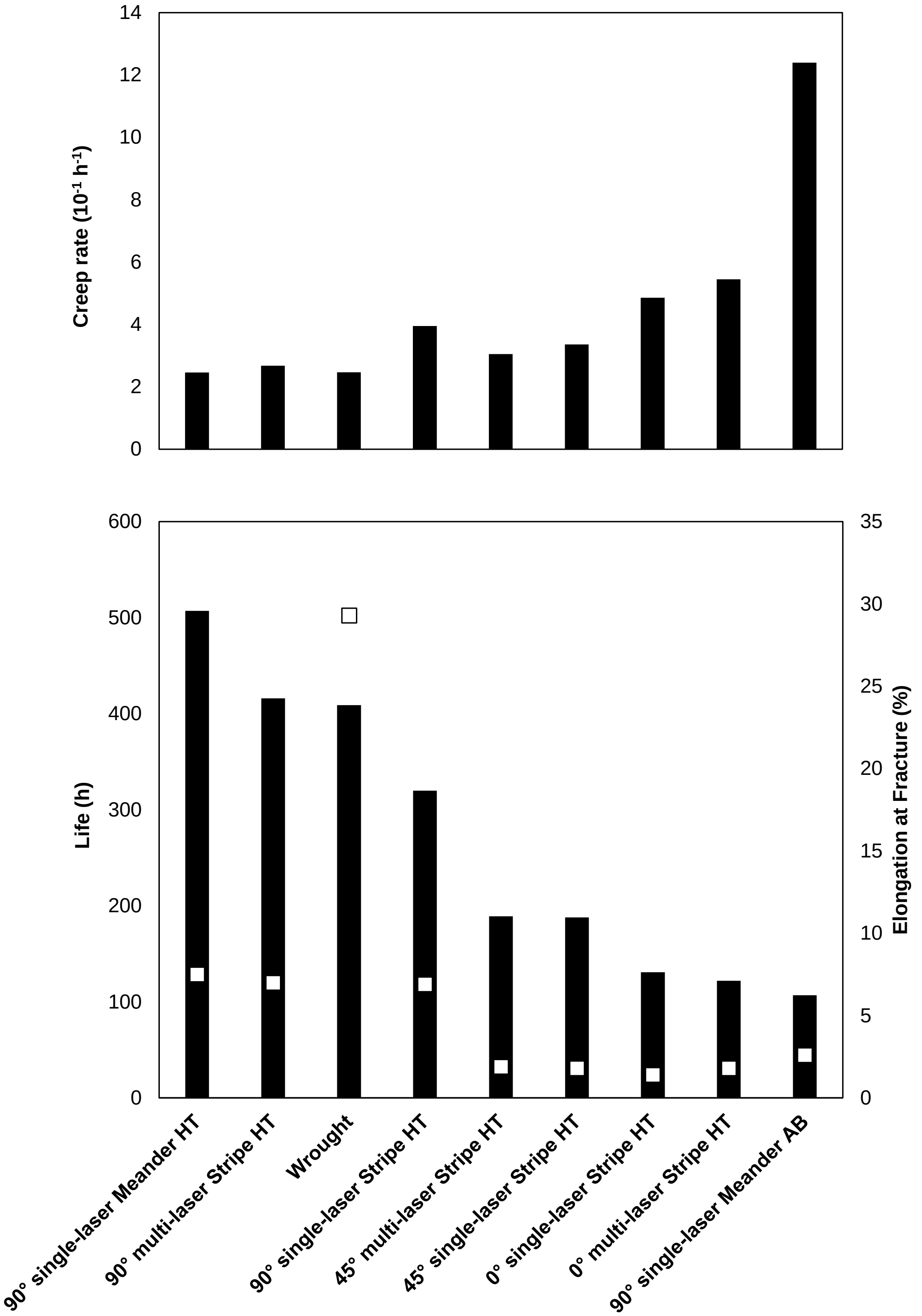

Figure 5.4: Minimum creep rate (black bars in top graph), creep life (black bars in bottom graph) and elongation at fracture (white square scatter points in bottom graph) for all the specimens. This shows that the 90° single and multi-laser specimens had similar minimum creep rates and lives as the wrought material. The 90° AB specimen performed the worst both in terms of creep rate and life. The elongation at fracture of the wrought material is the highest, followed by the 90° specimens.

5.2.1 As-built and heat treated

Figure 5.5 shows that the 90° single-laser Meander AB specimens had an inferior creep life, compared to their heat treated counterparts, by a factor of 5, which is in line with other studies [64]. The minimum creep rate for 90° single-laser Meander HT was also 80% lower than its AB equivalent. This shows the beneficial effect of heat treatment and confirms the choice to heat treat the remaining specimens. Furthermore, Figure 5.5 shows that while 90° single-laser Meander HT had a full creep curve, the 90° single-laser Meander AB specimen failed at the onset of tertiary creep. The 90° single-laser Meander AB specimens also had a lower elongation at fracture by a factor of 2.9 than their heat treated counterpart (Table 5.3). The difference in ductility is also evident in the fracture surface.

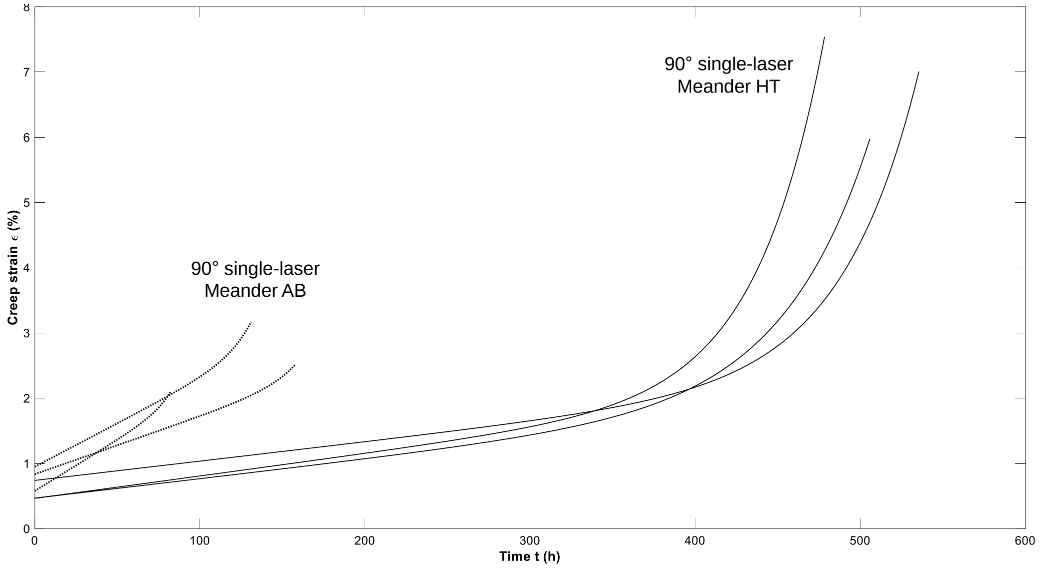

Figure 5.5: Creep curves for 90° single-laser Meander AB and 90° single-laser Meander HT, clearly displaying the differences in minimum creep rate, creep life and elongation at fracture between as-built and heat treated specimens.

Table 5.3: Quantification of the creep performance for the AB and HT 90° single-laser Meander specimens.

Specimen	**Creep Life** *(h)*	**Minimum creep rate** *$(10^{-1}\ h^{-1})$*	**Elongation at fracture** *(%)*
90° single-laser Meander **HT**	507 ± 13	2.46 ± 0.1	7.5 ± 0.5
90° single-laser Meander **AB**	107 ± 17	12.4 ± 1.1	2.6 ± 0.3

The fracture surface and the cross-section of the fracture surface for 90° single-laser Meander AB and 90° single-laser Meander HT, are shown in Figure 5.6. The fracture surface of the AB specimen had ductile aspects, such as dimples (Figure 5.6d), but also more brittle indicators, like cleavage steps (Figure 5.6e). This shows that although ductile mechanisms were present during failure, the LPBF specimens tested in the present work showed much more brittle behaviour than wrought alloy 718. This was also observed by Vielle et al. [246] on the fracture behaviour of AM alloy

718. Additionally, the 90° single-laser Meander HT specimen presented scan lines from the Meander scanning strategy (Figure 5.6h,i). A similar appearance was noticed after tensile testing at 650°C for the AB 90° single-laser Stripe specimens by Hilaire et al. [124].

Table 5.4: Quantification of damage for LPBF 90° single-laser Meander AB and HT specimens.

Specimen	**Crack density** *(± 0.15 %Area)*	**Maximum crack length** *(± 0.5 µm)*	**Height difference in fracture surface** *(mm with ISO 4287 [245] error)*
90° single-laser Meander **AB**	0.37	236	1.68
90° single-laser Meander **HT**	0.77	183	2.31

From a microstructural perspective, both the 90° single-laser Meander AB and HT specimens had visible cracks at low magnification and coalesced microvoids at the grain boundaries (Figure 5.6b,g). Table 5.4 quantifies the damage present after failure of the specimens and shows that creep damage occurred in both specimens, but in different quantities. The HT specimen had twice as many cracks present at fracture than its AB equivalent. This is due to the more brittle behaviour of the AB specimens, which fractured even though there were only a few microvoids present (Figure 5.6b), compared to the HT specimen which had many coalesced microvoids (Figure 5.6b,g). The brittle behaviour of the AB specimens is further confirmed with the maximum crack length, which is about 29% bigger than the HT specimens. The HT specimen on the other hand had a multitude of smaller cracks, highlighting the less brittle behaviour where cracks, even close to each other, did not necessarily propagate to form a bigger crack. The fracture height was also smaller for the AB specimen, which means that the specimen failed over a small number of layers, which hints to the flat fracture surfaces observed in brittle failures.

Overall, heat treatment greatly improved the creep life, minimum creep rate and elongation at fracture of the LPBF specimens. Section 4.4 showed how LPBF process parameters affected the microstructure of LPBF specimens. It is also clear from Figure 5.3 and Figure 5.4 that the build orientation, the scan strategy and the number of lasers affect the minimum creep rate, the creep life and the failure modes of the different LPBF specimens. The effects of these process parameters on the creep behaviour are presented in the following sections.

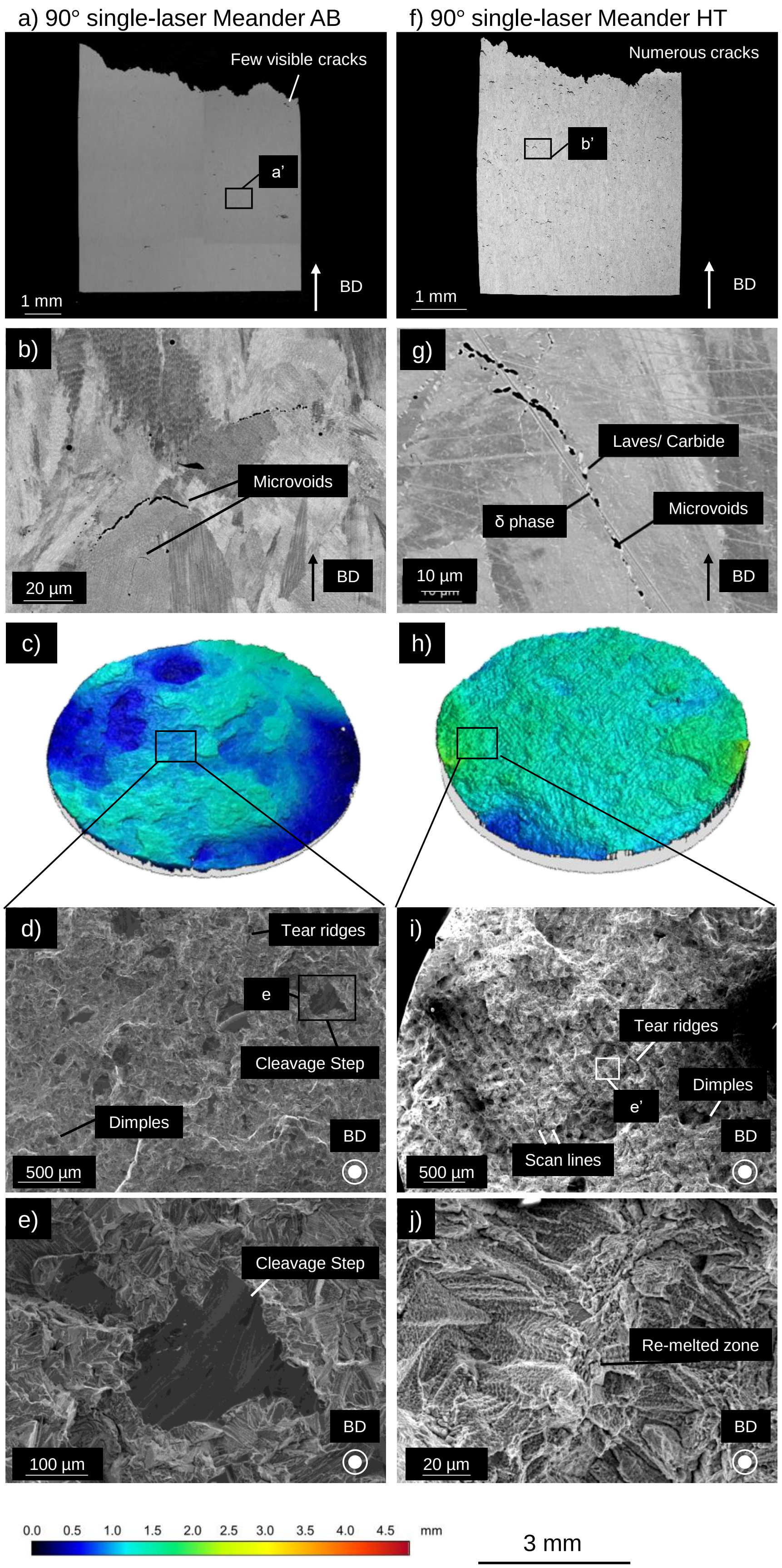
a) 90° single-laser Meander AB
f) 90° single-laser Meander HT
Few visible cracks
a'
1 mm
BD
Numerous cracks
b'
1 mm
BD
b)
Microvoids
20 µm
BD
g)
Laves/ Carbide
δ phase
Microvoids
10 µm
BD
c)
h)
d)
Tear ridges
e
Cleavage Step
Dimples
500 µm
BD
i)
Tear ridges
e'
Dimples
Scan lines
500 µm
BD
e)
Cleavage Step
100 µm
BD
j)
Re-melted zone
20 µm
BD
0.0 0.5 1.0 1.5 2.0 2.5 3.0 3.5 4.0 4.5 mm
3 mm

Figure 5.6: Fracture images of the AB and HT 90° single-laser Meander specimens. a), b) Fracture cross-section of the AB specimen, with very little creep damage, although microvoid coalescence is still occurring. c)-e) Fracture surface of the AB specimen with signs of quasi-cleavage failure. f), g) Fracture cross-section of the HT specimen, with creep damage and microvoid coalescence visible on the short side of the grains. h)-j) Fracture surface of the HT specimen with scan tracks visible on the fracture surface and indicators of quasi-cleavage failure.

5.2.2 Meander and stripe scan strategies

Figure 5.7 shows that 90° single-laser Stripe and Meander HT specimens had a full creep life with primary, secondary and tertiary creep phases (Figure 5.7). The shapes of the creep curves and the elongation at fracture are similar (9% difference). The 90° single-laser Meander HT and 90° single-laser Stripe HT specimens have a 58 % difference in creep rupture time and a 38% difference in minimum creep rate (Table 5.5) whereas only the scan strategy is different.

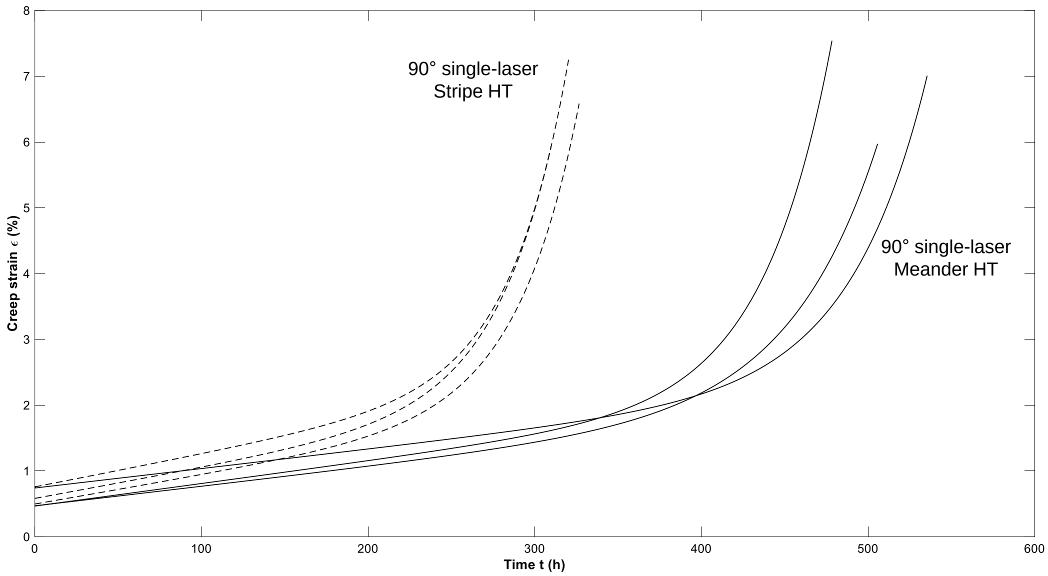

Figure 5.7: Creep curves for 90° single-laser Meander HT and 90° single-laser Stripe HT. Both specimens had full creep curves and the Stripe specimen had a shorter creep life than its Meander counterpart.

Table 5.5: Quantification of the creep performance for the Stripe and Meander 90° single-laser HT specimens.

Specimen	**Crack density** *(± 0.15 %Area)*	**Maximum crack length** *(± 0.5 µm)*	**Height difference in fracture surface** *(mm with ISO 4287 [245] error)*
90° single-laser **Meander** HT	507 ± 13	2.46 ± 0.1	7.5 ± 0.5
90° single-laser **Stripe** HT	320 ± 4	3.95 ± 0.1	6.9 ± 0.3

Figure 5.8 shows the cross-section of the fracture for both 90° single-laser Stripe and Meander HT specimens. For both specimens, microvoids initiated on grain boundaries where small δ phase precipitates were present (Figure 5.8b). The microvoids then coalesced and formed cracks on the "short side" of the columnar grains (Figure 5.8d). This is to be expected as material separation usually occurs on the plane perpendicular to the loading direction [247]. The top of the fracture surface (Figure 5.8a,c) does not have the typical indicators of either ductile (cup and cone) or brittle (flat) fracture surfaces, indicating that quasi-cleavage or mixed mode fracture occurred.

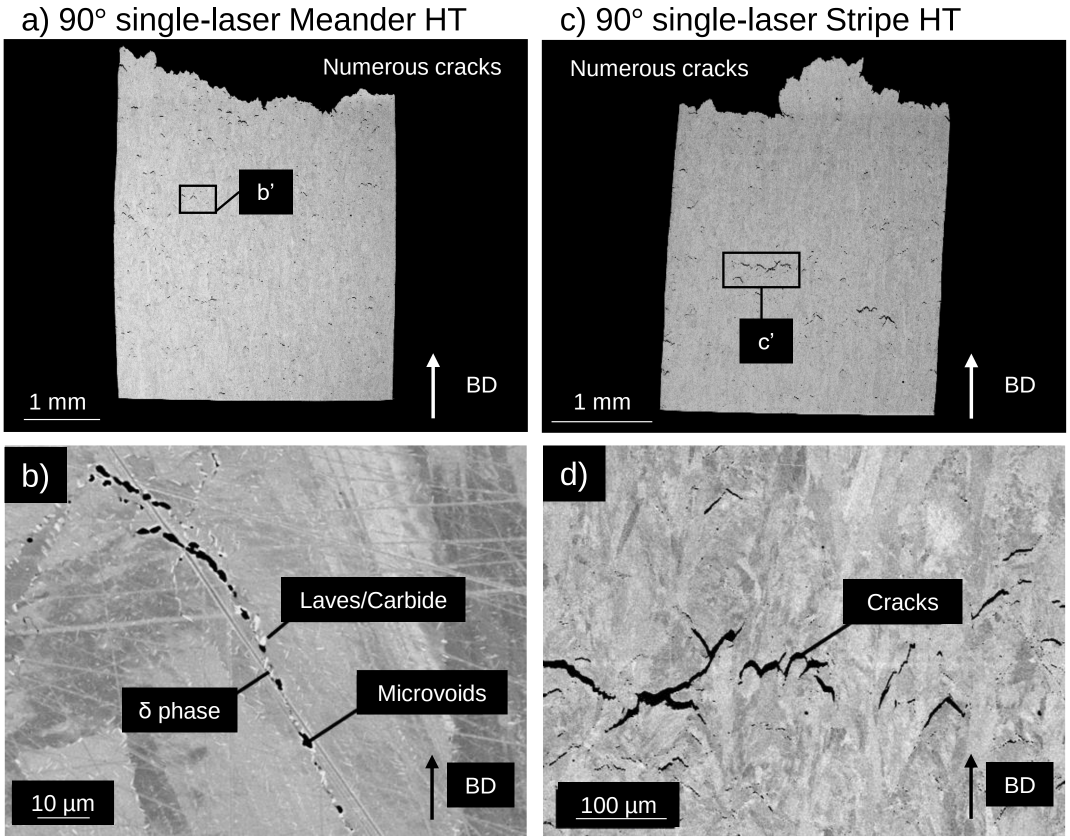
a) 90° single-laser Meander HT

c) 90° single-laser Stripe HT

Figure 5.8: SEM images of the Fracture cross-section for the 90° single-laser HT specimens with different scan strategies. a), b) Meander strategy. c), d) Stripe strategy. Both types of specimens showed signs of creep damage with microvoid coalescence on the short side of the grains.

Table 5.6 indicates that the 90° single-laser Stripe HT specimens had a slightly greater number of cracks and amount of creep damage, 6% more than the 90° single-laser Meander HT and 89% more than wrought alloy 718, which had the lowest amount of cracks due to the very small number of microvoids present, as described in Section 5.1. The damage in the Meander and Stripe specimens were also distributed throughout the section, with no obvious localised damage.

Table 5.6: Quantification of damage for the 90° single-laser Stripe and Meander HT specimens.

Specimen	**Crack density** *(± 0.15 %Area)*	**Maximum crack length** *(± 0.5 µm)*	**Height difference in fracture surface** *(mm with ISO 4287 [245] error)*
90° single-laser **Stripe** HT	0.82	709	2.96
90° single-laser **Meander** HT	0.77	183	2.31

Although the fracture height of the Meander specimen was about 22% smaller than its Stripe counterpart, both specimens seemed to have failed in a similar fashion. Figure 5.9 shows the fracture surface of both specimens. Both ductile and brittle fracture indicators, such as dimples (Figure 5.9b,e) and cleavage steps (Figure 5.9f), respectively, are present on the fracture surface. This indicates that the specimens failed by quasi-cleavage. Both specimens showed signs of the scan strategy employed on the fracture surface and the different laser scan paths of the Meander and Stripe strategies are also visible (Figure 5.9a,b and d,e).

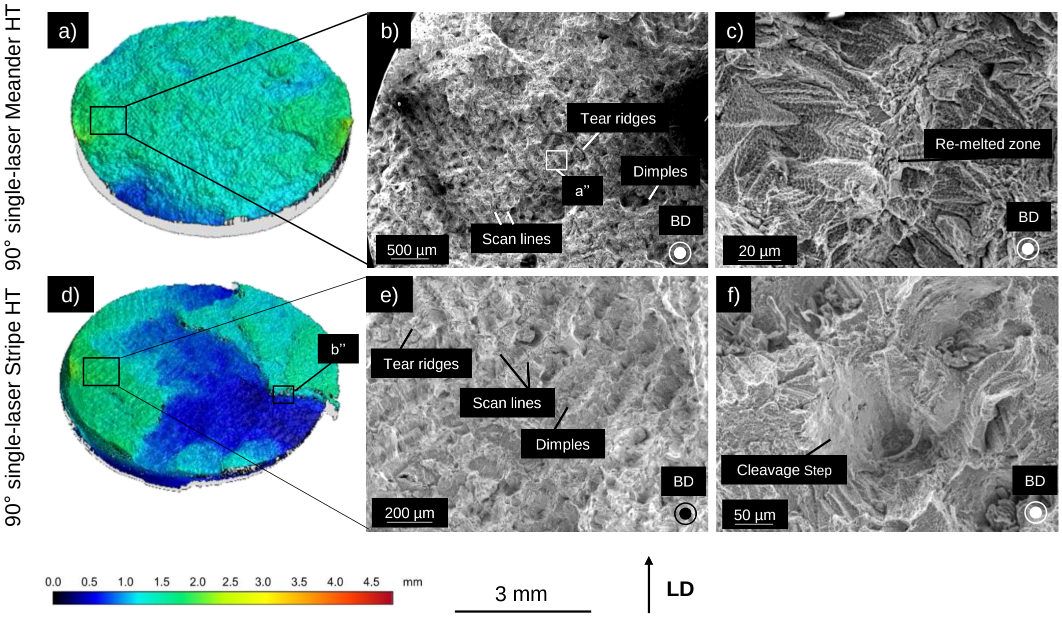
90° single-laser Meander HT
90° single-laser Stripe HT
a)
b)
Tear ridges
Dimples
a''
Scan lines
500 µm
BD
c)
Re-melted zone
BD
20 µm
d)
b''
e)
Tear ridges
Scan lines
Dimples
BD
200 µm
f)
Cleavage Step
BD
50 µm
0.0 0.5 1.0 1.5 2.0 2.5 3.0 3.5 4.0 4.5 mm
3 mm
LD

Figure 5.9: Fracture surface for the 90° single-laser HT specimens built with different scan strategies. a)-c) Meander strategy. d)-f) Stripe strategy. Both specimens present scan lines on the fracture surface as well as dimples and cleavage steps, indicating a failure by quasi-cleavage.

5.2.3 Build orientations

Figure 5.10 presents the creep curves for the different build orientations and Table 5.7 quantifies the creep life, minimum creep rate and elongation at fracture for the different specimens. The 90° single-laser Stripe HT specimens had a longer creep life than specimens built at 0° and 45° by 144% and 70%, respectively, which is in line with findings from the literature [33]. However, this is the opposite of the trend observed in other mechanical tests, such as tensile tests, where the 0° specimens performed better than the 90° ones [124]. Figure 5.10 also reveals that the creep curves for the various build orientations were different in terms of secondary creep, tertiary creep and elongation at fracture. The 90° single-laser Stripe HT specimens had a full creep life with primary, secondary, and tertiary creep phases, whereas 0° and 45° specimens failed at the onset of tertiary creep (Figure 5.10), resulting in an incomplete creep curve and shorter creep life. The 0° single-laser Stripe HT specimens also had the lowest LPBF elongation at fracture of 1.4%, out of all the LPBF specimens in this work. These elongations are all considerably smaller than for the wrought material. This lack of ductility in the LPBF specimens is also observed in the fracture surfaces of the specimens.

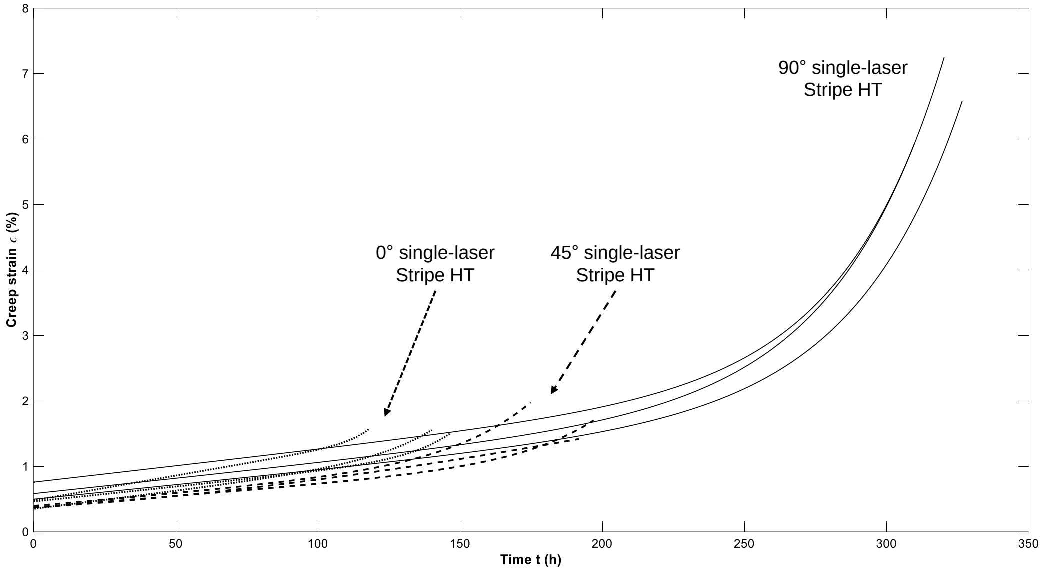

Figure 5.10: Creep Curves for the different test cases, showing the clear differences in creep performance with regards to orientation, heat treatment and scan strategy. This also shows the differences in tertiary creep for the different specimens.

Table 5.7: Quantification of the creep performance for single-laser Stripe HT specimens built at 0°, 45° and 90°.

Specimen	**Creep Life** *(h)*	**Minimum creep rate** *(10^{-1} h^{-1})*	**Elongation at fracture** *(%)*
90° single-laser Stripe HT	320 ± 4	3.95 ± 0.1	6.9 ± 0.3
45° single-laser Stripe HT	188 ± 5	3.36 ± 0.2	1.8 ± 0.1
0° single-laser Stripe HT	131 ± 16	4.86 ± 0.8	1.4 ± 0.1

Figure 5.11 shows the fracture surfaces for the different build orientations. The fracture surfaces of the 90° and 0° single-laser Stripe HT specimens exhibited clear intergranular ductile failure signs, such as dimples and tear ridges (Figure 5.11b,h), however cleavage steps (Figure 5.11c,i) were also present indicating that the specimen actually failed by quasi-cleavage. This has been observed in other creep studies [64]. There were also some signs of trans-dendritic failure (Figure 5.13a), which was observed as well in a high temperature tensile test by Hilaire et al. [124] with AB 0° stripe specimens where the specimens fractured by shearing. This more brittle type of failure is in line with the low elongation at fracture observed in the specimens. The 90° specimen also had signs of the Stripe scan strategy on its fracture surface, as mentioned in the previous section. This was also noted in different studies at 90° and 0° build orientations [124]. However, within this work, 0° specimens did not show traces of scan strategies. The 45° specimens' fracture surface was at a 30-45° angle (Figure 5.12c) and had similar aspects to the 0° specimen surface with few dimples and a rock-candy appearance (Figure 5.11e,f), which are intergranular failure signs. As this specimen failed at 45° from the loading direction, it may suggest failure by mixed mode mechanisms.

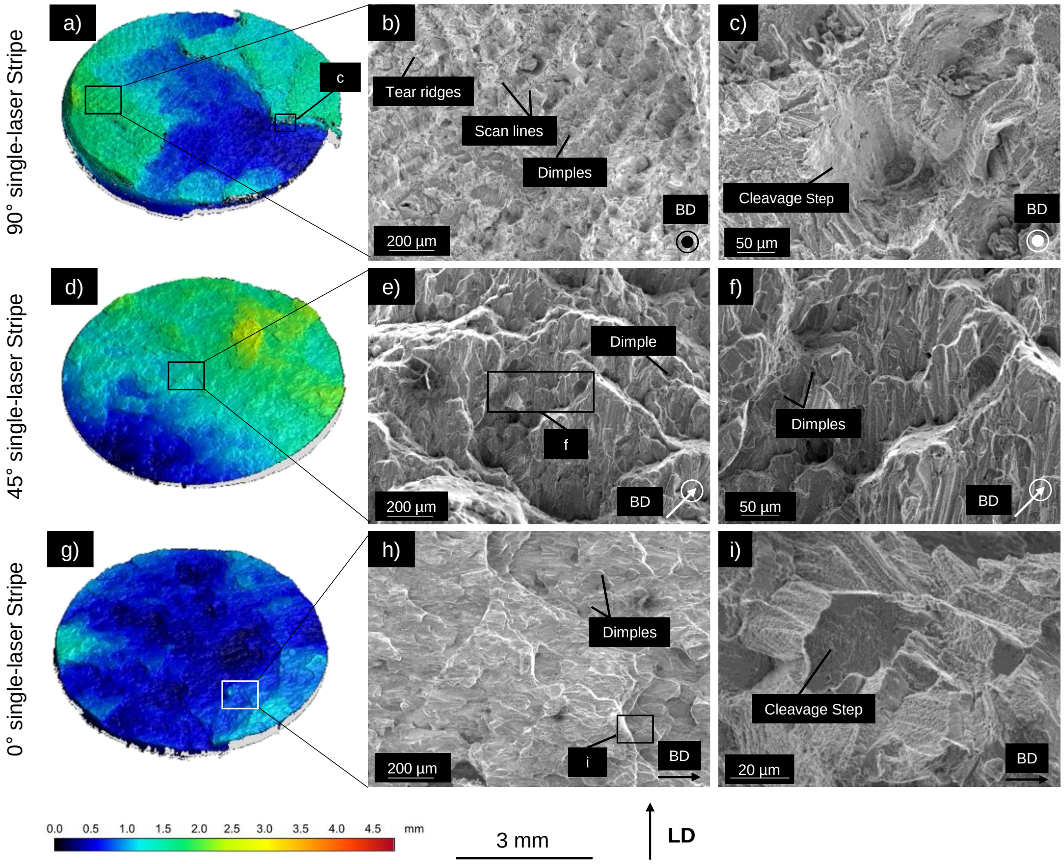
90° single-laser Stripe
45° single-laser Stripe
0° single-laser Stripe
a)
b)
c)
c
Tear ridges
Scan lines
Dimples
Cleavage Step
BD
200 µm
50 µm
d)
e)
f)
Dimple
f
Dimples
BD
200 µm
50 µm
g)
h)
i)
Dimples
i
Cleavage Step
BD
200 µm
20 µm
0.0 0.5 1.0 1.5 2.0 2.5 3.0 3.5 4.0 4.5 mm
3 mm
LD

Figure 5.11: Fracture surface for the different build orientations. a)-c) 90° single-laser Stripe HT specimen. d)-f) 45° single-laser Stripe HT specimen. g)-i) 0° single-laser Stripe HT specimen. 90° and 0° spciemens failed by quasi-cleavage, as indicated by the mixture of dimples anc cleavage steps in their fracture surface. The 45° specimen failed by mixed mode failure.

The microstructural mechanisms of fracture can distinctly be seen in Figure 5.12 and the creep damage, including crack /void density, is quantified in Table 5.8. The 90° single-laser Stripe HT specimens had the greatest number of coalesced microvoids, as qualitatively observed from Figure 5.12a and quantitively from the crack density in Table 5.8, compared to the other build orientations (Figure 5.12a,c,e), 486% and 215% more than 0° and 45° single-laser Stripe HT specimens, respectively. The short side of the grains, perpendicular to the loading direction, contained most of the microvoids in the 90° single-laser Stripe HT, resulting in V-shaped cracks (Figure 5.12b). The 0° single-laser Stripe HT and 45° single-laser Stripe HT specimens were similar, with grain boundary cavities and δ-precipitates on the long side of the grains (perpendicular to loading direction and parallel to build direction), but in much lower quantity (Figure 5.12d,f).

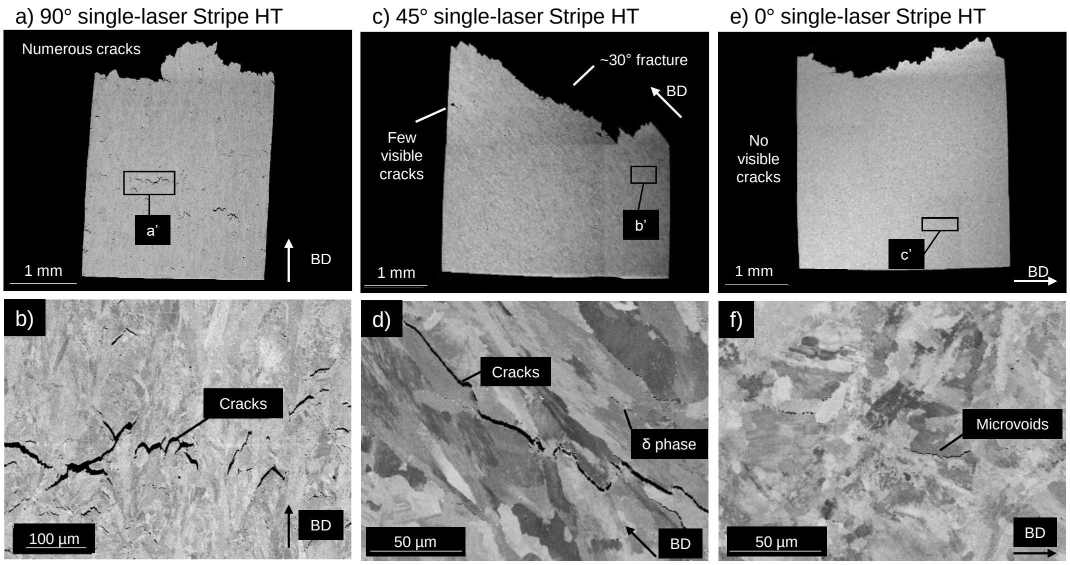
a) 90° single-laser Stripe HT
c) 45° single-laser Stripe HT
e) 0° single-laser Stripe HT

Figure 5.12: Fracture cross-section for the different build orientations. a),b) 90° single-laser Stripe HT specimen. c),d) 45° single-laser Stripe HT specimen. e),f) 0° single-laser Stripe HT specimen. Cracks on the grain boundaries are clearly visible with material separation perpendicular to the loading direction.

Table 5.8: Quantification of damage in the different build orientations.

Specimen	**Crack density** *(± 0.15 %Area)*	**Maximum crack length** *(± 0.5 µm)*	**Height difference in fracture surface** *(mm with ISO 4287 [245] error)*
90° single-laser Stripe HT	0.82	709	2.96
45° single-laser Stripe HT	0.26	317	2.69
0° single-laser Stripe HT	0.14	28	1.69

The 0° single-laser Stripe HT specimens had a small number of cracks (Table 5.8), which were all located close to the fracture surface (Figure 5.12e). This indicates a local weakness in 0° specimens, instead of failure of the material as a whole from creep damage. 0° specimens also had some transgranular cracks present (Figure 5.13b). Hilaire et al. [124] also observed transgranular cracks in tensile testing at 650°C for AB 0° and 90° specimens. This was the case only for heat treated 0° single-laser Stripe HT specimens here and along with cleavage steps, this highlights the brittle failure mechanisms of the 0° specimens.

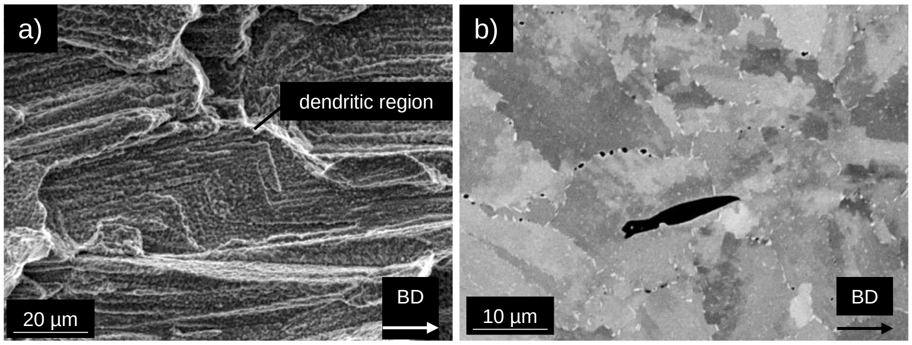

Figure 5.13: Fracture indicators in 0° single-laser Stripe HT specimens. a) Trans-dendritic failure surface indicator. b) Transgranular crack. All images oriented with respect to the loading direction, with the build direction indicated.

Table 5.8 presents the height difference in the fracture surface. The 45° single-laser Stripe HT specimen failed over a height of 2.69 mm. However, this is partly due to the specimen failing at an angle of around 30° (Figure 5.12c). By taking this into account, the 45°single-laser Stripe HT specimens actually failed in a small number of layers (~ 20 layers). This is illustrated in Figure 5.14. The 90° single-laser Stripe HT specimen clearly failed over multiple layers (~ 50 layers) and 0° single-laser Stripe HT specimens failed across all its layers due to its build orientation and plane of failure combination.

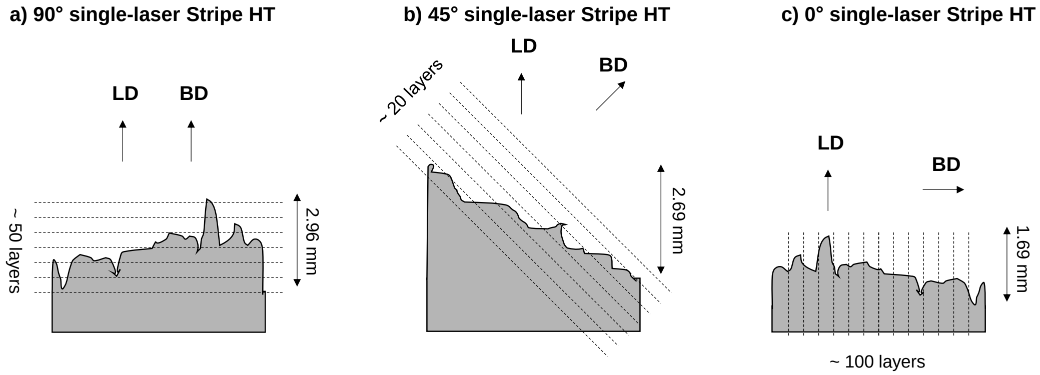
a) 90° single-laser Stripe HT
LD
BD
~ 50 layers
2.96 mm
b) 45° single-laser Stripe HT
LD
BD
~ 20 layers
2.69 mm
c) 0° single-laser Stripe HT
LD
BD
1.69 mm
~ 100 layers

Figure 5.14: Schematic of failure across layers for the different specimens, with respect to the loading direction and showing the build direction. a) 90° single-laser Stripe HT. b) 45° single-laser Stripe HT. c) 0° single-laser Stripe HT. This shows the number of layers failure occurred on.

Overall, the build orientation of the specimens had clear effects on the specimens' creep behaviour and particularly their failure modes.

5.2.4 Multi-laser scan strategies

Figure 5.15 presents the creep curves of the LPBF specimens. While the 90° specimens had full creep curves, the 45° and 0° specimens failed at the onset of tertiary creep, regardless of the number of lasers. The 90° multi-laser Stripe HT specimens outperformed their single-laser counterpart while single and multi-laser specimens had an equal performance for 0° and 45° orientations (Figure 5.15).

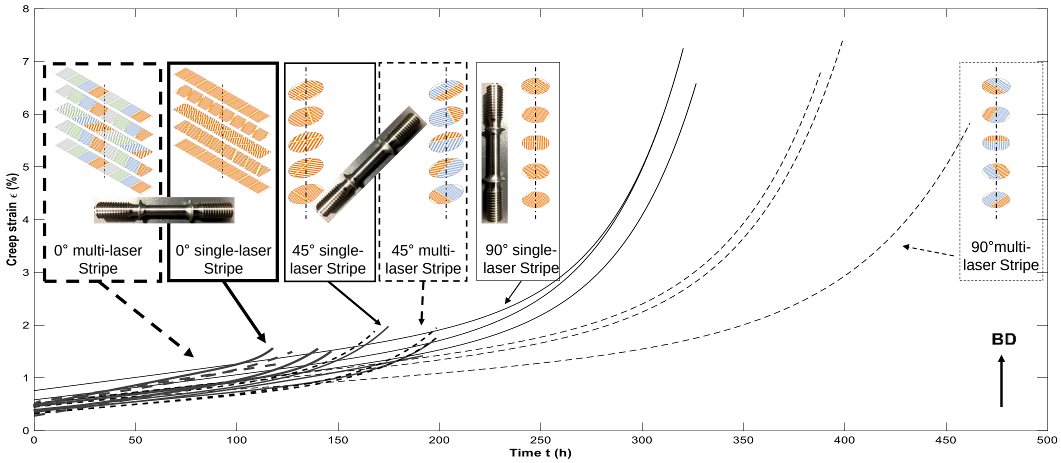

Figure 5.15: Creep curves of the single and multi-laser LPBF specimens. This is showing similar performances for 0° and 45° single and multi-laser specimens and the longer creep life of the 90° multi-laser specimen, compared to its single laser counterpart.

Table 5.9: Quantification of the creep performance for Stripe HT single and multi-laser specimens at multiple build orientations.

Specimen	**Creep Life** *(h)*	**Minimum creep rate** *(10^{-1} h^{-1})*	**Elongation at fracture** *(%)*
90° multi-laser Stripe HT	416 ± 19	2.68 ± 0.2	7.0 ± 0.4
90° single-laser Stripe HT	320 ± 4	3.95 ± 0.1	6.9 ± 0.3
45° multi-laser Stripe HT	189 ± 8	3.05 ± 0.04	1.9 ± 0.03
45° single-laser Stripe HT	188 ± 5	3.36 ± 0.2	1.8 ± 0.1
0° single-laser Stripe HT	131 ± 16	4.86 ± 0.8	1.4 ± 0.1
0° multi-laser Stripe HT	122 ± 6	5.45 ± 0.2	1.8 ± 0.6

Table 5.9 shows that the 90° multi-laser Stripe HT specimens had a similar creep lifetime to the wrought alloy (1% difference), however, the minimum creep rate for the wrought alloy was 8% lower. The 90° single-laser specimens showed poorer creep properties, with a shorter creep life and higher minimum creep rate than the 90° multi-laser specimens. The 45° multi and single-laser specimens had similar creep rupture times, but the multi-laser specimens had a 9% lower minimum creep rate.

The 0° specimens had the worst creep properties of all the specimens, in this case the multi-laser specimens had similar but slightly poorer minimum creep rates and life than their single-laser counterparts by 10% and 7%, respectively.

Figure 5.16 shows the cross-sections of the fracture surface for the various single and multi-laser specimens. All the specimens had microvoid formation on the grain boundaries, perpendicular to the loading direction. Figure 5.16b,d and Table 5.10 show that the crack density in the 90° single-laser specimens was 35% higher than their multi-laser counterparts. It is safe to say that more creep damage has occurred in the single-laser specimen. The maximum crack length was also higher in the 90° single-laser specimen (Figure 5.16b) than in the equivalent multi-laser specimen. A similar comparison between the single and multi-laser specimens can be observed for the 45° specimens, which had the longest crack length. The 0° specimens had the lowest crack density and length and the differences between single and multi-laser specimens were negligible.

Table 5.10: Quantification of damage in failed single and multi-laser specimens for different build orientations.

Specimen	**Crack density** *(± 0.15 %Area)*	**Maximum crack length** *(± 0.5 µm)*	**Height difference in fracture surface** *(mm with ISO 4287 [245] error)*
90° single-laser Stripe HT	0.82	709	2.96
90° multi-laser Stripe HT	0.53	74	2.52
45° single-laser Stripe HT	0.26	317	2.69
45° multi-laser Stripe HT	0.30	721	4.8
0° single-laser Stripe HT	0.14	28	1.69
0° multi-laser Stripe HT	0.15	33	1.43

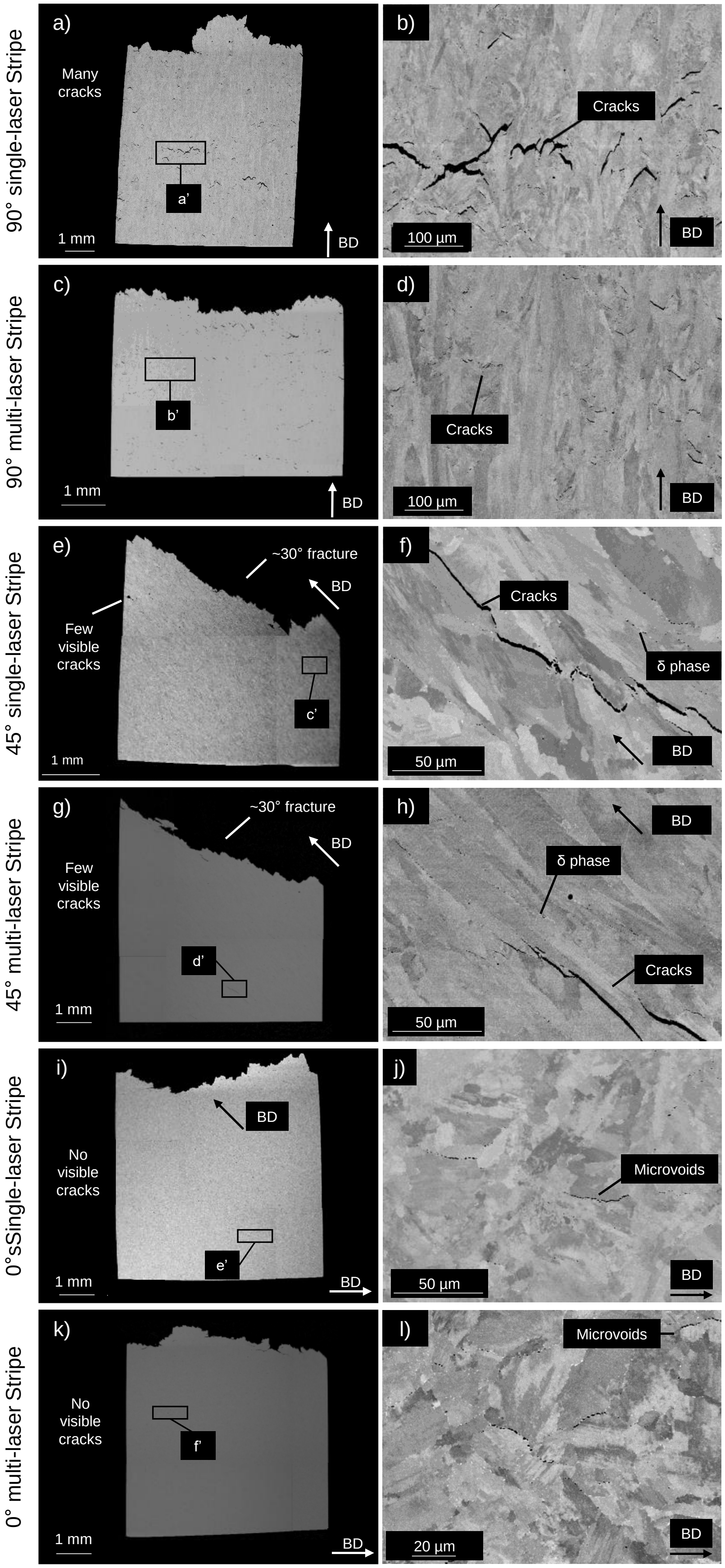
90° single-laser Stripe
a)
Many cracks
a'
1 mm
BD
b)
Cracks
100 µm
BD
90° multi-laser Stripe
c)
b'
1 mm
BD
d)
Cracks
100 µm
BD
45° single-laser Stripe
e)
~30° fracture
BD
Few visible cracks
c'
1 mm
f)
Cracks
δ phase
50 µm
BD
45° multi-laser Stripe
g)
~30° fracture
BD
Few visible cracks
d'
1 mm
h)
BD
δ phase
Cracks
50 µm
0°sSingle-laser Stripe
i)
BD
No visible cracks
e'
1 mm
BD
j)
Microvoids
50 µm
BD
0° multi-laser Stripe
k)
No visible cracks
f'
1 mm
BD
l)
Microvoids
20 µm
BD

Figure 5.16: Cross sectional view of the fracture surface for the different single and multi-laser specimens in different build orientations. a),b) 90° single-laser. c),d) 90° multi-laser. e),f) 45° single-laser. g),h) 45° multi-laser. i),j) 0° single-laser. k),l) 0° multi-laser. Showing similar microstructures at failure for each build orientation, regardless of the number of lasers.

The fracture surfaces of all the specimens are shown in Figure 5.17. Although the fracture surfaces look different for the different build orientations, as previously established, the single and multi-laser specimens, for a given build orientation, seem identical, with similar characteristics such as scan tracks, dimples, cleavage steps and planes of failure. Both single and multi-laser 90° specimens showed scan tracks (Figure 5.17a,d) on their fracture surfaces and failed by quasi-cleavage. Similarly, the single and multi-laser 0° specimens both failed by quasi-cleavage as well and by mixed mode failure for the 45° single and multi-laser specimens.

Overall, the use of multi-laser scan strategies did not detriment the creep properties. Indeed, the single and multi-laser specimens performed similarly at 0° and 45° build orientation and the multi-laser 90° specimen even outperformed its single-laser counterpart by 30% and had a similar life to wrought alloy 718 by 1% in creep life. The multi-laser scan strategy also did not affect the mode of failure of the components.

The results showed that the creep behaviour was different for wrought and LPBF specimens as well for the different process parameters employed. The following sections provide an explanation of the different creep and failure behaviours of the various specimens. The effect of the LPBF microstructure will first be discussed, followed by the effects of heat treatment and LPBF process parameters.

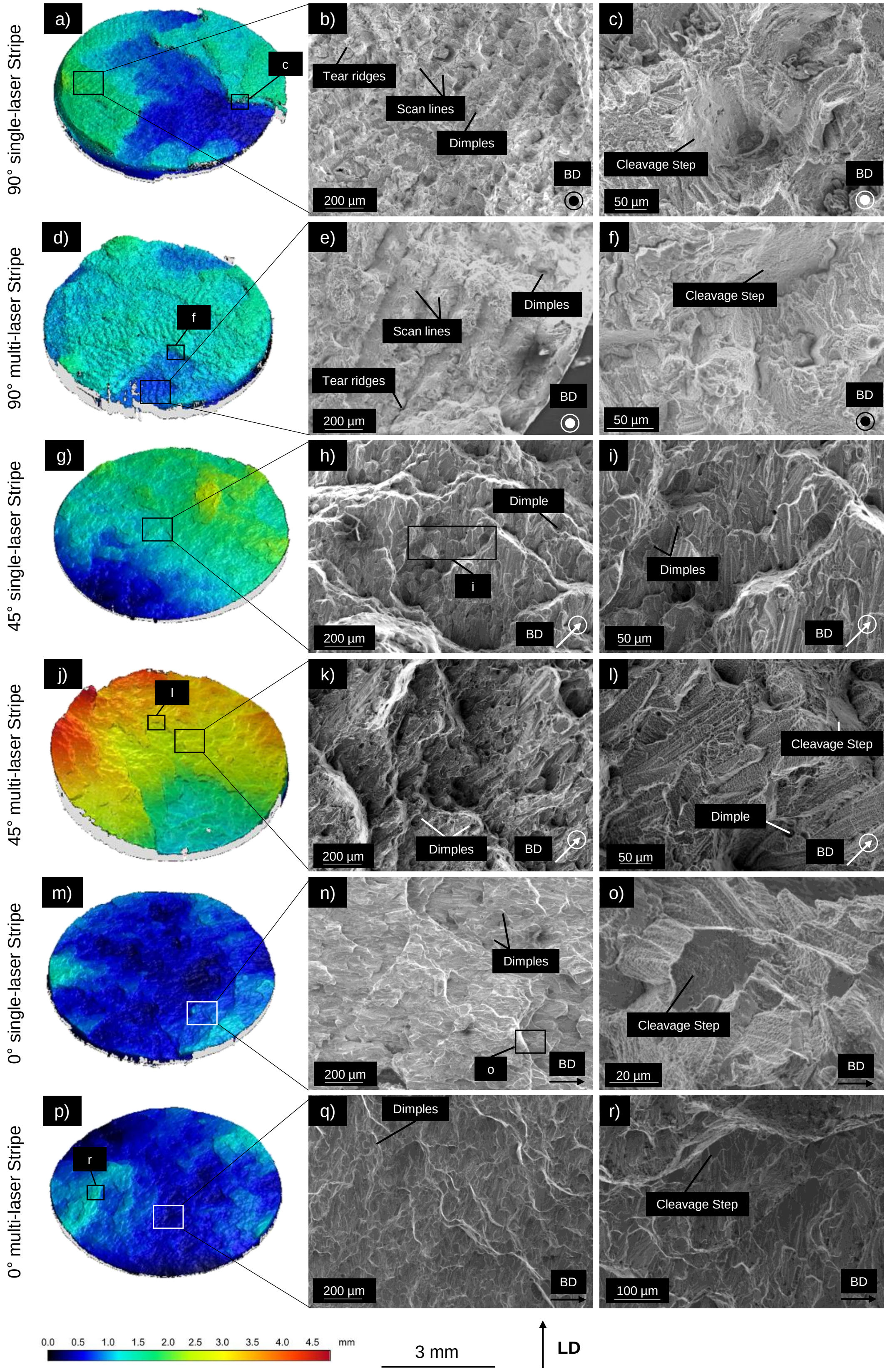
90° single-laser Stripe
a)
c
b)
Tear ridges
Scan lines
Dimples
BD
200 µm
c)
Cleavage Step
BD
50 µm
90° multi-laser Stripe
d)
f
e)
Dimples
Scan lines
Tear ridges
BD
200 µm
f)
Cleavage Step
BD
50 µm
45° single-laser Stripe
g)
h)
Dimple
i
BD
200 µm
i)
Dimples
BD
50 µm
45° multi-laser Stripe
j)
l
k)
Dimples
BD
200 µm
l)
Cleavage Step
Dimple
BD
50 µm
0° single-laser Stripe
m)
n)
Dimples
o
BD
200 µm
o)
Cleavage Step
BD
20 µm
0° multi-laser Stripe
p)
r
q)
Dimples
BD
200 µm
r)
Cleavage Step
BD
100 µm
0.0
0.5
1.0
1.5
2.0
2.5
3.0
3.5
4.0
4.5
mm
3 mm
LD

Figure 5.17: Fracture surfaces of the different single and multi-laser scan strategies for the various build orientations. a)-c) 90° single-laser. d)-f) 90° multi-laser. g)-i) 45° single-laser. j)-l) 45° multi-laser. m)-o) 0° single-laser. p)-r) 0° multi-laser. All specimens aligned with the loading direction, with the build direction clearly marked. This shows the similar fracture indicators in the single and multi-laser specimens for a given build orientation.

5.3 Effect of laser powder bed fusion microstructure

The differences in creep behaviour between the various LPBF specimens and wrought alloy 718 are in part due to the specific LPBF microstructure. Section 0 demonstrated that LPBF resulted in a different microstructure from wrought material, regarding porosity, precipitate density, grain size and morphology, and texture, which affected the creep performance of alloy 718.

5.3.1 Effect of porosity

One of the key differences between LPBF and wrought specimens is the higher porosity in the former. The pores come from the LPBF process. Spherical pores come from gas entrapment and irregular pores form from process parameters such as scan strategy [233] and laser energy density [248]. Porosity has always been a determining factor for creep performance, as it contributes to higher minimum creep rates and cause premature failure in the material [249]. Indeed, typical LPBF porosities can act as stress initiation points and lead to failure [250]. When creep occurs, voids form on the grain boundaries or in high stress concentration areas such as irregular pores, Laves phase or carbides [251]. Xu et al. [190] looked at the defect evolution of LPBF alloy 718 porosity during creep and found that the number and size of pores and defects increased with time as the material is creeping. This means that the low minimum creep rate of the 45° specimens could be due to the higher density, and hence lower porosity present compared to other specimens (Table 4.5). In another study, machine learning was used to predict minimum creep rate of LPBF alloy 718 by using porosity data and process parameters as inputs to the model [252]. This study found that rather than process parameters, the main factor affecting minimum creep rates was porosity [252]. Porosity data was also shown to successfully predict the fatigue life of LPBF alloy 718 [232]. This clearly shows the strong link between porosity and creep performance and the detrimental effect of the former. However, one paper by Babamiri et al. [253] argues that rather than porosity, the morphology and distribution of precipitates has a bigger effect on mechanical properties.

5.3.2 Effect of precipitates

The main precipitates observed in both wrought and LPBF alloy 718 were δ phase, carbides and Laves phase. Although γ'' was present and is the main strengthening phase of alloy 718, this discussion will focus on the δ and Laves phases. The γ'' phase has the same composition as the δ phase and the latter forms by depleting the γ matrix of Nb and hence this results in less γ''.

Although, δ-precipitates were stated to serve as void initiation points [247] this present work argues that the size and number of those particles was an impediment to microvoid formation and coalescence. Indeed, the size of the δ-precipitates on the grain boundaries in the wrought specimen meant that there was little space for microvoids to form and link (Figure 5.2c), hence impeding microvoid coalescence and slowing down the minimum creep rate. A study by Rafiei et al. [254] also observed that δ-processed alloy 718 (obtained by an over-aging heat treatment,) showed lower minimum creep rates and longer creep lifetimes than conventional alloy 718. Yeh et al. [255] found that the precipitation of δ-precipitates during the heat treatment of wrought alloy 718 also influenced the morphology of grain boundaries, which in turn resulted in an extended creep life. Pröbstle et al. [157] also argued that δ-precipitates pin the grain boundaries in wrought material during compression creep of LPBF alloy 718.

A study by Chen et al. [247] investigated a number of precipitate-enhancing heat treatments in order to optimise precipitate density in wrought alloy 718 and suggested that for wrought alloy 718 low densities of δ-precipitates would isolate creep voids, resulting in fracture mainly due to wedge cracks at triple point grain boundaries, whereas a high density of precipitates would mean that the fracture would be controlled by cavity growth and grain boundary sliding. The lower number of δ-precipitates in the 90° single-laser Stripe HT specimen (Table 4.6) may explain why it resulted in poorer minimum creep rate and life than its multi-laser counterpart (Table 5.2). Figure 5.18 shows the relationship between the density of δ-precipitates and the creep life (Figure 5.18a), minimum creep rate (Figure 5.18b) and elongation at fracture (Figure 5.18c). From this figure, it seems that no trend can be discerned between the precipitate density and creep life (despite some significant variriation in life between some specimens), minimum creep rate and elongation at fracture of the test cases. This is probably due to the similar amounts of precipitates present in the LPBF specimens whereas their minimum creep rate and life varied significantly. Chen et al. [247] observed that with a δ density between 0% and 45% of the wrought material, there was a decrease in creep lifetime and elongation at fracture whereas for a δ density of more than 45%, rupture time and elongation at fracture increased. Trosch et al. [256] also observed that the elongation at fracture of LPBF alloy 718 reduced greatly at high temperatures, compared to wrought, due to the distribution of δ-precipitates. Although this type of trend is not visible here, this confirms the hypothesis that δ-precipitates can be both detrimental and beneficial to creep properties depending on their amount and size. However, despite having significantly more δ-precipitates, wrought specimens still had a lower creep life and a similar minimum creep rate to the 90° single-laser Meander HT specimens. This means that other factors, such as the orientation of the δ phase must also affect the creep behaviour.

The orientation of the δ-precipitates (see Section 4.2.3) can either benefit or damage the material's mechanical properties and could explain the differences in creep performances observed between the different build orientations (Figure 5.3). Indeed, in 90° specimens the δ phase was in line with the loading direction (Figure 4.8c) and hence, the higher number of δ-precipitates in the 90° multi-laser Stripe HT specimens is a potential reason for the lower minimum creep rate observed, compared to the 90° single-laser Stripe HT. However, in the 0° specimens, the δ-precipitates were perpendicular to the loading direction (Figure 4.8i) which has been shown to reduce the ductility of the specimen when compared to a 90° specimens [257], hence the higher δ phase content in the multi-laser scan strategy may have been detrimental for the 0° specimens. For the 45° specimens, the δ phase was oriented halfway between a beneficial 90° and a detrimental 0° (with respect to the loading direction, as seen in Figure 4.8f) and hence the amount of δ phase may have had less of an impact on the minimum creep rate, which may explain why the creep performance of the 45° specimens is similar, regardless of the number of lasers.

Detrimental phases, such as Laves phase, also influenced the creep behaviour of materials. As most detrimental phases get dissolved during heat treatment, this was mainly an issue for the 90° single-laser Meander AB specimens. The presence of Laves phase may have contributed to the lack of ductility observed, as shown by Schirra et al. [226]. This phase was detrimental to creep performance as, in line with other studies, the Laves phase has been found to serve as crack initiation points [258]. Hence, even though not all Laves phases were dissolved in heat treated specimens, the lesser quantity proved beneficial to creep performance. However, a study by Sui et al. [158] demonstrated that by controlling the LPBF parameters and heat treatments, the size, morphology and distribution of Laves phases could be controlled. For example, Sui et al. [158] managed to dissolve the sharp corners and grooves of the Laves phase through heat treatments, causing it to change from a long-striped to a granular shape. They then found that the granular Laves phases were more beneficial to the plastic deformation of LPBF alloy 718 than long-striped Laves phases and that a certain amount of Laves phase was the best combination for strength and ductility of the specimen [159]. Similarly, Xiao et al. [160] found that fine discrete Laves phase improved the tensile properties and elongation of LPBF alloy 718, outperforming wrought alloy 718, whereas long-chain-like Laves phase had a more brittle nature and suboptimal properties.

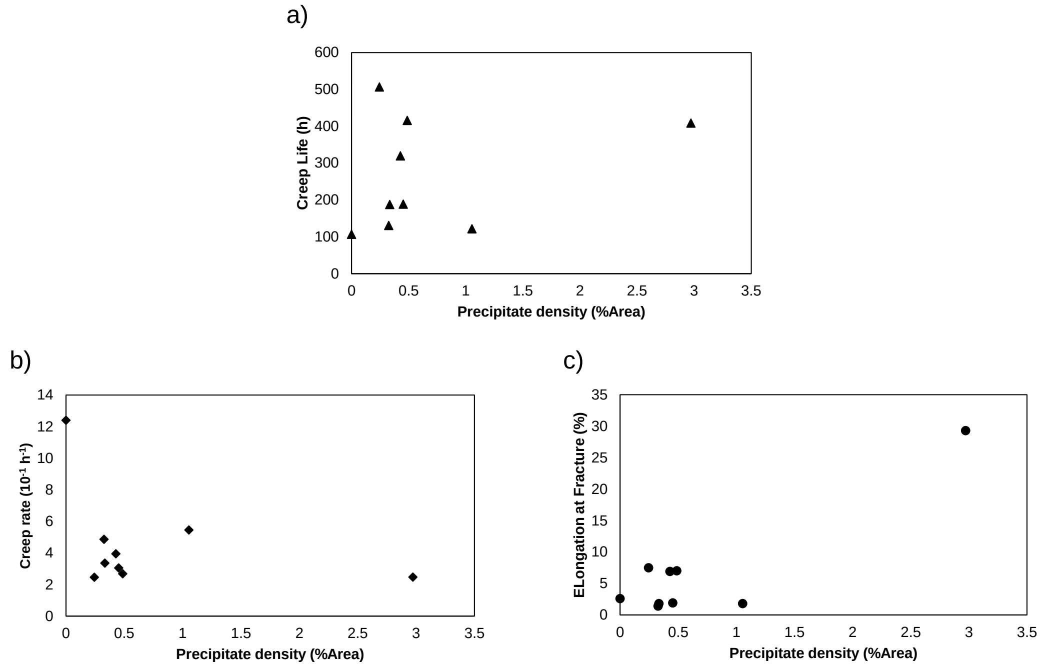

Figure 5.18: Effect of precipitate density on the minimum creep rate, creep life and elongation at fracture for all the specimens tested. a) Creep life VS precipitate density. b) Minimum creep rate VS precipitates density. c) Elongation at fracture VS precipitate density.

Thus, it is evident that precipitates play a key role in the creep performance of materials. The effect of the different types of precipitates were mentioned in the previous paragraphs, however, these precipitates all interact with each other and so have relative effects on the creep behaviour. In the wrought alloy 718, the δ phase precipitates both initiated microvoids and impeded their coalescence while their carbides and Laves phase were detrimental to the creep properties. In the LPBF specimens, all of the precipitates present on the grain boundaries (δ phase, Laves phase and carbides) were detrimental, serving as void initiation points and aiding decohesion. The δ phase seems to have been the most influential precipitate in the creep performance of the LPBF specimens, due to the fact that this phase precipitates at the expense of γ" and that it is the most common precipitate found in these specimens. Laves and carbides are present in much smaller quantities in the LPBF specimen and so, although they have a detrimental effect on creep, they are less influential on the creep performance of LPBF alloy 718 than the δ phase. The effect of these grain boundary precipitates is caused by their morphology which was not optimal and hence were not beneficial to the creep performance. Consequently, there is potential to improve the creep performance of both wrought and LPBF alloy 718 by controlling the amount, size and morphology of precipitates through LPBF process parameters and heat treatment optimisation.

5.3.3 Effect of grain size and morphology

Another main microstructural difference between LPBF alloy 718 and its wrought counterpart is the size and morphology of their grains. It is well established that larger grains are beneficial for creep performance [60], as a low grain boundary density is favourable for high creep resistance. This is because less grain boundaries means less sites for microvoid initiation and propagation. The wrought specimens had significantly smaller grains, by at least 57% (and up to 205%), than any of the LPBF specimens while its creep life and minimum creep rate outperformed the majority of LPBF specimens. However, previous studies on the creep of wrought alloy 718 found that an increasing grain size reduced the total creep rupture time [247]. Similarly, Figure 5.19 shows the effect of grain size on the creep life (Figure 5.19a), the minimum creep rate (Figure 5.19b) and the elongation at fracture (Figure 5.19c) of the different test cases and showed that an increasing grain size was detrimental to both creep life and creep strain rate. This trend may have been affected by the wrought specimens, which had significantly smaller grains than any of the LPBF specimens while its creep life and minimum creep rate outperformed the majority of LPBF specimens.

There are various creep models which can explain the effect of grain size on the minimum creep rate. Garofalo's model states that grain boundaries are both a source and a barrier to dislocation motion [259] and Berger et al. [260] found that a modified Garofalo equation was able to model the creep behaviour of Waspaloy. In the current work, the grain size of LPBF specimens may also obey Garofalo's model, as despite a 57% larger grain size, the 90° single-laser Meander HT specimen had a lower minimum creep rate and longer life than the wrought material, but a lower elongation at fracture (Table 5.2). Therefore, the differences observed may not be due to grain size alone, but also due to the grain morphology.

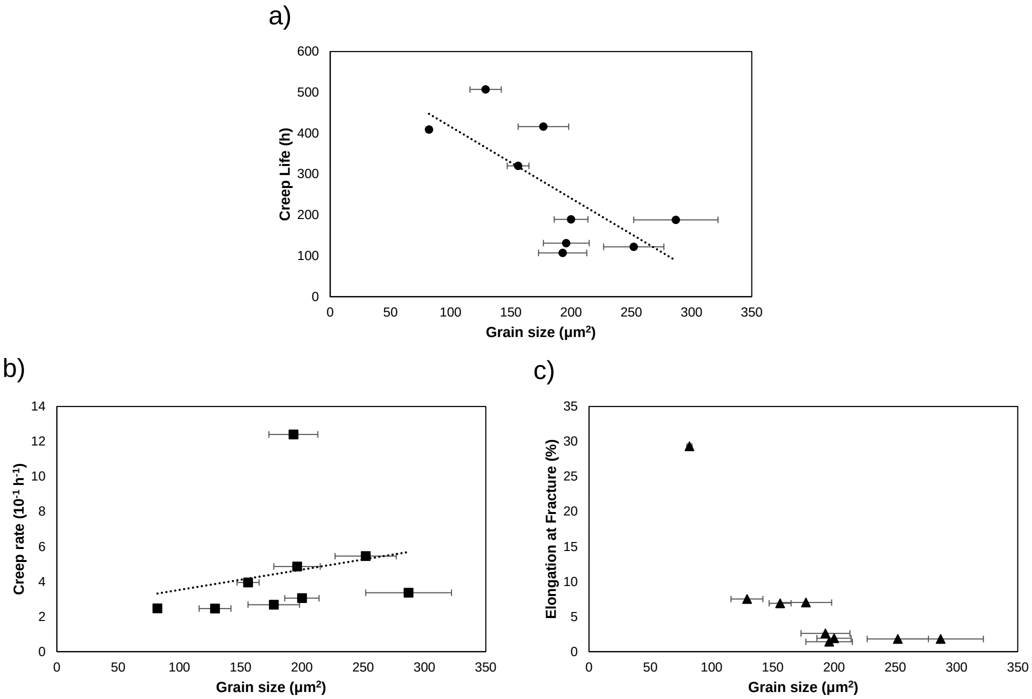

Figure 5.19: Effect of grain size on the minimum creep rate, creep life and elongation at fracture for all the specimens tested. a) Creep life VS grain size. b) Minimum creep rate VS grain size. c) Elongation at fracture VS grain size. The data points corresponding to the wrought material can be identified due to their small (almost absent) error bar.

The morphology and aspect ratio of the grains affect creep. The columnar aspect of LPBF grains affected the creep response of the material. Xu et al. [69] observed that large columnar grain structures make it difficult for the grains to pivot during creep deformation, which means that local stress concentrations were not alleviated, which led to poor creep life and elongation at fracture. Whereas for the wrought specimen, the small equiaxed grains were able to rotate during deformation, which released accumulated local stress concentrations and led to better minimum creep rates and elongations at fracture. Hence, the equiaxed nature of the wrought grains were beneficial to creep performance despite their small size, particularly in terms of elongation at fracture.

The orientation of the columnar grains also affects the ductility of the part, with higher ductility observed when the columnar grains are parallel to the loading direction [261]. This may be one of the reasons that the 90° specimens had a higher elongation at fracture than their 0° and 45° counterparts. Furthermore, having columnar grains parallel to the loading direction is the basis of directionally solidified alloys, which are often used in turbine blades for their high creep resistance [61]. This feature may further explain why the present LPBF specimen (90° Meander single laser HT) outperformed its wrought equivalent.

As well as grain boundaries, twins and twin boundaries can also provide strong obstacles to dislocation motion [69]. Annealing twins are formed by growth accidents during recrystallisation [262] and have been shown to enhance yield strength and creep resistance as their boundaries impede stacking fault motion and dislocations cannot penetrate them [263]. Additionally, well defined and recrystallised grains and the formation of annealing twins have been shown to enhance strengthening mechanisms and improve ductility in quasi-static and dynamic tests of LPBF alloy 718 [253]. Hence, annealing twins can contribute to strengthening as they can impede dislocation motion [264]. The lack of annealing twins in LPBF specimens could explain the better elongation at fracture of wrought material and the low minimum creep rate.

The grain size, morphology and the presence of annealing twins impacted the creep properties of the materials. The crystallographic orientation of the grains also contributed to the differences in creep properties.

5.3.4 Effect of crystallographic orientation

Compared to wrought material, LPBF specimens all had a <001> texture parallel to their build orientation (Figure 4.9). This crystallographic orientation played a role in the creep performance. For example, the 90° single-laser Meander AB specimens had the strongest texture out of the LPBF specimens and the poorest creep properties, whereas its heat treated counterpart had less texture and the best creep properties, compared to all test cases. This suggests that texture influenced the creep performance. In fact, Yu et al. [265] found that the preferred orientations during creep were <001> and <111>. For alloy 718, Bean et al. [222] found that the grain texture alignment with the tensile axis reduced yield strength but enhanced ductility. The texture of the 90° specimens was in line with the tensile axis (loading direction) during creep (Figure 4.9a), which could be the reason for the higher elongation at fracture than other build orientations. This could also explain why 0° single-laser Stripe HT specimen performed more poorly in terms of elongation at fracture. Another study also suggested that a strong crystallographic texture can trigger a texture-related strengthening mechanisms [266].

This section has discussed how the differences in microstructure between wrought and LPBF alloy 718 affected the creep performance. The discussion will now proceed to analysing the effects of heat treatment and LPBF process parameters on the creep properties.

5.4 Effect of heat treatment

Heat treated specimens had a vastly superior performance from their as-built counterpart in terms of creep life and elongation at fracture (see Section 5.2.1). This difference in performance between the AB and HT specimens may be explained by the microstructural anisotropy and the role of grain size and strengthening precipitates γ'' and δ that appear during heat treatment, as described in Section 4.2.1.

The differences in grain size between the AB and HT specimens showed that, for the 90° single-laser Stripe AB an increasing grain size and the ill-defined grain boundaries were detrimental to both creep rupture time and creep strain rate. Despite having better hardness than the heat treated specimens, the ductility was reduced in the AB specimen [132]. Hence, the low ductility of the AB specimens in this thesis explains the low elongation at fracture and brittle failure at the onset of tertiary creep.

Section 5.3 showed that anisotropy and texture can influence the mechanical properties, including creep. Hence, the AB specimens' anisotropic microstructure and crystallographic orientation played a role in the poor creep performance. The strong texture in the <001> direction present in AB specimens and absent in its heat treated counterpart, shows that heat treatment reduces some of the in-built LPBF anisotropy and is therefore beneficial to the subsequent creep performance.

The 90° single-laser Meander HT specimens which had the lowest density of δ-precipitates of all the LPBF specimens. As stated in Section 5.3, δ-precipitates are assumed to be able to impede dislocation motion during creep. It is evident from Figure 5.6g that due to the smaller size of δ-precipitates in the 90° single-laser Stripe HT specimens, these precipitates serve as microvoid initiation and do not impede coalescence. There is potential for improvement in creep performance by modifying the number of δ-precipitates through heat treatment and LPBF parameters. However, despite having significantly more δ-precipitates, wrought specimens still had a lower creep life and a similar minimum creep rate to the 90° single-laser Meander HT specimens. This means that other factors, such as the presence of Laves phase must also affect the creep behaviour.

As well as precipitating strengthening phases, heat treatment is also used to dissolve detrimental phases such as the Laves phase. Since AB was not heat treated, Laves phase was present and may have contributed to the lack of ductility observed, as shown by Schirra et al. [226]. However, their size was much smaller than the Laves phase present in the wrought specimens. This phase was detrimental to the creep performance as discussed in Section 5.3. Thus, even though not all Laves phases were dissolved in heat treated specimens (Figure 4.3), the lesser quantity proved beneficial to creep performance.

Overall, although heat treatment significantly improved creep performance (e.g. creep life increased by a factor of 5), the sub-optimal precipitation and dissolution of secondary phases, and the texture in the build direction show that it is still not optimal. This is clearly illustrated by the scan tracks visible on the fracture surface (Figure 5.9), which show that despite heat treatment, an AM-specific failure still occurred. Future work should focus on improving heat treatments to further enhance creep performance.

5.5 Effect of laser powder bed fusion process parameters

As observed in Section 4.4, the LPBF process affects the microstructure, which in turn affects the creep properties. This section will investigate how the LPBF process parameters affect the creep behaviour and failure mode of the material. First, the effect of scan strategies will be determined, followed by the effect of build orientation and finally the effect of multi-laser scan strategies.

5.5.1 Effect of scan strategies

The visible scan tracks on the 90° specimens (Figure 5.9) were caused by the laser overlapping region which results in small equiaxed grains and more δ-precipitates perpendicular to the loading direction, as discussed in Section 4.4.1. These small equiaxed grains provided more grain boundaries, which may have been detrimental to the creep properties. Indeed, since cavities form on grain boundaries and that laser overlapping areas result in more grain boundaries, this may have been the cause of the faster minimum creep rate and shorter creep life of 90° single-laser Stripe HT specimens as compared to Meander specimens. It was shown in Section 4.4.1 that the overlap region could result in more porosity and defects which could have also affected creep behaviour as these defects could be acting as crack initiation points and favour crack propagation in this region. This can be confirmed from where the number of cracks and the longest cracks were observed in the Stripe specimen (Table 5.6). This difference in crack length reveals that there are more crack-prone areas in the Stripe specimen, i.e. the laser overlapping areas. Hence, this overlapping area is weaker than the centre of the melt-pool and this means that creep damage appeared mostly in these regions and when material separation occurred, this resulted in the scan tracks being visible. Indeed, the laser overlapping areas could have provided an "easier" crack propagation area than the rest of the meltpool and grain boundaries. This means that crack tended to preferentially propagate around the grain boundaries and meltpools until reaching a laser overlap zone (as shown in Figure 5.21a). Hence, when material separation occurred, the crack path followed the scanning strategy employed. A schematic representation of possible crack propagation in the Stripe and Meander specimens is shown in Figure 5.21.

Overall, the reason why the Meander strategy resulted in a better creep rate and creep life than the Stripe strategy can mainly be attributed to the difference in microstructure between these two strategies. The number of laser overlap zones influenced the crack propagation in the material and resulted in visible scan tracks on the fracture surface. However, the mode of failure for both strategies was similar and so it can be concluded that the scan strategy does not influence the failure mode, as opposed to the build orientation, which will be discussed in the following section.

5.5.2 Effect of build orientation

As seen in Section 5.2.3, there was no clear difference in failure surface and mechanism between the 90° single-laser Stripe HT and 90° single-laser Meander HT specimens (except for the different scan tracks), which shows that the failure mechanism is dominated by specimen orientation and by extrapolation, the grain orientation. The 45° and 0° specimens both failed at the onset of tertiary creep, which indicates that they may have failed due to material weakness rather than creep damage. For the 45° single-laser Stripe HT specimens, because of the orientation of the grain boundaries (30-45° from the loading direction), it seems that the failure was due to mixed mode loading I and II, from the tension from the creep test and the shear stress acting perpendicular to the build direction due to the specimen's grain orientation. Indeed, although a fracture on a plane at a 45° angle is usually a sign of ductile failure, the orientation of the grains with respect to the loading direction provided an opportunity for grain boundaries sliding which induced a premature mixed mode fracture. Hovig et al. [267] observed a similar phenomenon with the fracture of a 45° single-laser Stripe HT tensile specimen where the grain boundaries aligned with the slip line and caused decohesion. They also noticed that when grains were parallel to the loading direction, this limited the possibility of a pure Mode I failure [267]. Although it is possible that creep damage is present in a different plane with respect to the loading direction, the implication is that the 45° single-laser Stripe HT specimens did not fail because of creep damage but due to their oriented LPBF microstructure and stress state.

The differences in performance and failure for the different build orientations were also related to the stress state of the specimens. The 45° single-laser Stripe HT specimens failed approximately, at a 45° angle with respect to the loading direction, which is a plane of maximum shear stress and the expected plane for ductile failure. The 90° and 0° specimens failed on a plane perpendicular to the loading direction (Figure 5.12a,e and Figure 5.20a,c), which corresponds to the plane of maximum tensile stress. Furthermore, 90° and 45° single-laser Stripe HT specimens failed on a plane perpendicular to their build direction while the 0° single-laser Stripe HT specimens failed on a plane parallel to their build direction (Figure 5.20). This shows that where a plane of maximum tensile or shear stress is perpendicular to the build direction, this will be the preferred plane of fracture, as is the case for 90° and 45° specimens. In the case of the 0° specimen, where the plane of maximum tensile stress is parallel to the build direction, the specimen will still fail on the plane of maximum tensile stress. This shows that the stress state of the specimen may have an impact on the failure mode of the specimen in interaction with the build orientation of that specimen.

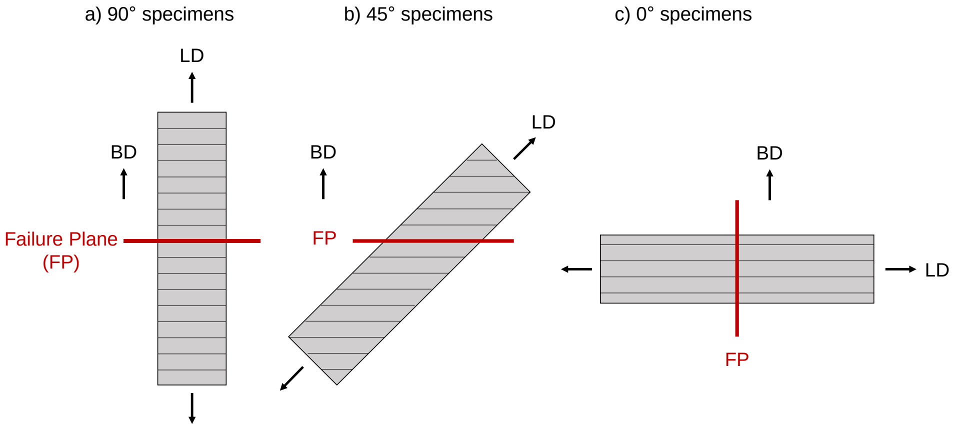

Figure 5.20: Schematic representation of the failure planes of the different test cases, with respect to specimens' layers and build direction and with the loading direction shown. a) 90° specimens. b) 45° specimens. c) 0° specimens. This shows the effect of the stress state on the failure mode of the specimens.

Other than the effects of grain and texture orientation, the orientation of δ-precipitates could also affect the creep rupture life. As seen in Section 4.2.3, the LPBF specimens had elongated grains and δ-precipitates in the build direction. Hence, for the 90° specimens, the precipitates were aligned with the loading direction while they were normal to the loading direction for 0° single-laser Stripe HT specimens. Indeed, the orientation of the δ-precipitates, normal to the loading direction for the 0° single-laser Stripe HT specimens is likely the reason for the reduced creep life, as also shown by Kuo et al. [33], by causing decohesion and fracture (Figure 5.12b,d,f) [257] and may explain the lack of observed tertiary creep. Although δ-precipitates have a relatively small lattice mismatch, there is still a difference and hence, it could be a point of weakness in the specimen that causes an early fast fracture instead of a creep fracture. This mismatch could also be a contributing factor in the grain sliding seen in the 45° single-laser Stripe HT specimen. This shows that the spatial orientation of defects and dendrites are important features in the damage evolution process [124].

Figure 5.21 shows the schematic crack paths for the different specimens due to their grain orientation, precipitate orientation and stress state. The 90° and the 45° specimens failed preferentially between layers while the 0° specimens failed between melt pools. This is probably due to the stresses acting on the specimens, which causes the 90° and the 0° specimen to fail on the plane of maximum tensile stress. It would be beneficial to test more building angles to determine the cause and the point at which specimens fail preferentially on a layer or on a plane of maximum tensile/shear stress.

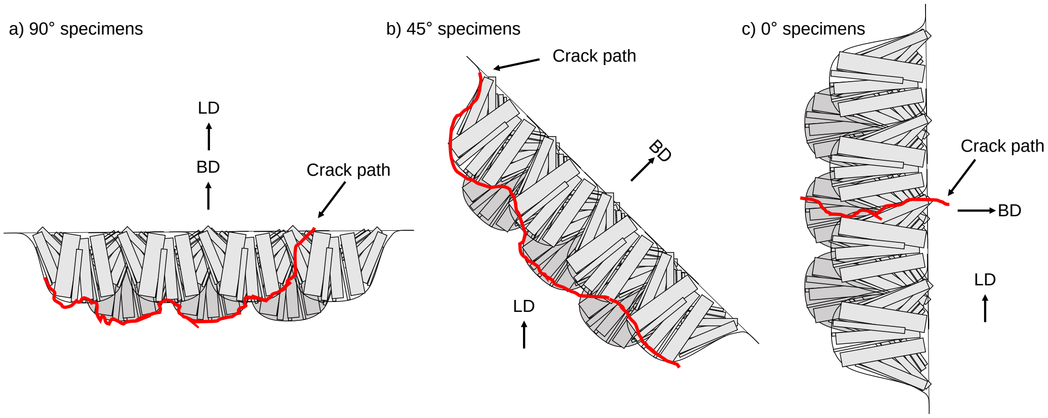

Figure 5.21: Schematic representation of the crack paths for the different build orientations. a) 90° specimens, where intergranular cracking occurred with some cleavage steps. b) 45° single-laser Stripe HT specimens where the intergranular cracking caused grain boundaries decohesion and sliding. and c) 0° single-laser Stripe HT specimens where Quasi-Cleavage occurred.

Overall, the build orientation appears to be the main factor controlling the failure mode of the specimens. This was apparently mainly caused by the grain orientation and morphology, precipitate orientation, and the stress state of the specimen.

5.5.3 Effect of multi-laser scan strategies

The 90° single-laser specimens showed poorer creep properties (Table 5.9), with a shorter creep and higher minimum creep rate than the 90° multi-laser specimens. This can be partly attributed to the larger grain size of the specimens fabricated with the multi-laser scan strategy, the increased number of δ-precipitates, as well as the decreased number of irregular pores, as described in Section 4.2.4.

As stated in Section 5.3, δ-precipitates have been shown to impede dislocation motion and microvoid coalescence [133]. This may explain why the higher amount of δ-precipitates in the 90° single-laser specimens (Table 4.6) resulted in more creep damage and voids than its multi-laser counterpart (Table 5.10). Furthermore, as was mentioned in Section 5.2.3 the orientation of the δ-precipitates can either benefit or detriment the material's mechanical properties. In the case of the 90° specimens, the multi-laser scan strategy resulted in less precipitates, but for the 0° specimens, there was a higher number of precipitates which could have reduced the ductility of the specimens. For the 45° specimens, the orientation of the δ phase has less of an impact on the minimum creep rate and ductility (see Section 5.2.3), which may explain why the creep performance of the 45° specimens is similar, regardless of the number of lasers.

Thus section showed that multi-laser scan strategies and the resulting differences in grain size, texture and precipitate density, do not negatively impact the creep life, the minimum creep rate or the failure mode of LPBF alloy 718.

5.6 Summary of findings

This section on the creep properties of alloy 718 showed that the creep behaviour, particularly the failure mode, of LPBF specimens is different than that of wrought alloy 718. The microstructural differences between LPBF and wrought material – porosity, precipitate density, texture and grain size and morphology – affected the creep behaviour. Some of the key findings were:

- The creep mechanism in the wrought and LPBF alloy 718 is microvoid coalescence.
- The role of δ-precipitates, thought to initiate cracks, was argued to be beneficial in stopping microvoid coalescence and hence, slowing down the minimum creep rate, whereas Laves phases served as crack initiation points.
- The small grain size of the wrought alloy 718 was not detrimental to the creep performance thanks to their equiaxed morphology.
- It was further highlighted that heat treatment is still necessary to obtain adequate creep properties as the anisotropy and lack of strengthening precipitates present in AB specimens result in poorer creep properties.
- The build orientation has a significant effect on the creep properties with specimens built at 90° performing the best in terms of minimum creep rate and creep life, followed by 45° and 0° specimens. This was mainly caused by the orientation of the grains, orientation of the precipitates and due to the stress state of the specimen. This resulted in build orientation controlling the failure mode, elongation at fracture and creep properties of the component.
- The scan strategy affected the crack propagation path which tends to follow “weaker” material areas such as the laser overlap zones. The higher number of laser overlap zones in the Stripe specimens resulted in a lower minimum creep rate and life as well as visible scan tracks on the fracture surface.
- The multi-laser scan strategies did not have any detrimental effects on the creep properties or the failure mode of the material.

Overall, this chapter showed that LPBF specimens have the potential to outperform conventionally built specimens and hence, demonstrates the applicability of LPBF for high temperature applications. Preliminary process-structure-property relationships have been investigated. The following section will further investigate the evolution of the microstructure of the best performing LPBF specimen: 90° single-laser Meander HT. This will provide more information on the differences with wrought material and inform a potential heat treatment to improve creep performance.

6 Microstructural evolution

The 90° single-laser Meander HT specimen had the best minimum creep rate and creep life from all the specimens tested and the highest elongation at fracture for the LPBF specimens. This specimen was chosen to be observed during creep and thermal exposure to understand the evolution of its microstructure, compared to that of wrought alloy 718. The secondary and tertiary creep breakpoints - where the interrupted creep tests and the thermal exposure tests will be stopped - were identified from the creep curves presented previously for the 90° single-laser Meander HT and wrought alloy 718 and are presented in Table 6.1. Although each specimen was different, the low scatter of creep results for 90° single-laser Meander HT specimen (Figure 5.3), gives confidence that the different specimens evolve similarly during creep testing.

Table 6.1: Breakpoints for the Interrupted creep tests.

Specimen	Mid-secondary	Mid-tertiary	Fracture	Thermal exposure test
90° single-laser Meander HT	121 h	430 h	507 h	Yes
Wrought	123 h	331 h	409 h	No

The evolution of the microstructure during creep for wrought and LPBF alloy 718 will be presented followed by the evolution of the LPBF alloy during thermal exposure. Then, the evolution of the microstructural features will be discussed and finally, an ideal creep microstructure as well as a potential heat treatment to improve creep performance will be recommended.

6.1 Microstructure during creep

The texture evolution of the different types of specimens is shown in Figure 6.1 and will be referred to in the following sub-sections. Table 6.2 quantifies and summarises the material descriptors, such as density, grain size and precipitate density present at different stages of time for the specimens and will be referred to in the following sub-sections as well.

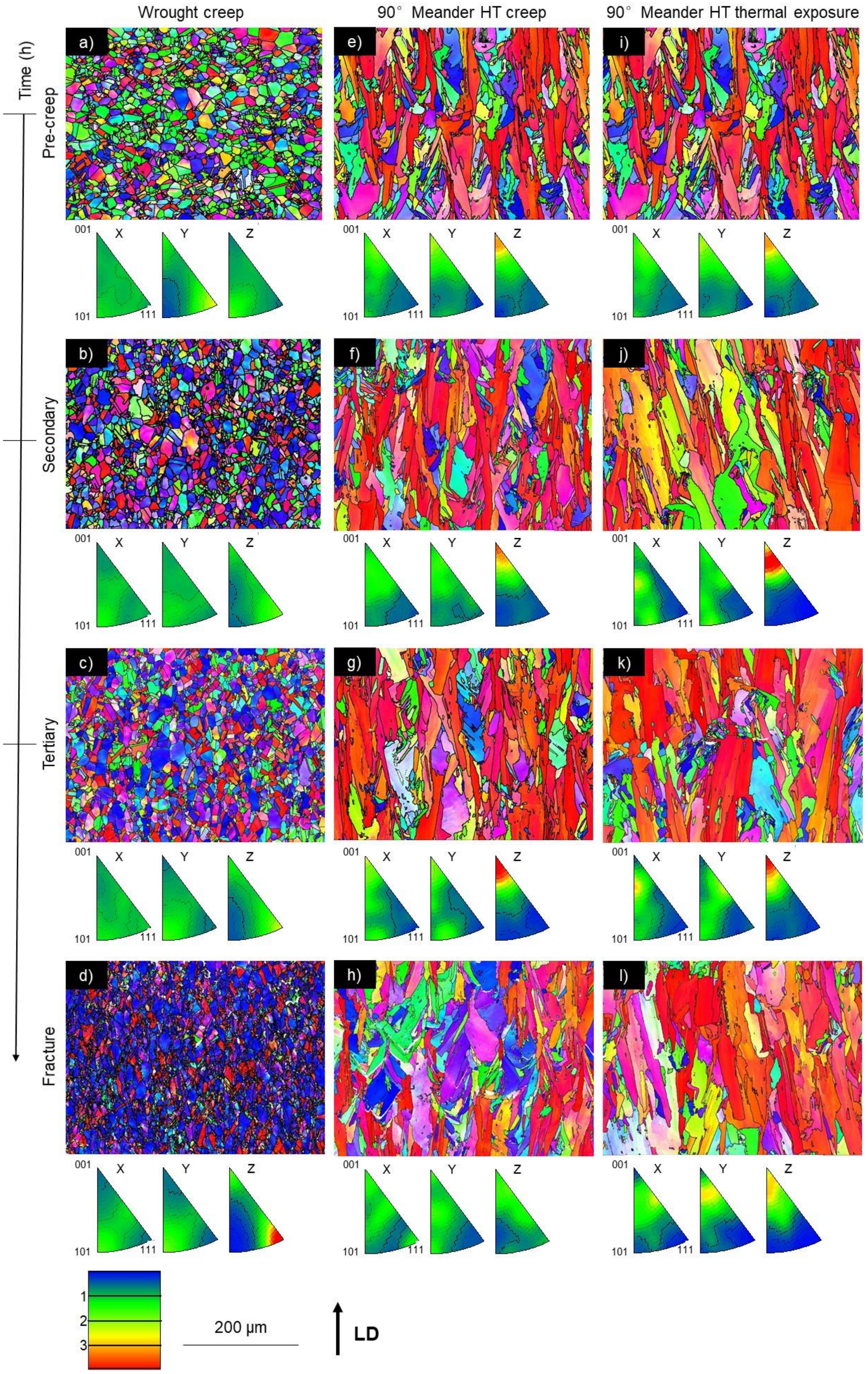
Wrought creep
90° Meander HT creep
90° Meander HT thermal exposure
Time (h)
Pre-creep
Secondary
Tertiary
Fracture
a)
b)
c)
d)
e)
f)
g)
h)
i)
j)
k)
l)
001
101
111
X
Y
Z
1
2
3
200 µm
LD

Figure 6.1: EBSD maps and Inverse pole figures showing the evolution of texture with time for the different specimens. a)-d) Wrought alloy 718 during creep showing an increase in texture along the loading direction as creep progresses. e)-h) 90° single-laser Meander HT during creep where the texture increases in the loading direction (Z) as creep progresses before disappearing at fracture. i)-l) 90° single-laser Meander HT during thermal exposure showing an increase then decrease in texture, highlighting the instability of the microstructure. The Z direction corresponds to the loading direction for all specimens and to the build direction as well for the LPBF specimens.

Table 6.2: Quantification of the evolution of damage during for wrought and 90° single-laser Meander HT specimen during creep and for the thermally exposed 90° single-laser Meander HT specimen. The average densities have an error of ±0.15 %Area.

Specimen	**Average density** *(%Area)*	**Average precipitate (δ, Laves and carbides) density** *(%Area)*	**Grain size** *(μm²)*	**Aspect ratio**
Wrought *Pre-creep*	100	2.97	82 ± 2	2.53 ± 0.03
Wrought *Mid-Secondary*	99.9	2.79	103 ± 3	2.26 ± 0.03
Wrought *Mid-Tertiary*	99.9	3.22	70 ± 2	2.49 ± 0.03
Wrought *Fracture*	99.8	4.12	48 ± 1	2.26 ± 0.02
90° single-laser Meander HT *Pre-creep*	99.9	0.22	129 ± 13	3.08 ± 0.08
90° single-laser Meander HT *Mid-Secondary*	95.0	0.48	179 ± 16	3.36 ± 0.07
90° single-laser Meander HT *Mid-Tertiary*	88.5	0.59	222 ± 24	3.86 ± 0.11
90° single-laser Meander HT *Fracture*	86.0	0.61	346 ± 35	3.58 ± 0.10
90° single-laser Meander HT *thermal exposure of 0h*	99.9	0.22	129 ± 13	3.08 ± 0.08
90° single-laser Meander HT *thermal exposure of 121h*	99.88	0.82	360 ± 63	4.19 ± 0.16
90° single-laser Meander HT *thermal exposure of 430h*	99.83	1.27	246 ± 45	3.36 ± 0.08
90° single-laser Meander HT *thermal exposure of 505h*	98.37	1.47	362 ± 61	3.98 ± 0.12

6.1.1 Wrought alloy 718

Figure 6.2 shows the microstructure evolution for the wrought alloy 718 during creep. Before creep, the grains were small and equiaxed (Figure 6.2a) and as creep time increases, the grains of wrought alloy 718 have a 41.5 % reduction in area (Table 6.2 and Figure 6.1d) and their morphology seems to change from equiaxed to elongated in the loading direction (Figure 6.1c), although the average aspect ratio of is relatively unchanging, with a 12% difference between the pre-creep and fracture microstructures (Table 6.2). The elongation of the grains in the loading direction is expected as the material deforms under creep and necks. This elongation is also accompanied by an increase in <111> texture in the loading direction increased as creep progressed with a maximum texture at the time of fracture (Figure 6.1a-d).

The wrought alloy 718 had δ-precipitates visible on the grain boundaries as thin needle-shaped precipitates throughout the creep test (Figure 6.2b,d,f,h). However, this chapter will focus on the carbides present in the material as large globular precipitates on the grain boundaries (Figure 6.2b,d,f). These were identified (Table 4.2) from their Nb-rich content compared to the matrix [268] and their preferred precipitation on the grain boundaries [269], which are typical for alloy 718 [270]. As time progresses during the creep test, the number of carbides seems to increase (Figure 6.2c,e), which is consistent with the data presented in Table 6.2 that shows an augmentation of precipitate density as creep progresses. The voids initiated by the carbides are also responsible for the decreasing density of the material, as described in Table 6.2. These carbides crack probably serve as fracture initiation points (Figure 6.2d,f). The small microvoids initiated by δ-precipitates on the grain boundaries (Figure 6.2h) also contribute to the accumulated creep damage and decreasing density. These observations will be used as reference and comparison with the 90° single-laser Meander HT specimen.

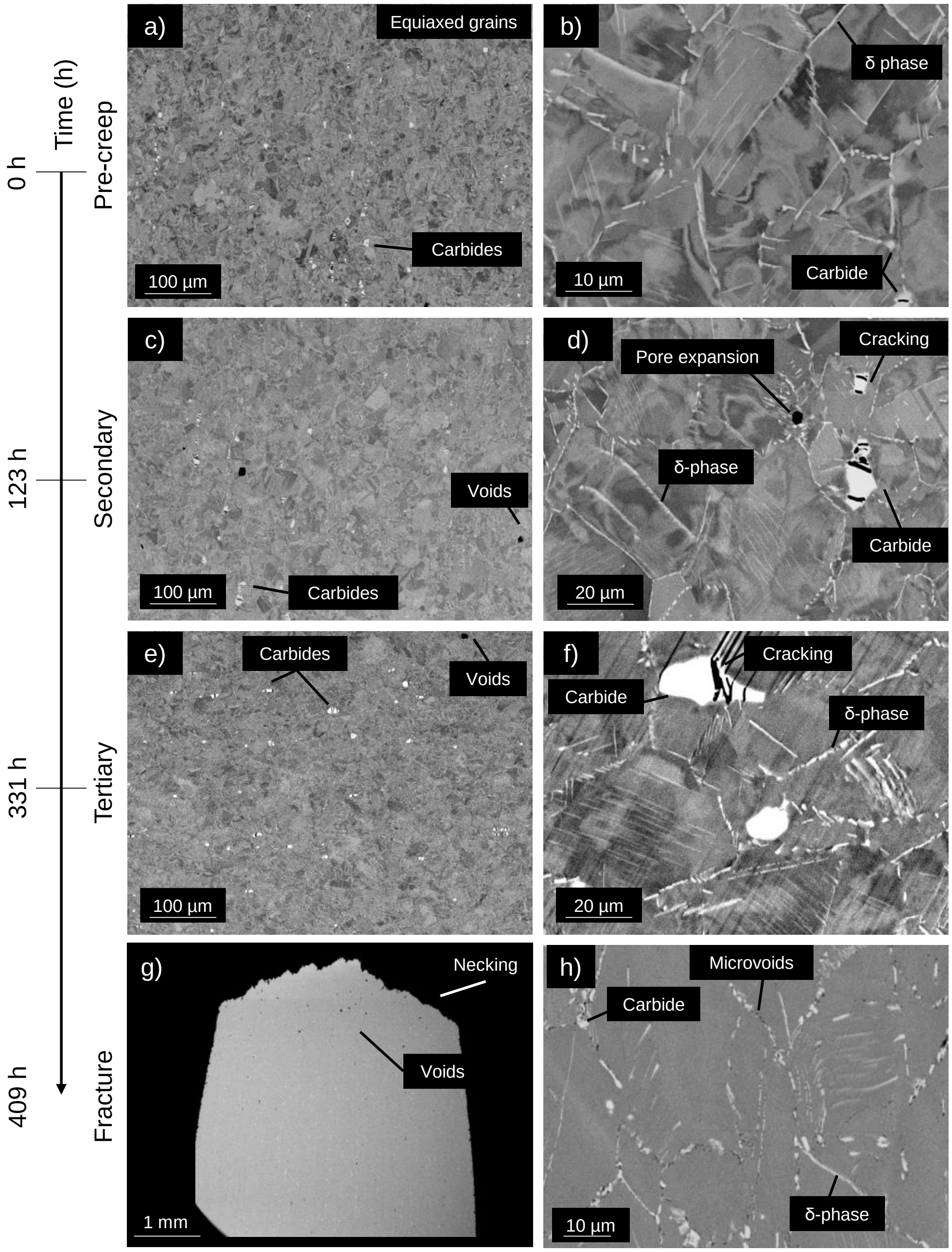
Time (h)
0 h
123 h
331 h
409 h
Pre-creep
Secondary
Tertiary
Fracture
a)
Equiaxed grains
Carbides
100 µm
b)
δ phase
Carbide
10 µm
c)
Voids
Carbides
100 µm
d)
Pore expansion
Cracking
δ-phase
Carbide
20 µm
e)
Carbides
Voids
100 µm
f)
Cracking
Carbide
δ-phase
20 µm
g)
Necking
Voids
1 mm
h)
Microvoids
Carbide
δ-phase
10 µm

Figure 6.2: SEM images of the microstructural evolution of wrought alloy 718 during creep. a),b) Pre-creep microstructure. c),d) Microstructure in the secondary region, after 123h of creep. e),f) Microstructure in the tertiary region, after 331h of creep test. g),h) Microstructure after fracture. This shows the increase in the number of carbides and carbide cracking.

6.1.2 90° single-laser Meander HT specimen

Figure 6.3 shows the microstructure of the 90° Meander HT specimen at the different stages during testing. There were pores and defects present both in the grains and at grain boundaries, as shown in the SEM images (Figure 6.3a). As the creep test progresses, microvoids initiate (Figure 6.3d) and coalesce (Figure 6.3f) until cracks form (Figure 6.3g,h). As shown in Figure 6.3, most of the microvoids are smaller than 2 µm in diameter. As previously described in Section 5, most microvoids initiate on the grain boundaries near δ-precipitates, which have previously been shown to cause crack initiation [69, 247]. As well as δ-precipitates, the 90° Meander HT specimen also had small and globular carbides (Figure 6.3b).

The grain size of the 90° Meander HT specimen increased by a factor of 2.7 during creep (Table 6.2 and Figure 6.1e,h). The grains also became more elongated during creep due to the loading, which could have increased their area (Figure 6.3a,e), although this is not clearly visible in SEM and EBSD images. The aspect ratio has a 16% increase from pre-creep to fracture, which confirms the elongation of the grains during creep (Table 6.2). The texture of the 90° Meander HT specimen also varied during creep, as shown in Figure 6.1e-h. Before creep, there is a <001> texture parallel to the build direction, thereafter, the texture increases as creep progresses, in a similar fashion to wrought alloy 718, but intriguingly, the texture disappears after fracture (Figure 6.1h). This phenomenon will be explained in Section 6.2.2.

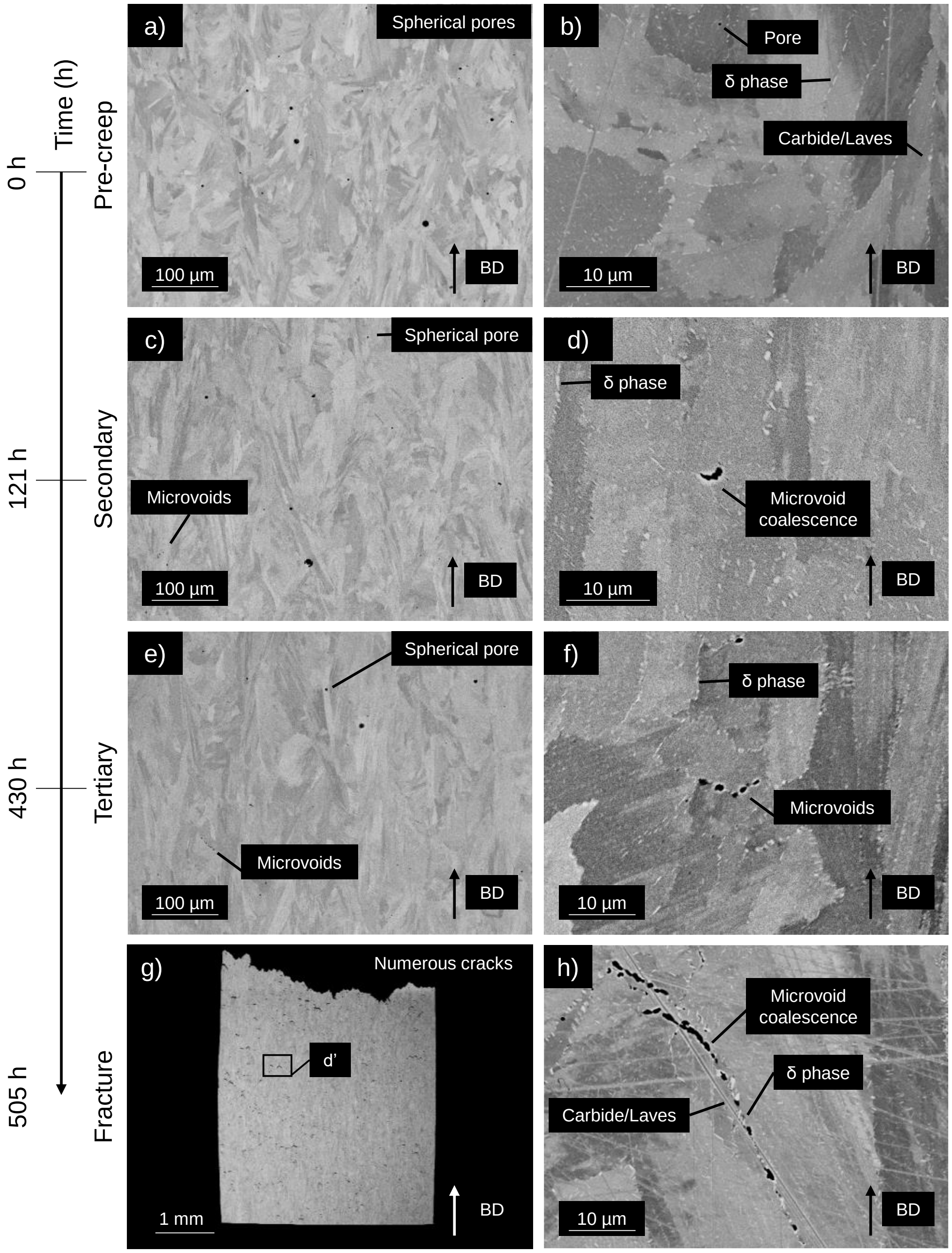
Time (h)
0 h
121 h
430 h
505 h
Pre-creep
Secondary
Tertiary
Fracture
a)
Spherical pores
100 µm
BD
b)
Pore
δ phase
Carbide/Laves
10 µm
BD
c)
Spherical pore
Microvoids
100 µm
BD
d)
δ phase
Microvoid coalescence
10 µm
BD
e)
Spherical pore
Microvoids
100 µm
BD
f)
δ phase
Microvoids
10 µm
BD
g)
Numerous cracks
d'
1 mm
BD
h)
Microvoid coalescence
δ phase
Carbide/Laves
10 µm
BD

Figure 6.3: SEM images of the microstructural evolution of 90° Meander HT specimen during creep. a),b) Pre-creep microstructure. c),d) Microstructure in the secondary region, after 121h of creep. e),f) Microstructure in the tertiary region, after 430h of creep test. g),h) Microstructure after fracture (505h). This shows microvoid initiation at δ-phase on the grain boundaries and their coalescence as creep progresses.

The changes in microstructure observed in the 90° Meander HT specimens are due to the load and temperature applied during the creep test. To differentiate the effects of load and temperature, the microstructure evolution of the thermally loaded specimens without mechanical load was observed.

6.1.3 90° single-laser Meander HT specimen during thermal exposure

Figure 6.4 shows the microstructure evolution of the thermally exposed 90° Meander HT specimens (for the pre-creep microstructure, the reader is directed to Figure 6.3a,b). After 121h, the microstructure of the thermally exposed specimen seems similar to that of pre-creep (Figure 6.4a), with elongated columnar grains parallel to the build direction and δ-precipitates, carbides and Laves phase on the grain boundaries (Figure 6.4b). The main difference observed is the more important presence of large pores (Figure 6.4c). These pores seem to thermally expand with time, becoming larger (Figure 6.4f,g). This is particularly noticeable in Figure 6.4i. This increase in pore size is the main reason for the decreasing density observed in Table 6.2. Both spherical and irregular pores expanded.

From Table 6.2, the grain size of the thermally exposed specimen increased by a factor of 2.8 from pre-exposure to 505h, which is similar to the creep tested specimen. However, the grains first observe a strong increase after 121h before the grain size lowers at 430h and increases again before 505h. This unsteady variation clearly shows the instability of the microstructure and will be discussed later. The morphology of the grains remains elongated and columnar but also seemed to be more defined (Figure 6.4a,g). The aspect ratio of the grains increases by 29% with time (Table 6.2), confirming the columnar aspect of the grains after 505h. The number of precipitates increases with time during the thermal exposure, by a factor of 6.7 (Table 6.2), although this is not clearly visible in the SEM images (Figure 6.4b,e,h).

The thermally exposed specimen had a <001> texture parallel to the build direction before the test and the texture increased until 121h. Then, it decreased after 430h before becoming weak at the time of fracture (Figure 6.1i-l). The variation in crystallographic orientation of the thermally exposed specimen indicates that the heat treatment used for the LPBF specimens is not adequate and results in an unstable microstructure.

The results show the differences in microstructural behaviour during creep of the 90° Meander HT specimens and wrought alloy 718. These highlighted the unstable nature of the LPBF microstructure, further indicating the need for an appropriate heat treatment to improve creep performance. The separate effects of the creep loading conditions and thermal exposure of the LPBF alloy 718 were also observed and will be discussed in the next section.

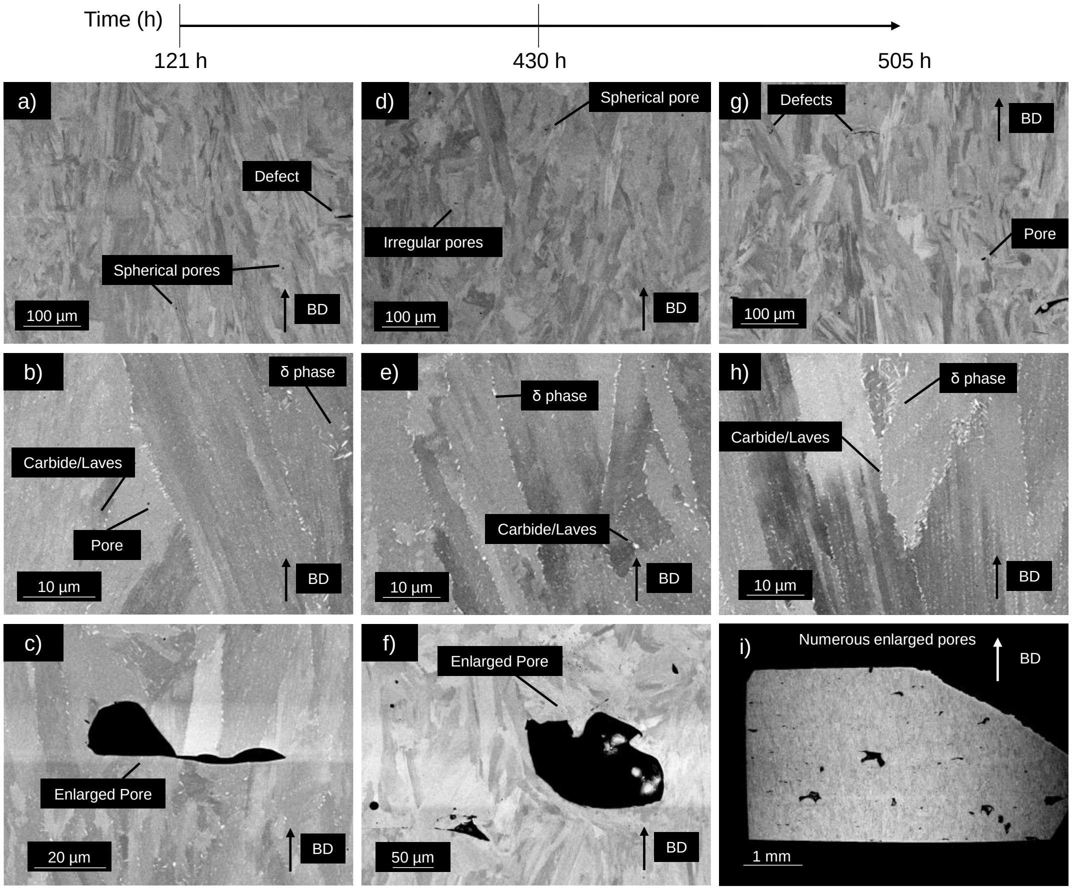
Time (h)
121 h
430 h
505 h
a)
Defect
Spherical pores
100 µm
BD
d)
Spherical pore
Irregular pores
100 µm
BD
g)
Defects
BD
Pore
100 µm
b)
δ phase
Carbide/Laves
Pore
10 µm
BD
e)
δ phase
Carbide/Laves
10 µm
BD
h)
δ phase
Carbide/Laves
10 µm
BD
c)
Enlarged Pore
20 µm
BD
f)
Enlarged Pore
50 µm
BD
i)
Numerous enlarged pores
BD
1 mm

Figure 6.4: SEM images of the microstructural evolution of 90° Meander HT specimen during creep. a)-c) Microstructure after 121h of thermal exposure. d)-f) Microstructure after 430h of thermal exposure. g)-i) Microstructure after 505h of thermal exposure. This shows the expansion of pores in the specimen and the increase in grain size.

6.2 Evolution of microstructural features

This discussion will analyse the changes in porosity, texture, precipitates, grain size and morphology.

6.2.1 Evolution of porosity

Figure 6.5 shows the evolution in part density with time for the creep tested and thermally exposed 90° Meander HT specimens. The density steadily decreases in the creep tested 90° Meander HT specimen, at a faster rate than the thermally exposed equivalent. The reduction in density in the thermally exposed LPBF specimen corresponds to the pore expansion. For the creep tested 90° Meander HT specimen, the slightly larger reduction in density corresponds to creep damage, in the form of microvoids and cracks, which ultimately gave rise to fracture. Pore expansion likely occurs as well in the creep tested specimen but to a lesser degree. The expansion of pores here is due to the thermal exposure and to the opening of the pores caused by the creep load.

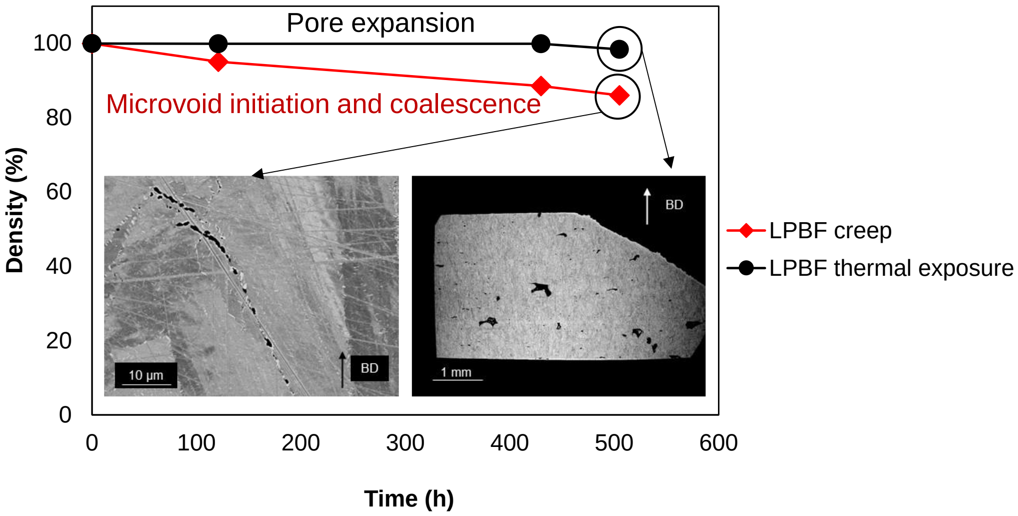

Figure 6.5: Evolution of part density for the 90° Meander HT specimens during creep testing and thermal exposure. This figure was based on the data available in Table 6.2. This shows the increase in porosity in both specimens due to pore enlargement (thermal exposure) and creep damage (creep tested specimen).

Section 5.3.1 highlighted the negative impact of porosity on minimum creep rate and life and another interrupted creep study also found that the main crack initiation points were pores [271], more specifically irregular pores [250]. Therefore, it is evident that porosity in LPBF specimens must be reduced to improve the creep performance.

6.2.2 Evolution of texture

Figure 6.1a-d showed the evolution of texture in the wrought alloy 718 during creep. It was observed that the texture increases throughout the creep life, being the strongest at the time of fracture. This increase in texture was also observed by another study before and after creep for forged alloy 718 [69]. That study proposes that the increase in texture may be due to grain rotation which occurs due to stress accommodation in the build material [69]. It is proposed that the strain of the equiaxed grains in the loading direction (which can be qualitatively observed from Figure 6.1a,a’’’) is the reason for the increase in texture.

Similarly to wrought alloy 718, the 90° Meander HT creep tested specimens had an increasing texture with life as an effect of the creep load (Figure 6.1e-g). This is different from what was observed in another study where there was almost no texture difference between before and after creep in the 90° Meander HT specimen [69].

In comparison, the thermally exposed only specimens had an increase of texture until at least 121h before the texture started to reduce and almost disappear around the time of fracture (Figure 6.1i-l). Hence, it can be inferred that the point at which the texture starts to reduce happens between 121h and 430h when exposed at 650°C. Since the texture has not fully disappeared by 505h (Figure 6.1l), it can be assumed that more time is needed at 650°C to fully remove the texture. Huang et al. [54] also found that a minimum amount of time is required at a given solution temperature to result in similar microstructures and mechanical properties than longer hold times and inversely, that for a fixed amount of time, a higher solution temperature would result in similar microstructures.

Compared to the creep tested 90° Meander HT specimen, there is more texture at the time of fracture in the thermally exposed specimen (Figure 6.1h,l), whereas it was expected that the strongest texture would be present at the time of fracture in the creep tested LPBF specimen. This was caused by a prolonged exposure at 650°C for 35h in the furnace after the creep test, which was conducted to confirm the effects of thermal exposure on the texture of this alloy. This explains the lack of texture due to the creep load at fracture and shows that, in this work, for the 90° Meander HT specimen, texture disappears at some point between 505h and 540h when thermally exposed at 650°C.

Additionally, the variation in texture observed in the thermally exposed LPBF specimen shows the instability of the LPBF microstructure and hence, demonstrates that the conventional heat treatment used is not suitable for the microstructure of the 90° Meander HT specimen. This is to be expected since the heat treatment used was design for wrought alloy 718, which has a different condition of supply microstructure when compared to the 90° Meander HT specimen.

From Figure 6.1, the <001> texture observed in the creep tested specimen was parallel to the build direction which also coincided with the loading direction. In the thermally exposed specimens, the texture was also mostly present in the build direction, even after 430 h. Hence, both the build direction and the loading direction, influence the direction of texture in LPBF material. The build direction dictates the original orientation of texture, while the loading direction influences the orientation of texture which develops during creep. The texture in the build direction is explained by the preferential grain growth in <001> which is promoted by the elongated columnar structure of the LPBF grains. This in turn is caused by the dominant direction of heat flux on cooling which drives solidification and crystallization [272]. The loading direction impacts where the texture develops during creep due to elongating the grains, as shown by the increasing aspect ratio in the LPBF specimen (Table 6.2). However, because the loading direction and build direction of the LPBF specimens are coincident in this work, it is difficult to evaluate how the different effects of the build and loading directions on the texture evolution would interact with other build orientations and would be worthy of future work. It is hypothesised that when the texture of the specimen is off-axis with the load, the texture would be reduced through creep.

Section 5.3.4 presented the potentially beneficial and detrimental effects of texture. Due to the possibilities to build at different build orientations, it would be recommended to either remove texture or to engineer it such that it is optimised for creep life within in the blank geometry of service components.

6.2.3 Evolution of grain size and morphology

Figure 6.6 shows the evolution of grain size with time for the wrought and 90° Meander HT specimens. The grain size of wrought alloy 718 is observed to decrease with creep time (Figure 6.6). This is probably caused by dynamic recrystallisation, which is the nucleation and growth of new grains during deformation processes, as opposed to heat treatments. In dynamic recrystallisation, new grains form with strain by consuming atoms from pre-existing grains. Rettberg et al. [273] observed localised dynamic recrystallisation during creep of two nickel-based superalloys, primarily near voids and clusters of carbides. The small variation in grain size (Figure 6.6) is an indicator of the stability of the wrought microstructure as well as its very low standard variation (which cannot be observed in the error bars of Figure 6.6 due to its small size).

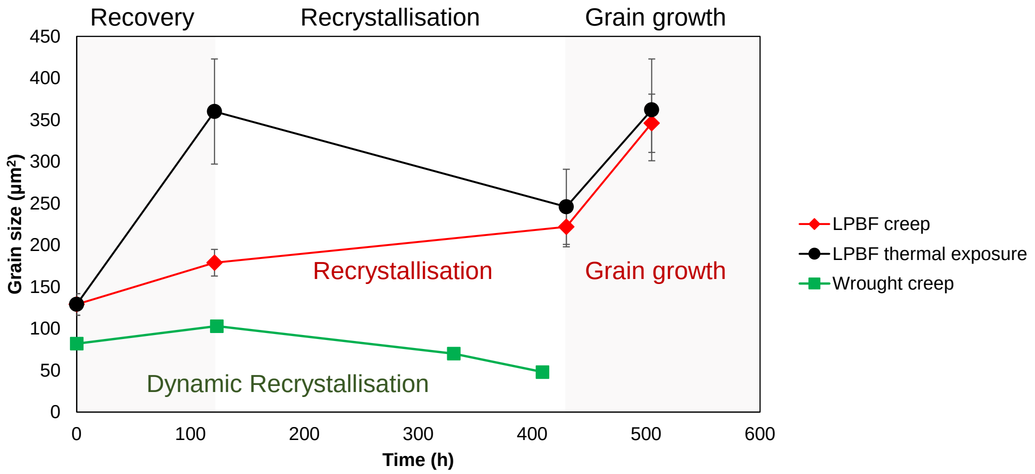

Figure 6.6: Evolution of the grain size for the wrought alloy 718 during creep and the 90° Meander HT specimens during creep and thermal exposure. This figure was based off the data available in Table 6.2. This shows the dynamic recrystallisation of grains in the wrought alloy 718 during creep and the instability of the grains and their growth in both LPBF specimens.

In contrast, the evolution of the 90° Meander HT specimen grain size shows the instability of the LPBF microstructure and the lack of appropriate heat treatment. For the LPBF specimen, the thermal exposure resulted in a large increase in grain size, probably caused by recovery, before recrystallisation and grain growth occurred (Figure 6.6). Thermodynamic effects [274] and residual stresses [275] are thought to drive grain growth and recrystallisation at high temperatures. The texture may have driven the rapid grain growth until 121h (Figure 6.1k) and when the texture started to reduce (Figure 6.1k), recrystallisation may have started to take place. The creep tested LPBF specimen's grain growth occurred at a slower rate due to the load effect during creep which may have caused it to grow in a more controlled manner (similar to wrought alloy 718).

A study found that a longer solution time led to an increase in grain size in forged alloy 718, which was attributed to the dissolution of δ-phase [276]. Here, the final grain size (354 ± 48 μm on average) may be the stabilised size for LPBF alloy 718 since it was achieved after similar periods of time, regardless of loads applied, by both 90° Meander HT specimens during creep or thermal exposure only.

Grain size is not the only determinant factor for the superior creep strength of LPBF alloy 718 [277]. One of these other factors is grain morphology and aspect ratio. The grain morphology of the different specimens also changes during creep. The thermally exposed 90° Meander HT specimens retained and emphasised their columnar morphology, as was observed from the 29% increase in their aspect ratio (Table 6.2). A study found that the columnar grain structure was retained and that there was no increase in grain size during solution treating at 980°C [278], which was the solution temperature used in the present work. The creep tested LPBF specimen also retained a mainly columnar morphology as creep progressed, achieving its highest aspect ratio at the time of mid-tertiary creep (Table 6.2 and Figure 6.1k). Although the aspect ratio was slightly less at the time of fracture (Table 6.2) and the grains looked slightly less columnar (Figure 6.1), compared to the time in tertiary. This could be explained by the prolonged thermal exposure after fracture which started to make the grains more equiaxed, reducing their directionality and hence, reducing the texture. This indicates that an appropriate heat treatment could make the grains more equiaxed and reduce texture in LPBF specimens.

From Section 5.3.3, it was found that large grains are beneficial to creep, as well as either equiaxed grains or columnar grains in line with the loading direction. However, microstructural design in this case must be undertaken with the upmost regard for the loading case in question which may not be uniaxial as reported here.

6.2.4 Evolution of precipitates

Figure 6.7 shows the evolution of precipitate density with time for the different specimens. This shows that in all specimens the number of precipitates particles increased with time, but to different degrees. The loss of mechanical performance can be attributed to the coarsening or decrease of strengthening precipitates [244]. More specifically, creep life is said to be attributed to the type, amount and distribution of γ’, γ’’ and δ phase [206]. The precipitates observed here include δ phase, carbides and Laves. The γ’’ were too small to be observed and are not included in the average precipitate density but should be present, nonetheless. This discussion will focus on the evolution of carbides, δ phase and γ’’.

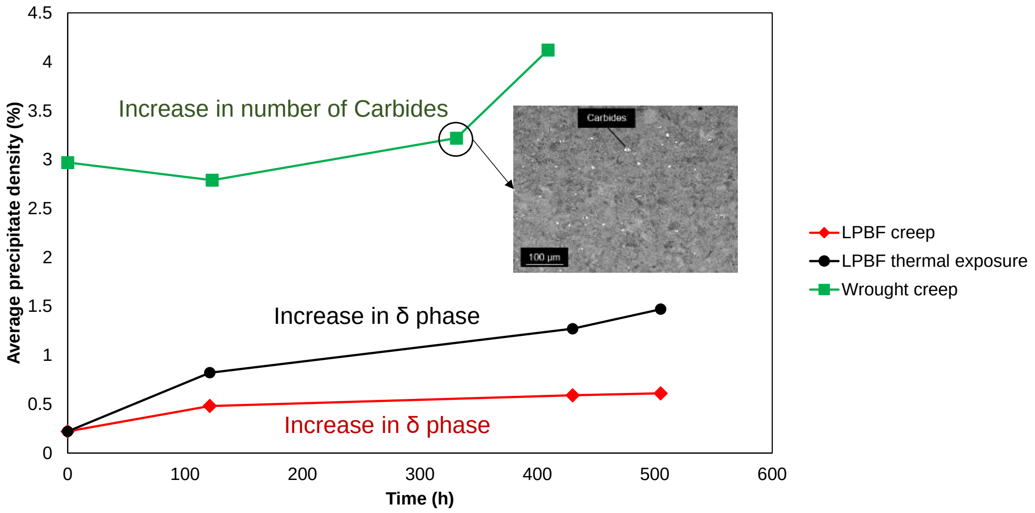

Figure 6.7: Evolution of the average precipitate density in the wrought alloy 718 during creep and the 90° Meander HT specimens during creep and thermal exposure. This figure was based off the data obtained from SEM image analysis and is available in Table 6.2. This shows the increase in precipitate density in the wrought alloy, caused by an increasing number of carbides. It also shows the smaller increase in precipitate density between the creep tested and thermally exposed 90° Meander HT specimens.

The precipitates in the wrought material increased by 39% between the beginning of the creep test and the time of fracture (Figure 6.7). This is probably due to the formation and growth of carbides. $M_{23}C_6$ carbides form at lower temperatures on the grain boundaries and have a block or granular appearance, as reported elsewhere [60]. A study which performed interrupted creep tests at 950°C and 210 MPa on a nickel-based superalloy found that carbides parallel to the loading direction cracked at regular intervals after 100h [271]. Cracked carbides were also visible in the present work after 123h (Figure 6.2d). This cracking can serve as crack initiation and propagation points during creep and accelerate damage in tertiary creep [271]. This may explain why, despite having a similar minimum creep rate to the LPBF alloy 718, the wrought material had a shorter creep life, mainly caused by having a rapid and short tertiary creep (Figure 6.1a,d).

Despite these negative effects, other studies have found that small, coherent, closely packed needle-shaped $M_{23}C_6$ on the grain boundaries can improve rupture life [271]. These types of carbides could be present in the 90° Meander HT specimen (Figure 6.3b) as they were not as large and globular as the ones found in their wrought equivalent. These smaller carbides may contribute to pinning the grain boundaries, acting as a strengthener [279].

Some studies observed that heat treatments (ageing at 650°C for 168h [270], solution treating at 980°C for 1h [280]) and HIP treatments [135] did not affect the formation or growth of carbides, probably because the temperatures were too low. Indeed, high homogenization temperatures were shown to result in larger carbide size [281], which is said to be stable up to 1200°C [282]. Earlier literature demonstrated that after 200h at 1200°C, the carbide size did not change, indicating an equilibrium had been reached [283]. Therefore, it is unlikely that the increase in precipitate density in the wrought alloy 718 was from an increase in carbide size. Elemental composition and solidification rates control carbide morphology. For example, by increasing the cooling rates, more discrete, blocky-type MC carbides are formed [284]. Slower cooling rates were shown to result in larger carbides [135], which could explain the size of the carbides in the wrought specimen since it was furnace cooled at the different breakpoints during the interrupted creep testing. The increase in precipitate density in the wrought material is more likely to be an increase in carbide number. A qualitative inspection of Figure 6.2a,c,e clearly shows the increase in the number of large globular precipitates, identified as carbides, which correlates to the increase in precipitates observed in Figure 6.7. In the 90° Meander HT specimens, although some carbides were present, most of the precipitates on the grain boundaries appeared to be δ phase.

Both creep and thermally exposed 90° Meander HT specimens had small needle shaped δ phase on the grain boundaries with the occasional small blocky/globular carbides (Figure 6.3 and Figure 6.4). The formation temperature of the δ phase is between 650°C and 980°C [285] and precipitation strengthening of the γ'/γ" phases occurs around 600°C to 750°C [266]. The heat treatment employed in this work (980°C/1h/Gas quench, 720°C/8h/Furnace cooling to 620°C/8h/Gas quench) means that both δ phase and γ'/γ" would have been precipitated, although γ" precipitates are not visible here. The creep deformation rate is controlled by the rate of γ" coarsening [183] and creep damage increases as the amount of γ" decreases [69]. In forged material, γ" size and shape remain stable during creep whereas in LPBF material, γ" size increases and transforms into δ phase [69, 286]. Hence, the amount of γ" precipitates decreases when the amount of δ-precipitates increases, as they both require Nb [206]. Thus, in theory, the fewer the number of δ-precipitates, the higher the number of γ" precipitates which results in better creep performance. Indeed, certain studies found that without δ-precipitates, creep life is doubled and elongation at fracture quintupled [70]. Another study found that when the amount of δ phase was reduced to a minimum, larger grain sizes were obtained, which are beneficial to creep performance [276]. Conversely, too little δ phase resulted in crack initiation, just enough δ phase could stabilise the microstructure, improve strength and prevent grain growth, while too much δ phase decreased the strength and plasticity of the material [69, 287].

From Figure 6.7, the thermally exposed specimens exhibited a higher increase in precipitate density than their creep tested counterpart. This may be another sign of the instability of the microstructure. Xu et al. [69] found that there was an unstable transformation of γ" to δ phase during creep of LPBF alloy 718 potentially driven by residual stresses. In a study on alloy 718, δ-precipitates were mainly stable but slightly coarsened when exposed for 10,000 h at 650°C and γ" showed very little coarsening [282]. This shows that with the adequate temperature and hold time, the precipitates can be stabilised.

The difference in precipitate density between the thermally exposed and creep tested specimen (Figure 6.7) also indicates that the load applied during creep affects the precipitate density. A study observed that the total amount of δ phase increased with strain [288], which affects the precipitation kinetics [289]. This was observed previously for wrought alloy 718 [290]. However, despite the overall increase in δ-precipitates, the number of needle shaped δ-precipitates decreased while blocky ones increased [288]. In this thesis, neither the increase in precipitate density nor morphology were observed in the 90° Meander HT creep specimens (Figure 6.3 and Figure 6.4). This may be because δ-precipitates form on grain boundaries and that in the 90° Meander HT specimens, grain size increases, which results in less grain boundaries and hence, less opportunities for δ-phase to nucleate. Therefore, the lower increase in precipitate density (corresponding to δ phase, carbides or Laves) observed in Figure 6.7 for the 90° Meander HT creep tested material could be one of the reasons for the longer creep life observed in the 90° Meander HT specimen compared to the wrought specimen as this would allow more precipitation of γ'' and less sites for crack initiation.

Overall, from Section 5.3.2 and the above discussion, the relationship between the δ phase and the strengthening γ'' phase, which is the most important for creep performance, was discussed along with the dissolution of the detrimental phases. Small discrete carbides also seem to be useful for improving creep performance while large globular ones need to be avoided. This can be achieved though heat treatment.

6.3 Strategies for improved creep performance

From the previous observations and discussion, it is possible to understand the microstructural evolution during creep of both wrought and LPBF alloy 718, which is schematically represented in Figure 6.8, drawn to relative scale. In the wrought alloy 718, the grains become smaller and more elongated during creep and rotate to accommodate stresses, while the grains in the LPBF material become larger, more elongated and columnar and do not rotate. The texture increases in the loading direction during creep for both specimens, but the LPBF specimen starts with a much stronger texture. In the wrought alloy 718, the number of carbides increases, and carbide cracking occurs perpendicular to the loading direction. The carbides, the carbide cracks and the δ-precipitates serve as microvoid initiation points which result in accelerated creep damage in the tertiary creep region, compared to LPBF alloy 718, which explains their shorter creep life. In the LPBF material, microvoids initiate at the δ phase and small carbides on the grain boundaries and pores expand. The microvoids then coalesce and form cracks on the grain boundaries perpendicular to the loading direction, leading to fracture.

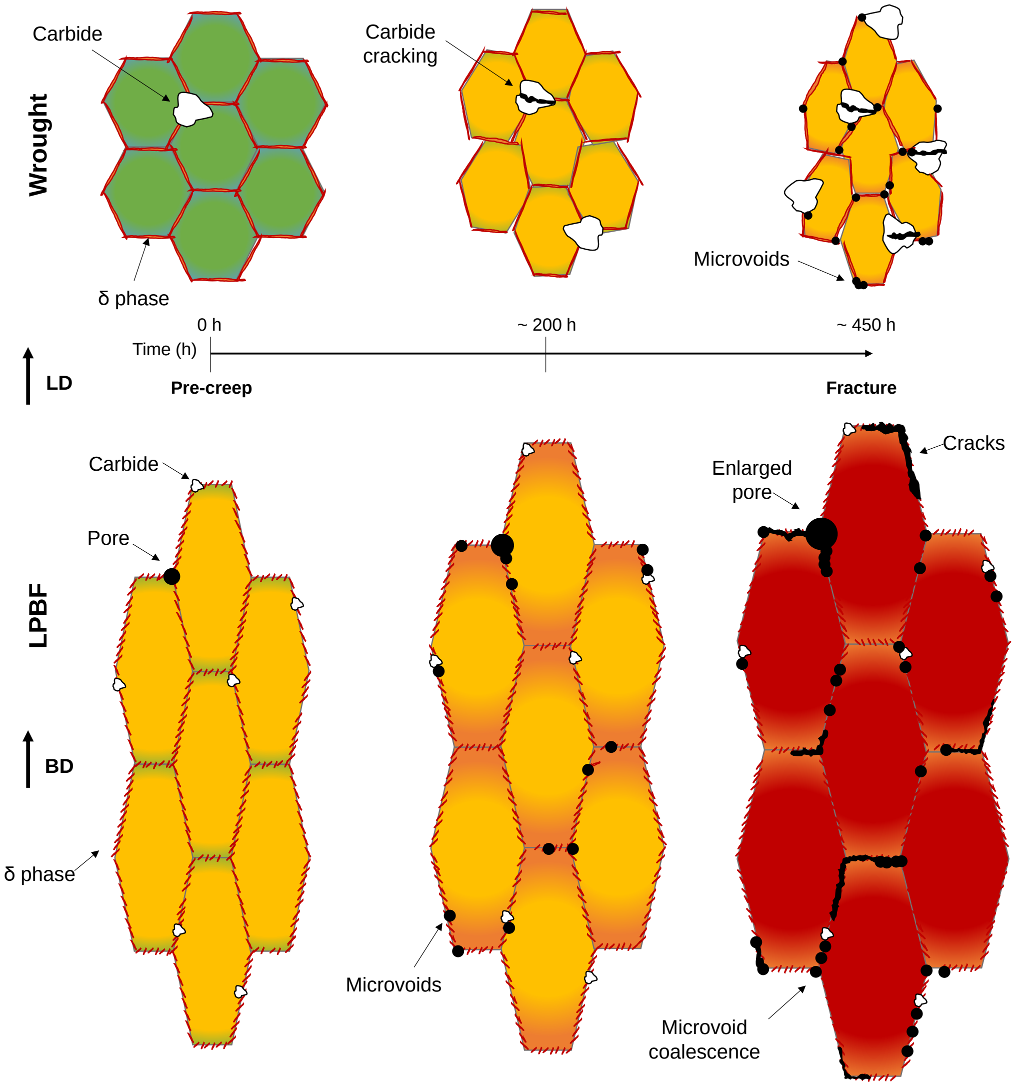
Carbide
Carbide cracking
Wrought
Microvoids
δ phase
0 h
~ 200 h
~ 450 h
Time (h)
LD
Pre-creep
Fracture
Cracks
Enlarged pore
Carbide
Pore
LPBF
BD
δ phase
Microvoids
Microvoid coalescence

Figure 6.8: Schematic representation of the microstructural evolution of wrought and 90° Meander HT specimen during creep. The microstructures are drawn in relative scales, highlighting the bigger grain size of 90° Meander HT specimen, compared to its wrought equivalent. The colour in the figure symbolises the texture in the specimen, with warmer colours representing stronger textures. The time stamps given are approximately ± 50h.

The Standard Specification for Additive Manufacturing Nickel Alloy (UNS N07718) with Powder Bed Fusion [136] provides recommendations for thermal processing of LPBF nickel-based superalloys. For heat treatments, the UNS N07718 points the practitioners to the AMS2774 standard for heat treatment of wrought nickel alloy and cobalt alloy parts [137]. This standard provides different heat treatment options based on the geometry and type of nickel-based superalloy. However, these heat treatments were designed for conventionally manufactured materials and not for LPBF ones, which have a very different starting microstructure than their wrought, cast or forged equivalents. Therefore, the current heat treatments in use are potentially suboptimal, resulting in an unstable microstructure with a lack of strengthening phase precipitation, partial dissolution of detrimental phases and semi-recrystallized grains, as was observed throughout this work. This clearly indicates the need to develop LPBF specific heat treatments, to obtain superior mechanical properties. From Section 5 and the above discussion, useful features for high creep performance were identified as:

- Low porosity
- Large equiaxed grains
- No texture
- Precipitation of γ” and small discrete carbides on the grain boundaries
- Dissolution of Laves and δ phases

To reduce the porosity, HIP treatments could be used as they have been shown to cause densification [291] and close cracks [148]. HIP has also been shown to reduce anisotropy [123] and improve fatigue resistance [292] and other mechanical properties [146]. However, a reduction in porosity can also be achieved through LPBF process parameter optimisation. For example, the scan strategy [233] and the volumetric energy density [248] have been shown to affect porosity. By controlling porosity through the process instead of using thermal treatments, this saves researchers time and resources and further increases the appeal of using LPBF as a suitable manufacturing method for critical engineering components.

While recent studies have found that the distribution, size and morphology of Laves phase can be advantageous to mechanical properties [158-160], the general consensus is still that Laves phase is detrimental to creep properties and should be dissolved. A study found that a solution treatment at 1100°C for 7h of LPBF alloy 718 resulted in the dissolution of Laves and δ phase [152]. Controlling the amount of δ phase is key to tailoring the mechanical properties of LPBF materials [157]. However, dissolving the δ phase and Laves phase is best for maximizing strength as it allows more γ” precipitation [293]. The δ phase has a solvus temperature of 1010°C and can precipitate between 650°C and 980°C [285] preferentially at grain boundaries, and less preferentially near MC carbides [294]. The amount of δ phase is proportional to the ageing time [70] and the size of the δ-precipitates increases consistently with decreasing cooling rate [294].

The high number of large globular carbides were identified as one of the key factors for why wrought alloy 718 had a shorter creep life than some LPBF specimens, as they accelerate damage in tertiary creep. However, closely packed needle-shaped $M_{23}C_6$ on the grain boundaries were shown to improve rupture life [284] and intergranular fracture was achieved with a near continuous carbide layer on grain boundaries [270]. By increasing the cooling rates, more discrete, blocky-type MC carbides can be formed [284] and could be beneficial to LPBF, by increasing their elongation at fracture.

Although some studies argue that phase precipitation is not necessary to strengthen AM materials if dislocation cells are retained [295], promoting strengthening precipitates, such as γ” should increase creep strength. Indeed, higher compressive creep strength after solution HT at 1000°C attributed to higher precipitation of γ” since there is less Nb depletion from δ and Laves phases [157]. Precipitation strengthening of the γ’/γ” phases occurs around 600 to 750°C [266]. In LPBF alloy

718, γ'' precipitation occurred during double ageing typically performed at 720°C and 620°C [291, 296]. Although double ageing is the norm for γ'' precipitation, the temperatures at which these are typically performed result in δ phase precipitation as well, which should be avoided for creep performance. This is because in solution and ageing treatment, Nb segregation only partially dissolves and this results in δ-precipitates at the grain boundaries and in inter-dendritic regions [206]. Therefore, double ageing may not be recommended for creep performance.

While the columnar grain morphology and strong texture parallel to the loading direction present in LPBF materials strengthen the specimen, this is dependent on the build direction. Indeed, other build orientations (e.g. 0° and 45°) have performed less well in terms of minimum creep rate and life, which is partly due to their grain orientation and texture at an angle from the loading direction. To eliminate texture, a more equiaxed microstructure is key [47]. Therefore, eliminating the columnar aspect of the grains would allow parts manufactured at different build orientations to have similar mechanical performances. Tucho et al. [152] found that a solution treatment at 1100°C for 7h of LPBF alloy 718 resulted in grain coarsening which suggests the completion of recrystallisation.

Taking the above requirements into account, a recrystallisation heat treatment developed by Kouraytem et al. [297], consisting of a 625°C/h ramp up rate, a 1 h dwell time at 1250°C, and a 625°C/h ramp down rate, should produce the desired features. Indeed, the heat treatment resulted in a 3-fold increase in grain size, a change in grain morphology from columnar to equiaxed, a reduction in the <001> texture, the dissolution of Laves phase and of the majority of the δ phase (only 1 in 30 grains had small intergranular δ-precipitates), as well as the precipitation of nano γ' and γ'' precipitates [297]. This heat treatment appears to satisfy the requirements to obtain the suggested microstructure required for improved creep performance, however, this was not verified here. If larger grains are required, the dwell time could be increased. For an increase in γ'' precipitation the ramp down rate could be reduced to 300°C/h maximum, or a single aging step at 620°C could be undertaken, which should not trigger the precipitation of δ phase.

Finally, although heat treatments can contribute to microstructure engineering [298], research should also focus on obtaining the desired microstructure through the LPBF process alone. This would greatly improve the appeal of AM technologies and allow more microstructural engineering design freedoms. Furthermore, there is also a need to creep test LPBF specimens at different stresses and temperatures in order to obtain a more comprehensive understanding of the creep behaviour of LPBF specimens and to inform models which will then be able to extrapolate the creep properties over other ranges of stresses and temperatures.

6.4 Summary of findings

The aim of this chapter was to explore the evolution of LPBF alloy 718 during creep to provide suggestion on how to improve creep performance. The interrupted creep tests were designed and wrought and LPBF alloy 718 were analysed at breakpoints in secondary and tertiary creep regions. Thermal exposure of some LPBF specimens at the same breakpoints were also performed to understand the effects of load and temperature on the creep performance. Some of the key findings are summarised below:

- The increase in grain size and precipitate density in the LPBF alloy 718 is an indication of unstable microstructure caused by an unsuitable heat treatment designed for wrought alloy 718.
- The load applied during creep causes grains to elongate in wrought and LPBF alloy 718, resulting in an increase in crystallographic texture with time. Thermal exposure at 650°C for over 540h was shown to eliminate texture in LPBF alloy 718.
- Dynamic recrystallisation is responsible for the decrease in grain size in wrought alloy 718 during creep. The large variation in grain size for the thermally exposed specimen is a clear indicator of the inadequacy of the heat treatment employed. A stabilised grain size of 354 ± 48 μm was obtained after around 505h to 540h at 650°C, regardless of load applied.
- An increase in the number of carbides in the wrought alloy 718 during creep caused damage to accelerate in tertiary creep which results in a reduced creep life compared to LPBF alloy 718, despite having similar minimum creep rates.
- The increase in precipitate density (δ phase, carbides or Laves phase) during creep is detrimental to the creep performance as it does not allow as much γ'' precipitation, which is the main strengthening mechanism for creep, and provides void initiation sites.
- During thermal exposure, pores expand and result in an increase in porosity. However, this amount is still less than the porosity caused by microvoids and damage during creep.
- The recommended microstructure for creep performance includes large equiaxed grains, elimination of texture, dissolution of Laves and δ phase and the precipitation of small carbides and γ'' precipitates. It is surmised that this microstructure could be obtained by following Kouraytem et al.'s [297] recrystallisation heat treatment (625°C/h ramp up rate, a 1 h dwell time at 1250°C, and a 625°C/h ramp down rate) and improve creep properties. This was not demonstrated in this work.

Conclusion

To conclude, this thesis investigated the effects of HT, build orientation, scanning strategy and multi-lasers on the creep performance of LPBF alloy 718 and provided an insight into microstructural evolution during creep. The results showed that the best creep performance was obtained for 90° specimens with a Meander scanning strategy which obtained a creep life 24% longer than the wrought alloy 718 specimen, with a similar minimum creep rate. The use of multi-laser LPBF were also shown to result in positive effects as build time can be significantly reduced whilst having no detrimental effect on the mechanical performance. The evolution of the microstructure during creep also showed the instability of LPBF due to inadequate heat treatments and a new heat treatment was proposed. The key findings can be summarised as:

- The creep response of the different LPBF specimens was anisotropic, clearly affected by the build direction and scan strategy employed.
- Heat treatment reduces anisotropy and improves creep life by partial recrystallisation of the grains, dissolution of Laves phase, precipitation of δ phase and by reducing the crystallographic texture.
- The density, size and orientation of δ-precipitates are key for creep performance as they impede void coalescence and hence slow the minimum creep rate.
- The multi-laser scan strategy has the potential to control Nb-rich precipitates as the segregation of elements is controlled by the cooling rate during the melting of layers.
- An increase in the number of carbides in the wrought alloy 718 during creep caused damage to accelerate in tertiary creep which results in a reduced creep life compared to LPBF alloy 718, despite having similar minimum creep rates.
- LPBF components all had similar porosity (0.04% difference).
- The build orientation and stress state of the specimens are responsible for the different failure modes, which all had ductile indicators with some cleavage steps. The various test cases presented different degrees of creep damage (microvoid coalescence).
- The scanning strategy is responsible for the quantity of laser overlapping regions which have poorer creep resistance due to the presence of small equiaxed grains and a higher density of δ-precipitates. Perpendicular to the loading direction, these particles can increase the brittleness of the specimen and result in a lower creep resistance.
- The multi-laser scan strategy was found to affect grain size. Larger grain sizes were seen in the 90° and 0° multi-laser Stripe Specimens (due to higher heat input and slower cooling rate during LPBF) and smaller grains in the 45° multi-laser stripe specimen (due to the higher cooling rate caused by supports structures acting as a heat sink during the build).
- The increase in grain size and precipitate density in the 90° single-laser Meander HT specimen during creep and thermal exposure indicates an unstable microstructure caused by an unsuitable heat treatment designed for wrought alloy 718.

- By controlling the LPBF process parameters (such as laser shape, type and power), the size, distribution and amount of γ'' and δ phase can be controlled. This work showed that heat treatment of wrought alloy 718 resulted in beneficial δ phase and hence, controlling these key precipitates can lead to an enhanced creep performance.

The recommended microstructure for creep performance includes large equiaxed grains, elimination of texture, dissolution of Laves and δ phase and the precipitation of small carbides and γ'' precipitates. It is surmised that this microstructure could be obtained by following Kouraytem et al.'s [297] recrystallisation heat treatment (625 °C/h ramp up rate, a 1 h dwell time at 1250 °C, and a 625 °C/h ramp down rate) and improve creep properties. This was not proven in this work.

Further research is recommended to focus on the following topics:

- Testing additional build orientations and their effect on the failure mode and texture evolution.
- Modelling creep using different models, including stress-based models which have the potential to take into account the residual stresses present in LPBF materials.
- Modelling creep using a continuum damage model (e.g. Kachanov model) to take into account creep micro-mechanisms in LPBF. A model similar to Murchú et al. [179] could also be used to include the effect of precipitate evolution during creep in the material.
- Undertaking more creep testing with different parameters (load, temperature) to allow a better understanding of the creep behaviour of LPBF alloys and to inform creep models to permit the extrapolation of data.
- Attempting Kouraytem et al.'s [297] heat treatment to determine whether or not the desired microstructure and creep performance can be obtained.
- Developing more process-structure-property relationships by testing different build orientations, scan strategies and laser types to engineer the microstructure to obtain desired properties.

Overall, this thesis showed that LPBF components could perform better than wrought and conventional equivalents by developing an appropriate heat treatment and provides an insight into process-structure-property relationships for the creep properties of LPBF alloy 718. The results shown are promising, despite future work being required, and this work demonstrates the applicability of using LPBF for critical high temperature applications.

Acknowledgments

This work has been supported by the Engineering and Physical Sciences Research Council [EP/S513854/1]. Thanks are given to Shane Maskill for conducting the creep testing, Alex Jackson Crisp for manufacturing the samples from AM built blanks, Nigel Neate and the nmRC for imaging some of the SEM pictures, Alistair Speidel for assistance with the MountainsMaps and ImageJ software, James Murray for performing Alicona scans. Thank you to Gabriele Gaspard for helping on the interrupted creep tests research and Divish Rengasamy for writing the code used in obtaining the porosity data from micrographs.

References

1. Chua, C.K., *3D printing and additive manufacturing : principles and applications (the 5th edition of Rapid prototyping : principles and applications)*. 5th ed. / Chee Kai Chua, Kah Fai Leong. ed. Three dimensional printing and additive manufacturing, ed. K.F. Leong. 2017, Singapore: Singapore : World Scientific.
2. ASTM International, *Standard Terminology for Additive Manufacturing Technologies,*. 2015, ASTM International,: West Conshohocken, PA.
3. Huang, S.H., P. Liu, A. Mokasdar, and L. Hou, *Additive manufacturing and its societal impact: a literature review.* The International Journal of Advanced Manufacturing Technology, 2013. **67**(5): p. 1191-1203.
4. Smith, R.J., G.J. Lewi, and D.H. Yates, *Development and application of nickel alloys in aerospace engineering.* Aircraft Engineering and Aerospace Technology, 2001. **73**(2): p. 138-147.
5. Boyer, R.R., J.D. Cotton, M. Mohaghegh, and R.E. Schafrik, *Materials considerations for aerospace applications.* MRS Bulletin, 2015. **40**(12): p. 1055-1066.
6. Pollock, T.M. and S. Tin, *Nickel-Based Superalloys for Advanced Turbine Engines: Chemistry, Microstructure and Properties.* Journal of Propulsion and Power, 2006. **22**(2): p. 361-374.
7. Davis, J.R., *ASM Specialty Handbook: Nickel, Cobalt, and Their Alloys*. 2000, Materials Park, OH: ASM International.
8. ROLLS ROYCE, *More Efficient Turbines*, in *NICKEL*. 2007, The Nickel Institute: Toronto, Canada. p. 7.
9. Choudhury, I.A. and M.A. El-Baradie, *Machinability of nickel-base super alloys: a general review.* Journal of Materials Processing Technology, 1998. **77**(1–3): p. 278-284.
10. Ezugwu, E.O., J. Bonney, and Y. Yamane, *An overview of the machinability of aeroengine alloys.* Journal of Materials Processing Technology, 2003. **134**(2): p. 233-253.
11. Catchpole-Smith, S., N. Aboulkhair, L. Parry, C. Tuck, I.A. Ashcroft, and A. Clare, *Fractal scan strategies for selective laser melting of 'unweldable' nickel superalloys.* Additive Manufacturing, 2017. **15**: p. 113-122.
12. Liu, A., C.K. Chua, and K.F. Leong, *Properties of test coupons fabricated by selective laser melting*, in *Key Engineering Materials*. 2010. p. 780-784.
13. Yap, C.Y., C.K. Chua, Z.L. Dong, Z.H. Liu, and D.Q. Zhang. *State-of-the-art review on selective laser melting of non-ferrous metals*. in *Proceedings of the International Conference on Progress in Additive Manufacturing*. 2014.
14. Lewandowski, J.J. and M. Seifi, *Metal Additive Manufacturing: A Review of Mechanical Properties*, in *Annual Review of Materials Research*. 2016. p. 151-186.
15. Sing, S.L., J. An, W.Y. Yeong, and F.E. Wiria, *Laser and electron-beam powder-bed additive manufacturing of metallic implants: A review on processes, materials and designs.* Journal of Orthopaedic Research, 2016. **34**(3): p. 369-385.
16. Gorsse, S., C. Hutchinson, M. Gouné, and R. Banerjee, *Additive manufacturing of metals: a brief review of the characteristic microstructures and properties of steels, Ti-6Al-4V and high-entropy alloys.* Science and Technology of Advanced Materials, 2017. **18**(1): p. 584-610.

17. Grasso, M. and B.M. Colosimo, *Process defects and in situ monitoring methods in metal powder bed fusion: A review.* Measurement Science and Technology, 2017. **28**(4).

18. Zhang, D., S. Sun, D. Qiu, M.A. Gibson, M.S. Dargusch, M. Brandt, M. Qian, and M. Easton, *Metal Alloys for Fusion-Based Additive Manufacturing.* Advanced Engineering Materials, 2018. **20**(5).

19. Ezugwu, E.O., Z.M. Wang, and A.R. Machado, *The machinability of nickel-based alloys: a review.* Journal of Materials Processing Technology, 1999. **86**(1): p. 1-16.

20. Bernstein, J.A., A. Bravato, B. Ealy, M. Ricklick, J.S. Kapat, I. Mingareev, M. Richardson, W. Meiners, and I. Kelbassa, *Fabrication and Analysis of Porous Superalloys for Turbine Components Using Laser Additive Manufacturing*, in *49th AIAA/ASME/SAE/ASEE Joint Propulsion Conference*. 2013, American Institute of Aeronautics and Astronautics: San Jose, California.

21. Guo, N. and M.C. Leu, *Additive manufacturing: technology, applications and research needs.* Frontiers of Mechanical Engineering, 2013. **8**(3): p. 215-243.

22. Yadroitsev, I., I. Shishkovsky, P. Bertrand, and I. Smurov, *Manufacturing of fine-structured 3D porous filter elements by selective laser melting.* Applied Surface Science, 2009. **255**(10): p. 5523-5527.

23. Li, L., C. Diver, J. Atkinson, R. Giedl-Wagner, and H.J. Helml, *Sequential Laser and EDM Micro-drilling for Next Generation Fuel Injection Nozzle Manufacture.* CIRP Annals, 2006. **55**(1): p. 179-182.

24. Gisario, A., M. Kazarian, F. Martina, and M. Mehrpouya, *Metal additive manufacturing in the commercial aviation industry: A review.* Journal of Manufacturing Systems, 2019. **53**: p. 124-149.

25. Yong, C.K., G.J. Gibbons, C.C. Wong, and G. West, *A critical review of the material characteristics of additive manufactured in718 for high-temperature application.* Metals, 2020. **10**(12): p. 1-22.

26. Balbright. *NASA Tests More Printed Rocket Engine Parts*. 2014 [cited 2018 22/01]; Available from: http://www.rapidreadytech.com/2014/11/nasa-tests-more-printed-rocket-engine-parts/.

27. Newman, J. *MTU Aero Engines Parts Built Using Selective Laser Melting*. 2014 [cited 2018 22/01]; Available from: http://www.rapidreadytech.com/2014/03/mtu-aero-engines-parts-built-using-selective-laser-melting/.

28. Wits, W.W., S.J. Weitkamp, and J. van Es, *Metal Additive Manufacturing of a High-pressure Micro-pump.* Procedia CIRP, 2013. **7**: p. 252-257.

29. Newman, J. *GE Aviation Continues to Push Ahead with Additive Manufacturing*. 2015 [cited 2018 22/01]; Available from: http://www.rapidreadytech.com/2015/05/ge-aviation-continues-to-push-ahead-with-additive-manufacturing/.

30. Kellner, T. *The FAA Cleared The First 3D Printed Part To Fly In A Commercial Jet Engine From GE*. 2015 [cited 2018 22/01]; Available from: http://www.gereports.com/post/116402870270/the-faa-cleared-the-first-3d-printed-part-to-fly/.

31. Adair, D., M. Kirka, and D. Ryan. *Additive manufacture of prototype turbine blades for hot-fired engine performance validation trials*. in *Proceedings of the ASME Turbo Expo*. 2019.

32. Sanchez, S., P. Smith, Z. Xu, G. Gaspard, C.J. Hyde, W.W. Wits, I.A. Ashcroft, H. Chen, and A.T. Clare, *Powder Bed Fusion of nickel-based superalloys: A review.* International Journal of Machine Tools and Manufacture, 2021. **165**: p. 103729.

33. Kuo, Y.-L., S. Horikawa, and K. Kakehi, *Effects of build direction and heat treatment on creep properties of Ni-base superalloy built up by additive manufacturing.* Scripta Materialia, 2017. **129**: p. 74-78.

34. McLouth, T.D., D.B. Witkin, G.E. Bean, S.D. Sitzman, P.M. Adams, J.R. Lohser, J.-M. Yang, and R.J. Zaldivar, *Variations in ambient and elevated temperature mechanical behavior of IN718 manufactured by selective laser melting via process parameter control.* Materials Science and Engineering: A, 2020. **780**: p. 139184.

35. Kuo, Y.-L., T. Nagahari, and K. Kakehi, *The Effect of Post-Processes on the Microstructure and Creep Properties of Alloy718 Built Up by Selective Laser Melting.* Materials (Basel, Switzerland), 2018. **11**(6): p. 996.

36. Frazier, W.E., *Metal Additive Manufacturing: A Review.* Journal of Materials Engineering and Performance, 2014. **23**(6): p. 1917-1928.

37. Herzog, D., V. Seyda, E. Wycisk, and C. Emmelmann, *Additive manufacturing of metals.* Acta Materialia, 2016. **117**: p. 371-392.

38. Sames, W.J., F.A. List, S. Pannala, R.R. Dehoff, and S.S. Babu, *The metallurgy and processing science of metal additive manufacturing.* International Materials Reviews, 2016. **61**(5): p. 315-360.

39. Zhang, J., S. Li, Q. Wei, Y. Shi, L. Wang, and L. Guo, *Cracking behavior and inhibiting process of inconel 625 alloy formed by selective laser melting.* 2015. **39**: p. 961-966.

40. Criales, L., Y. Arisoy, B. Lane, S. Moylan, M. Donmez, and T. Özel, *Predictive Modeling and Optimization of Multi-Track Processing for Laser Powder Bed Fusion of Nickel Alloy 625.* Additive Manufacturing, 2016. **13**.

41. Malekipour, E. and H. El-Mounayri, *Common defects and contributing parameters in powder bed fusion AM process and their classification for online monitoring and control: a review.* International Journal of Advanced Manufacturing Technology, 2018. **95**(1-4): p. 527-550.

42. Kuo, Y., S. Horikawa, and K. Kakehi, *The effect of interdendritic δ phase on the mechanical properties of Alloy 718 built up by additive manufacturing.* Materials & Design, 2017. **116**: p. 411-418.

43. Choi, J.-P., G.-H. Shin, S. Yang, D.-Y. Yang, J.-S. Lee, M. Brochu, and J.-H. Yu, *Densification and microstructural investigation of Inconel 718 parts fabricated by selective laser melting.* Powder Technology, 2017. **310**: p. 60-66.

44. Calandri, M., S. Yin, B. Aldwell, F. Calignano, R. Lupoi, and D. Ugues, *Texture and microstructural features at different length scales in Inconel 718 produced by selective laser melting.* Materials, 2019. **12**(8).

45. Tao, P., H. Li, B. Huang, Q. Hu, S. Gong, and Q. Xu, *The crystal growth, intercellular spacing and microsegregation of selective laser melted Inconel 718 superalloy.* Vacuum, 2019. **159**: p. 382-390.

46. Nataliya, P., R. Jordan, S. Yu, H. Martin, F. Barrie, L. Elena, and W. Xinhua, *Optimisation of selective laser melting parameters for the Ni-based superalloy IN-738 LC using Doehlert's design.* Rapid Prototyping Journal, 2017. **23**(5): p. 881-892.

47. Chlebus, E., K. Gruber, B. Kuźnicka, J. Kurzac, and T. Kurzynowski, *Effect of heat treatment on the microstructure and mechanical properties of Inconel 718 processed by selective laser melting.* Materials Science and Engineering: A, 2015. **639**: p. 647-655.

48. Kirka, M.M., K.A. Unocic, N. Raghavan, F. Medina, R.R. Dehoff, and S.S. Babu, *Microstructure Development in Electron Beam-Melted Inconel 718 and Associated Tensile Properties.* JOM, 2016. **68**(3): p. 1012-1020.

49. Sames, W.J., K.A. Unocic, R.R. Dehoff, T. Lolla, and S.S. Babu, *Thermal effects on microstructural heterogeneity of Inconel 718 materials fabricated by electron beam melting.* Journal of Materials Research, 2014. **29**(17): p. 1920-1930.

50. Deng, D., R.L. Peng, H. Söderberg, and J. Moverare, *On the formation of microstructural gradients in a nickel-base superalloy during electron beam melting.* Materials & Design, 2018. **160**: p. 251-261.

51. Polonsky, A.T., M.P. Echlin, W.C. Lenthe, R.R. Dehoff, M.M. Kirka, and T.M. Pollock, *Defects and 3D structural inhomogeneity in electron beam additively manufactured Inconel 718.* Materials Characterization, 2018.

52. Gonzalez, J.A., J. Mireles, S.W. Stafford, M.A. Perez, C.A. Terrazas, and R.B. Wicker, *Characterization of Inconel 625 fabricated using powder-bed-based additive manufacturing technologies.* Journal of Materials Processing Technology, 2019. **264**: p. 200-210.

53. Strantza, M., B. Vrancken, M.B. Prime, C.E. Truman, M. Rombouts, D.W. Brown, P. Guillaume, and D. Van Hemelrijck, *Directional and oscillating residual stress on the mesoscale in additively manufactured Ti-6Al-4V.* Acta Materialia, 2019. **168**: p. 299-308.

54. Huang, W., J. Yang, H. Yang, G. Jing, Z. Wang, and X. Zeng, *Heat treatment of Inconel 718 produced by selective laser melting: Microstructure and mechanical properties.* Materials Science and Engineering A, 2019. **750**: p. 98-107.

55. Bartlett, J.L. and X. Li, *An overview of residual stresses in metal powder bed fusion.* Additive Manufacturing, 2019. **27**: p. 131-149.

56. Gu, C., J. Lian, Y. Bao, and S. Münstermann, *Microstructure-based fatigue modelling with residual stresses: Prediction of the microcrack initiation around inclusions.* Materials Science and Engineering A, 2019. **751**: p. 133-141.

57. Liu, A.F., *Mechanics and mechanisms of fracture : an introduction*. 2005, Materials Park, OH ; [Great Britain]: ASM International.

58. Ashby, M.F., *Engineering materials 1 : an introduction to properties, applications and design / by Michael F. Ashby, David R.H. Jones*. 4th ed. ed. Engineering materials one, ed. D.R.H. Jones. 2012, Oxford: Butterworth-Heinemann.

59. Ashby, M.F. and D.R.H. Jones, *Engineering materials 2 : an introduction to microstructures and processing*. 4th ed. ed. 2013, Boston, Mass.: Elsevier/Butterworth-Heinemann.

60. Reed, R.C., *The superalloys: fundamentals and applications*, ed. R.C. Reed. 2006, Cambridge (UK): Cambridge University Press.

61. Mittemeijer, E.J., *Fundamentals of materials science : the microstructure-property relationship using metals as model systems / Eric J. Mittemeijer*. 2010, London: Springer.

62. Geddes, B., H. Leon, and X. Huang, *Superalloys : alloying and performance*. 2010, Materials Park, OH: ASM International.

63. Schirra, J.J., R.H. Caless, and R.W. Hatala, *The Effect of Laves Phase on the Mechanical Properties of Wrought and Cast + HIP Inconel 718*. 1991. 375-388.

64. Xu, Z., C.J. Hyde, C. Tuck, and A.T. Clare, *Creep behaviour of inconel 718 processed by laser powder bed fusion.* Journal of Materials Processing Technology, 2018. **256**.

65. Parimi, L.L., G.A. Ravi, D. Clark, and M.M. Attallah, *Microstructural and texture development in direct laser fabricated IN718.* Materials Characterization, 2014. **89**: p. 102-111.

66. Thompson, R.G., J.R. Dobbs, and D.E. Mayo, *The effect of heat treatment on microfissuring in alloy 718.* Welding Journal, 1986(65): p. 299s-304s.

67. Fournier, D. and A. Pineau, *Low cycle fatigue behavior of inconel 718 at 298 K and 823 K.* Metallurgical Transactions A, 1977. **8**(7): p. 1095-1105.

68. Chaturvedi, M.C. and Y. Han, *Effect of particle size on the creep rate of superalloy Inconel 718.* Materials Science and Engineering, 1987. **89**: p. L7-L10.

69. Xu, Z., L. Cao, Q. Zhu, C. Guo, X. Li, X. Hu, and Z. Yu, *Creep property of Inconel 718 superalloy produced by selective laser melting compared to forging.* Materials Science and Engineering: A, 2020. **794**: p. 139947.

70. Kuo, C.M., Y.T. Yang, H.Y. Bor, C.N. Wei, and C.C. Tai, *Aging effects on the microstructure and creep behavior of Inconel 718 superalloy.* Materials Science and Engineering: A, 2009. **510-511**: p. 289-294.

71. Griffiths, S., H. Ghasemi Tabasi, T. Ivas, X. Maeder, A. De Luca, K. Zweiacker, R. Wróbel, J. Jhabvala, R.E. Logé, and C. Leinenbach, *Combining alloy and process modification for micro-crack mitigation in an additively manufactured Ni-base superalloy.* Additive Manufacturing, 2020. **36**.

72. Kalentics, N., N. Sohrabi, H.G. Tabasi, S. Griffiths, J. Jhabvala, C. Leinenbach, A. Burn, and R.E. Logé, *Healing cracks in selective laser melting by 3D laser shock peening.* Additive Manufacturing, 2019. **30**.

73. Vilanova, M., R. Escribano ‑ garcía, T. Guraya, and M.S. Sebastian, *Optimizing laser powder bed fusion parameters for IN ‑ 738LC by response surface method.* Materials, 2020. **13**(21): p. 1-12.

74. Zhang, X., C.J. Yocom, B. Mao, and Y. Liao, *Microstructure evolution during selective laser melting of metallic materials: A review.* Journal of Laser Applications, 2019. **31**(3).

75. Oliveira, J.P., A.D. LaLonde, and J. Ma, *Processing parameters in laser powder bed fusion metal additive manufacturing.* Materials and Design, 2020. **193**.

76. Snow, Z., A.R. Nassar, and E.W. Reutzel, *Invited Review Article: Review of the formation and impact of flaws in powder bed fusion additive manufacturing.* Additive Manufacturing, 2020. **36**.

77. Kumara, C., A.R. Balachandramurthi, S. Goel, F. Hanning, and J. Moverare, *Toward a better understanding of phase transformations in additive manufacturing of Alloy 718.* Materialia, 2020. **13**: p. 100862.

78. Sudbrack, C.K., B.A. Lerch, T.M. Smith, I.E. Locci, D.L. Ellis, A.C. Thompson, and B. Richards, *Impact of powder variability on the microstructure and mechanical behavior of selective laser melted alloy 718*, in *Minerals, Metals and Materials Series*. 2018. p. 89-113.

79. Sutton, A.T., C.S. Kriewall, M.C. Leu, and J.W. Newkirk, *Powder characterisation techniques and effects of powder characteristics on part properties in powder-bed fusion processes.* Virtual and Physical Prototyping, 2017. **12**(1): p. 3-29.

80. Tan, J.H., W.L.E. Wong, and K.W. Dalgarno, *An overview of powder granulometry on feedstock and part performance in the selective laser melting process.* Additive Manufacturing, 2017. **18**: p. 228-255.

81. Mancisidor, A.M., F. Garciandia, P.M. García-Riesco, and M. San Sebastian. *Influence of Hastelloy X composition on cracking susceptibility during SLM*. in *Euro PM 2018 Congress and Exhibition*. 2020.

82. Ardila, L.C., F. Garciandia, J.B. González-Díaz, P. Álvarez, A. Echeverria, M.M. Petite, R. Deffley, and J. Ochoa, *Effect of IN718 Recycled Powder Reuse on Properties of Parts Manufactured by Means of Selective Laser Melting.* Physics Procedia, 2014. **56**: p. 99-107.

83. Nandwana, P., W.H. Peter, R.R. Dehoff, L.E. Lowe, M.M. Kirka, F. Medina, and S.S. Babu, *Recyclability Study on Inconel 718 and Ti-6Al-4V Powders for Use in Electron Beam Melting.* Metallurgical and Materials Transactions B, 2016. **47**(1): p. 754-762.

84. Nguyen, Q.B., M.L.S. Nai, Z. Zhu, C.-N. Sun, J. Wei, and W. Zhou, *Characteristics of Inconel Powders for Powder-Bed Additive Manufacturing.* Engineering, 2017. **3**(5): p. 695-700.

85. Gasper, A.N.D., B. Szost, X. Wang, D. Johns, S. Sharma, A.T. Clare, and I.A. Ashcroft, *Spatter and oxide formation in laser powder bed fusion of Inconel 718.* Additive Manufacturing, 2018. **24**: p. 446-456.

86. Tomus, D., P.A. Rometsch, M. Heilmaier, and X. Wu, *Effect of minor alloying elements on crack-formation characteristics of Hastelloy-X manufactured by selective laser melting.* Additive Manufacturing, 2017. **16**: p. 65-72.

87. W. J. Sames, F. Medina, W. H. Peter, S. S. Babu, and R.R. Dehoff. *Effect of process control and powder quality on Inconel 718 produced using electron beam melting*. in *8th International Symposium on Superalloy 718 and Derivatives*. 2014.

88. Engeli, R., T. Etter, S. Hövel, and K. Wegener, *Processability of different IN738LC powder batches by selective laser melting.* Journal of Materials Processing Technology, 2016. **229**: p. 484-491.

89. Zhang, Y., H. Wang, X. Song, and Z. Nie, *Preparation and Performance of Spherical Ni Powder for SLM Processing.* Jinshu Xuebao/Acta Metallurgica Sinica, 2018. **54**(12): p. 1833-1842.

90. Pleass, C. and S. Jothi, *Influence of powder characteristics and additive manufacturing process parameters on the microstructure and mechanical behaviour of Inconel 625 fabricated by Selective Laser Melting.* Additive Manufacturing, 2018. **24**: p. 419-431.

91. Montero-Sistiaga, M.L., M. Godino-Martinez, C. Hautfenne, M. Deprez, A. Martín, M.T. Pérez-Prado, J.P. Kruth, and K. Vanmeensel. *Fast screening of modified powder compositions for selective laser melting*. in *Euro PM 2018 Congress and Exhibition*. 2020.

92. Pollock, T.M., A.J. Clarke, and S.S. Babu, *Design and Tailoring of Alloys for Additive Manufacturing.* Metallurgical and Materials Transactions A: Physical Metallurgy and Materials Science, 2020. **51**(12): p. 6000-6019.

93. Aota, L., P. Bajaj, H. Sandim, and E. Jägle, *Laser Powder-Bed Fusion as an Alloy Development Tool: Parameter Selection for In-Situ Alloying Using Elemental Powders.* Materials, 2020. **13**: p. 3922.

94. Poorganji, B., E. Ott, R. Kelkar, A. Wessman, and M. Jamshidinia, *Review: Materials Ecosystem for Additive Manufacturing Powder Bed Fusion Processes.* JOM, 2020. **72**(1): p. 561-576.

95. Traore, S., M. Schneider, I. Koutiri, F. Coste, R. Fabbro, C. Charpentier, P. Lefebvre, and P. Peyre, *Influence of gas atmosphere (Ar or He) on the laser powder bed fusion of a Ni-based alloy.* Journal of Materials Processing Technology, 2021. **288**: p. 116851.

96. Gasper, A.N.D., D. Hickman, I. Ashcroft, S. Sharma, X. Wang, B. Szost, D. Johns, and A.T. Clare, *Oxide and spatter powder formation during laser powder bed fusion of Hastelloy X.* Powder Technology, 2019. **354**: p. 333-337.

97. Zhao, Y., K. Aoyagi, K. Yamanaka, and A. Chiba, *Role of operating and environmental conditions in determining molten pool dynamics during electron beam melting and selective laser melting.* Additive Manufacturing, 2020. **36**.

98. Gruber, H., M. Henriksson, E. Hryha, and L. Nyborg, *Effect of Powder Recycling in Electron Beam Melting on the Surface Chemistry of Alloy 718 Powder.* Metallurgical and Materials Transactions A: Physical Metallurgy and Materials Science, 2019. **50**(9): p. 4410-4422.

99. Yu, H., S. Hayashi, K. Kakehi, and Y.L. Kuo, *Study of formed oxides in IN718 alloy during the fabrication by selective laser melting and electron beam melting.* Metals, 2019. **9**(1).

100. Wong, H., K. Dawson, G.A. Ravi, L. Howlett, R. Jones, and C. Sutcliffe, *Multi-Laser Powder Bed Fusion Benchmarking—Initial Trials with Inconel 625.* The International Journal of Advanced Manufacturing Technology, 2019. **105**.

101. Yeung, H. and B. Lane, *A residual heat compensation based scan strategy for powder bed fusion additive manufacturing.* Manufacturing Letters, 2020. **25**: p. 56-59.

102. Sebastian, R., S. Catchpole-Smith, M. Simonelli, A. Rushworth, H. Chen, and A. Clare, *'Unit cell' type scan strategies for powder bed fusion: The Hilbert fractal.* Additive Manufacturing, 2020. **36**: p. 101588.

103. Helmer, H., A. Bauereiß, R.F. Singer, and C. Körner, *Grain structure evolution in Inconel 718 during selective electron beam melting.* Materials Science and Engineering: A, 2016. **668**: p. 180-187.

104. Karimi, P., E. Sadeghi, J. Ålgårdh, and J. Andersson, *EBM-manufactured single tracks of Alloy 718: Influence of energy input and focus offset on geometrical and microstructural characteristics.* Materials Characterization, 2019. **148**: p. 88-99.

105. Fernandez-Zelaia, P., M.M. Kirka, S.N. Dryepondt, and M.N. Gussev, *Crystallographic texture control in electron beam additive manufacturing via conductive manipulation.* Materials and Design, 2020. **195**.

106. McLouth, T.D., G.E. Bean, D.B. Witkin, S.D. Sitzman, P.M. Adams, D.N. Patel, W. Park, J.-M. Yang, and R.J. Zaldivar, *The effect of laser focus shift on microstructural variation of Inconel 718 produced by selective laser melting.* Materials & Design, 2018. **149**: p. 205-213.

107. Wang, Y. and J. Shi, *Developing very strong texture in a nickel-based superalloy by selective laser melting with an ultra-high power and flat-top laser beam.* Materials Characterization, 2020. **165**: p. 110372.

108. Sow, M.C., T. De Terris, O. Castelnau, Z. Hamouche, F. Coste, R. Fabbro, and P. Peyre, *Influence of beam diameter on Laser Powder Bed Fusion (L-PBF) process.* Additive Manufacturing, 2020. **36**.

109. Popovich, V.A., E.V. Borisov, A.A. Popovich, V.S. Sufiiarov, D.V. Masaylo, and L. Alzina, *Impact of heat treatment on mechanical behaviour of Inconel 718 processed with tailored microstructure by selective laser melting.* Materials & Design, 2017. **131**: p. 12-22.

110. Peng, K., R. Duan, Z. Liu, X. Lv, Q. Li, F. Zhao, B. Wei, B. Nong, and S. Wei, *Cracking behavior of rené 104 nickel-based superalloy prepared by selective laser melting using different scanning strategies.* Materials, 2020. **13**(9).

111. Grange, D., J.D. Bartout, B. Macquaire, and C. Colin, *Processing a non-weldable nickel-base superalloy by Selective Laser Melting: role of the shape and size of the melt pools on solidification cracking.* Materialia, 2020. **12**.

112. Serrano-Munoz, I., T. Mishurova, T. Thiede, M. Sprengel, A. Kromm, N. Nadammal, G. Nolze, R. Saliwan-Neumann, A. Evans, and G. Bruno, *The residual stress in as-built Laser Powder Bed Fusion IN718 alloy as a consequence of the scanning strategy induced microstructure.* Scientific Reports, 2020. **10**(1).

113. Rajendran, V.R.K., K. Mamidi, B. Ravichander, B. Farhang, A. Amerinatanzi, and N. Shayesteh Moghaddam. *Determination of residual stress for Inconel 718 samples fabricated through different scanning strategies in selective laser melting*. in *Proceedings of SPIE - The International Society for Optical Engineering*. 2020.

114. Marchese, G., G. Basile, E. Bassini, A. Aversa, M. Lombardi, D. Ugues, P. Fino, and S. Biamino, *Study of the Microstructure and Cracking Mechanisms of Hastelloy X Produced by Laser Powder Bed Fusion.* Materials, 2018. **11**(1): p. 106.

115. Amirjan, M. and H. Sakiani, *Effect of scanning strategy and speed on the microstructure and mechanical properties of selective laser melted IN718 nickel-based superalloy.* International Journal of Advanced Manufacturing Technology, 2019. **103**(5-8): p. 1769-1780.

116. Guo, C., S. Li, S. Shi, X. Li, X. Hu, Q. Zhu, and R.M. Ward, *Effect of processing parameters on surface roughness, porosity and cracking of as-built IN738LC parts fabricated by laser powder bed fusion.* Journal of Materials Processing Technology, 2020. **285**.

117. Wang, W., Y. Li, X. Li, L. Liu, and F. Chen, *Microstructures and Properties of Ni-Cr-B-Si Alloy Powders Prepared by Selective Laser Melting.* Cailiao Daobao/Materials Reports, 2020. **34**(1): p. 02077-02082.

118. Attard, B., S. Cruchley, C. Beetz, M. Megahed, Y.L. Chiu, and M.M. Attallah, *Microstructural control during laser powder fusion to create graded microstructure Ni-superalloy components.* Additive Manufacturing, 2020. **36**.

119. Jean, M.D. and Y.F. Tzeng, *Use of Taguchi Methods and Multiple Regression Analysis for Optimal Process Development of High Energy Electron Beam Case Hardening of Cast Iron.* Surface Engineering, 2003. **19**(2): p. 150-156.

120. Sun, J., Y. Yang, and D. Wang, *Parametric optimization of selective laser melting for forming Ti6Al4V samples by Taguchi method.* Optics & Laser Technology, 2013. **49**: p. 118–124.

121. Marrey, M., E. Malekipour, H. El-Mounayri, and E.J. Faierson, *A Framework for Optimizing Process Parameters in Powder Bed Fusion (PBF) Process Using Artificial Neural Network (ANN).* Procedia Manufacturing, 2019. **34**: p. 505-515.

122. Lim, C.H., M. Krishnan, and H. Li. *Methods of residual stress reduction for metal parts manufactured using selective laser melting (A Review)*. in *Proceedings of the International Conference on Progress in Additive Manufacturing*. 2018.

123. Ahmad, M., R. Ignacio Picazo, B. Vladimir, J. Mohammad, and M. Mamoun, *Structure, Texture and Phases in 3D Printed IN718 Alloy Subjected to Homogenization and HIP Treatments.* Metals, 2017. **7**(6): p. 196.

124. Hilaire, A., E. Andrieu, and X. Wu, *High-temperature mechanical properties of alloy 718 produced by laser powder bed fusion with different processing parameters.* Additive Manufacturing, 2019. **26**: p. 147-160.

125. Azarbarmas, M., M. Aghaie-Khafri, J.M. Cabrera, and J. Calvo, *Dynamic recrystallization mechanisms and twining evolution during hot deformation of Inconel 718.* Materials Science & Engineering A, 2016. **678**(C): p. 137-152.

126. Goel, S., M. Ahlfors, F. Bahbou, and S. Joshi, *Effect of Different Post-treatments on the Microstructure of EBM-Built Alloy 718.* Journal of Materials Engineering and Performance, 2018.

127. Parizia, S., G. Marchese, M. Rashidi, M. Lorusso, E. Hryha, D. Manfredi, and S. Biamino, *Effect of heat treatment on microstructure and oxidation properties of Inconel 625 processed by LPBF.* Journal of Alloys and Compounds, 2020. **846**.

128. Yoo, Y.S.J., T.A. Book, M.D. Sangid, and J. Kacher, *Identifying strain localization and dislocation processes in fatigued Inconel 718 manufactured from selective laser melting.* Materials Science & Engineering A, 2018. **724**: p. 444-451.

129. Manikandan, S.G.K., D. Sivakumar, K.P. Rao, and M. Kamaraj, *Effect of weld cooling rate on Laves phase formation in Inconel 718 fusion zone.* Journal of Materials Processing Technology, 2014. **214**(2): p. 358-364.

130. Zhang, D., W. Niu, X. Cao, and Z. Liu, *Effect of standard heat treatment on the microstructure and mechanical properties of selective laser melting manufactured Inconel 718 superalloy.* Materials Science and Engineering: A, 2015. **644**: p. 32-40.

131. Zhao, Y., K. Li, M. Gargani, and W. Xiong, *A comparative analysis of Inconel 718 made by additive manufacturing and suction casting: Microstructure evolution in homogenization.* Additive Manufacturing, 2020. **36**.

132. Jiang, R., A. Mostafaei, J. Pauza, C. Kantzos, and A.D. Rollett, *Varied heat treatments and properties of laser powder bed printed Inconel 718.* Materials Science & Engineering A, 2019. **755**: p. 170-180.

133. Balachandramurthi, A.R., J. Moverare, N. Dixit, D. Deng, and R. Pederson, *Microstructural influence on fatigue crack propagation during high cycle fatigue testing of additively manufactured Alloy 718.* Materials Characterization, 2019. **149**: p. 82-94.

134. Amato, K.N., S.M. Gaytan, L.E. Murr, E. Martinez, P.W. Shindo, J. Hernandez, S. Collins, and F. Medina, *Microstructures and mechanical behavior of Inconel 718 fabricated by selective laser melting.* Acta Materialia, 2012. **60**(5): p. 2229-2239.

135. Gundgire, T., S. Goel, U. Klement, and S. Joshi, *Response of different electron beam melting produced Alloy 718 microstructures to thermal post-treatments.* Materials Characterization, 2020. **167**: p. 110498.

136. ASTM International, *F3055-14a Standard Specification for Additive Manufacturing Nickel Alloy (UNS N07718) with Powder Bed Fusion*. 2014: West Conshohocken, PA.

137. SAE International, *Heat Treatment Wrought Nickel Alloy and Cobalt Alloy Parts*. 2001, SAE International.

138. Aydinöz, M.E., F. Brenne, M. Schaper, C. Schaak, W. Tillmann, J. Nellesen, and T. Niendorf, *On the microstructural and mechanical properties of post-treated additively manufactured Inconel 718 superalloy under quasi-static and cyclic loading.* Materials Science and Engineering: A, 2016. **669**: p. 246-258.

139. Ivanov, D., A. Travyanov, P. Petrovskiy, V. Cheverikin, E. Alekseeva, A. Khvan, and I. Logachev, *Evolution of structure and properties of the nickel-based alloy EP718 after the SLM growth and after different types of heat and mechanical treatment.* Additive Manufacturing, 2017. **18**: p. 269-275.

140. Holland, S., X. Wang, X.Y. Fang, Y.B. Guo, F. Yan, and L. Li, *Grain boundary network evolution in Inconel 718 from selective laser melting to heat treatment.* Materials Science and Engineering: A, 2018. **725**: p. 406-418.

141. Fang, X.Y., H.Q. Li, M. Wang, C. Li, and Y.B. Guo, *Characterization of texture and grain boundary character distributions of selective laser melted Inconel 625 alloy.* Materials Characterization, 2018. **143**: p. 182-190.

142. Gribbin, S., J. Bicknell, L. Jorgensen, I. Tsukrov, and M. Knezevic, *Low cycle fatigue behavior of direct metal laser sintered Inconel alloy 718.* International Journal of Fatigue, 2016. **93**: p. 156-167.

143. Zhang, Z.J., P. Zhang, L.L. Li, and Z.F. Zhang, *Fatigue cracking at twin boundaries: Effects of crystallographic orientation and stacking fault energy.* Acta Materialia, 2012. **60**(6): p. 3113-3127.

144. Chauvet, E., P. Kontis, E.A. Jägle, B. Gault, D. Raabe, C. Tassin, J.-J. Blandin, R. Dendievel, B. Vayre, S. Abed, and G. Martin, *Hot cracking mechanism affecting a non-weldable Ni-based superalloy produced by selective electron Beam Melting.* Acta Materialia, 2018. **142**: p. 82-94.

145. Han, Q., R. Mertens, M.L. Montero-Sistiaga, S. Yang, R. Setchi, K. Vanmeensel, B. Van Hooreweder, S.L. Evans, and H. Fan, *Laser powder bed fusion of Hastelloy X: Effects of hot isostatic pressing and the hot cracking mechanism.* Materials Science and Engineering: A, 2018. **732**: p. 228-239.

146. Tomus, D., Y. Tian, P.A. Rometsch, M. Heilmaier, and X. Wu, *Influence of post heat treatments on anisotropy of mechanical behaviour and microstructure of Hastelloy-X parts produced by selective laser melting.* Materials Science and Engineering: A, 2016. **667**: p. 42-53.

147. Sanchez-Mata, O., J.A. Muñiz-Lerma, X. Wang, S.E. Atabay, M. Attarian Shandiz, and M. Brochu, *Microstructure and mechanical properties at room and elevated temperature of crack-free Hastelloy X fabricated by laser powder bed fusion.* Materials Science and Engineering A, 2020. **780**.

148. Marchese, G., E. Bassini, A. Aversa, M. Lombardi, D. Ugues, P. Fino, and S. Biamino, *Microstructural evolution of post-processed Hastelloy X alloy fabricated by laser powder bed fusion.* Materials, 2019. **12**(3).

149. Peng, H., Y. Shi, S. Gong, H. Guo, and B. Chen, *Microstructure, mechanical properties and cracking behaviour in a* γ' *-precipitation strengthened nickel-base superalloy fabricated by electron beam melting.* Materials and Design, 2018. **159**: p. 155-169.

150. Sames, W.J., K.A. Unocic, G.W. Helmreich, M.M. Kirka, F. Medina, R.R. Dehoff, and S.S. Babu, *Feasibility of in situ controlled heat treatment (ISHT) of Inconel 718 during electron beam melting additive manufacturing.* Additive Manufacturing, 2017. **13**: p. 156-165.

151. Divya, V.D., R. Muñoz-Moreno, O.M.D.M. Messé, J.S. Barnard, S. Baker, T. Illston, and H.J. Stone, *Microstructure of selective laser melted CM247LC nickel-based superalloy and its evolution through heat treatment.* Materials Characterization, 2016. **114**: p. 62-74.

152. Tucho, W.M., P. Cuvillier, A. Sjolyst-Kverneland, and V. Hansen, *Microstructure and hardness studies of Inconel 718 manufactured by selective laser melting before and after solution heat treatment.* Materials Science and Engineering: A, 2017. **689**: p. 220-232.

153. Deshpande, A., S.D. Nath, S. Atre, and K. Hsu, *Effect of post processing heat treatment routes on microstructure and mechanical property evolution of haynes 282 Ni-based superalloy fabricated with selective laser melting (SLM).* Metals, 2020. **10**(5).

154. Stoudt, M.R., E.A. Lass, D.S. Ng, M.E. Williams, F. Zhang, C.E. Campbell, G. Lindwall, and L.E. Levine, *The Influence of Annealing Temperature and Time on the Formation of δ-Phase in Additively-Manufactured Inconel 625.* Metallurgical and Materials Transactions A, 2018. **49**(7): p. 3028-3037.

155. Zhang, F., L.E. Levine, A.J. Allen, M.R. Stoudt, G. Lindwall, E.A. Lass, M.E. Williams, Y. Idell, and C.E. Campbell, *Effect of heat treatment on the microstructural evolution of a nickel-based superalloy additive-manufactured by laser powder bed fusion.* Acta Materialia, 2018. **152**: p. 200-214.

156. Vikram, R.J., A. Singh, and S. Suwas, *Effect of heat treatment on the modification of microstructure of selective laser melted (SLM) IN718 and its consequences on mechanical behavior.* Journal of Materials Research, 2020. **35**(15): p. 1949-1962.

157. Pröbstle, M., S. Neumeier, J. Hopfenmüller, L.P. Freund, T. Niendorf, D. Schwarze, and M. Göken, *Superior creep strength of a nickel-based superalloy produced by selective laser melting.* Materials Science and Engineering: A, 2016. **674**: p. 299-307.

158. Sui, S., J. Chen, Z. Li, H. Li, X. Zhao, and H. Tan, *Investigation of dissolution behavior of laves phase in inconel 718 fabricated by laser directed energy deposition.* Additive Manufacturing, 2020. **32**: p. 101055.

159. Sui, S., H. Tan, J. Chen, C. Zhong, Z. Li, W. Fan, A. Gasser, and W. Huang, *The influence of Laves phases on the room temperature tensile properties of Inconel 718 fabricated by powder feeding laser additive manufacturing.* Acta Materialia, 2019. **164**: p. 413-427.

160. Xiao, H., S. Li, X. Han, J. Mazumder, and L. Song, *Laves phase control of Inconel 718 alloy using quasi-continuous-wave laser additive manufacturing.* Materials & Design, 2017. **122**: p. 330-339.

161. Sukhov, D.I., N.V. Petrushin, D.V. Zaitsev, and M.M. Tikhonov, *Features of VZhL21 Nickel-Base Superalloy Structure Formation During Selective Laser Melting, Vacuum Heat Treatment, and Hot Isostatic Compaction.* Metallurgist, 2019. **63**(3-4): p. 409-421.

162. Boswell, J.H., D. Clark, W. Li, and M.M. Attallah, *Cracking during thermal post-processing of laser powder bed fabricated CM247LC Ni-superalloy.* Materials and Design, 2019. **174**.

163. Ezugwu, E., Z.M. Wang, and A. Machado, *The machinability of nickel-based alloys: A review.* Journal of Materials Processing Technology, 1998. **86**: p. 1-16.

164. Lesyk, D.A., S. Martinez, B.N. Mordyuk, V.V. Dzhemelinskyi, A. Lamikiz, and G.I. Prokopenko, *Post-processing of the Inconel 718 alloy parts fabricated by selective laser melting: Effects of mechanical surface treatments on surface topography, porosity, hardness and residual stress.* Surface and Coatings Technology, 2020. **381**.

165. Lesyk, D., S. Martinez, O. Pedash, V. Dzhemelinskyi, and B. Mordyuk, *Combined Thermo-Mechanical Techniques for Post-processing of the SLM-Printed Ni-Cr-Fe Alloy Parts*, in *Lecture Notes in Mechanical Engineering*. 2020. p. 295-304.

166. Yang, L., C. O'Neil, and Y. Wu. *The use of electropolishing surface treatment on IN718 parts fabricated by laser powder bed fusion process*. in *Solid Freeform Fabrication 2017: Proceedings of the 28th Annual International Solid Freeform Fabrication Symposium - An Additive Manufacturing Conference, SFF 2017*. 2020.

167. Fei, J., G. Liu, K. Patel, and T. Özel, *Effects of machining parameters on finishing additively manufactured nickel-based alloy inconel 625.* Journal of Manufacturing and Materials Processing, 2020. **4**(2).

168. Yang, L., K.V. Patel, K. Jarosz, and T. Özel. *Surface integrity induced in machining additively fabricated nickel alloy Inconel 625*. in *Procedia CIRP*. 2020.

169. Fei, J., G. Liu, K. Patel, and T. Özel, *Cutting force investigation in face milling of additively fabricated nickel alloy 625 via powder bed fusion.* International Journal of Mechatronics and Manufacturing Systems, 2019. **12**(3-4): p. 196-210.

170. Periane, S., A. Duchosal, S. Vaudreuil, H. Chibane, A. Morandeau, M.A. Xavior, and R. Leroy. *Selection of machining condition on surface integrity of additive and conventional Inconel 718*. in *Procedia CIRP*. 2020.

171. Webster, S., H. Lin, F.M. Carter Iii, K. Ehmann, and J. Cao, *Physical mechanisms in hybrid additive manufacturing: A process design framework.* Journal of Materials Processing Technology, 2021. **291**: p. 117048.

172. Flynn, J.M., A. Shokrani, S.T. Newman, and V. Dhokia, *Hybrid additive and subtractive machine tools – Research and industrial developments.* International Journal of Machine Tools and Manufacture, 2016. **101**: p. 79-101.

173. Hyde, T.H., *Applied creep mechanics / Thomas H. Hyde, Wei Sun, Christopher J. Hyde*, ed. W.D. Sun and C.J. Hyde. 2014, New York: New York : McGraw-Hill.

174. Ashby, M.F. and B.F. Dyson, *Creep damage mechanics and micromechanisms*, in *Fracture 84*, S.R. Valluri, et al., Editors. 1984, Pergamon. p. 3-30.

175. Kowalewski, Z.L., D.R. Hayhurst, and B.F. Dyson, *Mechanisms-based creep constitutive equations for an aluminium alloy.* The Journal of Strain Analysis for Engineering Design, 1994. **29**(4): p. 309-316.

176. Mustata, R. and D.R. Hayhurst, *Creep constitutive equations for a 0.5Cr 0.5 Mo 0.25V ferritic steel in the temperature range 565°C–675°C.* International Journal of Pressure Vessels and Piping, 2005. **82**(5): p. 363-372.

177. Hyde, T.H., A.A. Becker, W. Sun, and J.A. Williams, *Finite-element creep damage analyses of P91 pipes.* International Journal of Pressure Vessels and Piping, 2006. **83**(11): p. 853-863.

178. Spigarelli, S., *Microstructure-based assessment of creep rupture strength in 9Cr steels.* International Journal of Pressure Vessels and Piping, 2013. **101**: p. 64-71.

179. Murchú, C.Ó., S.B. Leen, P.E. O'Donoghue, and R.A. Barrett, *A physically-based creep damage model for effects of different precipitate types.* Materials Science and Engineering: A, 2017. **682**: p. 714-722.

180. Larson, F.R. and J. Miller, *A Linear Temperature Relationship for Rupture Time-Temperature Relation for Extrapolaand Creep Stresses.* Trans ASME, 1952. **74**: p. 765-771.

181. Sundararajan, G., *The Monkman-Grant relationship.* Materials Science and Engineering: A, 1989. **112**: p. 205-214.

182. Kassner, M.E., *Fundamentals of creep in metals and alloys [electronic resource] / Michael E. Kassner*. 2nd ed. ed, ed. Knovel. 2009, London: Elsevier.

183. Hayes, R.W., *Creep Deformation of Inconel alloy 718 in the 650 ℃ to 760 ℃ temperature regime*, in *Superalloys 718, 625 and Various Derivatives*, E.A. Lorin, Editor. 1991: Northridge, California.

184. Sawada, K., M. Bauer, F. Kauffmann, P. Mayr, and A. Klenk, *Microstructural change of 9% Cr-welded joints after long-term creep.* Materials Science and Engineering: A, 2010. **527**(6): p. 1417-1426.

185. Brett, S., S. Holmstrom, J. Hald, U. Borg, S. Aakjaer Jensen, R.V. Vulpen, C. Degnan, K. Vinter Dahl, and T. Vilhelmsen, *Creep damage development in welded X20 and P91*. 2011: Sweden.

186. Eggeler, G., A. Ramteke, M. Coleman, B. Chew, G. Peter, A. Burblies, J. Hald, C. Jefferey, J. Rantala, M. deWitte, and R. Mohrmann, *Analysis of creep in a welded 'P91' pressure vessel.* International Journal of Pressure Vessels and Piping, 1994. **60**(3): p. 237-257.

187. Hautfenne, C., S. Nardone, and E. De Bruycker, *Influence of heat treatments and build orientation on the creep strength of additive manufactured IN718*, in *4th International ECCC Conference*. 2017: Düsseldorf Germany.

188. Brenne, F., A. Taube, M. Pröbstle, S. Neumeier, D. Schwarze, M. Schaper, and T. Niendorf, *Microstructural design of Ni-base alloys for high-temperature applications: impact of heat treatment on microstructure and mechanical properties after selective laser melting.* Progress in Additive Manufacturing, 2016. **1**(3): p. 141-151.

189. Kuo, Y.-L., A. Kamigaichi, and K. Kakehi, *Characterization of Ni-Based Superalloy Built by Selective Laser Melting and Electron Beam Melting.* Metallurgical and Materials Transactions A, 2018. **49**(9): p. 3831-3837.

190. Xu, Z., C.J. Hyde, A. Thompson, R.K. Leach, I. Maskery, C. Tuck, and A.T. Clare, *Staged thermomechanical testing of nickel superalloys produced by selective laser melting.* Materials & Design, 2017. **133**: p. 520-527.

191. Håkan Brodin, Olov Andersson, and Sten Johansson. *Mechanical testing of a selective laser melted superalloy*. in *13th International Conference on Fracture*. 2013. Beijing, China.

192. Rickenbacher, L., T. Etter, S. Hövel, and K. Wegener, *High temperature material properties of IN738LC processed by selective laser melting (SLM) technology.* Rapid Prototyping Journal, 2013. **19**(4): p. 282-290.

193. Kunze, K., T. Etter, J. Grässlin, and V. Shklover, *Texture, anisotropy in microstructure and mechanical properties of IN738LC alloy processed by selective laser melting (SLM).* Materials Science and Engineering: A, 2015. **620**: p. 213-222.

194. C. Hautfenne, S. Nardone, and E.D. Bruycker, *Influence of heat treatments and build orientation on the creep strength of additive manufactured IN718*, in *4th international ECCC Conference*. 2017: Germany.

195. Kuo, Y., S. Horikawa, and K. Kakehi, *Effects of build direction and heat treatment on creep properties of Ni-base superalloy built up by additive manufacturing.* Scripta Materialia, 2017. **129**: p. 74-78.

196. Popovich, V.A., E.V. Borisov, V. Heurtebise, T. Riemslag, A.A. Popovich, and V.S. Sufiiarov, *Creep and thermomechanical fatigue of functionally graded inconel 718 produced by additive manufacturing*, in *147th Annual Meeting and Exhibition of the Minerals, Metals and Materials Society, TMS 2018*. 2018. p. 85-97.

197. Xu, Z., C.J. Hyde, C. Tuck, and A.T. Clare, *Creep behaviour of inconel 718 processed by laser powder bed fusion.* Journal of Materials Processing Technology, 2018. **256**: p. 13-24.

198. Strondl, A., M. Palm, J. Gnauk, and G. Frommeyer, *Microstructure and mechanical properties of nickel based superalloy IN718 produced by rapid prototyping with electron beam melting (EBM).* Materials Science and Technology, 2011. **27**(5): p. 876-883.

199. Wang, L.Y., Z.J. Zhou, C.P. Li, G.F. Chen, and G.P. Zhang, *Comparative investigation of small punch creep resistance of Inconel 718 fabricated by selective laser melting.* Materials Science and Engineering: A, 2019. **745**: p. 31-38.

200. Sato, N., S. Nakano, T. Nagahari, T. Nagoya, and K. Kakehi, *Microstructure of nickel-based superalloy fabricated by selective laser melting in vacuum.* Funtai Oyobi Fummatsu Yakin/Journal of the Japan Society of Powder and Powder Metallurgy, 2020. **67**(3): p. 121-124.

201. Tang, H.P., G.Y. Yang, W.P. Jia, W.W. He, S.L. Lu, and M. Qian, *Additive manufacturing of a high niobium-containing titanium aluminide alloy by selective electron beam melting.* Materials Science & Engineering A, 2015. **636**(C): p. 103-107.

202. Hilal, H., R. Lancaster, S. Jeffs, J. Boswell, D. Stapleton, and G. Baxter, *The influence of process parameters and build orientation on the creep behaviour of a laser powder bed fused ni-based superalloy for aerospace applications.* Materials, 2019. **12**(9).

203. Shassere, B., D. Greeley, A. Okello, M. Kirka, P. Nandwana, and R. Dehoff, *Correlation of Microstructure to Creep Response of Hot Isostatically Pressed and Aged Electron Beam Melted Inconel 718.* Metallurgical and Materials Transactions A, 2018. **49**(10): p. 5107-5117.

204. Kuo, Y.-L., T. Nagahari, and K. Kakehi, *The Effect of Post-Processes on the Microstructure and Creep Properties of Alloy718 Built Up by Selective Laser Melting.* Materials, 2018. **11**(6): p. 996.

205. Kakehi, K., S. Banoth, Y.L. Kuo, and S. Hayashi, *Effect of yttrium addition on creep properties of a Ni-base superalloy built up by selective laser melting.* Scripta Materialia, 2020. **183**: p. 71-74.

206. Wang, L.Y., Y.C. Wang, Z.J. Zhou, H.Y. Wan, C.P. Li, G.F. Chen, and G.P. Zhang, *Small punch creep performance of heterogeneous microstructure dominated Inconel 718 fabricated by selective laser melting.* Materials and Design, 2020. **195**.

207. Davies, S.J., S.P. Jeffs, M.P. Coleman, and R.J. Lancaster, *Effects of heat treatment on microstructure and creep properties of a laser powder bed fused nickel superalloy.* Materials & Design, 2018. **159**: p. 39-46.

208. Guo, Q., C. Zhao, L.I. Escano, Z. Young, L. Xiong, K. Fezzaa, W. Everhart, B. Brown, T. Sun, and L. Chen, *Transient dynamics of powder spattering in laser powder bed fusion additive manufacturing process revealed by in-situ high-speed high-energy x-ray imaging.* Acta Materialia, 2018. **151**: p. 169-180.

209. Aerospace Material Specification, *Nickel Alloy, Corrosion and Heat Resistant, Bars, Forgings, and Rings 52.5Ni 19Cr 3.0Mo 5.1Cb 0.90Ti 0.50Al 18Fe, Consumable Electrode or Vacuum Induction Melted 1775°F (968°C) Solution Heat Treated, Precipitation Hardenable*. 1965, SAE International.

210. ASTM International, *Standard Test Methods for Tension Testing of Metallic Materials*. 2016, ASTM International: West Conshohocken, PA.

211. ASTM International, *Standard Test Methods for Conducting Creep, Creep-Rupture, and Stress-Rupture Tests of Metallic Materials*. 2018, ASTM International: West Conshohocken, PA.

212. Buehler. *SumMet method for Ni-based Superallys*. 2020 [cited 2020 05/2020]; Available from: https://www.buehler.co.uk/sumMet.php?material=Ni%20%26%2345%3BBased%20Superallys.

213. Gribbin, S., S. Ghorbanpour, N.C. Ferreri, J. Bicknell, I. Tsukrov, and M. Knezevic, *Role of grain structure, grain boundaries, crystallographic texture, precipitates, and porosity on fatigue behavior of Inconel 718 at room and elevated temperatures.* Materials Characterization, 2019. **149**: p. 184-197.

214. Sabelkin, V.P., G.R. Cobb, T.E. Shelton, M.N. Hartsfield, D.J. Newell, R.P. O'Hara, and R.A. Kemnitz, *Mitigation of anisotropic fatigue in nickel alloy 718 manufactured via selective laser melting.* Materials & Design, 2019. **182**: p. 108095.

215. Tillmann, W., C. Schaak, J. Nellesen, M. Schaper, M.E. Aydinöz, and K.P. Hoyer, *Hot isostatic pressing of IN718 components manufactured by selective laser melting.* Additive Manufacturing, 2017. **13**: p. 93-102.

216. Pham, M.-S., B. Dovgyy, P.A. Hooper, C.M. Gourlay, and A. Piglione, *The role of side-branching in microstructure development in laser powder-bed fusion.* Nature Communications, 2020. **11**(1): p. 749.

217. Newell, D.J., R.P. O'Hara, G.R. Cobb, A.N. Palazotto, M.M. Kirka, L.W. Burggraf, and J.A. Hess, *Mitigation of scan strategy effects and material anisotropy through supersolvus annealing in LPBF IN718.* Materials Science and Engineering: A, 2019. **764**: p. 138230.

218. Blackwell, P.L., *The mechanical and microstructural characteristics of laser-deposited IN718.* Journal of Materials Processing Technology, 2005. **170**(1): p. 240-246.

219. Geiger, F., K. Kunze, and T. Etter, *Tailoring the texture of IN738LC processed by selective laser melting (SLM) by specific scanning strategies.* Materials Science and Engineering: A, 2016. **661**: p. 240-246.

220. Li, X., J.J. Shi, C.H. Wang, G.H. Cao, A.M. Russell, Z.J. Zhou, C.P. Li, and G.F. Chen, *Effect of heat treatment on microstructure evolution of Inconel 718 alloy fabricated by selective laser melting.* Journal of Alloys and Compounds, 2018. **764**: p. 639-649.

221. Watring, D.S., J.T. Benzing, N. Hrabe, and A.D. Spear, *Effects of laser-energy density and build orientation on the structure–property relationships in as-built Inconel 718 manufactured by laser powder bed fusion.* Additive Manufacturing, 2020. **36**: p. 101425.

222. Bean, G.E., T.D. McLouth, D.B. Witkin, S.D. Sitzman, P.M. Adams, and R.J. Zaldivar, *Build Orientation Effects on Texture and Mechanical Properties of Selective Laser Melting Inconel 718.* Journal of Materials Engineering and Performance, 2019. **28**(4): p. 1942-1949.

223. Wan, H., Z.-J. Zhou, C.-P. Li, G.-F. Chen, and G.P. Zhang, *Enhancing Fatigue Strength of Selective Laser Melting-Fabricated Inconel 718 by Tailoring Heat Treatment Route.* Advanced Engineering Materials, 2018: p. 1800307.

224. Karabegović, I., *New Technologies, Development and Application III*. 2020.

225. Cao, Y., P. Bai, F. Liu, and X. Hou, *Investigation on the precipitates of IN718 alloy fabricated by selective laser melting.* Metals, 2019. **9**(10).

226. Schirra, J.J., R.H. Caless, and R.W. Hatala, *The effect of Laves phases on the mechanical properties of wrought and cast +HIP Inconel 718*, in *Superalloys 718,625 and Various Derivatives*, E.A. Loria, Editor. 1991, The Minerals, Metals & Materials Society. p. 375-388.

227. Zhao, Y., Q. Guo, Z. Ma, and L. Yu, *Comparative study on the microstructure evolution of selective laser melted and wrought IN718 superalloy during subsequent heat treatment process and its effect on mechanical properties.* Materials Science and Engineering: A, 2020. **791**: p. 139735.

228. Kanagarajah, P., F. Brenne, T. Niendorf, and H.J. Maier, *Inconel 939 processed by selective laser melting: Effect of microstructure and temperature on the mechanical properties under static and cyclic loading.* Materials Science and Engineering: A, 2013. **588**: p. 188-195.

229. Li, Y., K. Chen, R.L. Narayan, U. Ramamurty, Y. Wang, J. Long, N. Tamura, and X. Zhou, *Multi-scale microstructural investigation of a laser 3D printed Ni-based superalloy.* Additive Manufacturing, 2020: p. 101220.

230. Arısoy, Y.M., L.E. Criales, T. Özel, B. Lane, S. Moylan, and A. Donmez, *Influence of scan strategy and process parameters on microstructure and its optimization in additively manufactured nickel alloy 625 via laser powder bed fusion.* The International Journal of Advanced Manufacturing Technology, 2017. **90**(5): p. 1393-1417.

231. Wan, H.Y., Z.J. Zhou, C.P. Li, G.F. Chen, and G.P. Zhang, *Effect of scanning strategy on mechanical properties of selective laser melted Inconel 718.* Materials Science and Engineering: A, 2019. **753**: p. 42-48.

232. Sheridan, L., O.E. Scott-Emuakpor, T. George, and J.E. Gockel, *Relating porosity to fatigue failure in additively manufactured alloy 718.* Materials Science and Engineering: A, 2018. **727**: p. 170-176.

233. Mancisidor, A.M., F. Garciandia, M.S. Sebastian, P. Álvarez, J. Díaz, and I. Unanue, *Reduction of the Residual Porosity in Parts Manufactured by Selective Laser Melting Using Skywriting and High Focus Offset Strategies.* Physics Procedia, 2016. **83**: p. 864-873.

234. Du, D., A. Dong, D. Shu, G. Zhu, B. Sun, X. Li, and E. Lavernia, *Influence of build orientation on microstructure, mechanical and corrosion behavior of Inconel 718 processed by selective laser melting.* Materials Science and Engineering: A, 2019. **760**: p. 469-480.

235. Shi, R., S.A. Khairallah, T.T. Roehling, T.W. Heo, J.T. McKeown, and M.J. Matthews, *Microstructural control in metal laser powder bed fusion additive manufacturing using laser beam shaping strategy.* Acta Materialia, 2020. **184**: p. 284-305.

236. Järvinen, J.-P., V. Matilainen, X. Li, H. Piili, A. Salminen, I. Mäkelä, and O. Nyrhilä, *Characterization of Effect of Support Structures in Laser Additive Manufacturing of Stainless Steel.* Physics Procedia, 2014. **56**: p. 72-81.

237. Song, H., T. McGaughy, A. Sadek, and W. Zhang, *Effect of structural support on microstructure of nickel base superalloy fabricated by laser-powder bed fusion additive manufacturing.* Additive Manufacturing, 2019. **26**: p. 30-40.

238. Carter, W.T., M.G. Jones, L. Yuan, N. Zhou, and S.J. Duclos, *Control of solidification in laser powder bed fusion additive manufacturing using a diode laser fiber array*, U.S. Patent, Editor. 2020, General Electric Company: USA.

239. Sola, A. and A. Nouri, *Microstructural porosity in additive manufacturing: The formation and detection of pores in metal parts fabricated by powder bed fusion.* Journal of Advanced Manufacturing and Processing, 2019.

240. Xiao, H., P. Xie, M. Cheng, and L. Song, *Enhancing mechanical properties of quasi-continuous-wave laser additive manufactured Inconel 718 through controlling the niobium-rich precipitates.* Additive Manufacturing, 2020. **34**: p. 101278.

241. Brenne, F., S. Leuders, and T. Niendorf, *On the Impact of Additive Manufacturing on Microstructural and Mechanical Properties of Stainless Steel and Ni-base Alloys.* BHM Berg- und Hüttenmännische Monatshefte, 2017. **162**(5): p. 199-202.

242. Cui, L., H. Su, J. Yu, J. Liu, T. Jin, and X. Sun, *The creep deformation and fracture behaviors of nickel-base superalloy M951G at 900 °C.* Materials Science and Engineering: A, 2017. **707**.

243. Ni, T. and J. Dong, *Creep behaviors and mechanisms of Inconel718 and Allvac718plus.* Materials Science and Engineering: A, 2017. **700**: p. 406-415.

244. Chen, K., J. Dong, and Z. Yao, *Creep Failure and Damage Mechanism of Inconel 718 Alloy at 800–900 °C.* Metals and Materials International, 2019.

245. International Organization for Standardization, *ISO 4287:1997 Geometrical Product Specifications (GPS) — Surface texture: Profile method — Terms, definitions and surface texture parameters*. 2015, International Organization for Standardization,.

246. Vieille, B., C. Keller, M. Mokhtari, H. Briatta, T. Breteau, J. Nguejio, F. Barbe, M. Ben Azzouna, and E. Baustert, *Investigations on the fracture behavior of Inconel 718 superalloys obtained from cast and additive manufacturing processes.* Materials Science and Engineering: A, 2020. **790**: p. 139666.

247. Chen, W. and M.C. Chaturvedi, *Dependence of creep fracture of Inconel 718 on grain boundary precipitates.* Acta Materialia, 1997. **45**(7): p. 2735-2746.

248. Moussaoui, K., W. Rubio, M. Mousseigne, T. Sultan, and F. Rezai, *Effects of Selective Laser Melting additive manufacturing parameters of Inconel 718 on porosity, microstructure and mechanical properties.* Materials Science and Engineering: A, 2018. **735**: p. 182-190.

249. Černý, I., J. Kec, T. Vlasák, L. Remar, M. Jersák, and M. Zetek, *Mechanical Properties and Fatigue Resistance of 3D Printed Inconel 718 in Comparison with Conventional Manufacture.* Key Engineering Materials, 2018. **774**: p. 313-318.

250. Deng, D., *Additively Manufactured Inconel 718 : Microstructures and Mechanical Properties*, in *Linköping Studies in Science and Technology. Licentiate Thesis*. 2018, Linköping University Electronic Press: Linköping. p. 69.

251. Liu, Y., M. Kang, Y. Wu, M. Wang, H. Gao, and J. Wang, *Effects of microporosity and precipitates on the cracking behavior in polycrystalline superalloy Inconel 718.* Materials Characterization, 2017. **132**: p. 175-186.

252. Sanchez, S., D. Rengasamy, C.J. Hyde, G.P. Figueredo, and B. Rothwell, *Machine learning to determine the main factors affecting creep rates in laser powder bed fusion.* Journal of Intelligent Manufacturing, 2021.

253. Babamiri, B.B., J. Indeck, G. Demeneghi, J. Cuadra, and K. Hazeli, *Quantification of porosity and microstructure and their effect on quasi-static and dynamic behavior of additively manufactured Inconel 718.* Additive Manufacturing, 2020. **34**.

254. Rafiei, M., H. Mirzadeh, and M. Malekan, *Delta processing effects on the creep behavior of a typical Nb-bearing nickel-based superalloy.* Vacuum, 2021. **184**: p. 109913.

255. Yeh, A.-C., K.-W. Lu, C.-M. Kuo, H.-Y. Bor, and C.-N. Wei, *Effect of serrated grain boundaries on the creep property of Inconel 718 superalloy.* Materials Science and Engineering: A, 2011. **530**: p. 525-529.

256. Trosch, T., J. Strößner, R. Völkl, and U. Glatzel, *Microstructure and mechanical properties of selective laser melted Inconel 718 compared to forging and casting.* Materials Letters, 2016. **164**: p. 428-431.

257. Kuo, Y.-L., S. Horikawa, and K. Kakehi, *The effect of interdendritic δ phase on the mechanical properties of Alloy 718 built up by additive manufacturing.* Materials & Design, 2017. **116**: p. 411-418.

258. Cocks, A.C.F., *The nucleation and growth of voids in a material containing a distribution of grain-boundary particles.* Acta Metallurgica, 1985. **33**(1): p. 129-137.

259. Garofalo, F., *Effect of Grain Size on the Creep Behavior of an Austenitic lron - Base Alloy.* Trans. AIME, 1964. **230**: p. 1460-1467.

260. Berger, C., A. Thoma, and A. Scholz. *Creep modelling of waspaloy*. in *PARSONS 2003: Sixth International Charles Parsons Turbine Conference*. 2003.

261. Vilaro, T., C. Colin, J.D. Bartout, L. Nazé, and M. Sennour, *Microstructural and mechanical approaches of the selective laser melting process applied to a nickel-base superalloy.* Materials Science and Engineering: A, 2012. **534**: p. 446-451.

262. Mahajan, S., C.S. Pande, M.A. Imam, and B.B. Rath, *Formation of annealing twins in f.c.c. crystals.* Acta Materialia, 1997. **45**(6): p. 2633-2638.

263. Cui, C.Y., Y.F. Gu, Y. Yuan, T. Osada, and H. Harada, *Enhanced mechanical properties in a new Ni–Co base superalloy by controlling microstructures.* Materials science & engineering. A, Structural materials : properties, microstructure and processing, 2011. **528**(16): p. 5465-5469.

264. Shaw, L.L., J. Villegas, J.-Y. Huang, and S. Chen, *Strengthening via deformation twinning in a nickel alloy.* Materials Science and Engineering: A, 2008. **480**(1): p. 75-83.

265. Yu, Z., H. Jing, L. Xu, L. Zhao, and Y. Han, *Microstructure and texture study on an advanced heat-resistant alloy during creep.* Materials Characterization, 2017. **130**.

266. Gokcekaya, O., T. Ishimoto, S. Hibino, J. Yasutomi, T. Narushima, and T. Nakano, *Unique crystallographic texture formation in Inconel 718 by laser powder bed fusion and its effect on mechanical anisotropy.* Acta Materialia, 2021. **212**: p. 116876.

267. Hovig, E.W., A.S. Azar, F. Grytten, K. Sørby, and E. Andreassen, *Determination of Anisotropic Mechanical Properties for Materials Processed by Laser Powder Bed Fusion.* Advances in Materials Science and Engineering, 2018. **2018**.

268. Azadian, S., *Aspects of precipitation in alloy Inconel 718*. 2004, Luleå tekniska universitet.

269. Floreen, S., G.E. Fuchs, and W.J. Yang, *The metallurgy of alloy 625.* Superalloys, 1994. **718**(625): p. 13-37.

270. Sundararaman, M., P. Mukhopadhyay, and S. Banerjee, *Carbide precipitation in nickel base superalloys 718 and 625 and their effect on mechanical properties.* Superalloys, 1997. **718**: p. 625-706.

271. Chen, Q.Z., N. Jones, and D.M. Knowles, *The microstructures of base/modified RR2072 SX superalloys and their effects on creep properties at elevated temperatures.* Acta Materialia, 2002. **50**(5): p. 1095-1112.

272. Kumar, D., G. Shankar, K.G. Prashanth, and S. Suwas, *Texture dependent strain hardening in additively manufactured stainless steel 316L.* Materials Science and Engineering: A, 2021. **820**: p. 141483.

273. Rettberg, L.H. and T.M. Pollock, *Localized recrystallization during creep in nickel-based superalloys GTD444 and René N5.* Acta Materialia, 2014. **73**: p. 287-297.

274. Shams, S.A.A., G. Kim, J.W. Won, J.N. Kim, H.S. Kim, and C.S. Lee, *Effect of grain size on the low-cycle fatigue behavior of carbon-containing high-entropy alloys.* Materials Science and Engineering: A, 2021. **810**: p. 140985.

275. Song, B., S. Dong, Q. Liu, H. Liao, and C. Coddet, *Vacuum heat treatment of iron parts produced by selective laser melting: microstructure, residual stress and tensile behavior.* Materials & Design (1980-2015), 2014. **54**: p. 727-733.

276. Valle, L.C.M., L.S. Araújo, S.B. Gabriel, J. Dille, and L.H. de Almeida, *The Effect of δ Phase on the Mechanical Properties of an Inconel 718 Superalloy.* Journal of materials engineering and performance, 2013. **22**(5): p. 1512-1518.

277. Loria, E., *Superalloys 718, 625, 706 and various derivatives.* Pittsburgh, 1994: p. 1994.

278. Sadeghi, E., P. Karimi, S. Momeni, M. Seifi, A. Eklund, and J. Andersson, *Influence of thermal post treatments on microstructure and oxidation behavior of EB-PBF manufactured Alloy 718.* Materials characterization, 2019. **150**: p. 236-251.

279. Kaufman, M. and A. Palty, *The phase structure of Inconel-718 and Inconel-702 alloys.* Transactions of the metallurgical society of AIME, 1961. **221**(6): p. 1253-1262.

280. Goel, S., E. Zaninelli, J. Gårdstam, U. Klement, and S. Joshi, *Microstructure evolution-based design of thermal post-treatments for EBM-built Alloy 718.* Journal of Materials Science, 2021. **56**(8): p. 5250-5268.

281. Poole, J.M., K.R. Stultz, and J.M. Manning, *The Effect of INGOT Homogenization Practice on the Properties of Wrought Alloy 718 and Structure.* Superalloys, 1989: p. 219-228.

282. Brooks, J. and P. Bridges, *Metallurgical stability of Inconel alloy 718.* Superalloys, 1988. **88**: p. 33-42.

283. Mitchell, A., A. Schmalz, C. Schvezov, and S. Cockcroft, *The precipitation of primary carbides in alloy 718.* superalloys, 1994. **718**(625,706): p. 65-78.

284. Eriksson, R., J. Moverare, and Z. Chen, *A low cycle fatigue life model for a shot peened gas turbine disc alloy.* International Journal of Fatigue, 2019. **124**: p. 34-41.

285. Sims, C.T., N.S. Stoloff, and W.C. Hagel, *superalloys II*. Vol. 8. 1987: Wiley New York.

286. Xie, X.S., S.H. Fu, S.Q. Zhao, and J.X. Dong. *The precipitation strengthening effect of Nb, Ti and Al in cast/wrought Ni-base superalloys*. in *Materials Science Forum*. 2010. Trans Tech Publ.

287. Lin, Y.-C., J. Deng, Y.-Q. Jiang, D.-X. Wen, and G. Liu, *Hot tensile deformation behaviors and fracture characteristics of a typical Ni-based superalloy.* Materials & Design, 2014. **55**: p. 949-957.

288. Huang, Y. and T.G. Langdon, *The evolution of delta-phase in a superplastic Inconel 718 alloy.* Journal of Materials Science, 2007. **42**(2): p. 421-427.

289. Hassan, B. and J. Corney, *Grain boundary precipitation in Inconel 718 and ATI 718Plus.* Materials Science and Technology, 2017. **33**(16): p. 1879-1889.

290. Zhang, H., C. Li, Q. Guo, Z. Ma, Y. Huang, H. Li, and Y. Liu, *Delta precipitation in wrought Inconel 718 alloy; the role of dynamic recrystallization.* Materials Characterization, 2017. **133**: p. 138-145.

291. Goel, S., E. Zaninelli, T. Gundgire, M. Ahlfors, O. Ojo, U. Klement, and S. Joshi, *Microstructure evolution and mechanical response-based shortening of thermal post-treatment for electron beam melting (EBM) produced Alloy 718.* Materials Science and Engineering: A, 2021. **820**: p. 141515.

292. Balachandramurthi, A., J. Moverare, S. Mahade, and R. Pederson, *Additive Manufacturing of Alloy 718 via Electron Beam Melting: Effect of Post-Treatment on the Microstructure and the Mechanical Properties.* Materials, 2018. **12**(1): p. 68.

293. Bassini, E., G. Marchese, and A. Aversa, *Tailoring of the microstructure of laser powder bed fused inconel 718 using solution annealing and aging treatments.* Metals, 2021. **11**(6).

294. Geng, L., Y.-S. Na, and N.-K. Park, *Continuous cooling transformation behavior of Alloy 718.* Materials Letters, 1997. **30**(5): p. 401-405.

295. Gallmeyer, T.G., S. Moorthy, B.B. Kappes, M.J. Mills, B. Amin-Ahmadi, and A.P. Stebner, *Knowledge of process-structure-property relationships to engineer better heat treatments for laser powder bed fusion additive manufactured Inconel 718.* Additive Manufacturing, 2020. **31**: p. 100977.

296. Jiang, R., A. Mostafaei, Z. Wu, A. Choi, P.W. Guan, M. Chmielus, and A.D. Rollett, *Effect of heat treatment on microstructural evolution and hardness homogeneity in laser powder bed fusion of alloy 718.* Additive Manufacturing, 2020. **35**.

297. Kouraytem, N., J. Varga, B. Amin-Ahmadi, H. Mirmohammad, R.A. Chanut, A.D. Spear, and O.T. Kingstedt, *A recrystallization heat-treatment to reduce deformation anisotropy of additively manufactured Inconel 718.* Materials & Design, 2021. **198**: p. 109228.

298. Zhao, Y., N. Sargent, K. Li, and W. Xiong, *A new high-throughput method using additive manufacturing for alloy design and heat treatment optimization.* Materialia, 2020. **13**: p. 100835.